

**THE STUDY OF $^{29}\text{Si}(p,\gamma)^{30}\text{P}$ AND ITS IMPACT ON CLASSICAL NOVA
NUCLEOSYNTHESIS**

Lori Norene Downen

A dissertation submitted to the faculty of the University of North Carolina at Chapel Hill in partial fulfillment of the requirements for the degree of Doctor of Philosophy in the Department of Physics and Astronomy.

Chapel Hill
2019

Approved by:

Christian Iliadis

J. Christopher Clemens

Laurie E. McNeil

Arthur E. Champagne

Thomas B. Clegg

© 2019
Lori Norene Downen
ALL RIGHTS RESERVED

ABSTRACT

LORI NORENE DOWNEN: The Study of $^{29}\text{Si}(p,\gamma)^{30}\text{P}$ and Its Impact on Classical Nova Nucleosynthesis.

(Under the direction of Christian Iliadis)

Classical novae are stellar explosions occurring in binary systems consisting of a white dwarf and a main sequence partner. Thermonuclear runaways, occurring after the accretion of matter from the main sequence star onto the surface of the white dwarf, eject nuclear processed material into the interstellar medium and significantly contribute to the galactic chemical evolution. Novae can be observed spectroscopically as the ejecta shells disperse or isotopically after the matter condenses into presolar stardust grains, which are incorporated into meteors and sometimes arrive on earth many years later. These observables carry signatures of the processes that created them and aid our understanding of classical novae. However, open questions about the effect of reaction rate uncertainty compromise the effective use of these tools and our understanding of novae as a whole.

First, nova nucleosynthesis simulations were performed to explore the effect of reaction rate uncertainty on the final abundances of ejected matter. These results, when compared to elemental ratios from spectroscopic observations and the isotopic ratios of presolar grain measurements, revealed the critical importance of several reactions.

One of these reactions, $^{29}\text{Si}(p,\gamma)^{30}\text{P}$, was chosen as the focus of this dissertation. Several resonances in this reaction were investigated at the Laboratory for Experimental Nuclear Astrophysics. A new measurement of the $E_r^{lab} = 325.79 \pm 0.58$ keV resonance improved upon the uncertainty of the resonance strength measured by [Reinecke et al. \(1985\)](#) and found that the resonance strength, $\omega\gamma = 23 \pm 4$ meV, was a factor of 1.5 larger than previously thought. The $E_r^{lab} = 314.36 \pm 0.81$ keV resonance was observed for the first time, and its strength, $\omega\gamma = 100 \pm 20$ μeV , proved significantly

stronger than predicted by theoretical estimates. An experimental resonance strength upper limit comparable to theoretical estimates, $\omega\gamma < 3.69 \times 10^{-7}$ eV, was established for the unobserved $E_r^{lab} = 221$ keV resonance as well.

The impact of these measurements was clear upon the reevaluation of the $^{29}\text{Si}(p,\gamma)^{30}\text{P}$ rate. Compared to the recent evaluation of [Iliadis *et al.* \(2010c\)](#), the new thermonuclear rate shows a factor of 1.5 increase and a twofold reduction to its uncertainty in the Gamow window of classical nova nucleosynthesis.

“I’m sorry, I just started hearing really loud circus music in my head. What did you say?”

—Leslie Knope, *Parks & Recreation*

ACKNOWLEDGMENTS

If brevity is the soul of wit, I am afraid I am not very witty. The one thing I am, however, is incredibly grateful. I'm also beginning to realize that I probably shouldn't have left this section for last, because after over two hundred pages, I feel like I've written all of the words out of myself. Also, I've already used all of the sophisticated words I know so please forgive the casual tone.

I imagine very few people are born and bred nuclear astrophysicists, and my career trajectory would not be what it is if not for the guidance of a number individuals during my undergraduate years.

To begin, I would like to thank Drs. Ruth Chabay and Bruce Sherwood. I feel privileged to have benefited from your skilled teaching and thoughtful curricula, and it incited in me a passion for a subject that I had frankly written off as just another requirement on my way to an engineering degree. Oh, how wrong I was. Later on when I was hired to help teach the laboratory part of your Matter & Interactions courses, I was over the moon, and not just because I could quit my part-time job at Walmart. Helping other students, gaining a deeper understanding of the material, and becoming part of the community that you built is and will always be one of my most formative experiences.

Speaking of this M & I community, I would be remiss if I didn't recognize Dr. Prabha Ramakrishnan for taking me under her wing during my time as a teaching assistant. I learned so much about classroom and laboratory management from your example, and your generosity with your time, advice, and humor meant the world to me when physics (and physicists especially) still felt so intimidating and foreign. It also didn't hurt that you are an avid crafter like myself! Thank you so much.

It was also as part of this special group that I was introduced to the incomparable Dr. Laura Clarke, to whom I am so deeply indebted I cannot adequately put my gratitude into words. You took a chance in bringing me into your research group, and I can only hope I was worth the gamble. I learned so much from you: how to conduct an experiment and conduct yourself as a scientist, how to be conscientious in your work and in your treatment of your colleagues, how to be liberal with your expertise and your patience, and countless other lessons. I can only hope I've done justice to your mentorship. As part of your research group, I thought "This is how this is supposed to be." I still think that, and those experiences have guided me throughout my graduate career. I would be remiss if I didn't mention that my graduate career might not have been if you hadn't been helping me every step of the way ... and if you hadn't compared the graduate admission process to puppy adoption. It truly is the perfect analogy. In short, thank you for everything.

Guided by my first-rate undergraduate experiences, I knew when I first visited LENA that it was a special place: appearing somewhere between a scifi movie set and a mad scientist's lair and filled to the brim with people fervently trying to chip away at the mysteries of the stars. I have learned so much from this community of people that I will never be able to thank them enough. But I will endeavor to do so anyway in the most effusive, embarrassing way possible.

First and foremost, I would like to recognize the enormous debt I owe to Dr. Christian Iliadis, my thesis advisor for many years. Imagine for a moment that you could have every question that crosses your mind answered by the preeminent scientist and communicator in your field. Such has been my experience under Christian's tutelage. Thank you, Christian, for helping me through all of those "bookkeeping" challenges of my Master's project. Thank you for sending me to present my work at many exciting and far-flung conferences and, perhaps more importantly, coaching me through said presentations: we both know it is not my strong suit. Thank you for your many

hands-on lessons at a laptop or an electronics rack. Thank you for your seemingly endless well of patience while I've been writing this dissertation, and thank you for a multitude of other things I'm forgetting.

I am incredibly grateful for the support of Dr. Art Champagne. Whenever I ran into an issue outside of Christian's expertise, I knew that I could count on Art to help me through it. Thank you, Art, for your freely given and thoughtful advice during group meetings and for numerous lessons in the laboratory. I greatly appreciate all of your support over the years.

I'd also like to thank Dr. Tom Clegg for a goodly number of reasons. Thank you, Tom, for guiding the ECR modifications that made the latter part of my experiment possible, and thank you for your willingness to include me in these efforts. Being far removed from that project initially, I had a great deal of catching up to do, but your patience with my many questions never wavered. I will always happily remember the infectious enthusiasm that you brought to lab, your afternoon phone calls to check in, and countless control room troubleshooting discussions.

I'm afraid I am dating my graduate tenure here, but I have had the virtue of working with Dr. Richard Longland when he was a senior graduate student, a postdoc, and an assistant professor. I only have glowing praise for his caliber as a scientist and as an individual. Rich, thank you for finding time to show me the ropes when I was a rudderless and inexperienced grad student and you were more than busy enough finishing your own degree. Thank you for fielding my many (and occasionally impertinent) questions about your old codes that you would have been justified in abandoning to time. Your generosity with your time made me feel so welcome in LENA. I am positively overjoyed at your career success and for the generations of LENA students who will benefit from your guidance.

I have had the good fortune to work with a handful of stellar graduate students during my time in the hallowed halls of LENA. I have a great deal to thank these

folks —Dr. Keegan Kelly, Dr. Jack Dermigny, Dr. Sean Hunt, Dr. Andrew Cooper, and David Little—for, so much so that I don't think I would be able to fit their contributions in another 300 pages of text. Thank you, Keegan, for being the best research partner I could hope for. Thank you, Jack, for answering so many analysis and fraction fitting questions, and thank you for stealing food off my plate at group lunches as it never ceased to amuse me. Thank you, Sean, for keeping the JN in tip-top for my yield curve measurements and for always questioning my more idiosyncratic instructions. Thank you, Andrew, for your tireless work on the ECR that allowed me to complete my experiment, your infallible sense of fairness, and a multitude of discussions about military campaigns, punk culture, and a bunch of other things of which I was previously ignorant. Finally, thank you, David, for your generous aid with my GEANT4 software issues and for your willingness to offer encouragement in an academic setting. I know that, wherever I find myself working in the future, I will likely never work in a team of your equal.

It goes without saying that the laboratory would be nothing without the support of the TUNL technical staff. Actually, that's not true: the laboratory would be a lonely basement full of broken bits without them. I'd like to thank Chris Westerfeldt and John Dunham for their patience and help with the LENA ion implanter when I had nary a scrap of experience with vacuum systems. Thank you, Bret Carlin, for answering all of my (mostly dumb) electronics questions and for copious amounts of Futurama trivia. Richard O'Quinn, thank you for always making sure I was safe in the laboratory even when I was distracted and juggling too many tasks. Tom Calisto has my gratitude for his work on the ECR as well as my awe for his technical expertise and kindness in equal measure. I am deeply grateful to have worked along side all of you and learned from your instruction.

Based on the number of people I have to thank in the laboratory, someone may get the impression that I spent all of my waking hours there as well. On the occasion

that I did emerge from the lab, there were a few people in the department I wanted to spend my time with and to whom I owe a great deal.

The first person I would like is Jeffrey Olander. Technically, I've known Jeff since ancient annals of our undergraduate years, but I feel like we truly got to know each other during the trenches of our first year in graduate school and the years that have followed. Jeff, thank you for so many late nights working with me on problem sets via Skype. I'm incredibly grateful for all of those lunches where we discussed not just our work lives and frustrations but your interest in birding, my burgeoning passion for silversmithing, and so many other delights. Thank you for your support and camaraderie over the years.

I also owe a great deal of gratitude to the entire Hadsell family, Drs. Michael and Courtney Hadsell and their canine caretaker Bailey. What a serendipitous happenstance to be assigned as your officemate. Thank you for including a goofy newcomer on your trips to Franklin Street, movie nights, and trips to Colorado. My thanks go to Bailey, the littlest member of the Hadsell clan and an excellent person of fur, for always crawling into my lap when I was having a bad day. Mike, thank you all of those pep talks and your confidence in my abilities as a researcher when I was feeling decidedly less than confident. Most of all, thank you, Courtney, for being my personal cheerleader through the nightmare that was the qualifying exam and through the final, incredibly difficult years of my experimental work and thesis writing. I think I've finally defeated the main boss, Court.

Lastly, I would like to thank Dr. David Eby. I will admit I was more than a little skeptical when Art decided to assign a theorist to assist me with the ion implanter—a decidedly real, messy piece of machinery on the best of days. Clearly, my skepticism was premature as you were a tremendous help with both the implanter and keeping me going throughout the project, David. Later on, our early morning coffee dates got me through countless grueling days spent in the laboratory. Thank you for always

listening to my dramatic retellings of minor gripes, sometimes to play devil's advocate to help me gain some perspective and occasionally to tell me to "set it on fire" to make me laugh and stop taking things so seriously. I am keenly aware of just how fortunate I am to call you a friend.

Though some scientists may try to convince you otherwise, I do not think anyone can endure the rigors of a PhD program without copious support outside the ivory tower (or the basement laboratory, as the case may be). I, for one, have leaned on a few shoulders when things weren't going so well and shared the joys of a job well done when things were.

First, I would like to thank the absolute best group of friends a girl can ask for. Andrea, Pam, Ruth, and Sam—thank you! Thank you for caring about how I am faring instead of how my research is faring, for making sure we are always together for the holidays, and for every happy diversion over the years. I am so very lucky to have you all in my life.

To my parents, thank you for pushing me to do well in my classes, for encouraging my often eccentric interests, and for always being in my corner. Thank you for teaching me that life is not a zero-sum game, and for making me into the person I am today. I can only hope I've done justice to your example.

I would also like to thank my sister—the smartest, bravest person I know. Thank you for teaching me multiplication when I was in kindergarten. I acted like it didn't stick, but I was just an obstinate little kid. Thank you for your unending support and for ensuring our academic achievements never descended into competition.

Finally, I'd like to thank my fiancé, David Tredwell. Not many people can count themselves as lucky as I am for meeting my life partner in crime during freshman year of high school. Dave, thank you for listening to me rant when I was struggling, for the spontaneous dance parties with Arya when everything was going well, and for always producing tea at exactly the right moment. I love you, and I like you.

TABLE OF CONTENTS

LIST OF TABLES	xvi
LIST OF FIGURES	xviii
1 ASTROPHYSICAL MOTIVATION	1
1.1 Classical Novae	4
1.2 Decoding Classical Nova Nucleosynthesis	7
1.2.1 Elemental Abundances from Spectroscopic Observations	7
1.2.2 Isotopic Abundances from Presolar Grain Measurements	12
1.3 The Master Plan	17
2 NUCLEAR ASTROPHYSICS THEORY	19
2.1 The Nuclear Cross Section	19
2.2 The Coulomb Barrier	21
2.3 Thermonuclear Reaction Rates	24
2.3.1 Nonresonant Reaction Rates	25
2.3.2 Resonant Reaction Rates	30
3 CLASSICAL NOVA NUCLEOSYNTHESIS	35
3.1 Reaction Network & Input Parameters	36
3.2 Single- & Multiple-Zone Simulations	40
3.3 The Elemental Abundance Study	45
3.3.1 The Development of Nuclear Thermometers	46
3.3.2 Comparison to Spectroscopic Observations	53
3.3.3 Conclusions	61

3.4	The Isotopic Ratio Study	61
4	EXPERIMENTAL SETUP	65
4.1	Accelerators	66
4.1.1	LENA I: The 1-MV JN Van de Graaff Accelerator	66
4.1.2	LENA II: The 240 kV Electron Cyclotron Resonance Accelerator	67
4.2	Target Station	73
4.3	Detection System	75
4.3.1	HPGe Detector	77
4.3.2	NaI(Tl) Annulus	83
4.3.3	Muon Veto Shield	83
4.3.4	Coincidence Counting System	84
5	SILICON-29 ENRICHED TARGETS	89
5.1	Target Preparation & Maintenance	89
5.1.1	Chemical Etching	90
5.1.2	Resistive Heating	91
5.1.3	Implantation	92
5.1.4	Target Restoration	95
5.2	Yield Curve Target Studies	96
6	DATA ANALYSIS METHODS	101
6.1	Methodology	102
6.2	Template Generation	107
6.2.1	Template Corrections	109
6.3	Goodness of Fit Test	112
6.4	Summary	114

7	$^{29}\text{Si}(p,\gamma)^{30}\text{P}$ PROTON CAPTURE	116
7.1	416 keV Resonance	120
7.1.1	Measurement	123
7.1.2	Analysis	126
7.1.3	Resonance Energy	133
7.1.4	Target Stoichiometry Determination	135
7.2	324 keV Resonance	138
7.2.1	Measurement	141
7.2.2	Analysis	146
7.2.3	Resonance Energy	152
7.2.4	Resonance Strength	152
7.3	314 keV Resonance	155
7.3.1	Measurement	156
7.3.2	Analysis	159
7.3.3	Resonance Energy	164
7.3.4	Resonance Strength	166
7.4	221 keV Resonance	167
7.4.1	Measurement	168
7.4.2	Analysis	172
7.4.3	Resonance Strength	178
7.5	Summary	181
8	REACTION RATE EVALUATION	184
8.1	Monte Carlo Sampling and Rate Calculations	184
8.1.1	Rate Calculations	185

8.1.2	Direct Capture Reaction Rate Calculations	186
8.1.3	Narrow Resonance Reaction Rate Calculations	187
8.1.4	Reaction Rate Calculations Involving Unobserved Resonances .	188
8.2	Nonresonant Contributions	189
8.3	Resonant Contributions	191
8.3.1	$E_r^{CM} < 300$ keV	191
8.3.2	$E_r^{CM} = 300$ keV–500 keV	193
8.3.3	$E_r^{CM} > 500$ keV	193
8.4	The New $^{29}\text{Si}(p,\gamma)^{30}\text{P}$ Reaction Rate	197
8.5	Comparison to Previous Rate Evaluation	205
9	CONCLUSIONS	209
	APPENDIX A BOUND STATE BRANCHING RATIOS	211
	APPENDIX B PROBABILITY DENSITY FUNCTIONS	213
B.1	Gaussian distribution	213
B.2	Lognormal distribution	214
B.3	Porter-Thomas distribution	216
	REFERENCES	217

LIST OF TABLES

1.1	Assumed Average Elemental Masses and Uncertainties in Neon Novae . .	10
1.2	Summary of Spectroscopically Observed Abundances for Neon Novae . .	11
1.3	Summary of Isotopic Ratios from Nova Presolar Candidate Grains	16
3.1	Selected Properties of Evolutionary Neon Nova Models	38
3.2	Initial Composition of Presented Nova Simulations	39
3.3	Uncertainty Sources of Neon Nova Abundance Predictions	51
4.1	Specifications of the LENA Detection System	76
5.1	$^{29}\text{Si}(\text{p},\gamma)^{30}\text{P}$ $E_r^{\text{lab}} = 416$ keV Yield Curve Analysis	99
7.1	Summary of $^{29}\text{Si}(\text{p},\gamma)^{30}\text{P}$ Resonance Data Collection	117
7.2	Systematic Uncertainties of the $^{29}\text{Si}(\text{p},\gamma)^{30}\text{P}$ Resonance Study	119
7.3	$^{29}\text{Si}(\text{p},\gamma)^{30}\text{P}$ $E_r^{\text{lab}} = 416$ keV Resonance Strength Measurements	121
7.4	Energies & Decay Intensities for the $E_r^{\text{lab}} = 416$ keV Resonance	126
7.5	$E_r^{\text{lab}} = 416$ keV Fit Results	134
7.6	$^{29}\text{Si}(\text{p},\gamma)^{30}\text{P}$ $E_r^{\text{lab}} = 324$ keV Resonance Strength Measurements	140
7.7	Energies & Decay Intensities for the $E_r^{\text{lab}} = 324$ keV Resonance	145
7.8	$E_r^{\text{lab}} = 324$ keV Fit Results	151
7.9	Energies & Decay Intensities for the $E_r^{\text{lab}} = 314$ keV Resonance	158
7.10	$E_r^{\text{lab}} = 314$ keV Fit Results	165
7.11	Energies & Decay Intensities for the $E_r^{\text{lab}} = 221$ keV Resonance	172
7.12	$E_r^{\text{lab}} = 221$ keV Fit Results	177
7.13	Summary of the $^{29}\text{Si}(\text{p},\gamma)^{30}\text{P}$ Resonance Study Results	182
8.1	Probability Density Functions of Nuclear Properties	185
8.2	Astrophysical S-factor Approximation Parameters	190

8.3	Unobserved Resonance Parameters	192
8.4	Resonance Strengths for the $^{29}\text{Si}(p,\gamma)^{30}\text{P}$ Reaction Rate Calculation	194
8.5	$^{29}\text{Si}(p,\gamma)^{30}\text{P}$ Reaction Rates from the Current Study	199
A.1	Gamma Decay of ^{30}P Bound States	212

LIST OF FIGURES

1.1	Chart of the Nuclides Segment	2
1.2	Hertzsprung-Russell Diagram	3
1.3	Diagram of Binary Star System	4
1.4	Neon Nova Nucleosynthesis	6
1.5	Presolar Grain Images	13
1.6	Carbon & Nitrogen Isotopic Ratios of Presolar Grains	14
2.1	Nuclear Physics Experiment Setup	20
2.2	Nuclear & Coulomb Potentials	23
2.3	Nonresonant Cross Section & S-factor	27
2.4	Narrow Resonance Energy Level Diagram	31
3.1	Temperature-Density Curves for Innermost Shell of Nova Models	41
3.2	Temperature-Density Curves for Multiple Shells of a Nova Model	42
3.3	Comparison of Post-Processing & Hydrodynamic Elemental Abundances	44
3.4	Normalized Final Elemental Abundances versus Atomic Number	47
3.5	Nova Thermometer Candidates versus Peak Temperature	48
3.6	Eight Nuclear Thermometer Candidates versus Peak Temperature	50
3.7	Three-Element Plots Comparing Simulated & Observed Elemental Ratios	54
3.8	Observed & Simulated Values of Nuclear Thermometers in V838 Her	55
3.9	Peak Temperature & White Dwarf Mass Estimates for Select Novae	60
3.10	Comparison of Measured & Simulated Silicon Isotopic Ratios	63
4.1	LENA Facility Schematic	66
4.2	LENA I Ion Source Diagram	68
4.3	LENA I Plasma	69

4.4	LENA II Diagram	70
4.5	LENA Target Station	73
4.6	LENA $\gamma\gamma$ -Coincidence Detection System	77
4.7	HPGe Peak Efficiency Plot	82
4.8	Illustration of the LENA $\gamma\gamma$ -Coincidence Detector Operation	84
4.9	$\gamma\gamma$ -Coincidence 2D Histogram & Gating Scheme	85
4.10	Comparison of the HPGe Singles & $\gamma\gamma$ -Coincidence Spectra	87
5.1	Preparation of Target Backing	91
5.2	SNICS Source Diagram	94
5.3	^{29}Si -Implanted Target Photos	95
5.4	Cross Section & Yield Curve of the $^{29}\text{Si}(\text{p},\gamma)^{30}\text{P}$ $E_r^{\text{lab}} = 416$ keV Resonance .	97
6.1	Analysis Method Illustration	105
6.2	Decay of a Compound Nucleus via γ -ray Emission	107
7.1	^{30}P Energy Level Diagram	118
7.2	Pulse-Height Spectra of the $E_r^{\text{lab}} = 416$ keV Resonance	125
7.3	$E_r^{\text{lab}} = 416$ keV Singles Fit Posterior Plots	129
7.4	$E_r^{\text{lab}} = 416$ keV Singles Abridged Spectrum Fit	130
7.5	$E_r^{\text{lab}} = 416$ keV Coincidence Fit Posterior Plots	131
7.6	$E_r^{\text{lab}} = 416$ keV Coincidence Abridged Spectrum Fit	132
7.7	Yield Curve of $E_r^{\text{lab}} = 324$ keV Resonance	142
7.8	Yield Curve of the $E_r^{\text{lab}} = 314$ keV & 324 keV Resonances	143
7.9	Pulse-Height Spectra of the $E_r^{\text{lab}} = 324$ keV Resonance	144
7.10	$E_r^{\text{lab}} = 324$ keV Singles Abridged Spectrum Fit	147
7.11	$E_r^{\text{lab}} = 324$ keV Singles Fit Posterior Plots	148

7.12	$E_r^{lab} = 324$ keV Coincidence Fit Posterior Plots	149
7.13	$E_r^{lab} = 324$ keV Coincidence Abridged Spectrum Fit	150
7.14	Comparison of $E_r^{lab} = 324$ keV Resonance Strengths	154
7.15	Pulse-Height Spectra of the $E_r^{lab} = 314$ keV Resonance	157
7.16	$E_r^{lab} = 314$ keV Singles Abridged Spectrum Fit	160
7.17	$E_r^{lab} = 314$ keV Singles Fit Posterior Plots	161
7.18	$E_r^{lab} = 314$ keV Coincidence Fit Posterior Plots	163
7.19	$E_r^{lab} = 314$ keV Coincidence Abridged Spectrum Fit	164
7.20	Pulse-Height Spectra of the $E_r^{lab} = 221$ keV Resonance	171
7.21	$E_r^{lab} = 221$ keV Singles Fit Posterior Plots	173
7.22	$E_r^{lab} = 221$ keV Singles Abridged Spectrum Fit	174
7.23	$E_r^{lab} = 221$ keV Coincidence Fit Posterior Plots	175
7.24	$E_r^{lab} = 221$ keV Coincidence Abridged Spectrum Fit	176
7.25	Number of Reactions Posteriors from $E_r^{lab} = 221$ keV Analysis	180
8.1	Nonresonant S-factor Approximation	190
8.2	Temperature-Dependent $^{29}\text{Si}(p,\gamma)^{30}\text{P}$ Reaction Rate Probability Density . .	201
8.3	$^{29}\text{Si}(p,\gamma)^{30}\text{P}$ Reaction Rate Probability Density Functions	202
8.4	Fractional Contributions to the $^{29}\text{Si}(p,\gamma)^{30}\text{P}$ Reaction Rate	204
8.5	Comparison of Present $^{29}\text{Si}(p,\gamma)^{30}\text{P}$ Reaction Rate to Literature Rate.	206

CHAPTER 1: ASTROPHYSICAL MOTIVATION

Looking towards the sky, we observe the light of past astrophysical phenomena reaching forward in time, but while these awe-inducing spectacles probably seemed unfathomable to generations of curious onlookers, the stellar nuclear processes that light up the night are the same as those responsible for the synthesis of elements on Earth. Look no further than the carbon of which we are composed, the nitrogen and oxygen in the air that we breathe, the phosphorus and calcium in our bones, and the silicon and iron of our planet to see their outcome. Thus, the story of the stars is our story as well. In this respect, nuclear astrophysics—the field that encompasses the nucleosynthesis, energy generation, and evolution of stars—is truly a discipline unlike any other.

On a microscopic scale, the evolution of stars can be visualized using the chart of the nuclides. Figure 1.1 shows a section of this chart. Each square represents a stable (grey) or unstable (white) nuclear species arranged by neutron (N) and proton number (Z). One can imagine nuclear reactions forming a web of connections between the nuclei, describing the nucleosynthesis at hand.

To understand how nuclear burning translates to stellar evolution, it is useful to review a Hertzsprung-Russell diagram (Figure 1.2). This type of diagram plots the temperatures of stars against their luminosities, effectively grouping stars into different evolutionary phases. The most prominent group appears as a diagonal branch across the chart. This is known as the “main sequence” of stellar evolution and is composed of stars that fuse hydrogen into helium. Stars can be expected to spend most of their lives in this phase. After exhausting this fuel, a star will evolve off the

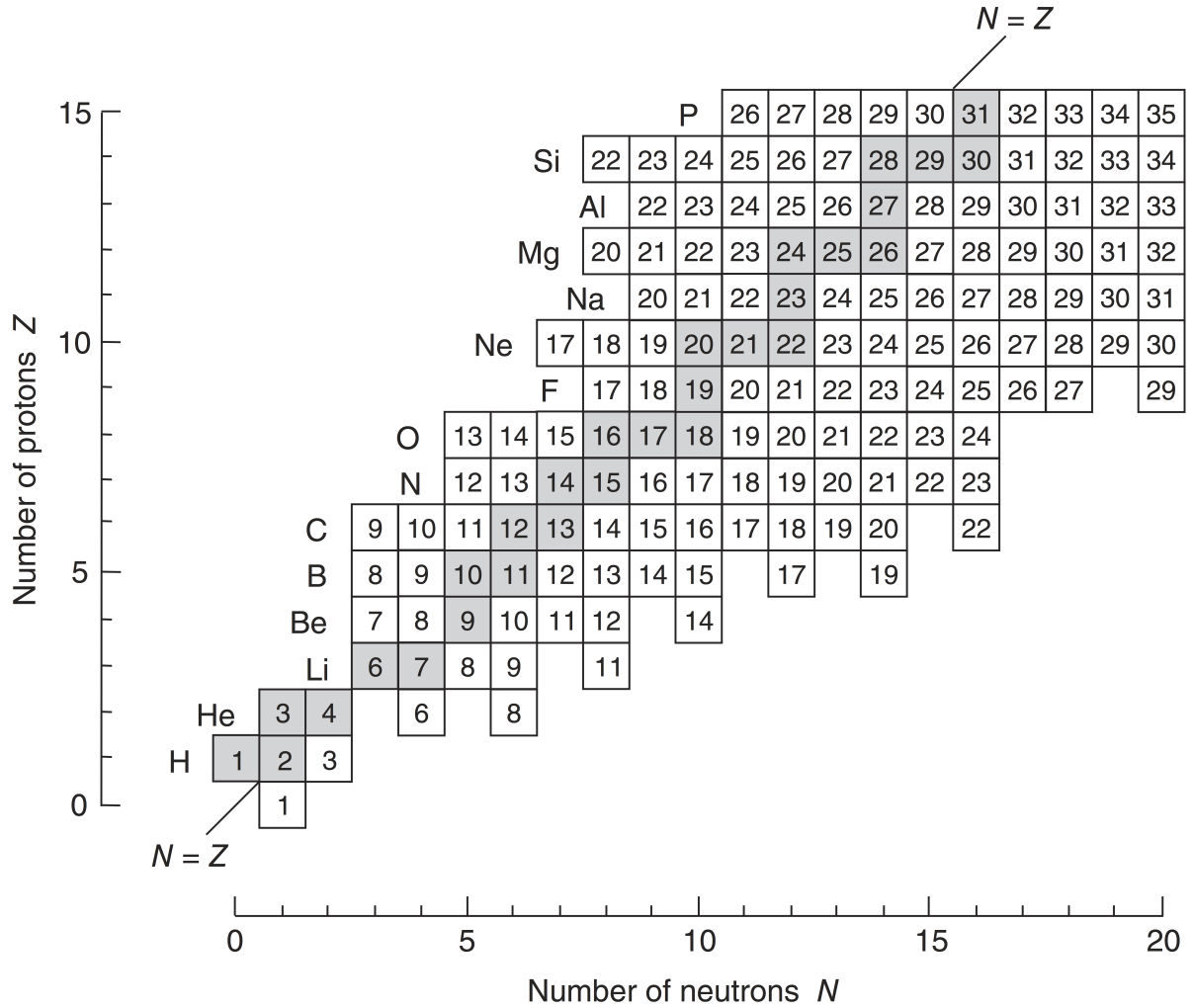


Figure 1.1: Section of the chart of the nuclides. Each square represents a stable (grey) or unstable (white) nuclear species arranged by neutron (N) and proton number (Z). Figure from Iliadis (2015).

main sequence, and, depending on its initial mass, it can become either a red giant or a supergiant star.

One final type of star, the white dwarf, is represented on this figure. These are hot, faint stars that become electron degenerate near the end of their lives. As such, their size is limited by the Chandrasekhar limit, the equilibrium between a star's gravity and degeneracy pressure. They can often be thought of as stellar corpses but as will be shown in the next section, they can take on new life when part of a binary star system.

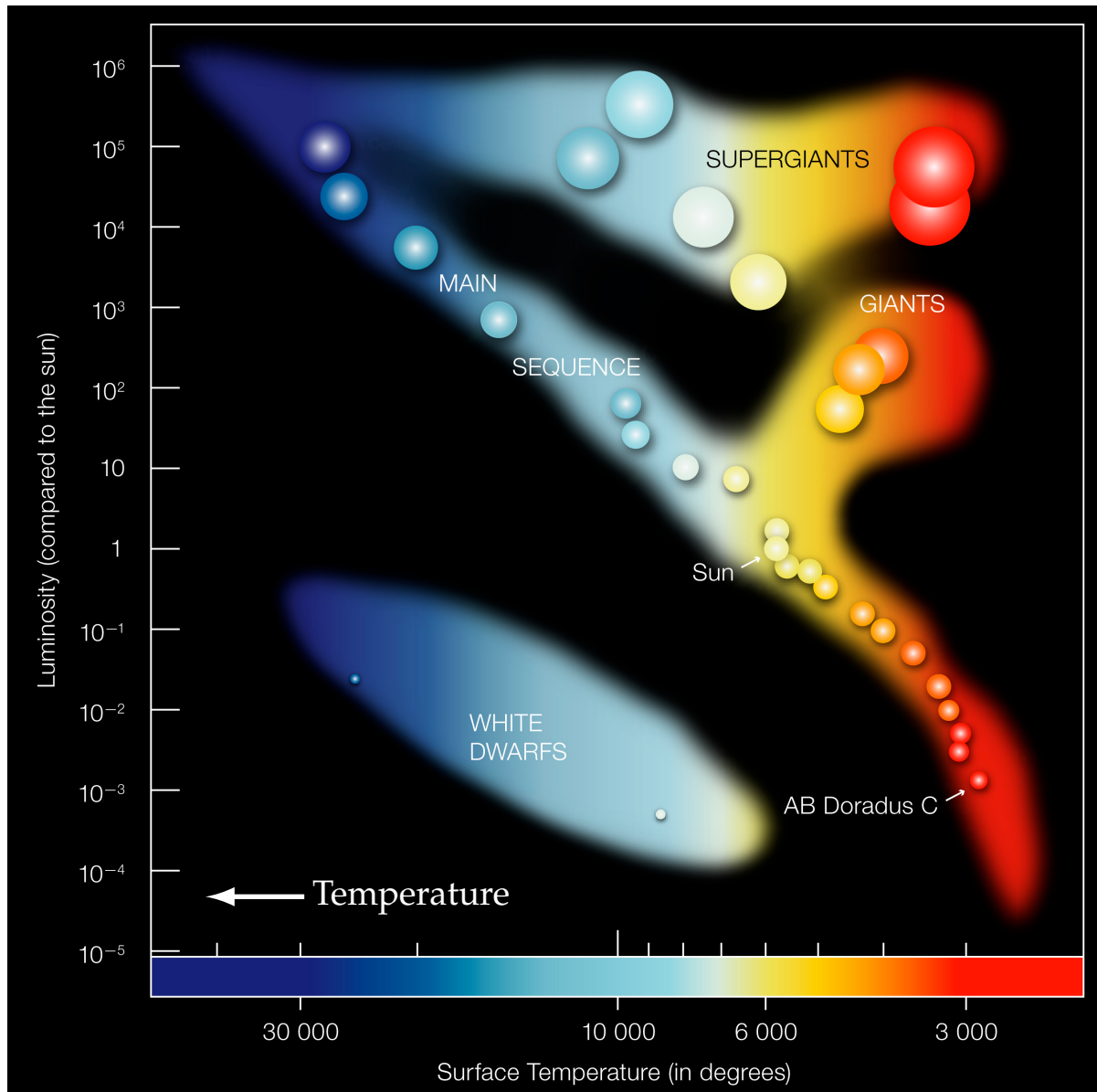


Figure 1.2: An example of a Hertzsprung-Russell diagram. In this type of diagram, the temperature of stars are plotted versus their luminosities. Note that surface temperature increases from right to left on the diagram. This method of grouping stars provides information about a star's current state and hints at its evolutionary fate. The diagonal branch, known as the "main sequence" of stellar evolution, consists of stars that fuse hydrogen into helium. After exhausting this fuel, the star evolves off the main sequence, becoming either a red giant or a supergiant depending on its initial mass. White dwarf stars, which become electron degenerate near the end of their evolutionary path, are shown toward the lower right corner of the diagram. Image from [ESO \(2007\)](#).

1.1 Classical Novae

Our sun, the star with which we are most familiar, lives a solitary existence, but this is not the case for all stars. Frequently, stars couple to form binary systems. These star pairs, particularly if closely bound together by their respective gravities, can evolve quite differently than they would have in isolation from each other. Figure 1.3 shows an illustration of a binary star system.

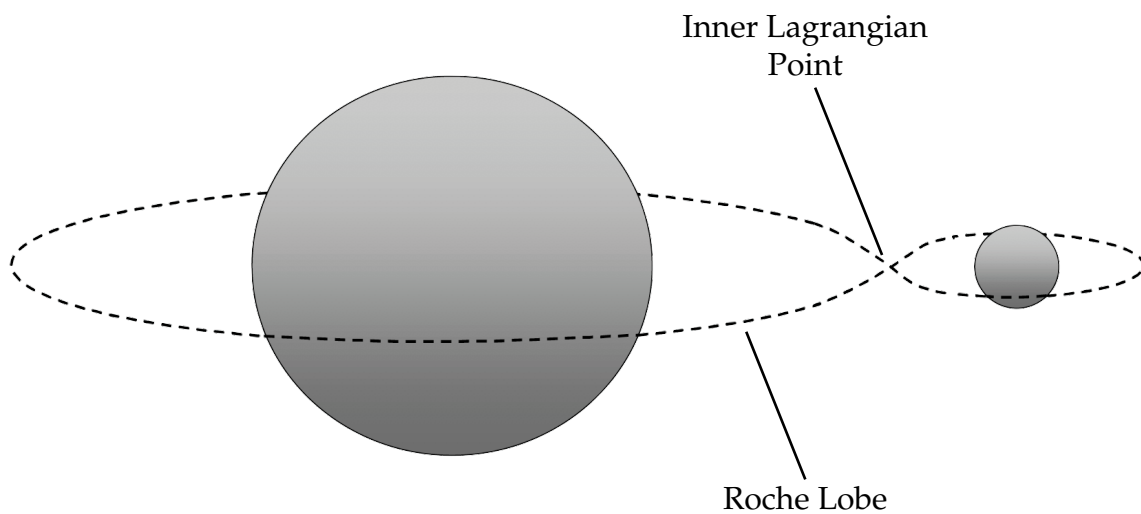


Figure 1.3: Diagram of a binary star system. The gravitational domain of each star, indicated by a dashed line, is known as the Roche lobe. The intersection of the Roche lobes, where there is no net gravitational force, is called the inner Lagrangian point. Figure from [Iliadis \(2015\)](#).

If a white dwarf and a main sequence star are tightly bound together in a binary system, a fascinating event called a *classical nova* can occur. To initiate this event, the main sequence star overflows its Roche lobe, transferring hydrogen-rich fuel through the inner Lagrangian point and into the gravitational domain of the quiescent white dwarf star. Most of this matter accumulates to form an accretion disk around the white dwarf, but a small amount falls directly into the surface of the white dwarf where it

is heated and compressed by the white dwarf’s intense surface gravity. In the bottom layer of this material, hydrogen begins to fuse to helium via proton-proton chain reactions, leading to a gradual increase in temperature, and electron degeneracy prevents the expansion of the accreted material. Without the means to cool the convective envelope, a thermonuclear runaway—an explosion governed by explosive hydrogen burning through the hot CNO cycles—occurs, expelling a 10^{-5} – 10^{-4} M_{\odot} mixture of white dwarf and nuclear processed material into the interstellar medium (Truran, 1981; Iliadis, 2015). Despite this impressive explosion, a classical nova does not disturb the underlying binary system meaning that the phenomenon can recur with a frequency of 10^4 – 10^5 years, and 35 ± 11 classical novae are expected to occur in the Galaxy every year (Starrfield *et al.*, 2008).

It should be noted that optical, infrared, and ultraviolet spectra of nova ejecta show that classical novae fall into two distinct groups. The first group exhibits overabundances of carbon and oxygen compared to solar values. Since some white dwarf material is expected to be expelled in the nova ejecta, it can be concluded that the first group of novae involve white dwarf stars of a primarily carbon-oxygen (CO) composition. This type of dwarf star is the result of a low-mass ($\lesssim 9 M_{\odot}$) star having undergone core helium burning (Iliadis, 2015).

On the other hand, the observations of the second group of novae reveal significant enrichments of neon (Gehrz *et al.*, 1998). Given that large (≈ 9 – $11 M_{\odot}$) stars that complete core carbon burning end their life cycles as oxygen-neon (ONe) composition white dwarf stars (Althaus *et al.*, 2010), the second group of novae are thought to occur on the surface of this rare variety of white dwarf. These events, often called *neon novae*, are the main interest of the current work. They are predicted to attain higher peak temperatures and conclude in a more violent explosion than CO novae (Starrfield *et al.*, 1986). While both nova varieties undergo explosive hydrogen burning through the hot CNO cycles, the elevated temperatures and high mass seed nuclei

($A \geq 20$) in neon novae also allow nucleosynthesis to occur beyond the CNO region and up to roughly $A = 40$.

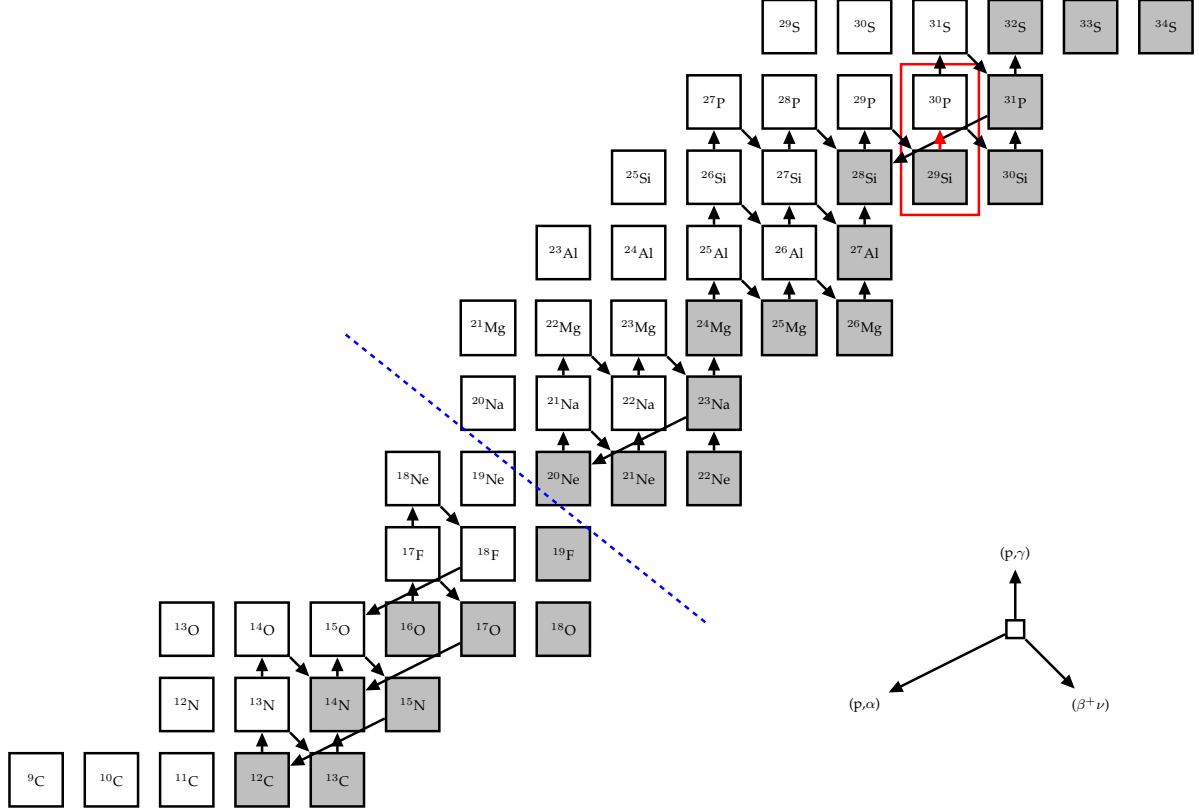


Figure 1.4: A section of the chart of the nuclides ($6 \leq Z \leq 16$) featuring the reactions important to neon nova nucleosynthesis. The shaded squares indicate stable species while the white squares depict unstable species. The arrows represent reactions—primarily (p,γ) , (p,α) , and $(\beta^+\nu)$ varieties—that frequently occur in neon nova nucleosynthesis. The reaction of interest for this dissertation, $^{29}\text{Si}(p,\gamma)^{30}\text{P}$, is shown in red. Note that the CNO region ($A < 20$) is essentially closed, meaning that material in this region is not synthesized into higher mass nuclides. In contrast, nuclides in the $A \geq 20$ region lead to a continuous flow of higher mass nuclides up to about ^{40}Ca . A blue dashed line indicates the approximate division of these two regions.

The nucleosynthesis of a typical neon nova is shown overlaid on a section of the chart of the nuclides in Figure 1.4. Reactions that occur frequently in this phenomenon are indicated by arrows, and the reaction of interest in this work, $^{29}\text{Si}(p,\gamma)^{30}\text{P}$, is indicated in red. The $A < 20$ region, governed by the hot CNO cycles, is essentially closed, meaning that no matter escapes this region to undergo further processing. However,

seed nuclei ($A \geq 20$) from the underlying ONe white dwarf allow for the nucleosynthesis of elements up to calcium. The division between these two mass regions is indicated by the dashed blue line in the figure.

The study of classical novae is crucial for a number of reasons. For instance, classical novae are thought to be abundant manufacturers of rare nuclear species including ^{13}C , ^{15}N , and ^{17}O , and given their ubiquitous presence in the Galaxy, novae are expected to figure significantly into the chemical evolution of the Galaxy (Starrfield *et al.*, 2008). Looking beyond our galaxy, properties of classical novae can also be used as distance indicators for extragalactic research (Warner, 2008). Lastly, it is also important to realize that the physics of the classical nova thermonuclear runaway is a complex amalgamation of hydrodynamics, nucleosynthesis, and convection (José, 2015), but the observational record of the nova outburst, although incomplete, provides a method by which stellar explosion models can be tested and refined (José and Shore, 2008). For these reasons, the study of classical novae drives research important to a variety of astrophysical phenomena forward (Warner, 2008).

1.2 Decoding Classical Nova Nucleosynthesis

Two distinct branches of study have helped scientists piece together the events of a classical novae explosion, but that is not to say that their techniques are without limitations. The first approach—consisting of optical, infrared, and ultraviolet spectral observations—will be discussed in the next section. The second approach, the study of presolar grains, will be explored in Section 1.2.2.

1.2.1 Elemental Abundances from Spectroscopic Observations

As a classical nova proceeds, the luminosity of the binary system increases many fold, and these dramatic emergences in the night sky have intrigued astronomers

since 200 BC ([Duerbeck, 2008](#)). This intellectual curiosity combined with the relatively high frequency of classical novae has given astronomers ample opportunity to learn more about these captivating events.

Given the complexity of a classical nova explosion ([Prialnik, 1986](#)) and the sheer number of nuclear species produced (Figure 1.4), it is not surprising that deriving reliable abundances from observed classical nova ejecta is a difficult task. There are several reasons for these difficulties as discussed at length in [José and Shore \(2008\)](#). It should be noted that tabulated mass fraction values of neon novae abundances have been available in the past ([Gehrz *et al.*, 1998](#); [Starrfield *et al.*, 1998](#); [Wanajo *et al.*, 1999](#)), but these compilations have a number of issues that required further attention. Those issues most relevant to this work and the treatment of said issues are detailed in this section.

Perhaps the most critical issue with nova observations is that different authors have used different procedures and assumptions to analyze the optical, infrared, and ultraviolet spectra of these events. For example, derived abundances are largely model dependent, but often models assume spherical symmetries when there is evidence to the contrary ([Casanova *et al.*, 2011](#)). The filling fraction, the fraction of a shell's volume that is occupied by gas, is not well known. Also, nova ejecta are thought to be chemically inhomogeneous, which adds further difficulty to the determination of abundances, and the abundance analysis must account for the sometimes substantial fraction of unobserved ionization states. Often nova abundances are presented without uncertainties even though uncertainties are crucial to gauging the quality of a measurement. Even so, some publications present mass fraction sums that differ significantly from unity, making it clear that these observations include a great deal of error. In summary, the presented abundances of a given nova event can vary over an order of magnitude between publications because there was no standard method of deriving abundances from nova observations.

Thankfully, the introduction of CLOUDY (Ferland, 2003), a photoionization code, coupled with the least-squares minimization code MINUIT (adopted from the CERN library) has mitigated some discrepancies in analytical method. The combination of these codes has allowed researchers to determine all spectral line intensities of a particular observation at once through successive minimizations. This coupling also provides for the derivation of meaningful uncertainties on the derived intensities. Therefore, one must still be aware of analytical deficiencies when using observations predating CLOUDY and MINUIT, and the abundances compiled here originate from studies derived following the development of these two codes.

The typical way that nova abundances are presented in literature is also problematic. Data is usually disseminated as ratios of number abundances “relative to hydrogen, relative to solar,”

$$\xi = \frac{N_{el}/N_H}{(N_{el}/N_H)_\odot}, \quad (1.1)$$

where N_{el} is the number abundance of a particular element, N_H is the number abundance of hydrogen, and the \odot subscript signifies solar abundances. Solar abundances have undergone significant revision over the past 20 years (see José and Shore, 2008), so the solar abundance compilation that is used to determine ξ can vary widely between publications. Therefore, all nova observations were renormalized using the solar abundances given by Lodders *et al.* (2009). Also, observations are sometimes presented with asymmetric uncertainties, which can create confusion in the event that no probability density function is given. For this reason, these data points have been symmetrized by adopting symmetric boundaries with the central value between the upper and lower bounds as the recommended value.

Even after correcting for different solar values and error boundaries, ξ is still dependent on number abundance, not the desired mass fraction. Converting these number abundance ratios to mass fractions is somewhat complicated. The definition of

Table 1.1. Assumed Average Elemental Masses and Uncertainties in Neon Novae

	Element											
	H	He	C	N	O	Ne	Mg	Al	Si	S	Ar	Fe
Mass	1(0)	4(0)	12.5(5)	14.5(5)	16.5(5)	20(0)	25(1)	26.5(5)	29(1)	33(1)	37(1)	56(0)

Note. — Values and uncertainties are assumed based on the masses of an element’s stable isotopes.

elemental mass fraction is

$$X_{el} \equiv \frac{N_{el} M_{el}}{\rho N_A} \quad (1.2)$$

where M_{el} is the relative atomic mass of a given element, ρ is the mass density, and N_A is Avogadro’s number (Iliadis, 2015). Clearly, ξ can be converted to a ratio of the mass fractions of a given element and hydrogen using

$$\frac{X_{el}}{X_H} = \frac{M_{el}}{M_H} \xi(N_{el}/N_H)_\odot. \quad (1.3)$$

While the average terrestrial mass of an element is known, the average mass of a given element in a classical nova is not known to any degree of certainty. Thus, average nova elemental masses were assumed, given the masses of an element’s stable isotopes (see Table 1.1).

Yet, elemental mass fractions involving hydrogen are not always the most practical presentation of nova observations. In order for the data to be more useful, the hydrogen mass fraction was determined so that the elemental mass fractions, not ratios, can be easily found. This calculation is not trivial, nor is it often explained in publications of nova observations. Observations essentially assume that all spectral data of an event have been observed, so any remaining “mass” must be hydrogen.

Table 1.2. Summary of Spectroscopically Observed Abundances for Neon Novae

	LMC 1990#1 ¹	V4160 Sgr ²	V838 Her ²	V382 Vel ³	QU Vul ⁴	V693 CrA ⁵	V1974 Cyg ⁶	V1065 Cen ⁷	Solar ⁸
X_{He}/X_H	4.8(8)E-1	7.1(4)E-1	5.6(4)E-1	4.0(4)E-1	4.6(3)E-1	5.4(22)E-1	4.8(8)E-1	5.4(10)E-1	3.85E-1
X_C/X_H	3.7(15)E-2	1.43(7)E-2	2.28(23)E-2	2.6(13)E-3	9.5(59)E-4	1.06(44)E-2	3.1(9)E-3	...	3.31E-3
X_N/X_H	1.48(42)E-1	1.27(8)E-1	3.29(47)E-2	2.28(54)E-2	1.61(10)E-2	1.84(67)E-1	6.0(15)E-2	1.40(33)E-1	1.14E-3
X_O/X_H	2.4(10)E-1	1.35(9)E-1	1.42(38)E-2	4.13(38)E-2	3.2(14)E-2	1.63(66)E-1	1.55(85)E-1	4.7(15)E-1	9.65E-3
X_{Ne}/X_H	1.6(10)E-1	1.38(5)E-1	1.22(5)E-1	4.0(7)E-2	5.1(4)E-2	6.7(34)E-1	9.7(40)E-2	5.34(98)E-1	2.54E-3
X_{Mg}/X_H	1.37(71)E-2	≈8.4E-3	1.2(7)E-3	2.45(14)E-3	1.02(49)E-2	9(7)E-3	4.3(28)E-3	4.4(13)E-2	9.55E-4
X_{Al}/X_H	2.3(11)E-2	...	1.8(13)E-3	1.63(16)E-3	4.1(11)E-3	5.0(46)E-3	>7.8E-5	...	8.74E-5
X_{Si}/X_H	4.8(39)E-2	1.09(6)E-2	7(2)E-3	5(3)E-4	2.4(18)E-3	2.4(18)E-2	1.08E-3
X_S/X_H	1.48(15)E-2	2.3(13)E-2	5.17E-4
X_{Ar}/X_H	4.0(3)E-5	4.6(17)E-3	1.29E-4
X_{Fe}/X_H	...	2.4(8)E-3	2.35(63)E-3	...	9.53(54)E-4	...	8.8(72)E-3	1.16(40)E-2	1.81E-3
X_H^9	4.7(9)E-1	4.65(37)E-1	5.63(36)E-1	6.6(4)E-1	6.3(3)E-1	3.8(14)E-1	5.5(8)E-1	3.6(10)E-1	7.11E-1

Note. — All abundances are given here in terms of mass fraction ratios, X_{el}/X_H (or mass fraction for hydrogen; see last row), by converting the “number abundances relative to hydrogen relative to solar” from the original literature (references provided below). The abundance uncertainties are given in parentheses. For example, 4.8(8)E-1 is equivalent to 0.48 ± 0.08 in this formalism. This table was originally published in [Downen et al. \(2013\)](#) and later adopted by [José \(2015\)](#).

¹From [Vanlandingham et al. \(1999\)](#).

²From [Schwarz et al. \(2007\)](#).

³From [Shore et al. \(2003\)](#).

⁴From [Schwarz \(2002\)](#).

⁵From [Vanlandingham et al. \(1997\)](#).

⁶From [Vanlandingham et al. \(2005\)](#); solar abundances assumed in their analysis are not listed; their adopted values were: $\log(N_{el}/N_H)_\odot = -1.0$ (He), -3.45 (C), -4.03 (N), -3.13 (O), -3.93 (Ne), -4.42 (Mg), -5.53 (Al), -4.45 (Si), -4.79 (S), -4.49 (Fe) ([Vanlandingham, 2012](#)).

⁷From [Helton et al. \(2010\)](#).

⁸From [Lodders et al. \(2009\)](#).

⁹Calculated from: $X_H = [1 + X_{He}/X_H + X_C/X_H + \dots + X_{Fe}/X_H]^{-1}$.

Then, the hydrogen mass fraction calculation takes the form of

$$X_H = (1 + \sum_i \frac{X_i}{X_H})^{-1} = [1 + \frac{X_{He}}{X_H} + \frac{X_C}{X_H} + \dots + \frac{X_{Fe}}{X_H}]^{-1}. \quad (1.4)$$

Nonetheless, it is worth noting that mass fractions of individual elements are more sensitive to issues involving spectral analysis, such as missing elements or unaccounted-for ionization states. As a result, it is recommended that the absolute hydrogen mass fraction, and by extension, other individual elemental mass fractions, be used with care.

The result of this work, originally published in [Downen et al. \(2013\)](#) and later

adopted by José (2015), is presented in Table 1.2. This table includes the elemental mass fractions and uncertainties for the eight neon nova observations where rigorous data analysis has been performed. Note that abundance analyses of V1370 Aql, performed by Snijders *et al.* (1987) and Andrea *et al.* (1994) without the use of CLOUDY and MINUIT, and U Sco, performed by Mason (2011) with scant few abundances presented, are not included in this table. All mass fractions, except for hydrogen, are presented as ratios over the hydrogen mass fraction. The hydrogen elemental abundance is given in the bottom row of the table. The far right column presents solar elemental abundances from the recent Lodders *et al.* (2009) compilation.

An inspection of this table exposes large overabundances of certain elements relative to their solar abundances. As will be discussed later (Section 3.3), discrepancies such as these can be exploited to determine the accuracy of classical nova nucleosynthesis models.

1.2.2 Isotopic Abundances from Presolar Grain Measurements

The emerging study of presolar grains, born in 1987 with the work of Anders and Zinner (1993), provides the other source of classical nova nucleosynthetic signatures. This field involves the study of stardust of unusual composition, or *presolar stardust grains*, found in primitive meteorites. The grains are thought to have condensed from the ejected material of stellar explosions. To determine the astrophysical origin of this submicrometer stardust, a secondary ion mass spectrometer such as a NanoSIMS ion probe (Hoppe *et al.*, 2017) must be employed. The resulting data is presented in the form of isotopic ratios of elements such as carbon, nitrogen, oxygen, and silicon.

Figure 1.5 shows images of a slice of a graphite presolar grain thought to have formed in a Type II supernova explosion. In the left panel, a transmission electron microscope (TEM) image of the grain slice is shown. Note the inhomogeneous composition of this grain. In this cross sectional view, it is clear that the grain has a distinct

core surrounded by layers of lower density material. In the right panel, an image of the same grain, which has been colorized to indicate the measured values of the $^{18}\text{O}/^{16}\text{O}$ ratio (relative to solar), is presented. It can be seen here that the structural inhomogeneity of the grain visible in the TEM image is echoed by the variation in the value of the oxygen isotopic ratio across the grain cross section.

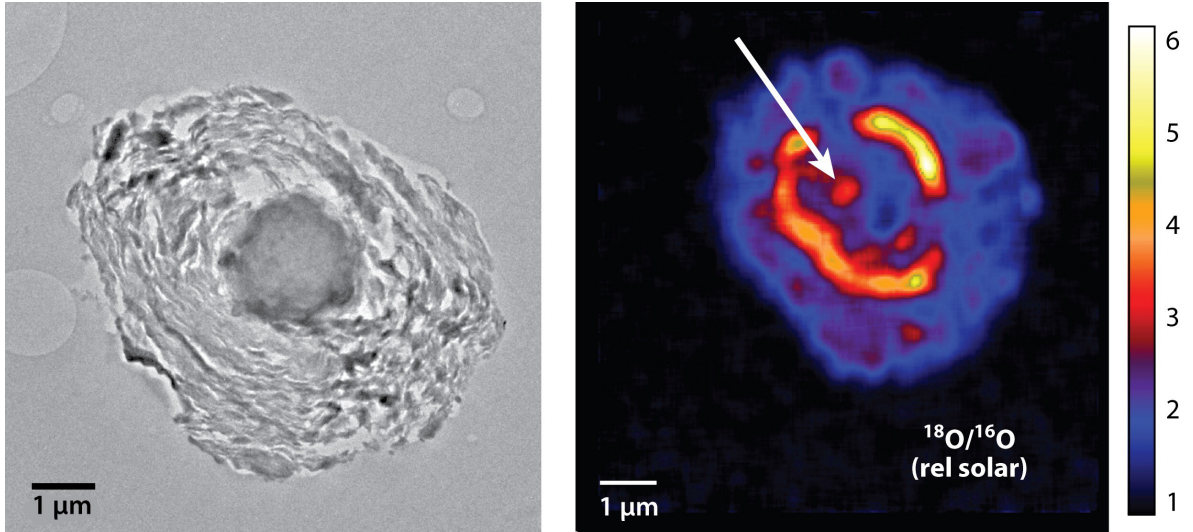


Figure 1.5: Images of a Type II supernova graphite presolar grain slice from [Nittler and Ciesla \(2016\)](#) and references therein. **Left:** TEM image of the grain showing a nanocrystalline core encompassed by layers of graphite. **Right:** O-isotopic map of the presolar grain shown in the left panel. The $^{18}\text{O}/^{16}\text{O}$ isotopic ratio displayed by the color map to the right is calculated relative to solar values. The variation of the isotopic ratio across the grain slice can provide information about the grain's condensation.

A large collection of carbon and nitrogen isotopic ratios from presolar grains is presented in Figure 1.6. The solar system values of the isotopic ratios are shown on the figure as dashed lines. From this figure, it is clear that presolar grain values can vary widely. These discrepancies are used to group the grains, and the grain populations can be attributed to a specific astrophysical phenomenon. In fact, it is astutely noted by [Nittler and Ciesla \(2016\)](#) that this type of plot is analogous to the Hertzsprung-Russell diagram (Figure 1.2). However, this type of attribution can only be made

based on the information at hand: available isotopic ratios, spectroscopic observations, and computational stellar models. Frequently, this process leads to a successful attribution of a specific presolar grain to a particular astrophysical event, and additional isotopic ratio measurements of the grain can be used to improve knowledge of the phenomenon. On the other hand, additional measurements can just as easily reveal that the astrophysical source attribution was incorrect. In this regard, the application of presolar grain ratios should be considered an iterative process (Nittler and Ciesla, 2016).

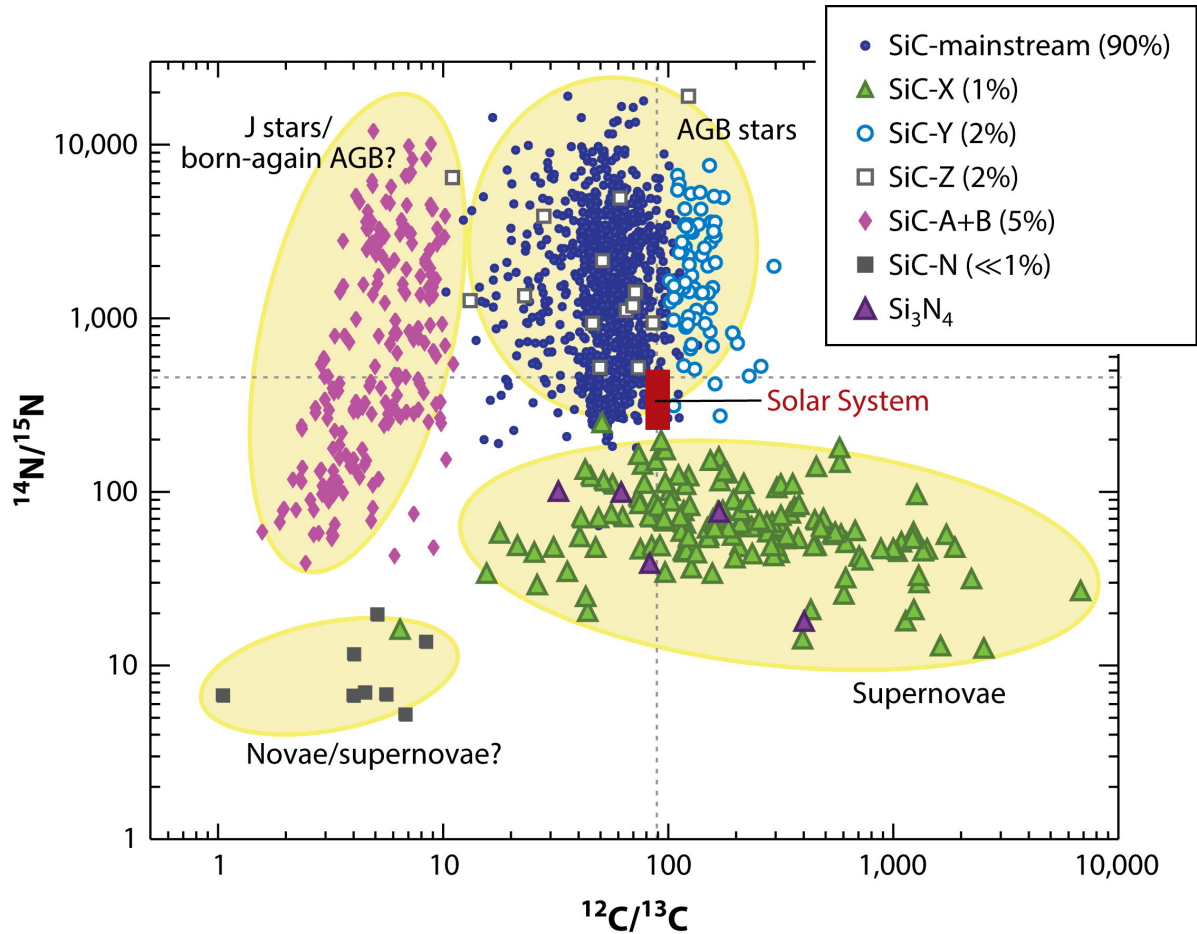


Figure 1.6: Carbon and nitrogen isotopic ratios measured in silicon carbide and silicon nitride presolar grains. The solar values of the carbon and nitrogen isotopic ratios are shown as dashed lines. It can be seen how grains can be roughly categorized by suspected astrophysical origin using isotopic ratios. As shown in this figure, grains of a nova origin are comparatively rare. Figure from Nittler and Ciesla (2016).

As indicated by this figure, presolar grains of a putative nova origin are fairly rare. Presolar grains from novae are expected to exhibit very high $^{13}\text{C}/^{12}\text{C}$, $^{15}\text{N}/^{14}\text{N}$, and $^{17}\text{O}/^{16}\text{O}$ ratios due to the aforementioned high production of ^{13}C , ^{15}N , and ^{17}O , respectively (Nittler and Ciesla, 2016). For neon novae where the presence of ^{20}Ne seed nuclei facilitates nucleosynthesis beyond the CNO cycle, high $^{30}\text{Si}/^{28}\text{Si}$ values compared to the solar ratio are also expected (Amari *et al.*, 2001).

However, the identification of presolar grains with a classical nova origin is not without its complications and ambiguities. First, it is unclear if classical nova explosions create the conditions necessary for presolar grain production. While classical novae have been observed to produce both carbon-rich and oxygen-rich dust (Gehrz *et al.*, 1992), this dust must be shielded from the ionizing ultraviolet radiation of the binary system's white dwarf in order to condense into presolar grains (Schwarz *et al.*, 2011). If the ejected matter forms a uniform shell, the dust is not shielded, and no grains are formed. As a result, it must be assumed that the ejecta is spatially inhomogeneous, providing shielding to allow for grain formation. While there is spectroscopic support for the latter scenario, the cause of the proposed inhomogeneity is unknown (Iliadis *et al.*, 2018, and references therein). Furthermore, it has been suggested that the presence of intermediate-mass elements in the nova ejecta could affect the condensation process as well (José *et al.*, 2004). Secondly, additional isotopic measurements for a number of suspected nova-origin grains (based on high $^{13}\text{C}/^{12}\text{C}$ and $^{15}\text{N}/^{14}\text{N}$ ratios) have revealed a likely supernova origin (Nittler and Ciesla, 2016). The final and most significant issue with classical nova presolar grain identification is the discrepancy between putative nova grain isotopic ratios and the isotopic ratios of nova ejecta predicted by hydrodynamic models. In short, simulations predict ejected matter with far more anomalous isotopic ratios than those measured in grains. As a result, it has been suggested that the ejected material is diluted with a much larger fraction (90–95%) of solar-like material prior to grain condensation (Amari *et al.*, 2001),

Table 1.3. Summary of Isotopic Ratios from Nova Presolar Candidate Grains

Grain	$\frac{^{12}\text{C}}{^{13}\text{C}}$	$\frac{^{14}\text{N}}{^{15}\text{N}}$	$\frac{^{17}\text{O}}{^{16}\text{O}}$ ($\times 10^{-4}$)	$\frac{^{18}\text{O}}{^{16}\text{O}}$ ($\times 10^{-3}$)	$\frac{^{25}\text{Mg}}{^{24}\text{Mg}}$	$\frac{^{26}\text{Mg}}{^{24}\text{Mg}}$	$\frac{^{26}\text{Al}}{^{27}\text{Al}}$ ($\times 10^{-3}$)	$\delta\left(\frac{^{29}\text{Si}}{^{28}\text{Si}}\right)$	$\delta\left(\frac{^{30}\text{Si}}{^{28}\text{Si}}\right)$	$\delta\left(\frac{^{33}\text{S}}{^{32}\text{S}}\right)$	$\delta\left(\frac{^{34}\text{S}}{^{32}\text{S}}\right)$
SiC Grains											
AF15bB-429-3 ^a	9.4 ± 0.2	28 ± 30	1118 ± 44
AF15bC-126-3 ^a	6.8 ± 0.2	5.22 ± 0.11	-105 ± 17	237 ± 20
Ag2 ^b	2.5 ± 0.1	7 ± 0.1	0.315 ± 0.037	62.0 ± 10.0 [†]	-304 ± 26	319 ± 38	-92 ± 222	162 ± 106
Ag2.6 ^b	16 ± 0.4	9 ± 0.1	-340 ± 57	263 ± 82	48 ± 334	-394 ± 106
KJC112 ^a	4.0 ± 0.2	6.7 ± 0.3
KJGM4C-100-3 ^a	5.1 ± 0.1	19.7 ± 0.3	11.4	55 ± 5	119 ± 6
KJGM4C-311-6 ^a	8.4 ± 0.1	13.7 ± 0.1	>80	-4 ± 5	149 ± 6
G1342 ^b	6.4 ± 0.08	7 ± 0.14	76 ± 19	15.4 ± 0.5	445 ± 34	513 ± 43
G1614 ^b	9.2 ± 0.07	35 ± 0.7	0.184 ± 0.024	42.5 ± 7.8 [†]	34 ± 5	121 ± 6
G1697 ^b	2.5 ± 0.01	33 ± 0.8	0.041 ± 0.008	15.6 ± 3.9 [†]	-42 ± 12	40 ± 15
G1748 ^b	5.4 ± 0.02	19 ± 0.2	0.150 ± 0.016	24.0 ± 4.6 [†]	21 ± 4	83 ± 5
G240-1 ^b	1.0 ± 0.01	7 ± 0.1	960 ± 280	29.8 ± 1.1	138 ± 14	313 ± 23
G270.2 ^b	11 ± 0.3	13 ± 0.3	-282 ± 101	-3 ± 131	-615 ± 385	-542 ± 175
G278 ^b	1.9 ± 0.03	7 ± 0.2	1570 ± 112	1673 ± 138
G283 ^b	12 ± 0.1	41 ± 0.5	1.913 ± 0.454	129.5 ± 43.2 [†]	-15 ± 3	75 ± 4
GAB ^b	1.6 ± 0.02	13 ± 0.2	16 ± 0.9	12.1 ± 0.8	230 ± 6	426 ± 7
M11-151-4 ^c	4.02 ± 0.07	11.6 ± 0.1	270 ± 50	-438 ± 9	510 ± 18
M11-334-2 ^c	6.48 ± 0.08	15.8 ± 0.2	390 ± 60	-489 ± 9	-491 ± 18
M11-347-4 ^c	5.59 ± 0.13	6.8 ± 0.2	-166 ± 12	927 ± 30
M26a-53-8 ^d	4.75 ± 0.23	10 ± 13	222 ± 25
M1-A8-G145 ^q	4.4 ± 0.01	50 ± 2.0	69.3 ± 0.9	31 ± 17	157 ± 15	-833 ± 167	-435 ± 131
M2-A1-G410 ^q	10.4 ± 0.3	38 ± 0.5	56.6 ± 1.1	19 ± 13	88 ± 17
M2-A3-G581 ^q	7.8 ± 0.22	31 ± 2.4	90.2 ± 3.3	52 ± 11	147 ± 12
M2-A4-G27 ^q	2.2 ± 0.05	3.8 ± 0.2	20.9 ± 7.9	-511 ± 7	76 ± 14
M2-A4-G672 ^q	9.6 ± 0.27	10 ± 0.8	126 ± 4.3	-90 ± 18	419 ± 28
M2-A1-G114 ^q	16.2 ± 0.5	56 ± 2.0	20 ± 25	107 ± 35
M2-A5-G1211 ^q	5.9 ± 0.13	50 ± 2.5	-554 ± 11	-56 ± 35
M2-A5-G269 ^q	8.5 ± 0.19	28 ± 1.3	7 ± 10	59 ± 13
KJD-1-11-5 ^r	3.7 ± 0.0	57 ± 1	205 ± 12	23 ± 9	136 ± 11	-303 ± 110	-94 ± 54
KJD-3-23-5 ^r	1.4 ± 0.0	42 ± 1	18 ± 2	132 ± 15	248 ± 20	-121 ± 141	15 ± 65
Silicate Grains											
1.07 ^e	49.1 ± 3.6	1.36 ± 0.19
4.2 ^f	128 ± 1.43	1.74 ± 0.05	1025 ± 29	92 ± 19	...	24 ± 40	134 ± 52
4.7 ^f	149 ± 1.98	1.30 ± 0.06	213 ± 56	19 ± 48	...	136 ± 46	-49 ± 80
A094.TS6 ^g	95.35 ± 1.14	1.50 ± 0.01	29 ± 43	43 ± 54
AH-106a ^h	50.11 ± 2.16	1.78 ± 0.07	15 ± 59	80 ± 67
B2-7 ⁱ	133 ± 1	1.43 ± 0.04	21 ± 56	57 ± 69
GR95.13.29 ^j	62.54 ± 2.51	1.96 ± 0.14	79 ± 21	70 ± 20	...	-16 ± 63	379 ± 92
Graphite Grains											
KFB1a-161 ^{d,k}	3.8 ± 0.1	312 ± 43	-27.82 ± 61.62	32.86 ± 62.03	...	-133 ± 81	37 ± 87
KFC1a-551 ^d	8.46 ± 0.04	273 ± 8	-157 ± 443	-88 ± 451	...	84.38 ± 54.06	760.86 ± 72.1
LAP-149 ^l	1.41 ± 0.01	941 ± 81	3.86 ± 0.34	1.94 ± 0.07	-8 ± 24	-23 ± 29	-23 ± 143	6 ± 70
Oxide Grains											
12-20-10 ^m	88.01 ± 2.97	1.18 ± 0.11
8-9-3 ^m	51.42 ± 1.05	1.89 ± 0.07	-66 ± 21	-25 ± 20
C4-8 ^m	440.36 ± 1.22	1.10 ± 0.02	949 ± 8	929 ± 8
KC23 ⁿ	58.5 ± 1.8	2.19 ± 0.06	45 ± 35	6 ± 35	<0.011
KC33 ⁿ	82.2 ± 0.6	0.680 ± 0.080
MCG67 ^j	47.3 ± 1.42	1.77 ± 0.03
MCG68 ^j	62.6 ± 1.08	1.89 ± 0.02
S-C6087 ^o	75.2 ± 0.3	2.18 ± 0.03	36 ± 22	36 ± 21
T54 ^p	141 ± 5	0.5 ± 0.2
Solar	89	272	3.83	2.01

Note. — Presented errors are 1σ . Some ratios are presented as deviations from solar abundances in permil, $\delta(^iX/^jX) \equiv [(^iX/^jX)/(^iX/^jX)_\odot - 1] \times 1000$. $^{12}\text{C}/^{13}\text{C}$ and $^{14}\text{N}/^{15}\text{N}$ (ratio in air) solar values are from José *et al.* (2004) and references therein; $^{17}\text{O}/^{16}\text{O}$ and $^{18}\text{O}/^{16}\text{O}$ solar values are from Leitner *et al.* (2012). Multiple values exist for the $^{16}\text{O}/^{18}\text{O}$ ratio of Grain KFC1a-551 and are not given here (Amari *et al.*, 1995; Bose, 2017; Hynes and Gyngard, 2009). Values marked with a † symbol should be considered lower limits due to the likelihood of Al contamination (for details, see Liu *et al.*, 2016).

References. — ^aAmari *et al.* (2001); ^bLiu *et al.* (2016); ^cNittler and Hoppe (2005); ^dNittler and Alexander (2003); ^eVollmer *et al.* (2007); ^fNguyen and Messenger (2014); ^gNguyen *et al.* (2007); ^hNguyen *et al.* (2010); ⁱBose *et al.* (2010); ^jLeitner *et al.* (2012); ^kJosé and Hernanz (2007); ^lHaenecour *et al.* (2016); ^mGyngard *et al.* (2010); ⁿNittler *et al.* (2008); ^oChoi *et al.* (1999); ^pNittler *et al.* (1997); ^qLiu *et al.* (2017); ^rHoppe *et al.* (2018).

but the mechanism of this proposed mixing is unknown.

Nonetheless, the isotopic data of all presolar grains of a putative classical nova origin are presented in Table 1.3. This table builds upon a similar table in Iliadis *et al.* (2018) with the inclusion of recent measurements from Liu *et al.* (2017) and Hoppe *et al.* (2018). The grain measurements are categorized by grain composition, and only isotopic ratios of interest to neon nova nucleosynthesis are presented. This table makes clear that the quantity $\delta(^{29}\text{Si}/^{28}\text{Si})$ is frequently measured in presolar grains and is useful in identifying grains with a classical nova origin. However, this tactic is only effective if the production and destruction of ^{29}Si is well understood, thereby motivating the current study of the $^{29}\text{Si}(p,\gamma)^{30}\text{P}$ reaction. In Chapter 3, the grain measurements in Table 1.3 will be compared to classical nova nucleosynthesis models and the motivation of $^{29}\text{Si}(p,\gamma)^{30}\text{P}$ study will be elucidated.

1.3 The Master Plan

By refining the $^{29}\text{Si}(p,\gamma)^{30}\text{P}$ rate, this dissertation aims to improve understanding of neon nova nucleosynthesis and answer some of the open questions presented in this chapter. This multifaceted process involving astrophysical observations, stellar nucleosynthesis models, and experimental nuclear physics will be explored in the following chapters. Chapter 2 presents an overview of the nuclear astrophysics concepts essential to understanding the experimental work presented in this dissertation. Next, Chapter 3 will present the post-processing nucleosynthesis modeling of neon novae as well as comparisons of their results to spectroscopic elemental abundances and presolar grain isotopic ratios. Chapters 4 and 5 will address the experimental setup and preparation of nuclear targets for the $^{29}\text{Si}(p,\gamma)^{30}\text{P}$ study, respectively. Chapter 6 follows with a description of the analysis method adopted in the current work. Chapter 7 will discuss the results of the current $^{29}\text{Si}(p,\gamma)^{30}\text{P}$ study at length. Then, a new

$^{29}\text{Si}(\text{p},\gamma)^{30}\text{P}$ reaction rate evaluation based on the current work and comparison to the $^{29}\text{Si}(\text{p},\gamma)^{30}\text{P}$ rate from [Iliadis *et al.* \(2010c\)](#) is presented in Chapter 8. Finally, Chapter 9 expounds on the conclusions and consequences of the current work.

CHAPTER 2: NUCLEAR ASTROPHYSICS THEORY

To understand the stellar phenomenon discussed in the previous chapter, a certain toolset is required. The required knowledge can be expansive and daunting, particularly in an interdisciplinary field like nuclear astrophysics. Thus, the contents of this chapter are intended to introduce the reader, who may not already be well versed in this field, to the concepts essential to understanding the work discussed in this dissertation. For a thorough discussion, the author directs the reader to any number of excellent texts, chief among them [Iliadis \(2015\)](#) and [Rolfs and Rodney \(1988\)](#).

2.1 The Nuclear Cross Section

With no access to the astrophysical phenomena of interest, scientists find themselves in the unenviable position of trying to recreate stellar plasma conditions in the laboratory. However, this endeavor is only worthwhile if it is probable that the nuclear interaction of interest will occur under laboratory conditions. It is useful to define a quantity—the total cross section—to describe this probability,

$$\sigma \equiv \frac{\text{interactions per time}}{(\text{incident particles per area per time}) (\text{target nuclei within the beam})}. \quad (2.1)$$

Figure 2.1 ([Iliadis, 2015](#)) shows the typical setup for a nuclear physics experiment and defines several useful quantities. A beam of projectiles numbering \mathcal{N}_b with a cross sectional area A is directed toward a nuclear target with target nuclei \mathcal{N}_t and area A_t ($A_t < A$). Interactions between the projectile beam and target nuclei, \mathcal{N}_R , produce \mathcal{N}_e interaction products which can then be counted by a detector with area

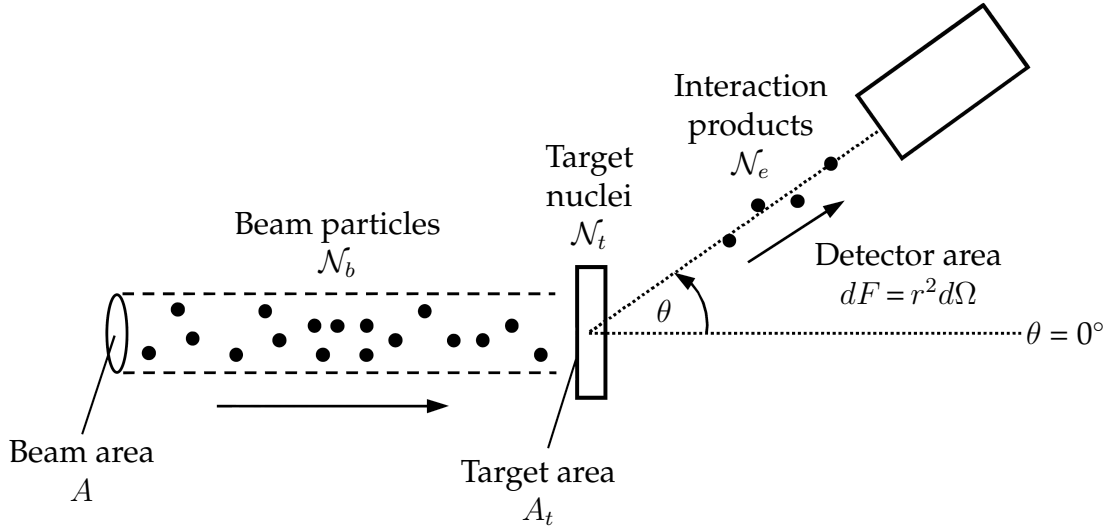


Figure 2.1: The typical setup for a nuclear physics experiment. A beam of projectiles numbering \mathcal{N}_b with area A interacts with a nuclear target of target nuclei \mathcal{N}_t and area A_t ($A_t < A$). \mathcal{N}_R interactions between the projectiles and target nuclei produce \mathcal{N}_e interaction products that are then counted by a detector with area dF located at angle θ relative to the particle beam. Figure from [Iliadis \(2015\)](#).

dF located at angle θ relative to the particle beam. The detector area is related to the solid angle, $d\Omega$, as $dF = r^2 d\Omega$. It is sometimes convenient to combine the number of emitted interaction products and the number of target nuclei into one term: the number of emitted interaction products per target nucleus,

$$\mathcal{N}_{et} \equiv \frac{\mathcal{N}_e}{\mathcal{N}_t}. \quad (2.2)$$

Then, the general expression in Equation 2.1 becomes

$$\sigma = \frac{(\mathcal{N}_e/t)}{(\mathcal{N}_b/(tA))(\mathcal{N}_t)} = \frac{(\mathcal{N}_{et}/t)}{(\mathcal{N}_b/(tA))}. \quad (2.3)$$

The differential cross section, $d\sigma/d\Omega$, can be derived in a similar manner,

$$\left(\frac{d\sigma}{d\Omega} \right) = \frac{(\mathcal{N}_{et}^{d\Omega}/t)}{(\mathcal{N}_b/At)d\Omega} \quad (2.4)$$

where $\mathcal{N}_{et}^{d\Omega}$ is the number of interaction products per target nucleus emitted at an angle θ into the solid angle $d\Omega$.

In the context of laboratory experiments, it is often advantageous to express the cross section in terms of current densities for the beam and interaction products,

$$j_b = \frac{(\mathcal{N}_b/t)}{A} \quad \text{and} \quad j_{et} = \frac{(\mathcal{N}_{et}^{d\Omega}/t)}{dF}, \quad (2.5)$$

respectively. It follows that the cross section can then be written as

$$\sigma = \int \left(\frac{d\sigma}{d\Omega} \right) d\Omega = \int \left(\frac{j_{et} r^2}{j_b} \right) d\Omega = \frac{(\mathcal{N}_{et}/t)}{j_b}. \quad (2.6)$$

The cross section is typically provided in units of barns (b) where

$$1 \text{ b} = 10^{-24} \text{ cm}^2. \quad (2.7)$$

In essence, the probability that a nuclear interaction will occur is given as an interaction area between the incident particle and the target nuclei, calling to mind an old fashioned game of darts, though the reality is considerably more complicated. Thus far, the cross section has been referred to as a singular quantity, but in truth it is composed of a number of component cross sections, one for each possible interaction between a pair of interacting nuclei. For the purposes of this dissertation, only the $^{29}\text{Si}(\text{p},\gamma)^{30}\text{P}$ reaction cross section, comprised of the cross sections for resonant and nonresonant processes, is considered and will be detailed in later sections.

2.2 The Coulomb Barrier

Before the resonant and nonresonant processes can be detailed, some of the physics involved in interacting particles must be understood. First, fusion reactions, such as

$^{29}\text{Si}(p,\gamma)^{30}\text{P}$, have positive Q -values, meaning that energy is released when the compound nucleus is formed. In the absence of other factors, these reactions should occur frequently and at relatively low energies. However, the Coulomb barrier impedes these reactions. However, one factor, the Coulomb barrier, impedes these reactions. The study undertaken for this dissertation involves the interaction of a positively charged projectile (proton) and a positively charged target nucleus (^{29}Si). Thus, the projectile will have to overcome the repulsive force from the Coulomb barrier in order to proceed. The Coulomb potential is given by

$$V_c(r) = \frac{Z_0 Z_1 e^2}{r} \quad (2.8)$$

where Z_0 is the charge of the projectile, Z_1 is the charge of the target nucleus, e is the unit charge, and r is the distance between the interacting particles. Figure 2.2 (Iliadis, 2015) shows the attractive nuclear potential and repulsive potential as functions of the interaction distance. The attractive nuclear potential dominates the $r < R_0$ region, and the repulsive Coulomb potential governs in the $r > R_0$ range where R_0 is the radius of the nuclear potential well. It is clear from this figure that if a particle interaction were treated classically, a projectile with energy E would be merely reflected by the potential at the classical turning radius, R_c . Only with a projectile energy $E > V_c$ would the reaction occur.

As discussed in Rolfs and Rodney (1988), this strict energy condition would cause a star's nuclear fuel to ignite in a single cataclysmic event rather than burning and sustaining the star for billions of years. The work of Gamow (1928), Gurney and Condon (1929), and Atkinson and Houtermans (1929) calculated the small but significant quantum mechanical probability for particles to tunnel through potential barriers and proposed this quantum mechanical tunneling as the explanation for the sustained nuclear fusion energy generation observed in stars.

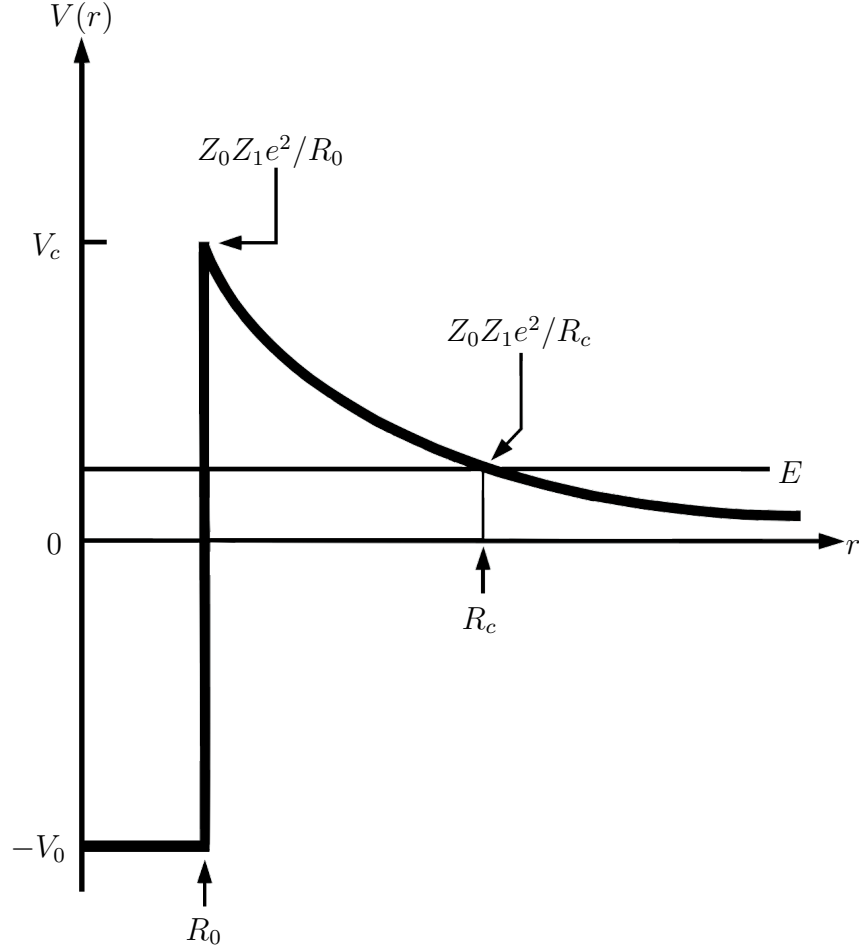


Figure 2.2: The attractive nuclear potential and repulsive Coulomb potential as functions of the distance between interacting particles. The potential is shown as a thick black line where the attractive nuclear potential dominates the the $r < R_0$ region and the repulsive Coulomb potential governs in the $r > R_0$ range. For more details, see text. Figure from [Iliadis \(2015\)](#).

The probability for an incident particle to *transmit* through a potential barrier such as this is referred to as the transmission coefficient, \hat{T} . For a positively charged incident particle with $E \ll V_c$ and no angular momentum ($\ell = 0$), the Coulomb barrier transmission coefficient can be estimated by treating the barrier as a series of thin

square-barrier potentials (for a detailed derivation, see [Iliadis, 2015](#)). This approximate transmission coefficient is called the Gamow factor,

$$\hat{T} \approx \exp \left(-\frac{2\pi}{\hbar} \sqrt{\frac{m_{01}}{2E}} Z_0 Z_1 e^2 \right) \equiv e^{-2\pi\eta} \quad (2.9)$$

where m_{01} is the reduced mass of the system,

$$m_{01} = \frac{m_0 m_1}{m_0 + m_1}, \quad (2.10)$$

and η is the Sommerfeld parameter,

$$\eta = \frac{Z_0 Z_1 e^2}{\hbar} \sqrt{\frac{m_{01}}{2E}}. \quad (2.11)$$

The importance of the Gamow factor will be seen in later sections of this chapter.

2.3 Thermonuclear Reaction Rates

Generally, the nuclear cross section is a function of the relative velocity between the incident particle and the target nucleus, and in a stellar plasma at thermodynamic equilibrium, there exists a distribution of relative velocities between interacting particles characterized by the probability function $P(v)$. Combining these factors gives an expression for the reaction rate of a pair of nonidentical interacting nuclei in a stellar plasma,

$$\langle \sigma v \rangle_{01} = \int_0^\infty v \sigma(v) P(v) dv \quad (2.12)$$

where 0 refers to the incident particle and 1 refers to the target nucleus. Furthermore, it has been shown that interacting nuclei in stellar plasmas are typically nonrelativistic and nondegenerate ([Wolf, 1965](#)). Consequently, the probability function can be

described by a Maxwell-Boltzmann distribution

$$P(v)dv = P(E)dE = \frac{2}{\sqrt{\pi}} \frac{1}{(kT)^{3/2}} \sqrt{E} e^{-E/kT} dE \quad (2.13)$$

such that the reaction rate becomes

$$\begin{aligned} N_A \langle \sigma v \rangle &= N_A \left(\frac{8}{\pi m_{01}} \right)^{1/2} \frac{1}{(kT)^{3/2}} \int_0^\infty E \sigma(E) e^{-E/kT} dE \\ &= \frac{3.7318 \times 10^{10}}{T_9^{3/2}} \sqrt{\frac{M_0 + M_1}{M_0 M_1}} \int_0^\infty E \sigma(E) e^{-11.605E/T_9} dE \left(\frac{\text{cm}^3}{\text{mol} \cdot \text{s}} \right) \end{aligned} \quad (2.14)$$

where N_A is Avogadro's number, k is the Boltzmann constant, T is the stellar temperature, and m_{01} is the reduced mass of the particle pair. For the numerical form of the reaction rate, T_9 is the temperature in GK, E is the energy in MeV, M_i are the atomic masses in u, and σ is the cross section in b.

2.3.1 Nonresonant Reaction Rates

As was mentioned earlier, there are multiple ways the $^{29}\text{Si}(p,\gamma)^{30}\text{P}$ reaction can occur, each type with its own probability for occurrence and its own form of the cross section accordingly. The first type of interaction to be discussed, the nonresonant reaction, involves the target nucleus' capturing the projectile to form a daughter nucleus in a bound state. This process is sometimes called direct capture because it involves a direct transition from the initial state to the final state. Any energy in excess of what is required to form the daughter nucleus is released in the form of a γ -ray. This γ -ray has an energy of

$$E_\gamma = E + Q - E_x \quad (2.15)$$

where E is the center-of-mass energy of the proton, Q is the Q-value of the $^{29}\text{Si}(p,\gamma)^{30}\text{P}$ reaction, and E_x is the bound state energy of the daughter nucleus.

As one might expect, the probability for this type of interaction is strongly dependent on the Coulomb barrier transmission probability (approximated by the Gamow factor in Equation 2.9). Consequently, the nonresonant cross section gradually increases with increasing energy but drops steeply at low energies as shown for the $^{16}\text{O}(\text{p},\gamma)^{17}\text{F}$ reaction in the top panel of Figure 2.3. Thus, the nonresonant cross section is given by

$$\sigma(E) \equiv \frac{1}{E} e^{-2\pi\eta} S(E). \quad (2.16)$$

This expression makes use of the Sommerfeld parameter introduced earlier (Equation 2.11) as well as a new term, $S(E)$, known as the astrophysical S-factor. It is advantageous to express the cross section in this manner because the astrophysical S-factor does not share the exponential energy dependence of the s-wave ($\ell = 0$) Coulomb barrier transmission probability and the nuclear cross section.

Figure 2.3 shows a comparison of the nuclear cross section (top panel) and the astrophysical S-factor (bottom panel) versus energy for $^{16}\text{O}(\text{p},\gamma)^{17}\text{F}$. This figure, originally published in Iliadis (2015) with data from Angulo *et al.* (1999), clearly illustrates the significant reduction in energy dependence of the S-factor versus that of the cross section even when $\ell > 0$.

Finally, combining Equation 2.16 with the expression for the reaction rate in a stellar plasma (Equation 2.14) gives the nonresonant reaction rate in a stellar plasma,

$$\begin{aligned} N_A \langle \sigma v \rangle_{\text{nonresonant}} &= N_A \left(\frac{8}{\pi m_{01}} \right)^{1/2} \frac{1}{(kT)^{3/2}} \int_0^\infty E \sigma(E) e^{-E/kT} dE \\ &= N_A \left(\frac{8}{\pi m_{01}} \right)^{1/2} \frac{1}{(kT)^{3/2}} \int_0^\infty e^{-2\pi\eta} S(E) e^{-E/kT} dE. \end{aligned} \quad (2.17)$$

While this expression governs how quickly nuclear reactions proceed in a stellar plasma, it also contains useful information about the temperature range at which most nuclear burning takes place. Assume for the moment that the astrophysical S-factor

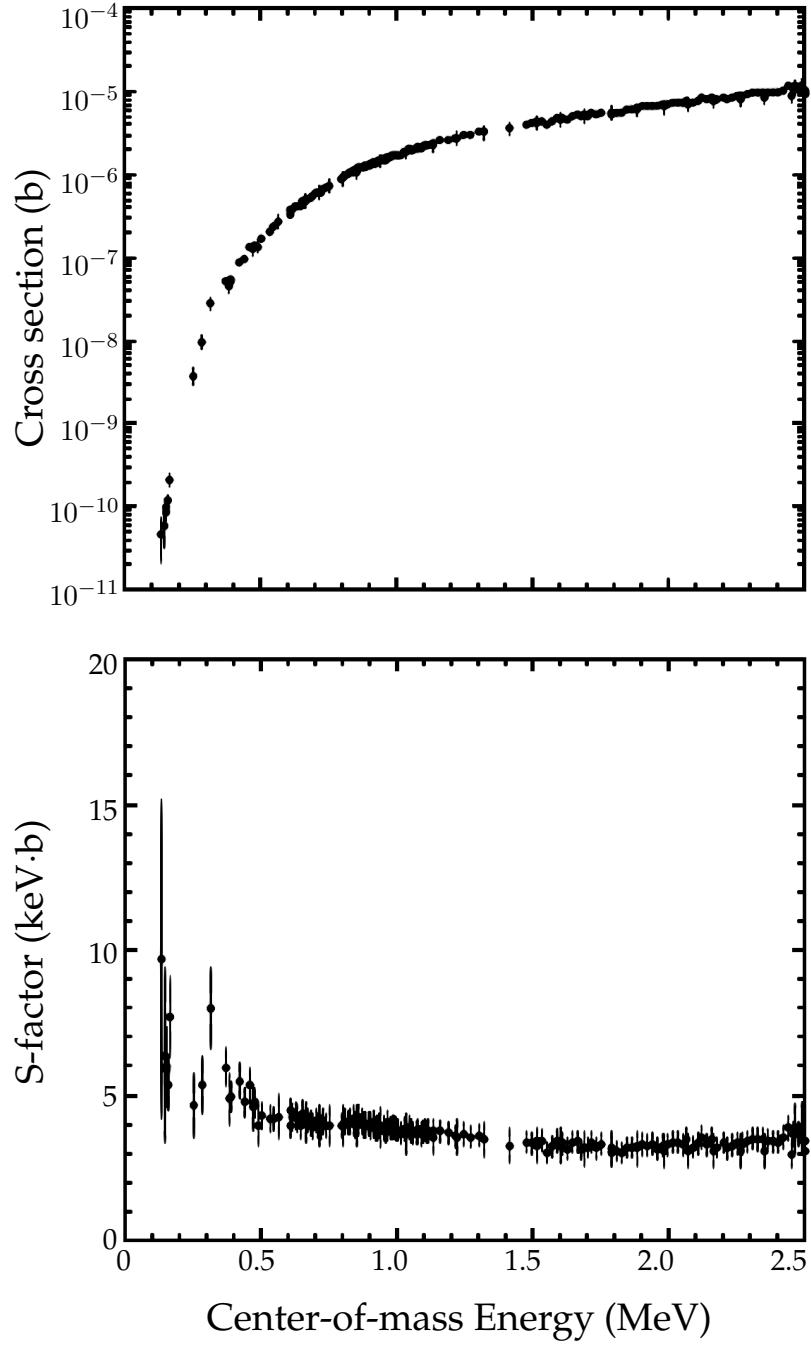


Figure 2.3: Comparison of the experimental cross section (top) and the corresponding S-factor (bottom) for $^{16}\text{O}(p,\gamma)^{17}\text{F}$. Figure from [Iliadis \(2015\)](#) based on data from [Angulo *et al.* \(1999\)](#).

is constant,

$$S(E) \approx S_0. \quad (2.18)$$

The reaction rate in Equation 2.17 becomes

$$N_A \langle \sigma v \rangle \propto \int_0^\infty e^{-2\pi\eta} e^{-E/kT} dE \quad (2.19)$$

where

$$2\pi\eta \propto \sqrt{\frac{1}{E}}. \quad (2.20)$$

The opposing energy dependencies of these terms dictate that most nuclear burning occurs in a narrow range of energies where the product of the terms is maximized. Consequently, the integrand in Equation 2.19 is commonly known as the Gamow peak.

The maximum of the Gamow peak, E_0 , is clearly the most potent energy for the occurrence of nonresonant thermonuclear reactions. It can be found in the usual manner by setting the first derivative equal to zero, yielding

$$\begin{aligned} E_0 &= \left[\left(\frac{\pi}{\hbar} \right)^2 (Z_0 Z_1 e^2)^2 \left(\frac{m_{01}}{2} \right) (kT)^2 \right]^{1/3} \\ &= 0.1220 \left(Z_0^2 Z_1^2 \frac{M_0 M_1}{M_0 + M_1} T_9^2 \right)^{1/3} \text{ (MeV)} \end{aligned} \quad (2.21)$$

where the atomic masses, M_i , are in units of u. By approximating the Gamow peak with a Gaussian function, an estimate of the peak width can be found,

$$\Delta = \frac{4}{\sqrt{3}} \sqrt{E_0 kT} = 0.2368 \left(Z_0^2 Z_1^2 \frac{M_0 M_1}{M_0 + M_1} T_9^5 \right)^{1/6} \text{ (MeV)}. \quad (2.22)$$

At a given temperature, most thermonuclear reactions occur in the $E_0 \pm \Delta/2$ energy range, which is frequently referred to as the Gamow window. Narrow resonances, an exception to this rule, will be discussed in the next section.

While the Gamow window serves as a convenient shorthand for understanding the nuclear burning in stellar environments, the zeroth-order approximation of the astrophysical S-factor (Equation 2.18) used to derive it is too crude to adequately describe many nonresonant reactions. As such, it becomes necessary to expand the astrophysical S-factor as a second-order Taylor series centered on $E = 0$,

$$\begin{aligned} S(E) &= \sum_{n=0}^{\infty} \frac{S^{(n)}(0)}{n!} (E - 0)^n \\ &\approx S(0) + S'(0)E + \frac{1}{2}S''(0)E^2. \end{aligned} \quad (2.23)$$

As shown in Fowler *et al.* (1967), substituting the second-order approximation for the S-factor into the expression for the reaction rate in Equation 2.17 gives

$$N_A \langle \sigma v \rangle = \left(\frac{4}{3} \right)^{3/2} \frac{\hbar}{\pi} \frac{N_A}{m_{01} Z_0 Z_1 e^2} S_{\text{eff}} \tau^2 e^{-\tau} \quad (2.24)$$

where

$$\tau \equiv \frac{3E_0}{kT} = 4.2487 \left(\frac{Z_0^2 Z_1^2}{T_9} \frac{M_0 M_1}{M_0 + M_1} \right)^{1/3} \quad (2.25)$$

and the effective astrophysical S-factor is

$$\begin{aligned} S_{\text{eff}}(E_0) &= S(0) \left[1 + \frac{5}{12\tau} + \frac{S'(0)}{S(0)} \left(E_0 + \frac{35}{36} kT \right) \right. \\ &\quad \left. + \frac{1}{2} \frac{S''(0)}{S(0)} \left(E_0^2 + \frac{89}{36} E_0 kT \right) \right]. \end{aligned} \quad (2.26)$$

Occasionally, the second-order S-factor approximation (Equation 2.23) can diverge from an experimentally determined S-factor curve. This means that the approximation cannot be used in the calculation of the reaction rate beyond the temperature where the divergence occurs. In this situation, the reaction rate expression presented

in Equation 2.24 must be multiplied by a cutoff factor (Fowler *et al.*, 1967),

$$f_{\text{cutoff}} \approx e^{-\left(T_9/T_{9,\text{cutoff}}\right)^2} \quad (2.27)$$

where $T_{9,\text{cutoff}}$ is the temperature (in GK) at which the S-factor approximation begins to significantly diverge from the experimental data. Beyond this cutoff, alternative methods of calculating the reaction rate must be employed.

2.3.2 Resonant Reaction Rates

Thus far, only reaction rates with smoothly varying astrophysical S-factors have been addressed. The cross section for this type of charged particle capture varies smoothly with energy as determined by transmission through the Coulomb barrier rather than the structure of the capturing nucleus. However, the opposite situation is true for phenomena known as resonances. Resonant capture involves the capture of a charged particle by the target nucleus followed by the formation of an excited compound nucleus. For positive-energy resonances, the combined energy of the entrance channel (i.e. the projectile-target system) must match that of the compound nucleus,

$$Q + E_r^{CM} = E_x \quad (2.28)$$

for the event to proceed. Q is the Q-value of the reaction, E_r^{CM} is the resonance energy in the center-of-mass frame, and E_x is the excited state of the compound nucleus in this expression. This condition is true for any excited state above the threshold energy defined by the Q-value.

The energy condition given by Equation 2.28 gives rise to the matching of the interior and exterior wave functions at the nuclear radius, resulting in a significant amplitude increase in the total nuclear wave function of the projectile-target system.

This manifests in a sharp spike in the reaction cross section in a narrow energy range centered on E_r^{CM} . For a theoretical reaction $A(a,b)B$, a subset of resonances—often referred to as narrow resonances—have roughly constant partial widths for the entrance and exit channels, Γ_a and Γ_b , over the total resonance width, Γ . Given the complex network of nucleon interactions possible in a heavy compound nucleus (Bohr, 1936), it is easy to see how a large number of narrow but closely spaced resonances might exist for a given reaction.

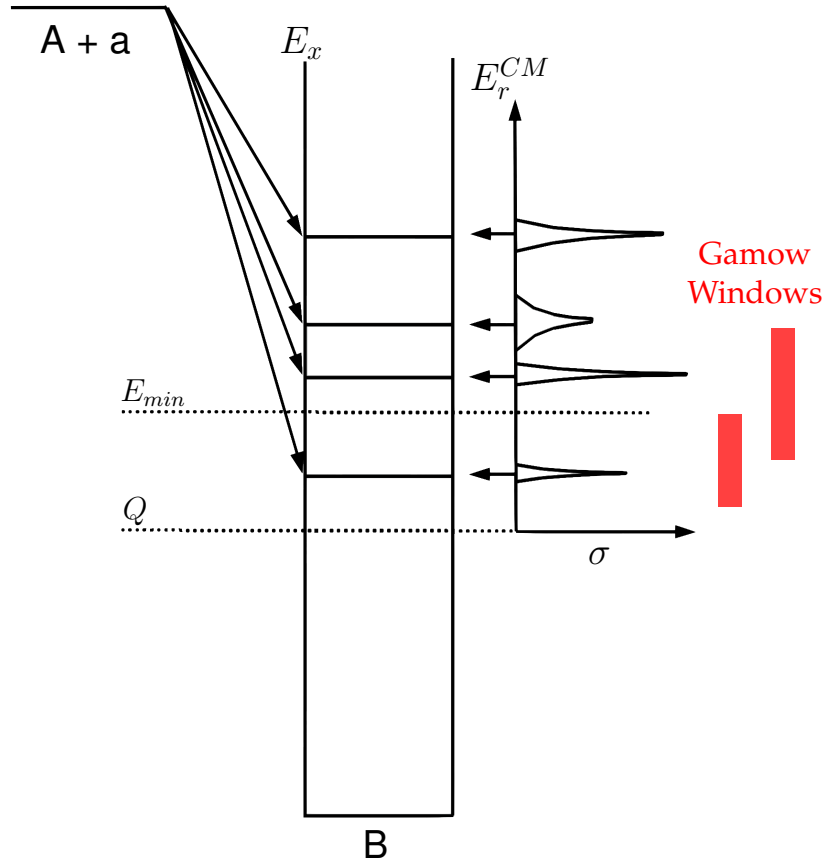


Figure 2.4: Narrow resonance energy level diagram illustrating the the radiative capture of projectile a by target nucleus A and the subsequent formation of compound nucleus B . The relationship of this process to the energy-dependent cross section and Gamow window is also shown. Figure from Iliadis (2015).

Illustrating these relationships, Figure 2.4 (Iliadis, 2015) shows a level diagram depicting the theoretical resonant capture of projectile a by target nucleus A , leading to the formation of compound nucleus B . The minimum energy attainable in direct laboratory measurements, E_{min} , and the reaction Q -value, Q , are indicated by dotted lines. Four excited states, E_x , exist above the Q -value and lead to narrow resonances at these energies. The sharp increases in the cross section due to the corresponding resonances are shown to the right of the level diagram. Two Gamow windows, representing different stellar burning temperature ranges, are shown in red. It is clear that the lowest lying resonance resides within the first Gamow window but falls below E_{min} , meaning that it cannot be directly measured in the laboratory. The lowest *observable* resonance falls within the temperature range of the second Gamow window. While resonances do not usually contribute strongly to the total cross section of a reaction, they can contribute significantly to stellar burning due to the fortuitous overlap of resonance energy and Gamow window pictured here.

Assuming a narrow resonance is relatively isolated, its cross section can be described by a one-level Breit-Wigner equation,

$$\begin{aligned}\sigma(E)_{\text{resonant}} &= \frac{\lambda^2}{4\pi} \frac{2J+1}{(2j_0+1)(2j_1+1)} \frac{\Gamma_a \Gamma_b}{(E_r - E)^2 + 1/4\Gamma^2} \\ &= \frac{\lambda^2}{4\pi} \omega \frac{\Gamma_a \Gamma_b}{(E_r - E)^2 + 1/4\Gamma^2}\end{aligned}\quad (2.29)$$

where J is the spin of the resonance, j_i are the spins of the projectile and target nuclei, Γ_i are the partial widths of the entrance and exit channels of the resonance, Γ is the total resonance width, and λ is the de Broglie wavelength, given by

$$\lambda = \frac{2\pi}{k} = \frac{2\pi\hbar}{\sqrt{2m_{01}E}}. \quad (2.30)$$

Equation 2.29 also introduces a new term, ω , which sequesters the angular properties

of the projectile-target system from the rest of the expression. This term is defined as

$$\omega \equiv \frac{2J + 1}{(2j_0 + 1)(2j_1 + 1)} \quad (2.31)$$

for a system of nonidentical particles in the reaction entrance channel. Combining the expression for the resonant cross section (Equation 2.29) with the general expression for the thermonuclear reaction rate in a stellar plasma (Equation 2.14) yields the thermonuclear reaction rate for narrow resonances,

$$\begin{aligned} N_A \langle \sigma v \rangle_{\text{resonant}} &= N_A \left(\frac{8}{\pi m_{01}} \right)^{1/2} \frac{1}{(kT)^{3/2}} \int_0^\infty E \sigma(E)_{\text{resonant}} e^{-E/kT} dE \\ &= \frac{N_A \hbar^2 \sqrt{2\pi}}{(m_{01} kT)^{3/2}} \omega \int_0^\infty \frac{\Gamma_a \Gamma_b}{(E_r - E)^2 + 1/4\Gamma^2} e^{-E/kT} dE. \end{aligned} \quad (2.32)$$

As mentioned earlier, a narrow resonance is being defined as a sufficiently narrow and isolated resonance such that the partial widths of the entrance and exit channels can essentially be treated as constant over the total width of the resonance. Furthermore, the Maxwell-Boltzmann factor, $e^{-E/kT}$, can also be treated as constant over such a narrow energy range. Consequently, the resonant reaction rate can be simplified to

$$\begin{aligned} N_A \langle \sigma v \rangle_{\text{resonant}} &\approx \frac{N_A \hbar^2 \sqrt{2\pi}}{(m_{01} kT)^{3/2}} \omega \frac{\Gamma_a \Gamma_b}{\Gamma} e^{-E_r/kT} \int_0^\infty \frac{\Gamma}{(E_r - E)^2 + 1/4\Gamma^2} dE \\ &\approx \frac{N_A \hbar^2 \sqrt{2\pi}}{(m_{01} kT)^{3/2}} \omega \frac{\Gamma_a \Gamma_b}{\Gamma} e^{-E_r/kT} (2\pi) \\ &\approx N_A \hbar^2 \left(\frac{2\pi}{m_{01} kT} \right)^{3/2} \omega \gamma e^{-E_r/kT} \end{aligned} \quad (2.33)$$

where

$$\omega \gamma \equiv \omega \left(\frac{\Gamma_a \Gamma_b}{\Gamma} \right). \quad (2.34)$$

This new term, $\omega \gamma$, is referred to as the resonance strength. It is proportional to the product of the maximum of the resonant cross section, $\sigma(E_r)$, and the total width of

the resonance, Γ , but independent of the shape of the cross section curve. As few partial and total widths of narrow resonances are experimentally known, the use of resonance strength measurements to improve reaction rate calculations is particularly advantageous.

If multiple narrow, isolated resonances are known to contribute to the reaction cross section, their contributions to the reaction rate can be summed coherently. Thus, the numerical expression for the reaction rate due to multiple resonances is given by [Iliadis \(2015\)](#) as

$$N_A \langle \sigma v \rangle = (1.5399 \times 10^{11}) \left(\frac{M_0 M_1}{M_0 + M_1} T_9 \right)^{-3/2} \sum_i (\omega \gamma)_i e^{-11.605 E_i / T_9} \left(\frac{\text{cm}^3}{\text{mol} \cdot \text{s}} \right) \quad (2.35)$$

where E_i are the corresponding resonance energies in MeV, $(\omega \gamma)_i$ are the resonance strengths in MeV, the atomic masses M_i are in units of u, and i denotes different contributing resonances.

CHAPTER 3: CLASSICAL NOVA NUCLEOSYNTHESIS

As shown in Chapter 2, the rate of a particular reaction in a stellar plasma can be found by studying the resonant and nonresonant processes through which the reaction proceeds. However, it can be seen in Figure 1.4 that a web of reactions governs the production and destruction of any given nuclear species. If the abundance of a nuclear species changes solely from nuclear processes, the abundance evolution of a nucleus i is given by Iliadis (2015) as

$$\frac{dN_i}{dt} = \left[\sum_{j,k} N_j N_k \langle \sigma v \rangle_{jk \rightarrow i} + \sum_l \lambda_{\beta, l \rightarrow i} N_l + \sum_m \lambda_{\gamma, m \rightarrow i} N_m \right] \quad (3.1)$$

$$- \left[\sum_n N_n N_i \langle \sigma v \rangle_{ni} + \sum_o \lambda_{\beta, i \rightarrow o} N_i + \sum_p \lambda_{\gamma, i \rightarrow p} N_i \right]. \quad (3.2)$$

The first bracketed group of terms includes all processes that produce nucleus i while the second bracketed group of terms represents all processes that destroy this nucleus. The first, second, and third terms in each bracket correspond to the change in the abundance of nucleus i caused by nuclear reactions, β -decay, and photodisintegration, respectively.

Of course, a single nuclide is typically one of many nuclear species involved in a given stellar burning process, and the evolution of all species must be considered simultaneously. Thus, nucleosynthesis is simulated using a system of coupled, nonlinear ordinary differential equations referred to as a *nuclear reaction network*. For simple cases, a reaction network can be solved analytically (see Clayton, 1983), but far more frequently reaction networks prove complex, requiring the application of numerical

techniques.

In this chapter, the methodology and results of neon nova nucleosynthesis simulations will be presented. Section 3.1 will detail the post-processing nuclear reaction network as well as the necessary input parameters used in these simulations. Next, the differences between single- and multiple-zone simulations will be addressed (Section 3.2). Summarizing the work of Downen *et al.* (2013), Section 3.3 presents the final elemental abundances of the nucleosynthesis study, the resulting nuclear thermometers, and the comparison to spectroscopic observations (Section 1.2.1). Finally, Section 3.4 will provide motivation for the current $^{29}\text{Si}(p,\gamma)^{30}\text{P}$ study by comparing isotopic ratios from neon nova simulations to those of the presolar grain measurements of Table 1.3.

3.1 Reaction Network & Input Parameters

Given the diversity of the nuclear species synthesized by classical novae, it is quite clear that an extensive reaction network of many nuclear species and processes was needed to properly model these explosions and explore the effects of reaction rate uncertainties. This type of calculation would ideally be carried out using a nova hydrodynamic model, which couples nucleosynthesis to the larger scale physics of the event. However, these simulations are computationally intensive, and while a few small-scale studies of key reaction rate uncertainties using hydrodynamic simulations have been carried out in the past (José *et al.*, 1999, 2001; Coc *et al.*, 2000), a full exploration of the reactions important to nova explosions and the effect of their rate uncertainties necessitates an alternate approach.

Thus, a post-processing simulation technique was employed in favor of hydrodynamic simulations. This requires that time-temperature-density profiles be extracted

from hydrodynamic models to be used as input for the post-processing nucleosynthesis simulations. The nucleosynthesis simulated by the post-processing reaction network was then directly dependent on these three parameters—time, temperature, and density—while some of the more complicated physics of the hydrodynamic models was implicitly included. Though they are still somewhat limited in their ability to account for the effects of convective mixing of material between burning zones and other complex issues, post-processing reaction networks have been used successfully in past classical nova reaction rate sensitivity research (Iliadis *et al.*, 2002).

For this work, an extensive post-processing reaction network was used to follow the evolution of over 100 distinct species, from hydrogen to titanium, through more than 600 nuclear processes important to nova nucleosynthesis including (p,γ) , (p,α) , (α,γ) , their reverse reactions, and weak interactions. Four new hydrodynamic models of neon novae were produced using the SHIVA code described in José and Hernanz (1998) to prepare the time-temperature-density profiles for use in the post-processing network. The white dwarf stars in these models range from $1.15 M_{\odot}$ to $1.35 M_{\odot}$, and the peak temperatures attained are considered representative of the average neon nova explosion. It must be noted that other models reach higher peak temperatures, resulting in the breakout of processed material from the hot CNO cycle to ^{20}Ne and above (Starrfield *et al.*, 2009), but were not explored in this work. Table 3.1 lists selected properties of these models.

Despite the lack of breakout, nucleosynthesis beyond the CNO region is able to proceed on $A \geq 20$ seed nuclei from underlying white dwarf material that was incorporated into the accreted envelope before the thermonuclear runaway occurred. The initial composition of the envelope, presented in Table 3.2, was assumed to be a mixture of 50% solar composition material and 50% ONe white dwarf material by mass. The solar composition abundances were taken from Lodders *et al.* (2009), and the white dwarf composition was adopted from Ritossa *et al.* (1996), who simulated

Table 3.1. Selected Properties of Evolutionary Neon Nova Models

Property	Model			
	J115	J125	J130	J135
$M_{WD} (M_{\odot})$	1.15	1.25	1.30	1.35
$T_{peak} \text{ (GK)}$	0.228	0.248	0.265	0.313
$M_{ej} (10^{-5} M_{\odot})$	2.46	1.89	1.17	0.455
$R_{WD}^{ini} \text{ (km)}$	4326	3788	3297	2255

Note. — All models assume the percentage of mixing between solar accreted matter and white dwarf material to be 50%. The initial luminosity and mass accretion rate for all models are $L_{ini} = 10^{-2} L_{\odot}$ and $\dot{M}_{acc} = 2 \times 10^{-10} M_{\odot}/\text{yr}$, respectively. This table was originally published in [Downen *et al.* \(2013\)](#).

the evolution of a $10 M_{\odot}$ main sequence star to the conclusion of core carbon burning. The accreted envelope was divided into 45 equal mass zones as additional divisions were not found to be advantageous. As will be discussed in Section 3.2, two types of time-temperature-density profiles were extracted from the hydrodynamic models: one including only the innermost and hottest hydrogen-burning region used in one-zone simulations and the second containing all 45 burning zones used in multi-zone simulations.

For both the hydrodynamic and post-processing simulations, reaction rates and their uncertainties were sourced from STARLIB ([Sallaska *et al.*, 2013](#)), a novel reaction rate library that was particularly well suited for use in classical nova reaction rate sensitivity studies. The library tabulates rates and their corresponding uncertainties at 60 grid points from 1 MK to 10 GK. In the mass range $A = 14\text{--}40$, the library includes 62 reaction rates that were calculated using a statistically rigorous Monte Carlo approach ([Longland *et al.*, 2010b](#); [Iliadis *et al.*, 2010a,b,c](#)) for the first time, and a number of these reactions are critical to classical nova nucleosynthesis. Most importantly, the STARLIB reaction rate uncertainties, determined by randomly sampling over the errors of

Table 3.2. Initial Composition of Presented Nova Simulations

Nuclide	Mass Fraction	Nuclide	Mass Fraction	Nuclide	Mass Fraction
^1H	3.56×10^{-1}	^{17}O	1.37×10^{-6}	^{29}Si	1.85×10^{-5}
^3He	4.23×10^{-5}	^{18}O	7.72×10^{-6}	^{30}Si	1.26×10^{-5}
^4He	1.37×10^{-1}	^{19}F	2.08×10^{-7}	^{31}P	3.50×10^{-6}
^6Li	3.44×10^{-10}	^{20}Ne	1.57×10^{-1}	^{32}S	1.74×10^{-4}
^7Li	4.91×10^{-9}	^{21}Ne	2.99×10^{-3}	^{33}S	1.42×10^{-6}
^9Be	7.51×10^{-11}	^{22}Ne	2.22×10^{-3}	^{34}S	8.24×10^{-6}
^{10}B	5.05×10^{-10}	^{23}Na	3.22×10^{-2}	^{35}Cl	1.87×10^{-6}
^{11}B	2.26×10^{-9}	^{24}Mg	2.77×10^{-2}	^{37}Cl	6.29×10^{-7}
^{12}C	5.74×10^{-3}	^{25}Mg	7.94×10^{-3}	^{36}Ar	3.84×10^{-5}
^{13}C	1.42×10^{-5}	^{26}Mg	4.98×10^{-3}	^{38}Ar	7.40×10^{-6}
^{14}N	4.04×10^{-4}	^{27}Al	5.43×10^{-3}	^{39}K	1.86×10^{-6}
^{15}N	1.59×10^{-6}	^{28}Si	3.51×10^{-4}	^{40}Ca	3.18×10^{-5}
^{16}O	2.59×10^{-1}				

Note. — Values are obtained assuming 50% mixing of solar accreted matter (Lodders *et al.*, 2009) with ONe white dwarf material (Ritossa *et al.*, 1996) by mass.

associated nuclear physics input and a probability coverage of 68%, provided crucial guidance as to the realistic range of reaction rate values worthy of exploration.

One final consideration was taken into account to ensure the nucleosynthesis calculations would parallel observational conditions as closely as possible. During a classical nova explosion, all matter that reaches escape velocity would be expected to be ejected into the interstellar medium, but this matter is typically not observed before some short-lived nuclei decay to stable species. Therefore, all profiles were extended by one hour (beyond the occurrence of peak temperature) at nominal temperature and density to allow these decays to take place before the final abundances were compiled. With all of these pieces in place, a post-processing network calculation can be completed in a matter of minutes on a consumer grade computer. The results of such calculations are presented in Sections 3.3 and 3.4.

3.2 Single- & Multiple-Zone Simulations

As mentioned in the previous section, two different types of time-temperature-density profiles were extracted from the SHIVA hydrodynamic models. Single-zone profiles, the simpler variety that only follows the conditions of the innermost burning shell, have been used in past classical nova sensitivity studies such as [Iliadis *et al.* \(2002\)](#). This served as a natural starting point for the exploration of reaction rate uncertainty effects on nova nucleosynthesis in this work. The temperature-density curves shown in Figure 3.1 illustrate the single-zone profiles of the innermost shell for the nova models presented in Table 3.1. These temperature-density curves represent the innermost, and generally hottest, zone of each nova model, meaning that the material in this region experienced the most nuclear processing. With only a single zone simulated, the computational time required for this type of simulation was significantly reduced in addition to the resources saved by using a post-processing network in favor of full hydrodynamic simulation. The use of single-zone post-processing simulations was thus an attractive method to study the reaction rate uncertainty effects on classical nova nucleosynthesis comprehensively.

However, any comparison of observational abundances with single-zone final abundances was fraught with numerous complications. For one, it was clear that even the most basic treatment of convection between this region and regions beyond was made impossible by the presence of only one burning shell in this type of simulation. Additionally, the innermost shell did not always reach escape velocity, which was necessary for the shell to be ejected into the interstellar medium and later observed spectroscopically or in presolar grains. Finally and most importantly, the extensive nuclear processing of material that occurred in the innermost shell of the accreted envelope was not necessarily representative of the processing in the whole envelope. Figure 3.2 displays the temperature-density curves for the innermost (1st), 10th, 20th,

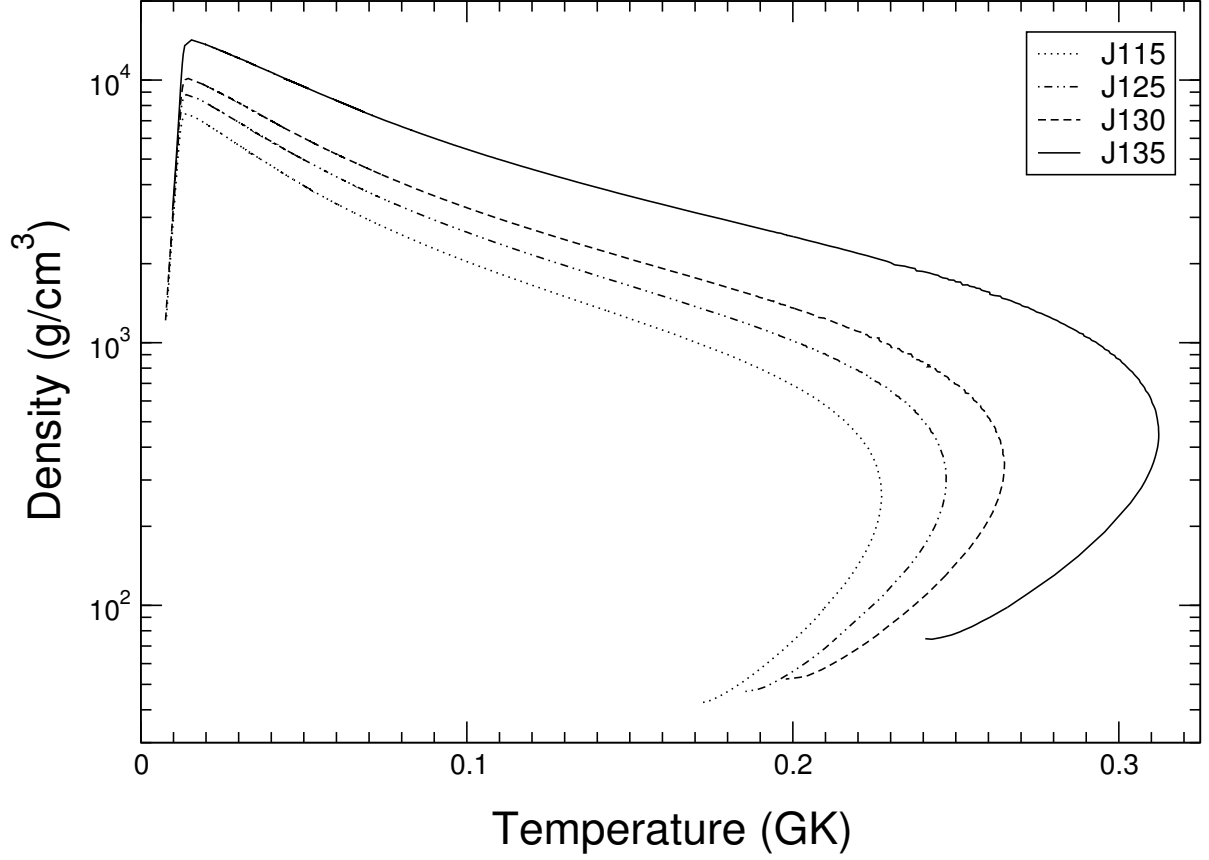


Figure 3.1: Temperature-density curves for the innermost burning shell of selected neon nova simulations. These curves correspond to the models presented in Table 3.1 and were used for the single-zone nucleosynthesis simulations in this work. Exponential smoothing was applied to the pictured curves to eliminate the effects of numerical instabilities. The curves, which show the evolution of the innermost shells from high to low density, were also truncated to display only the region of primary importance to nucleosynthesis.

30th, 40th, and outermost (45th) equal mass burning shells for the $1.25 M_{\odot}$ nova model. It can easily be seen that the temperature and density, upon which nuclear reactions are highly dependent, vary widely between the innermost and outermost shells. Since these shells are equal in mass, the largely unprocessed material from the outermost regions of the accreted envelope could be expected to dilute the highly processed material from the innermost regions when the envelope is ejected. It is this mixture that is observed and would likely be very different from the innermost shell abundances given by a single-zone simulation.

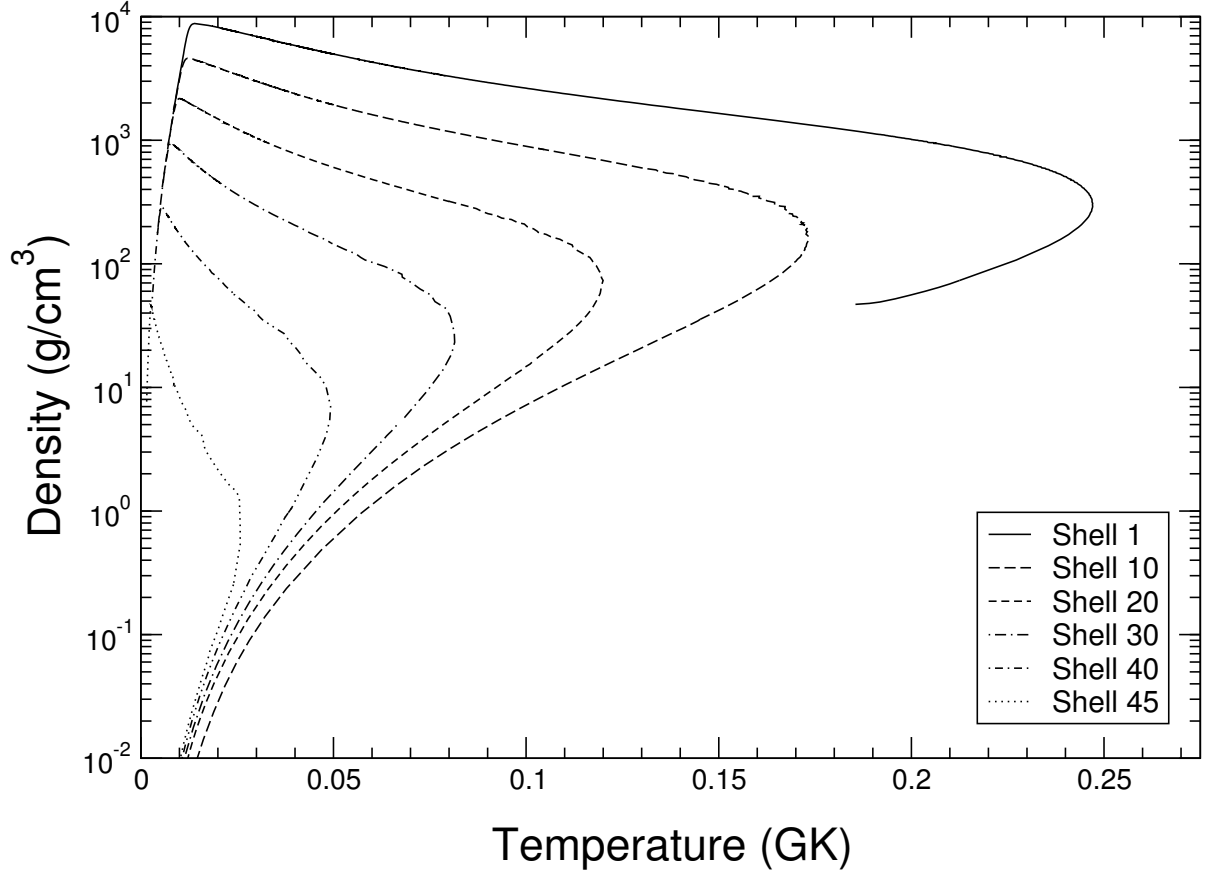


Figure 3.2: Temperature-density curves for the multiple burning shells of the $1.25 M_{\odot}$ ONe WD nova model. The curves for shells 1, 10, 20, 30, 40, and 45 are shown where shell 1 is the innermost shell (closest to the surface of the white dwarf) and shell 45 is the outermost shell (farthest from the surface of the white dwarf). Exponential smoothing was applied to the pictured curves to eliminate the effects of numerical instabilities, and the curves were truncated to display only the region important to nucleosynthesis. Select properties of this model are given in Table 3.1.

When some initial attempts to connect single-zone elemental abundances to observational data were made, it became apparent that the single-zone nucleosynthesis in the innermost burning region could not be used to study the effect of reaction rate variations and then meaningfully compare the results to observations. Consequently, the multiple-zone nova profiles were employed in order to simulate nucleosynthesis occurring throughout the accreted envelope. This type of profile, as mentioned previously, represents the entirety of the accreted envelope using 45 equal mass zones, but

the simulations that used these profiles essentially required 45 times as many calculations as the single-zone simulations as a result. Even so, this was substantially less computational time than necessary for hydrodynamic simulations.

This type of simulation also allowed for some treatment of convective mixing between burning shells. However, the post-processing reaction network was not directly coupled to the hydrodynamics of the nova outburst, so several methods of approximating the effects of convection have been developed in an attempt to compensate for this simplification. Three different approximations of convective mixing—no mixing, instantaneous mixing, and geometric mean mixing—were examined in this work.

The simplest of the three approaches, no mixing, relied upon the assumption that the time scale over which convective mixing takes place was considerably longer than the time scale of the nucleosynthesis and subsequent explosion. The outcome was that convection can be neglected, and the nucleosynthesis of each burning shell occurs independently. The final abundances of all shells were then mass averaged by species to give the final abundances for the nova as a whole. This procedure was similar to that of [Smith *et al.* \(2002\)](#).

Conversely, the second mixing approximation, instantaneous mixing, supposed that convection occurred on a much shorter time scale than nuclear processing. This assumption was presented by [Prialnik \(1986\)](#) in the context of a hydrodynamic model. As a result, convection was then presumed to occur instantaneously, even in the case of short nuclear time scales, and the thermonuclear rate for a given shell and reaction was approximated by the mass-averaged rate for the entire convective region.

In all likelihood, the actual impact of convective mixing existed between these two extremes. Geometric mean mixing, the third convection approximation, was chosen to represent this middle ground. This approach simply involved calculating the geometric mean of the instantaneous mixing and no mixing final abundances for each species.

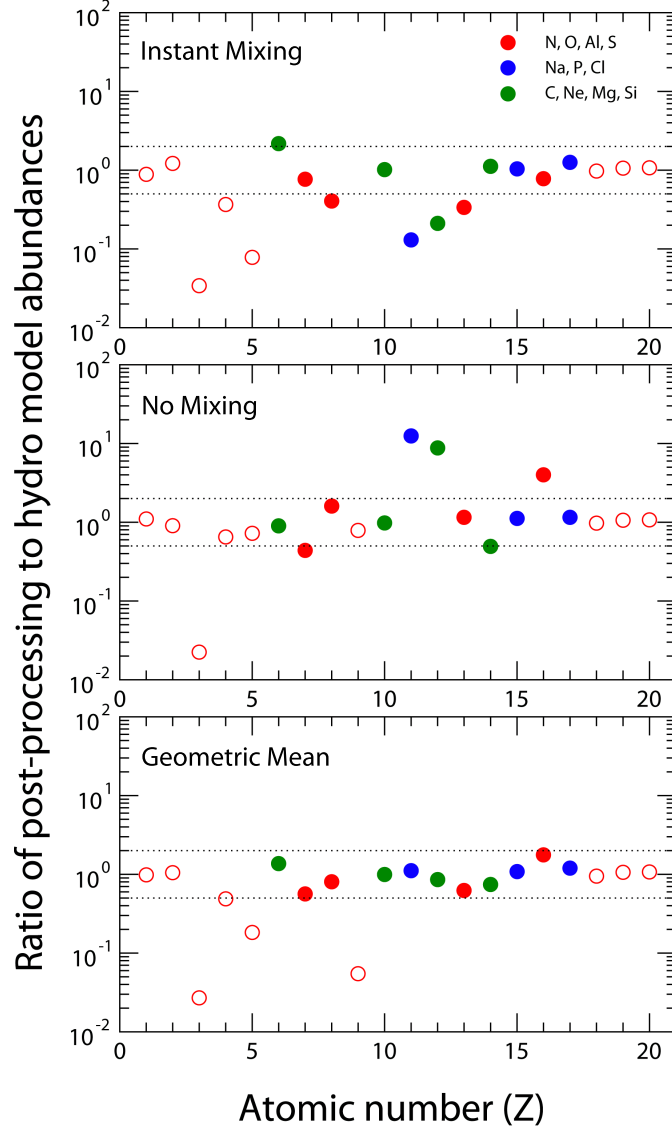


Figure 3.3: Comparison of final elemental abundances from post-processing calculations and full hydrodynamic simulations of the J125 nova model presented in Table 3.1. The ratio of post-processing final abundances to that of hydrodynamic models is shown versus atomic mass number, Z . The elements of interest are given in filled color; other elements are displayed as outlines. The three panels are obtained for the different mixing assumptions in the post-processing calculations. **Top:** instant-mixing. **Middle:** no-mixing. **Bottom:** geometric mean of abundances from the top and middle panels. Similar results were obtained for the other three nova models. Figure from Downen *et al.* (2013).

By considering these three treatments of convective mixing, the final abundances of all elements of interest were well represented by the multiple-zone post-processing

simulations and consistent with the abundances predicted by hydrodynamic models. Figure 3.3 shows the comparison of final abundances from multiple-zone post-processing calculations and hydrodynamic simulations for the $1.25 M_{\odot}$ WD ONe nova model. The ratio of final abundances is plotted versus mass number with dotted lines that represent a factor 2 deviation from the hydrodynamic results. Elements of interest are displayed in filled color while other elements appear in outline only. The top, middle, and bottom panels present this ratio for the instantaneous mixing, no mixing, and geometric mixing approximations, respectively. The elements of interest are approximated remarkably well by geometric mean mixing for this model, a result that holds true for all of the nova models explored in this work. Thus, the final abundances reported in later sections were generated using the convective mixing method that most closely predicted the hydrodynamic abundances of a given nova model.

In summary, the single-zone simulations used in previous work were ultimately found to be insufficient in producing final abundances comparable to those of observations. The subsequent development and use of the multiple-zone simulations allowed for the amelioration of several shortcomings inherent in the use of single-zone calculations for this work. In addition to better representing the physics of the nova explosion and the conditions preceding observation, the more complex multiple-zone simulations allowed for the introduction of convective mixing treatments. Three different mixing approximations were studied, and the final abundances presented in Sections 3.3 and 3.4 were generated using the convective mixing method that best predicted the abundances of the hydrodynamic models.

3.3 The Elemental Abundance Study

In the hope of better understanding classical novae, it is essential to find a way to connect measurable values from spectroscopic observations to simulation results and

then determine the quality of this metric. One of the most important properties of a classical nova from a nucleosynthesis perspective is the peak burning temperature achieved by the thermonuclear runaway. This can also be directly correlated to the mass of the underlying white dwarf, but there is no established method of extracting this information from spectroscopic observations of nova ejecta. Since observations provide information about the elemental makeup of the ejected envelope and classical nova nucleosynthesis simulations are designed to predict these values, a comparison of these two datasets over a range of peak temperatures was a natural choice to address these goals. This is precisely the work carried out in [Downen *et al.* \(2013\)](#), which is reviewed and expanded upon in this section.

3.3.1 The Development of Nuclear Thermometers

As a first step, the hydrodynamic final elemental abundances of the nova models presented in Table 3.1 were examined for dependence on peak temperature. In order to identify a peak-temperature dependence effectively, it was preferable that any elemental trends be independent of initial abundance. To this end, the hydrodynamic elemental abundances for the nova models were normalized to the initial abundances of the accreted envelope (see Table 3.2) and plotted as a function of mass number Z . These results are shown in Figure 3.4. It was determined that certain elements, such as N, Si, P, and S, were overproduced while others, such as O, Na, and Mg, were underproduced. Of these, N, O, Na, Al, P, and S demonstrate significant, monotonic dependence on peak temperature. It must be noted that F, Cl, and Ar also display these trends but their overall abundance in the ejected envelope was expected to be quite low ($< 10^{-5}$ in mass fraction); therefore, these elements would not be useful metrics and were not studied further.

As mentioned in Section 1.2.1, observed elemental abundances presented as ratios are less susceptible to systemic effects, so the elements with robust dependence

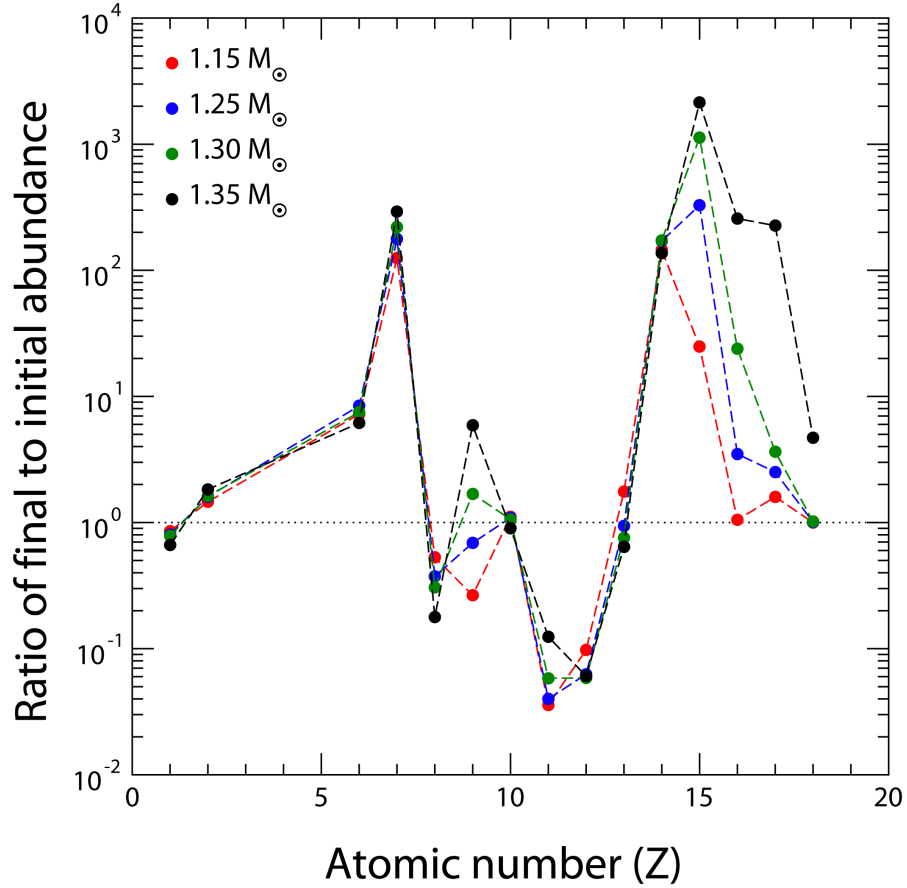


Figure 3.4: Final elemental abundances normalized to initial abundances and presented versus atomic number for all four hydrodynamic models. Each nova model is represented by a different color marker. The dotted line represents the point at which the final and initial abundances are equal for a given element. Using this as a guide, it is clear that some elements (O, Na, Mg) are underproduced while others (N, Si, P, S) are overproduced. If production is a monotonic function of temperature, the color sequence of the markers is red, blue, green, black, or the reverse. Originally published in [Downen et al. \(2013\)](#).

on peak temperature were combined to form elemental ratios that preserved this dependence. These ratios were designated potential *nuclear thermometers* as these ratios were designed to probe the peak temperature of classical nova explosions. The thermometer candidates are shown versus peak temperature in Figure 3.5. Naturally, it is preferable for the ratios to include only elements that are regularly observed spectroscopically, but four ratios include Na and P, elements that have not been observed in nova ejecta to date and are of limited utility as a result. These ratios are shown

as dotted lines. Of all the candidates, O/S and S/Al demonstrated the most extreme dependence on temperature, varying roughly 3 orders of magnitude over the peak temperature range of the four nova models explored here. The O/P and P/Al values spanned two orders of magnitude, and the remaining ratios increased or decreased by one order of magnitude each.

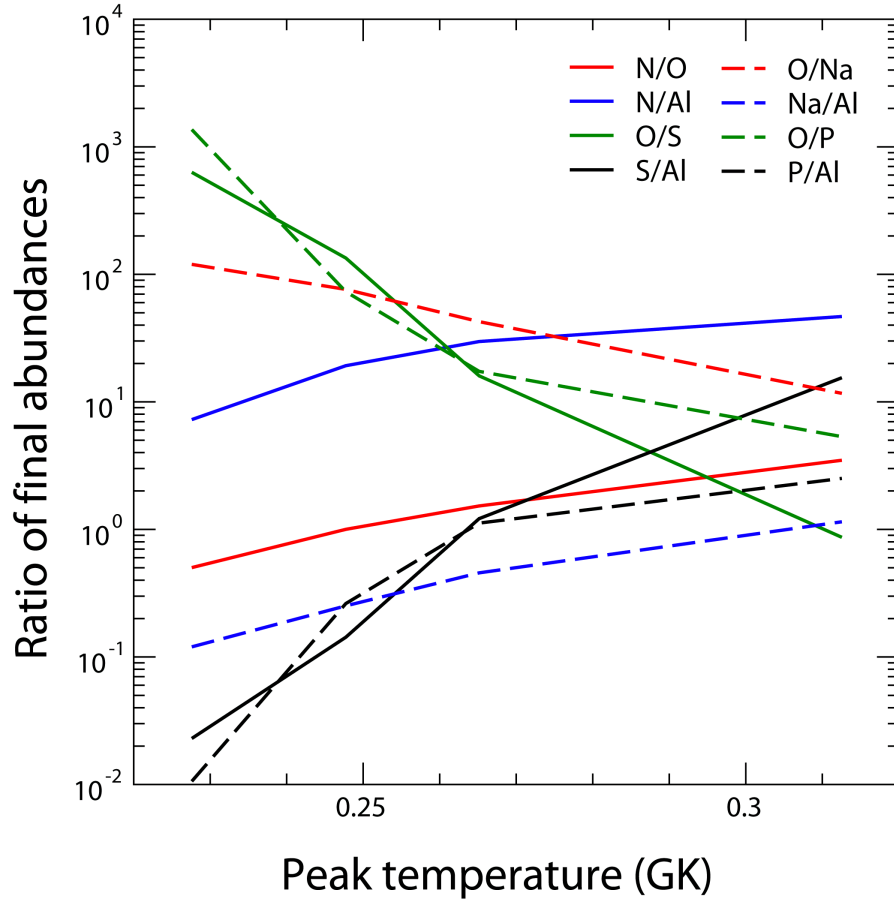


Figure 3.5: Mass fraction ratios of eight elemental abundances versus temperature. These ratios all demonstrate a dependence on peak temperature of an order of magnitude or more and are the prime candidates for nova thermometers. Solid lines indicate ratios involving elements that are spectroscopically observed regularly while dotted lines denote elemental ratios with the inclusion of elements that are not generally observed. Figure from [Downen *et al.* \(2013\)](#).

Of course, the utility of any thermometer would be sharply limited if the uncertainty in its value exceeded the already sizable uncertainty present in spectroscopic abundances, so the sensitivity of the nuclear thermometer candidates to reaction rate

uncertainties was investigated. More than 7000 simulations were carried out in order to independently vary the rates of 214 reactions by factors of 0.01, 0.1, 0.2, 0.5, 2, 5, 10, and 100. The final elemental abundances produced with these variations were then linearly interpreted to quantify the effect of the realistic reaction rate uncertainties provided by the STARLIB library. The results of this probe are given in Figure 3.6, which shows eight panels, each displaying a nuclear thermometer and its sensitivity to the STARLIB rate uncertainties graphed as a function of peak temperature. The panels on the left side of the figure pertain to elements that have been observed spectroscopically to date while the panels to the right involve nuclear thermometer candidates with at least one element that has not been observed. The solid red line in each panel is the hydrodynamic abundance of the thermometer, and the solid black line is the abundance as given by the post-processing reaction network with the convective mixing method that most closely reproduces the hydrodynamic values. The dotted black lines show the range in the thermometer value as a result of the STARLIB reaction rate uncertainties.

Several conclusions were drawn from the information displayed in this figure. First, there is compelling agreement between the values from the hydrodynamic simulations and the post-processing calculations. These values differ by a factor of 2 or less on average, confirming the hypothesis that post-processing calculations provide a viable method of approximating the results of hydrodynamic simulations for the elements of interest here. In regard to reaction rate uncertainties, the N/O and N/Al thermometers show promise since they have uncertainties of less than 30% and N, O, and Al have all been observed spectroscopically in the past. O/Na and Na/Al have similarly low uncertainties but limited use because sodium has not been successfully observed in the ejecta of neon novae. The utility of the four remaining ratios—O/S, S/Al, O/P, and P/Al—is restricted by substantial reaction rate uncertainty, leading to proportionally large (factor 3–6) uncertainties in their values. These ratios exhibit the

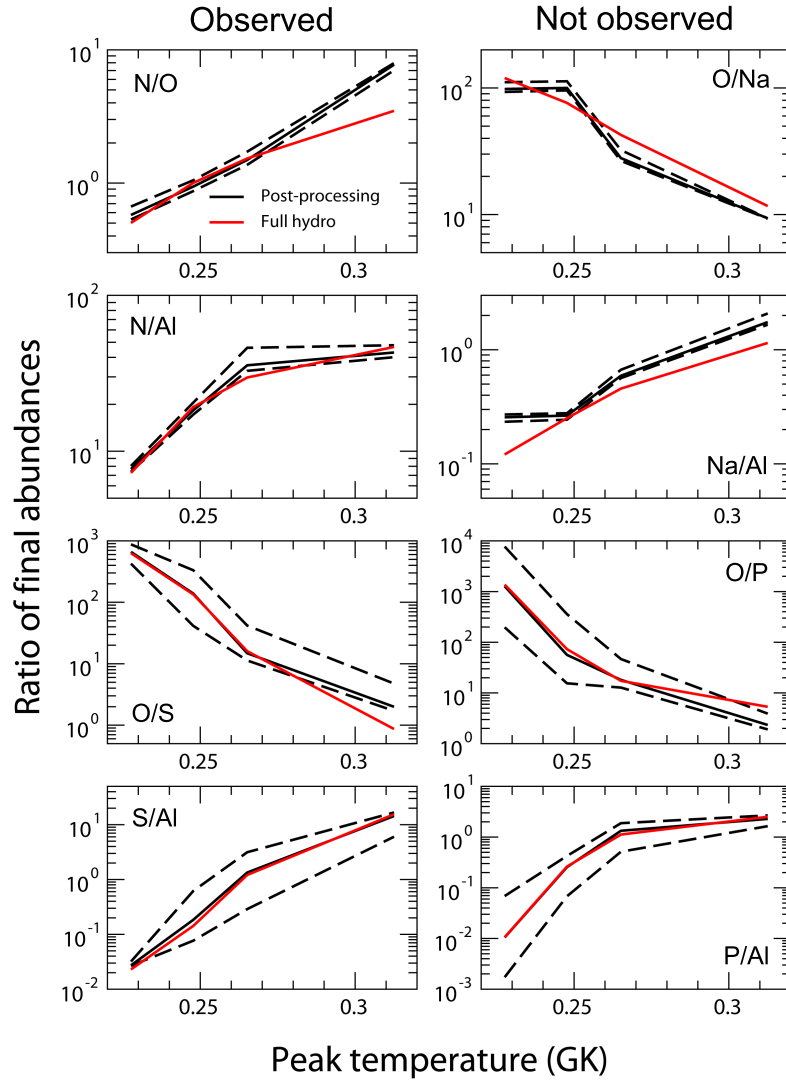


Figure 3.6: Eight nuclear thermometer candidates plotted as functions of peak temperature. These elemental ratios all demonstrated a strong, monotonic dependence on peak temperature. The panels to the left only involve elements that have been previously observed in nova ejecta, while the panels to the right include an element (Na or P) that has been searched for but not yet observed. Solid red and black lines indicate the ratios given by hydrodynamic and post-processing simulations, respectively, using recommended reaction rates. The dashed black lines represent the uncertainty in the elemental ratios due to reaction rate uncertainty. Broad uncertainty bands, such as the ones present in the lower four panels, indicate the need for improved measurements of the primary and secondary sources of uncertainty given in Table 3.3. This figure was originally published in [Downen *et al.* \(2013\)](#).

largest dependence on temperature though, thereby mitigating the effects of reaction rate uncertainty. While all four of these thermometers would benefit from the precise

Table 3.3. Uncertainty Sources of Neon Nova Abundance Predictions

Ratio	Range ^a	Primary Source		Secondary Source	
		Reaction	Uncertainty ^b	Reaction	Uncertainty ^b
N/O	13.4	$^{16}\text{O}(\text{p},\gamma)^{17}\text{F}$	1.16	$^{13}\text{N}(\text{p},\gamma)^{14}\text{O}$	1.06
N/Al	5.59	$^{20}\text{Ne}(\text{p},\gamma)^{21}\text{Na}$	1.29	$^{13}\text{N}(\text{p},\gamma)^{14}\text{O}$	1.18
O/S	332	$^{30}\text{P}(\text{p},\gamma)^{31}\text{S}$	3.36	$^{28}\text{Si}(\text{p},\gamma)^{29}\text{P}$	1.09
S/Al	529	$^{30}\text{P}(\text{p},\gamma)^{31}\text{S}$	4.62	$^{28}\text{Si}(\text{p},\gamma)^{29}\text{P}$	1.12
O/Na	10.8	$^{16}\text{O}(\text{p},\gamma)^{17}\text{F}$	1.16	$^{20}\text{Ne}(\text{p},\gamma)^{21}\text{Na}$	1.12
Na/Al	6.83	$^{23}\text{Na}(\text{p},\gamma)^{24}\text{Mg}$	1.19	$^{20}\text{Ne}(\text{p},\gamma)^{21}\text{Na}$	1.10
O/P	541	$^{30}\text{P}(\text{p},\gamma)^{31}\text{S}$	6.44	$^{16}\text{O}(\text{p},\gamma)^{17}\text{F}$	1.26
P/Al	216	$^{30}\text{P}(\text{p},\gamma)^{31}\text{S}$	6.53	$^{20}\text{Ne}(\text{p},\gamma)^{21}\text{Na}$	1.22

Note. — This table was originally published in [Downen *et al.* \(2013\)](#).

^aFactor variation of final elemental abundance ratio over range of nova models explored in present work, obtained from the solid black lines shown in Figure 3.6.

^bFactor uncertainty of final elemental abundance (mass fraction) ratio, caused by varying rate of individual reaction within its current uncertainty.

measurement of currently uncertain nuclear reactions, phosphorus would also need to be determined in observational spectra in order for the O/P and P/Al thermometer candidates to be applied. It was concluded that N/O, N/Al, O/S, and S/Al were viable nova thermometers in light of these considerations.

In order to guide efforts to further reduce the reaction rate uncertainty, the reactions acting as the primary and secondary sources of uncertainty for each nuclear thermometer were identified. This information is presented in Table 3.3. The first column lists the nuclear thermometer candidates where the first four entries only include elements that have been observed in the past, and the last four entries involve elements that have not been previously observed. The second column provides the range in value of each ratio over the entire peak temperature range as produced by the post-processing calculations. This value indicates the strength of a given ratio's

dependence on temperature and, therefore, its utility, irrespective of sensitivity to reaction rate uncertainty. The next two columns (columns 3 and 4) display the primary sources of uncertainty in the potential nova thermometers with the uncertain reaction to the left and its uncertainty at nova temperatures to the right. The final two columns (columns 5 and 6) provide the secondary sources of uncertainty in the same format.

A variety of information was extracted from Table 3.3. First, the secondary sources of uncertainty only result in abundance ratio variations of 30% or less, which has relatively little effect when the substantial uncertainties in the spectroscopically observed abundances are considered (see Table 1.2). Secondly, the ratios involving P and S—namely, O/S, S/Al, O/P, and P/Al—demonstrate the most potent dependence on temperature. The third and, perhaps, most significant conclusion is that one reaction, $^{30}\text{P}(p,\gamma)^{31}\text{S}$, bears nearly sole responsibility for the reaction rate uncertainty of the ratios including P and S. However, the importance of this rate to the production of sulfur and heavier elements is well-known (José *et al.*, 2001; Parikh *et al.*, 2011, among others). ^{30}P is a short-lived nuclide ($t_{1/2} = 2.498$ minutes, Basunia, 2010), meaning that direct studies of $^{30}\text{P}(p,\gamma)^{31}\text{S}$ can only be conducted at radioactive beam facilities. However, a sufficiently intense ^{30}P beam has not been produced to date, so only limited data from indirect studies (see Doherty *et al.*, 2012; Parikh *et al.*, 2011; Wrede *et al.*, 2009) is available. For a recent review on the status of this measurement, see Wrede (2014). As a result, the $^{30}\text{P}(p,\gamma)^{31}\text{S}$ rate included in the STARLIB library was adopted from the Hauser-Feshbach statistical model estimates of Rauscher and Thielemann (2000) with an assumed factor of 10 uncertainty in the classical nova temperature range. This rate is in agreement with the Parikh *et al.* (2011) rate, and its factor 20 uncertainty, determined using a Monte Carlo approach (Parikh *et al.*, 2008). In short, any improvement to the $^{30}\text{P}(p,\gamma)^{31}\text{S}$ rate uncertainty would significantly increase the viability of the P and S nuclear thermometers presented, and these results provide added motivation for the continuing efforts to experimentally measure this reaction.

3.3.2 Comparison to Spectroscopic Observations

Once the most viable nova thermometer candidates and their shortcomings were identified, comparisons between the simulated and observed thermometers could be made. A general impression of the two data sets was obtained using three-element plots of the simulated and observational elemental ratios and their uncertainties. Two examples of this type of plot are shown in Figure 3.7. The observed elemental ratios of various novae (calculated from Table 1.2) are given by the colored markers. The thick and thin black lines indicate the thermometer values and their uncertainties as determined by the post-processing reaction network calculations, respectively. It must be noted that because there is no explicit dependence on temperature in this figure, the direction of increasing temperature is indicated at the bottom lefthand corner of each panel and differs between the two panels.

The left panel of this figure involves N, O, and Al using the N/O and N/Al nuclear thermometers, and, as noted in Table 3.3, both of these thermometers are only mildly affected by reaction rate uncertainties. This can be seen by the relatively narrow region bounded by the thin black lines. In contrast, the uncertainties of the nova observations, with the exception of V382 Vel, eclipse the effects of reaction rate uncertainties. This comparison indicates the need for more precise measurements of N, O, and Al in ultraviolet, infrared, and optical nova spectra for this reason.

Similarly, the right panel of this figure includes O, Al, and S by incorporating the O/S and S/Al nuclear thermometers. These two thermometers, unlike N/O and N/Al displayed in the upper panel, are strongly affected by reaction rate uncertainties, particularly the uncertainty in the poorly-known $^{30}\text{P}(p,\gamma)^{31}\text{S}$ rate. This is clearly visible in the substantial area bounded by the thin black lines indicating the uncertainty of the post-processing abundance ratio. The width of this region is comparable to the error bars of the V838 Her observation, and this is the only observation in Table 1.2 where S, Al, and O measurements were available. To summarize, both the

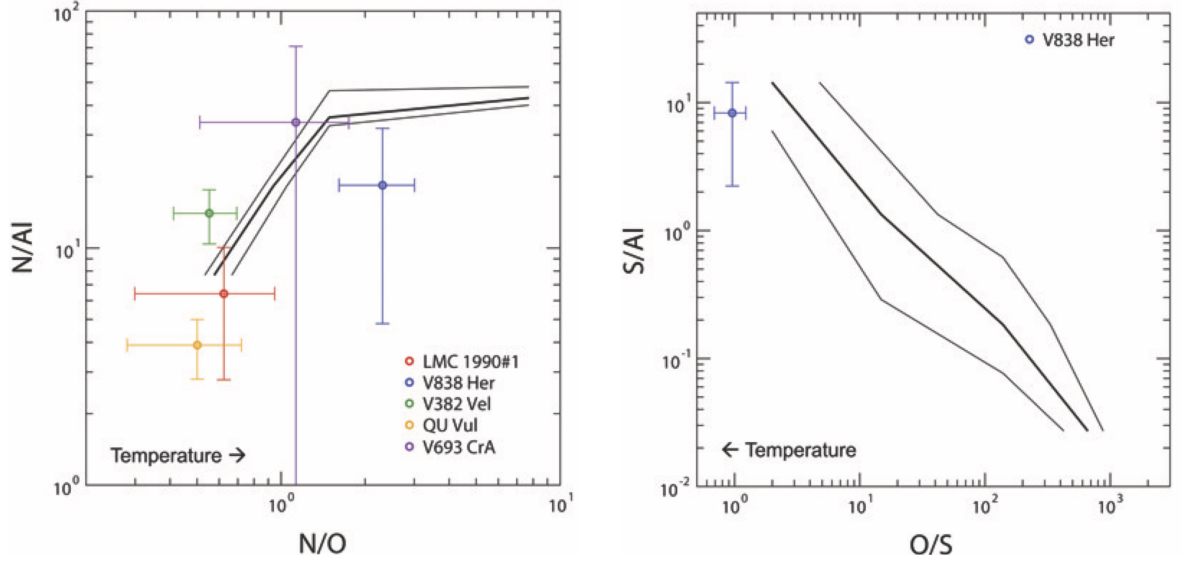


Figure 3.7: Three-element plots using nuclear thermometers to compare elemental ratios predicted by post-processing simulations to those observed in nova ejecta. **Left:** Three-element plot of N, O, and Al using the N/O and N/Al nuclear thermometers. **Right:** Three-element plot of O, Al, and S as given by the O/S and S/Al nuclear thermometers. In both plots, the solid black line indicates the elemental ratio values predicted by post-processing network simulations using recommended reaction rates while the thinner black lines represent the range in these values due to reaction rate uncertainty. The markers indicate the elemental ratio values calculated from observed nova spectra (see Table 1.2). Note that the direction of the peak temperature trend differs between the two panels and is indicated in the lower righthand corner of each panel. Figure from Downen *et al.* (2013).

substantial uncertainty in the $^{30}\text{P}(p,\gamma)^{31}\text{S}$ rate and the number of nova observations that simultaneously determine S, Al, and O need to be improved before the O/S and S/Al nova thermometers can be used to full effect.

The three-element plots presented in Figure 3.7 are effective for quantitative comparisons of simulated abundance and nova observation uncertainties, but they are less beneficial for illustrating the relationship between a given nuclear thermometer and the peak nova temperature. Hence, a different representation of this information was required. The simulated nuclear thermometers were plotted versus peak nova temperature (as seen in Figure 3.6), and the ratios calculated using the observations presented in Table 1.2 were juxtaposed with these trends for better comparison. For

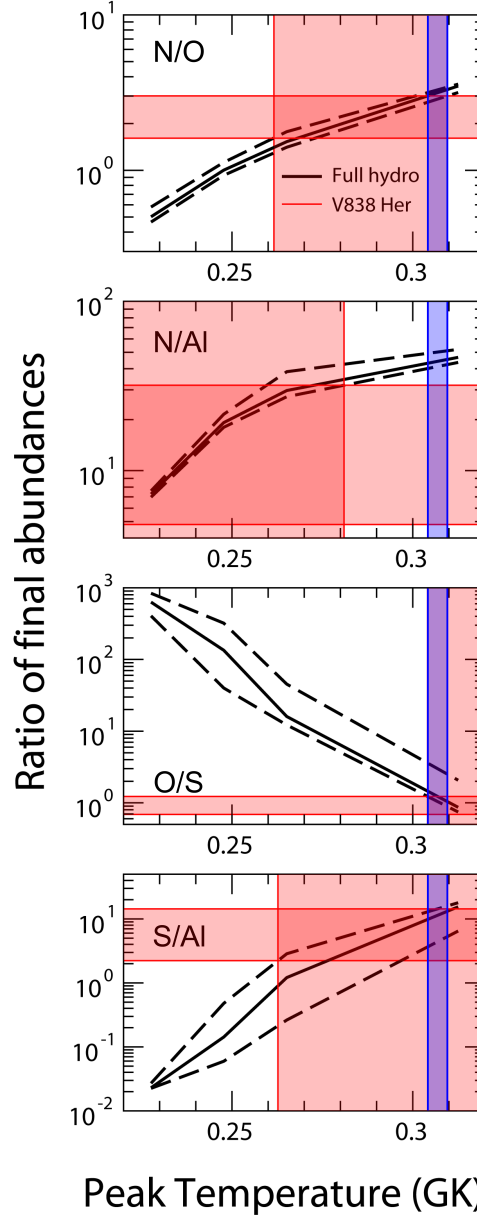


Figure 3.8: Comparison between predicted and observed values of all four nuclear thermometers in Nova V838 Her. Solid and dashed black lines indicate the median thermometer values and their uncertainties, respectively. Horizontal red bands denote the range of observed values of a nuclear thermometer for this nova. Each vertical red band indicates the estimated peak temperature range of Nova V838 Her for a particular nuclear thermometer. The vertical blue bands show the estimated peak temperature range of Nova V838 Her when all nuclear thermometers are considered. From [Downen *et al.* \(2013\)](#).

observed novae where multiple thermometers could be calculated, the intersection of the observational and simulated elemental ratios could be used to point to the peak

temperature range of the observed nova. Figure 3.8 displays the analysis of V838 Her as an example. Happily, the use of all four thermometers was possible for this nova. In each panel, a nuclear thermometer simulated using the full hydrodynamic models is shown as a thick black line, and the uncertainty in this ratio, determined using the post-processing network, is indicated by the dashed black lines. The horizontal red bar indicates the range of the observed ratio for this particular nova. Based on the intersection of the simulated nuclear thermometer ratio and the observed value for a given ratio, the possible peak temperature range of the nova can be estimated. The estimate resulting from each ratio is shown as a vertical red bar. Combining these restrictions for each ratio constrains the peak temperature range even further. Consequently, the vertical blue bar is the prediction for the peak temperature range of the observed nova based on the intersections of the simulated and observed ratios for all panels. Thus, the vertical bar is the same across every panel in Figure 3.8. Similar analyses were carried out for six novae—Novae V838 Her, V382 Vel, V693 CrA, LMC 1990#1, QU Vul, and V1065 Cen—and are discussed below. In the cases of V4160 Sgr and V1974 Cyg, N/O was the only available nova thermometer because of the limited number of elements presented in these observations, so peak temperature predictions for these novae were not addressed.

Nova V838 Her

As discussed above, Figure 3.8 displays the predicted and observed values for the nuclear thermometers used to study this nova. Four nuclear thermometers—N/O, N/Al, O/S, and S/Al—were available for this analysis, more than any other nova included in Table 1.2. Note that the uncertainties in the observed N/O and O/S values are significantly smaller than those of the other two thermometers, and as a result, N/O and O/S severely limit the estimated peak temperature range of this nova to $T_{peak} = 0.30\text{--}0.31$ GK, as shown by the narrow vertical blue bar that appears in all

four panels of the figure. Based on a linear interpretation of white dwarf mass as a function of peak temperature, this peak temperature range translates to a white dwarf mass range of $M_{WD} = 1.34\text{--}1.35 M_{\odot}$. It must be mentioned that the observed N/Al ratio is slightly lower than the values predicted by the hydrodynamic simulations for this temperature range. However, this ratio also includes too large an uncertainty to be fully trusted, so this inconsistency was ignored in favor of the agreement of the other three thermometer comparisons. The O/S and S/Al simulated abundances, as mentioned earlier, are impacted by the substantial uncertainty in the $^{30}\text{P}(p,\gamma)^{31}\text{S}$ rate, and that effect can clearly be seen here. Accordingly, the determination of white dwarf mass for this nova could be improved with a more precise N/Al observation and a reduction in the uncertainty of the $^{30}\text{P}(p,\gamma)^{31}\text{S}$ rate.

Previous literature reveals contradictory conclusions about the nature of this nova. Its prevailing features are the depletion of oxygen and enhancement of sulfur (versus solar values) observed in its ejecta. [Politano *et al.* \(1995\)](#) suggested that the white dwarf of this nova was “very massive” ($\sim 1.35 M_{\odot}$) based on these values, but [Wanajo *et al.* \(1999\)](#) proposed a more modest white dwarf mass of $1.05 M_{\odot}$ after reproducing these features with their low ($Z \simeq 0.01$) metallicity model. To complicate matters further, [Schwarz *et al.* \(2007\)](#) argued that these anomalies were actually the result of breakout of matter from the CNO cycle via α -capture. On the whole, the results presented in Figure 3.8 were found to be in agreement with [Politano *et al.* \(1995\)](#) since multiple metallicity models were not explored and no evidence of breakout was seen in any of the models studied here.

Nova V382 Vel For this nova, sulfur was not observed, so only N/O and N/Al were used to estimate the nova’s peak temperature range. Both of the simulated and observed values of these ratios are fairly precise, as shown in Table 3.3 and Figure 3.7, respectively. These thermometers indicate a narrow, relatively low peak temperature

range, $T_{peak} = 0.23\text{--}0.24$ GK ($M_{WD} = 1.18\text{--}1.21 M_{\odot}$) as a result. As seen in Figure 3.5, the production of sulfur increases dramatically with temperature, so the absence of sulfur in this low peak temperature range is consistent with expectations of this nova.

Nova V693 CrA Like Nova V382 Vel, sulfur was not observed in Nova V693 CrA. The observed values of the N/O and N/Al thermometers, however, include substantial uncertainties, complicating the determination of peak temperature range. Only an upper limit value of $T_{peak} \leq 0.28$ GK, or $M_{WD} \leq 1.3 M_{\odot}$, was determined in this case. More precise observations of N, O, and Al would greatly improve the predictive value of the N/O and N/Al thermometers for this nova. If the mass of this nova's white dwarf is near the $1.3 M_{\odot}$ upper limit, sulfur should be readily visible, and observation of this element would allow additional thermometers to be employed as well.

Nova LMC 1990#1 Similar to Nova V693 CrA, the estimation of this nova's peak temperature suffers from imprecise observed N/O and N/Al values. The centroid value of the observation shown in Figure 3.7 could indicate that the peak temperature achieved by this nova is below the coldest peak temperature explored in this work. However, the large uncertainty in the observed abundances makes this determination impossible. Therefore, it was concluded that the peak temperature of this nova had an upper limit of $T_{peak} \leq 0.24$ GK, corresponding to white dwarf mass of $M_{WD} \leq 1.2 M_{\odot}$. Clearly, the study of this nova would also benefit from the availability of subsequent observations with additional elemental abundances and higher precision.

Nova QU Vul The observed values of N/O and N/Al appear to place the peak temperature of this nova well below the $T_{peak} = 0.228\text{--}0.313$ GK range explored in this

work. The observed value of N/O does overlap with the simulated values of this ratio, but this is not the case for the N/Al nuclear thermometer. As such, only an upper limit of peak temperature, $T_{peak} \leq 0.22$ GK, can be determined. This temperature translates to a white dwarf mass upper limit of $M_{WD} \leq 1.20 M_{\odot}$. This upper limit is in agreement with the $M_{WD} = 1.05\text{--}1.1 M_{\odot}$ range given by [Wanajo *et al.* \(1999\)](#) and approaches the lower limit on ONe white dwarf mass reported by [Doherty *et al.* \(2010\)](#).

Nova V1065 Cen For this nova, no aluminum observation was available, so only the N/O and O/S thermometers were used to estimate the peak temperature. However, these two thermometers do not indicate a consistent mass range. The observation of this nova exhibits the highest abundance of oxygen and sulfur of the novae presented in Table 1.2. Nova V838 Her has a similarly high observed sulfur abundance, leading to a white dwarf mass prediction extending to $1.35 M_{\odot}$, the highest white dwarf mass included in this work. Because the production of sulfur is thought to be largely driven by high temperatures, it is possible that the mass of the white dwarf in V1065 Cen is greater than $1.35 M_{\odot}$, but this mass is strictly limited to a maximum of $\simeq 1.37 M_{\odot}$. At this mass, the occurrence of electron capture inevitably leads to core collapse ([Nomoto, 1984](#)). Clearly, additional observations of this nova would greatly clarify the situation.

The peak temperature and white dwarf mass estimates for the V838 Her, V382 Vel, V693 CrA, LMC 1990#1, and QU Vul novae are shown in Figure 3.9. Bars terminating with straight lines define the peak temperature and white dwarf mass range for a given observed nova. Bars terminating in an arrow indicate that only an upper limit could be estimated. The successful application of the nuclear thermometers was promising, but it must be kept in mind that the classical nova models studied in this

work occupied a very narrow parameter space. The accretion rate, white dwarf luminosity and metallicity, mixing fraction between accreted (solar) matter and white dwarf matter, and other properties were not varied in the presented analysis. The subsequent and enlightening study by [Kelly *et al.* \(2013\)](#) challenged the veracity of the 50% mixing fraction assumption, and the exploration of other parameter spaces would certainly complement the work presented here as well.

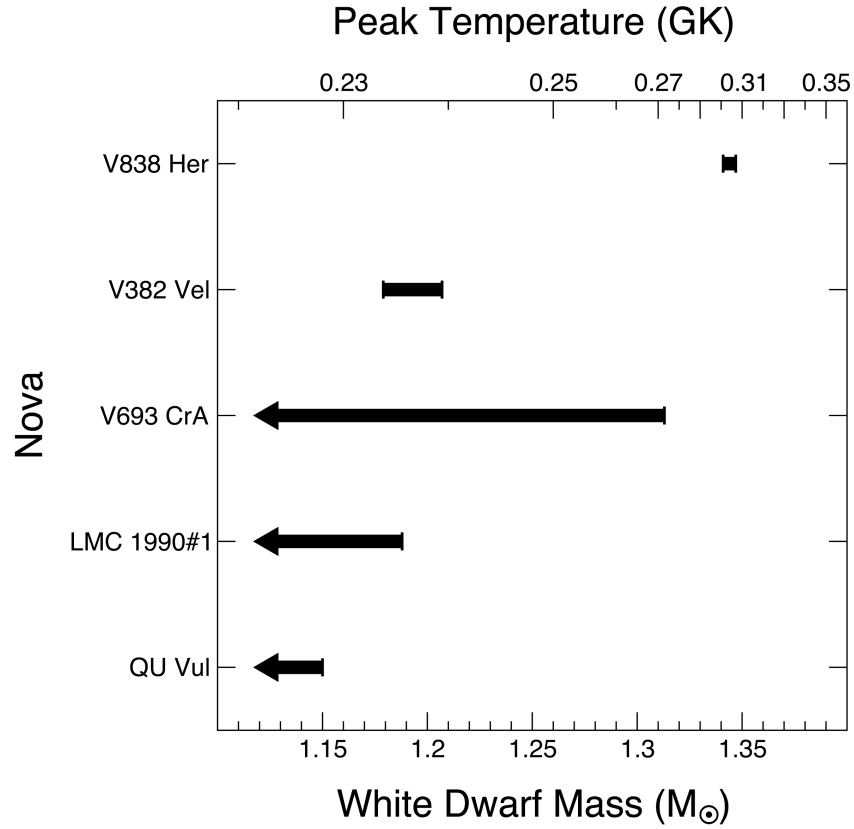


Figure 3.9: Peak temperature and white dwarf mass range estimates for select nova observations. These estimates were determined by the intersection of observed and simulated values for nuclear thermometers (see Figure 3.8 for a detailed look at this analysis method). Bars terminating with straight lines indicate a definite range resulting from this analysis. Bars terminating in an arrow denote where only upper limits could be determined. This figure was originally published in [Downen *et al.* \(2013\)](#).

3.3.3 Conclusions

On the whole, there were two intertwined goals for this work. First, a metric to relate neon nova abundances extracted from spectroscopic observations to those of post-processing network simulations was sought, and then the stability of this metric under the effects of reaction rate uncertainty was quantified. Thus, the concept of a nuclear thermometer, a ratio of elemental abundances with strong peak-temperature dependence, was devised, and a number of potential thermometers were considered. Of these, N/O, N/Al, O/S, and S/Al were chosen because they included only elements that have been observed spectroscopically at present. While N/O and N/Al values did not deviate much under the influence of reaction rate uncertainties, the O/S and S/Al thermometers were found to be quite sensitive to the substantial uncertainty of the $^{30}\text{P}(p,\gamma)^{31}\text{S}$ rate at nova temperatures. The latter two thermometers proved useful nonetheless because they demonstrated the most dramatic temperature dependence of those investigated. The second goal was to use the developed metric to extract key information about the nature of classical novae from spectroscopically observed abundances. To that end, the nuclear thermometers' marked dependence on peak temperature was exploited in order to estimate peak temperature ranges (and the correlated white dwarf mass ranges) for five of the eight observed novae presented in Section 1.2.1. This analysis provided motivation for a variety of research including the determination of high precision elemental abundances from spectroscopically observed novae and the continued efforts to directly measure the $^{30}\text{P}(p,\gamma)^{31}\text{S}$ reaction.

3.4 The Isotopic Ratio Study

Though the nucleosynthesis study presented in Section 3.3 motivates the study of the $^{30}\text{P}(p,\gamma)^{31}\text{S}$ reaction, this experiment is unfortunately beyond the capabilities

of the LENA facility (Chapter 4). However, presolar stardust grains offer another source of neon nova nucleosynthetic signatures, and, as will be discussed, provide the experimental motivation for this dissertation.

To begin, it should be noted that many of the putative nova presolar grain measurements (Table 1.3) were not available until very recently. When the current work was initiated, the collection of putative nova presolar grains only numbered about two dozen measured for a limited variety of isotopic ratios. Within this limitation, it followed that reactions affecting $Z \geq 10$ isotopic ratios are of interest given that only neon novae, not CO novae, synthesize nuclear species in this mass range. Silicon isotopic ratio measurements, in addition to meeting the aforementioned criterion, have frequently been used to identify grains of suspected nova origin and are available for the majority of these grains. Reactions affecting silicon abundances in nova nucleosynthesis, such as the $^{29}\text{Si}(p,\gamma)^{30}\text{P}$ reaction, are prime candidates for study as a result. Furthermore, $^{29}\text{Si}(p,\gamma)^{30}\text{P}$ is the main reaction responsible for producing ^{30}P in nova nucleosynthesis, so it serves as a precursor to the crucial $^{30}\text{P}(p,\gamma)^{31}\text{S}$ reaction identified in the previous section. Lastly, $^{29}\text{Si}(p,\gamma)^{30}\text{P}$ is particularly well suited for study because of experimental factors which will be addressed in Chapter 7.

Figure 3.10 provides a comparison of the silicon isotopic ratios determined from nova nucleosynthesis models and measurements of putative nova presolar grains, highlighting the importance of the $^{29}\text{Si}(p,\gamma)^{30}\text{P}$ reaction to neon nova nucleosynthesis. To determine the expected silicon abundances in the nova ejecta, the SHIVA hydrodynamic code (José and Hernanz, 1998) was employed with recommended reaction rates adopted from STARLIB (Sallaska *et al.*, 2013) and the model parameters given in Table 3.1. The resulting silicon ratios are indicated by the solid black line in the figure. To estimate the effect of reaction rate uncertainty on the silicon isotopic ratios, a factor of 5 uncertainty was adopted for the $^{29}\text{Si}(p,\gamma)^{30}\text{P}$ reaction in the post-processing reaction network, and the resulting uncertainty band is communicated by the grey

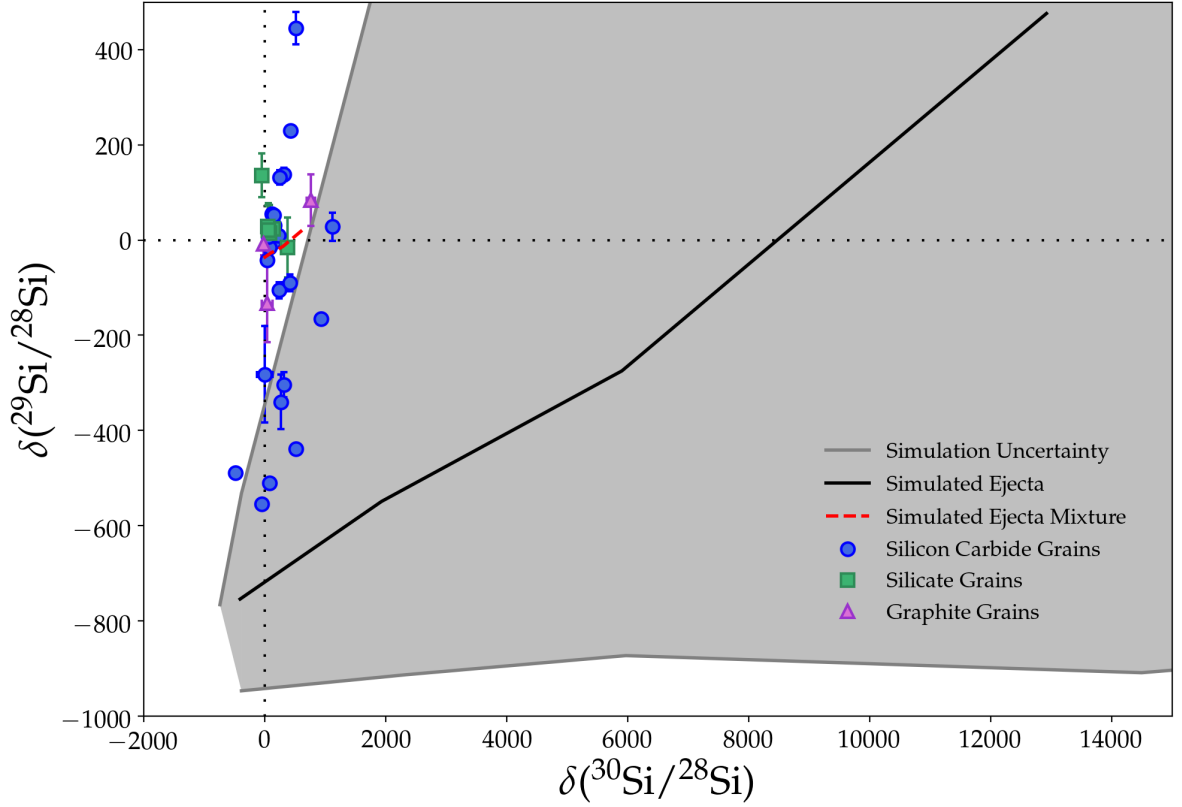


Figure 3.10: Comparison of silicon isotopic ratios from nucleosynthesis simulations and presolar grain measurements. Isotopic ratios are given as deviations from solar system values in permil where $\delta(^i\text{Si}/^{28}\text{Si}) \equiv [(^i\text{Si}/^{28}\text{Si}) \div (^i\text{Si}/^{28}\text{Si})_{\odot} - 1] \times 1000$ (Amari *et al.*, 2001). Ratios given by SHIVA hydrodynamic simulations are shown as a black solid line. Uncertainty in the simulated ratios, produced by adopting a factor 5 uncertainty in the $^{29}\text{Si}(p,\gamma)^{30}\text{P}$ rate, is indicated by the grey shaded region. Measurements of putative nova grains from Table 1.3 are classified by grain composition and shown as data markers. Simulated ejecta material mixed with a large amount of solar-like material is indicated by a red dashed line. The solar values of the silicon isotopic ratios are indicated by black dotted lines.

shaded region. The isotopic ratios of putative nova presolar grain measurements, presented by Table 1.3 and classified by grain composition, are indicated by the data markers in the figure. The solar value of each silicon isotopic ratio is indicated by a black dotted line.

As mentioned in Section 1.2.2, the isotopic ratios predicted by nova nucleosynthesis models are far more anomalous than those measured in putative nova presolar

grains, and this discrepancy is clearly visible in Figure 3.10. An unknown mixing mechanism between a large fraction ($\sim 95\%$) of solar-like material and a smaller proportion ($\sim 5\%$) of nova ejecta matter has been proposed to defend this divergence (Amari *et al.*, 2001). The effect of this proposed mixing is shown by the red dashed line in the figure.

While this simulated ejecta mixture does overlap with the highest density region of presolar grain measurements, many grain measurements fall far from this line. In fact, a fair number of isotopic grain measurements instead fall within the grey shaded region indicating the uncertainty in the simulated composition of the pure, unmixed ejecta material arising solely from the $^{29}\text{Si}(p,\gamma)^{30}\text{P}$ reaction rate uncertainty. Clearly, the large effect that $^{29}\text{Si}(p,\gamma)^{30}\text{P}$ uncertainties have on the silicon isotopic ratios proves that this reaction warrants further study and motivates the $^{29}\text{Si}(p,\gamma)^{30}\text{P}$ study undertaken in the current work. Furthermore, this impact also indicates that the assumption of mixing between ejecta and solar-like materials before grain condensation is perhaps premature without a thorough exploration of the effect of reaction rate uncertainty.

CHAPTER 4: EXPERIMENTAL SETUP

In order to carry out nuclear resonance measurements to a high accuracy and precision, an advanced laboratory is required. Particularly, accelerators capable of generating high fluence, well-defined particle beams and a detection system that produces a highly resolved spectrum of the resonance's γ -ray cascade are of utmost importance. The Laboratory for Experimental Nuclear Astrophysics (LENA) was founded specifically for this purpose and is uniquely suited to facilitate these experiments. Figure 4.1 provides a top-down schematic of this facility. LENA is a subfacility of the larger, collaborative Triangle Universities Nuclear Laboratory (TUNL) in Durham, North Carolina. While the other two TUNL subfacilities, the 10 MV FN tandem Van de Graaff accelerator and the High Intensity Gamma-Ray Source (HI γ S), are used for a variety of experiments, LENA is a nuclear astrophysics laboratory used exclusively for the measurement of nuclear cross sections critical to astrophysical nucleosynthesis.

Naturally, a high degree of specialization is required for this work. First, nucleosynthesis in most astrophysical phenomena occurs at significantly lower energies than most accelerator facilities can replicate. Furthermore, these low energies typically result in a reduced transmission probability (and a correspondingly low cross section strength) because of the Coulomb barrier, but this effect can be mitigated by an intense ion beam. Thus, a low-energy, high-fluence ion accelerator is needed. Accordingly, LENA has two such ion accelerators: the LENA I, a 1-MV JN Van de Graaff accelerator (Section 4.1.1), and LENA II, the 240-kV Electron Cyclotron Resonance accelerator (Section 4.1.2).

Of course, the aforementioned efforts would be fruitless without precise charge

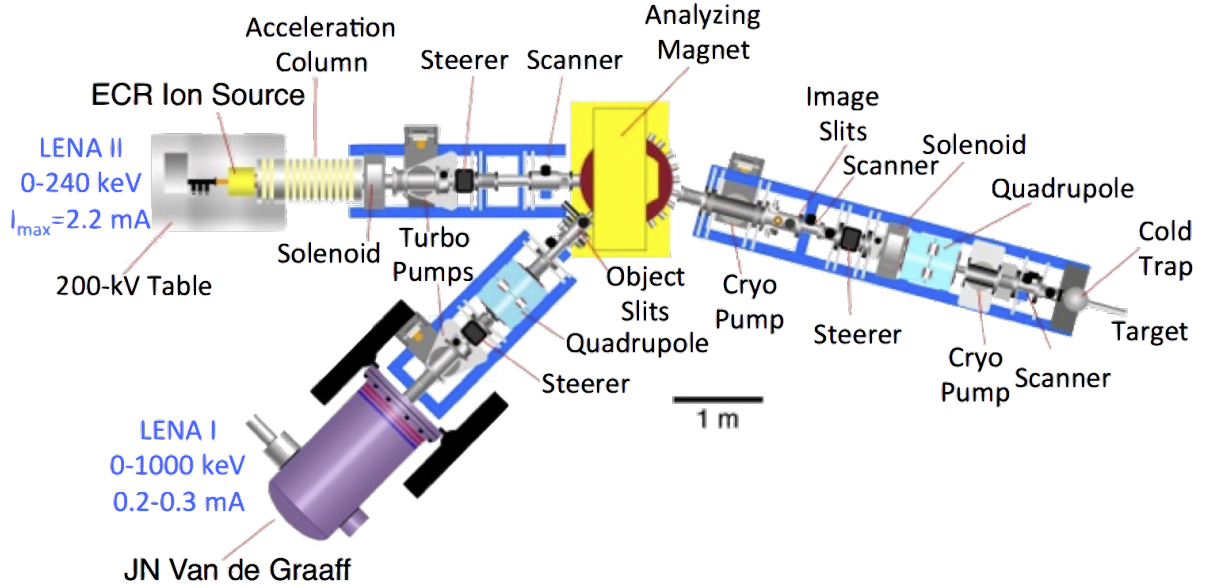


Figure 4.1: An overhead schematic of the LENA facility. The facility houses two particle accelerators, the 1-MV JN Van de Graaff accelerator (LENA I) and the 240-kV ECR accelerator (LENA II), as well as an analyzing magnet, beamline and beam-shaping systems, and a shared target station. Figure courtesy of A. E. Champagne.

collection, target cooling, efficient spectroscopy, and the like. Consequently, the features of the target station (Section 4.2) and the LENA $\gamma\gamma$ -coincidence detection system (Section 4.3) will be detailed. The former is responsible for all aspects of the experiment concerning the target and keeping it in prime condition. The latter utilizes a variety of detectors to strike the optimum balance between energy resolution, efficiency, and the exclusion of environmental radiation to facilitate the study of four $^{29}\text{Si}(p,\gamma)^{30}\text{P}$ resonances (Chapter 7).

4.1 Accelerators

4.1.1 LENA I: The 1-MV JN Van de Graaff Accelerator

The sole accelerator of the LENA facility for years, the LENA I accelerator is a heavily modified 1-MV JN Van de Graaff accelerator manufactured by the High Voltage Engineering Corporation (HVEC). This ion source is composed of a high-voltage

terminal, radio-frequency (RF) ion source, and acceleration column contained in a high pressure tank with an electrically-isolating atmosphere of sulfur hexafluoride (25%) and nitrogen-carbon-dioxide (75%) (see Figure 4.2 for illustration). It is primarily used to produce low-intensity proton beams of up to 150 μA ranging in energy from 150 keV to 1000 keV as a complement to the low-energy, high-fluence capabilities of the LENA II accelerator (Section 4.1.2). Figure 4.3 shows a typical hydrogen plasma generated by this ion source. It was used to monitor target degradation (Section 5.2) as well as study the $E_r^{lab} = 314$ keV, 324 keV, and 417 keV resonances in $^{29}\text{Si}(p,\gamma)^{30}\text{P}$ (Chapter 7).

In recent years, the LENA I has undergone extensive maintenance including two acceleration column replacements, multiple charging belt replacements, and several realignments. Modifications and improvements have been made to the terminal power supply and the terminal potential stability (TPS) system also. The accelerator has been successfully used to produce stable α -particle beams (Downen *et al.*, 2015; Hunt *et al.*, 2019). However, most of these improvements were made following the experiments detailed in this work. Thus, the system used here more closely resembles that detailed in Cesaratto *et al.* (2010) and, more recently, Kelly (2016). The LENA I accelerator was very recently decommissioned, and efforts to install a newer accelerator with improved capabilities are currently underway.

4.1.2 LENA II: The 240 kV Electron Cyclotron Resonance Accelerator

Whereas the LENA I accelerator is capable of producing relatively high-energy, low-intensity proton beams, the LENA II accelerator is limited to producing protons in a narrower range of energies, but its proton current intensity dwarfs that of the LENA I and many other proton accelerators. The LENA II is an electron cyclotron resonance (ECR) accelerator similar to the system described in Wills *et al.* (1998). The ion source exploits the electron cyclotron resonance phenomenon to produce a dense

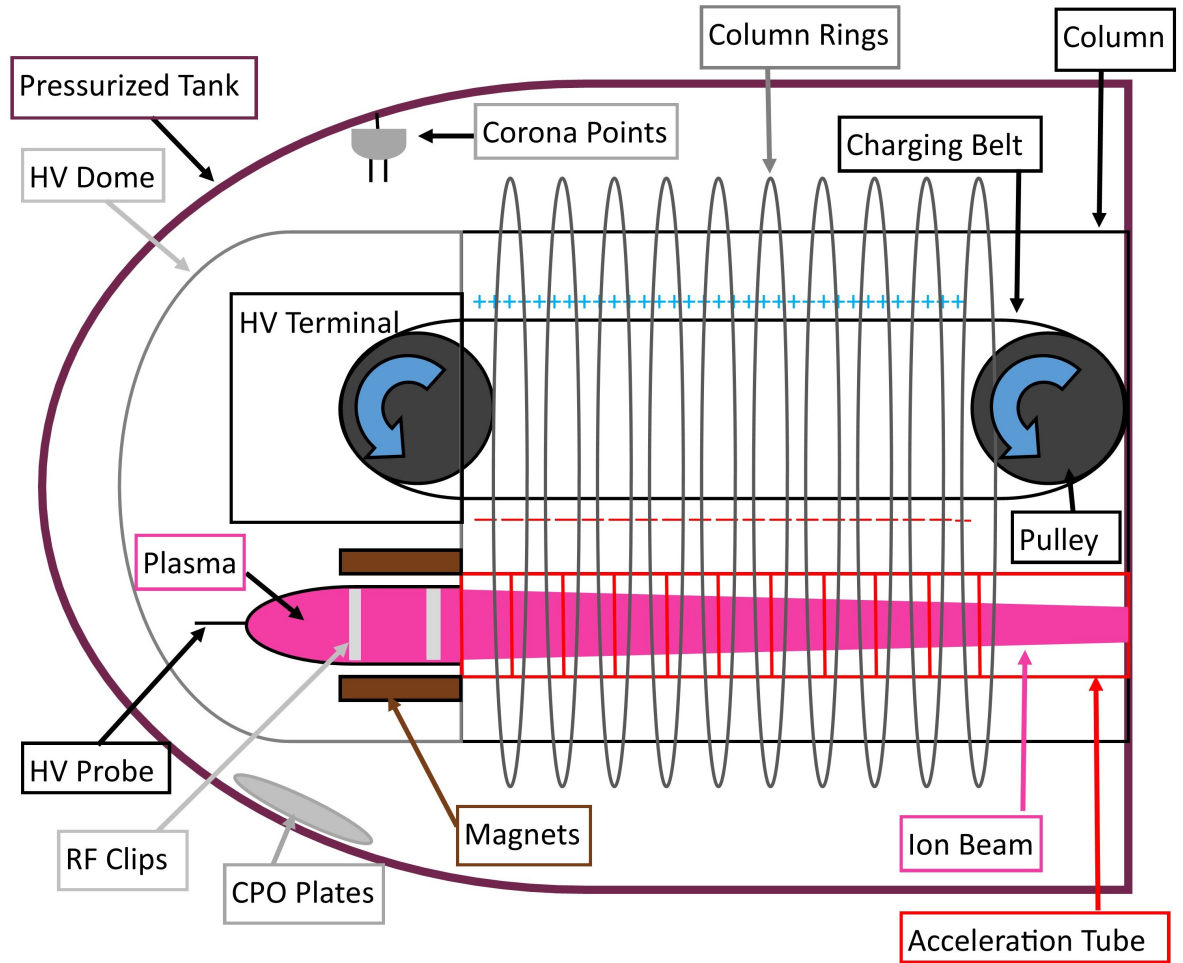


Figure 4.2: A diagram of the LENA I ion source. A high voltage power supply applies charge to an electrically isolated metal screen in contact with the surface of the charging belt. The charging belt receives the positive charge and transports it to the terminal end of the system via a pulley system. A second metal screen picks up the charge and transfers it to the terminal end of the plasma bottle (shown in Figure 4.3). From here, the gas (hydrogen or helium) is ionized, extracted, and accelerated. For more information regarding similar charging systems and their operation, see [West-erfeldt \(2005\)](#). Diagram courtesy of A. L. Cooper.

proton plasma through the use of microwave radiation and a solenoidal magnetic field. The ion source, acceleration column, and source electronics are mounted on a high voltage table that is electrically isolated by air during operation. The combined voltage applied to the table and the plasma chamber determines the energy of the produced proton beam.

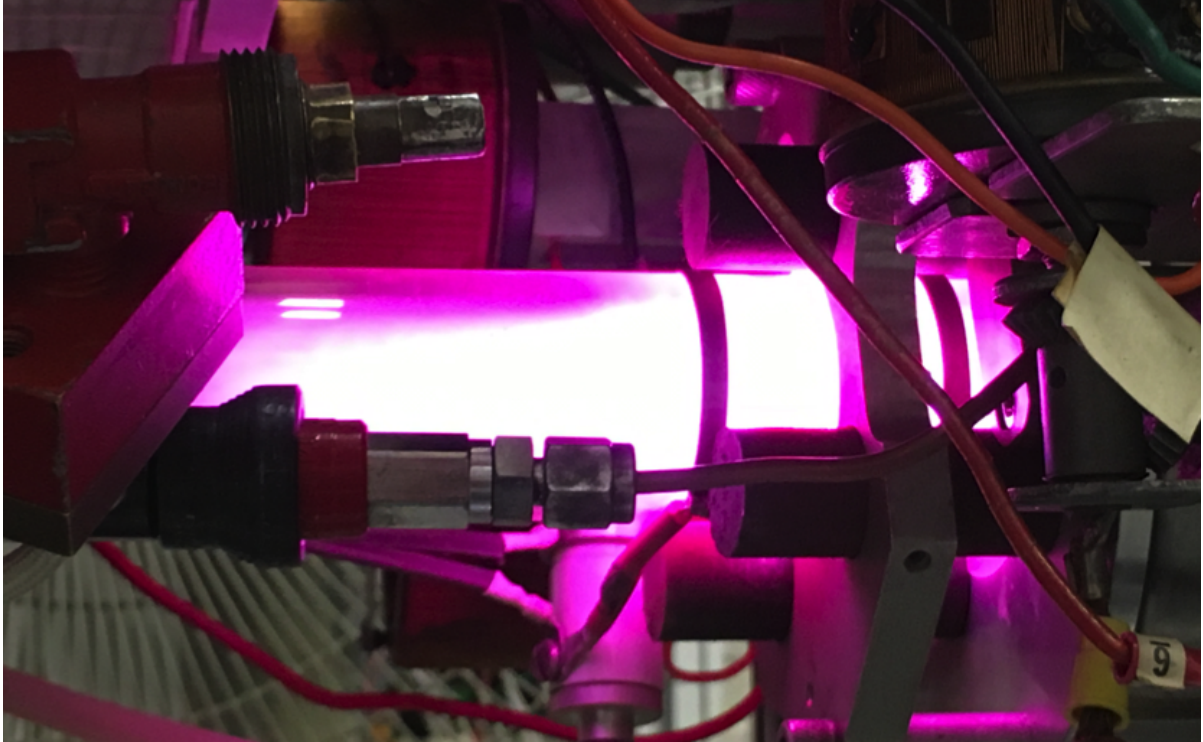


Figure 4.3: LENA I plasma bottle with hydrogen plasma, ready to be extracted and accelerated. Note the clear, fuchsia color. The color, intensity, and clarity of the plasma often provided useful diagnostic information for the operation and optimization of the source. For example, the plasma would appear milky and dull in color if the hydrogen gas became contaminated with air.

While the basic operation of this system is well documented in [Cesaratto *et al.* \(2010\)](#), the acceleration column detailed in this publication underwent extensive damage over the course of recent experiments. In essence, a small amount of neutral hydrogen would escape the plasma chamber during operation of the system (and the subsequent ionization of the gas), and a low-conductance path in the pumping system forced this gas to flow along the acceleration column. Once beam was extracted and transmitted to the acceleration column, protons would strike the neutral atoms, producing electrons that were then accelerated back toward the ion source. High levels of bremsstrahlung radiation were then produced by collisions of these electrons with the interior of the acceleration column.

After several experiments, this issue resulted in extensive damage that eventually

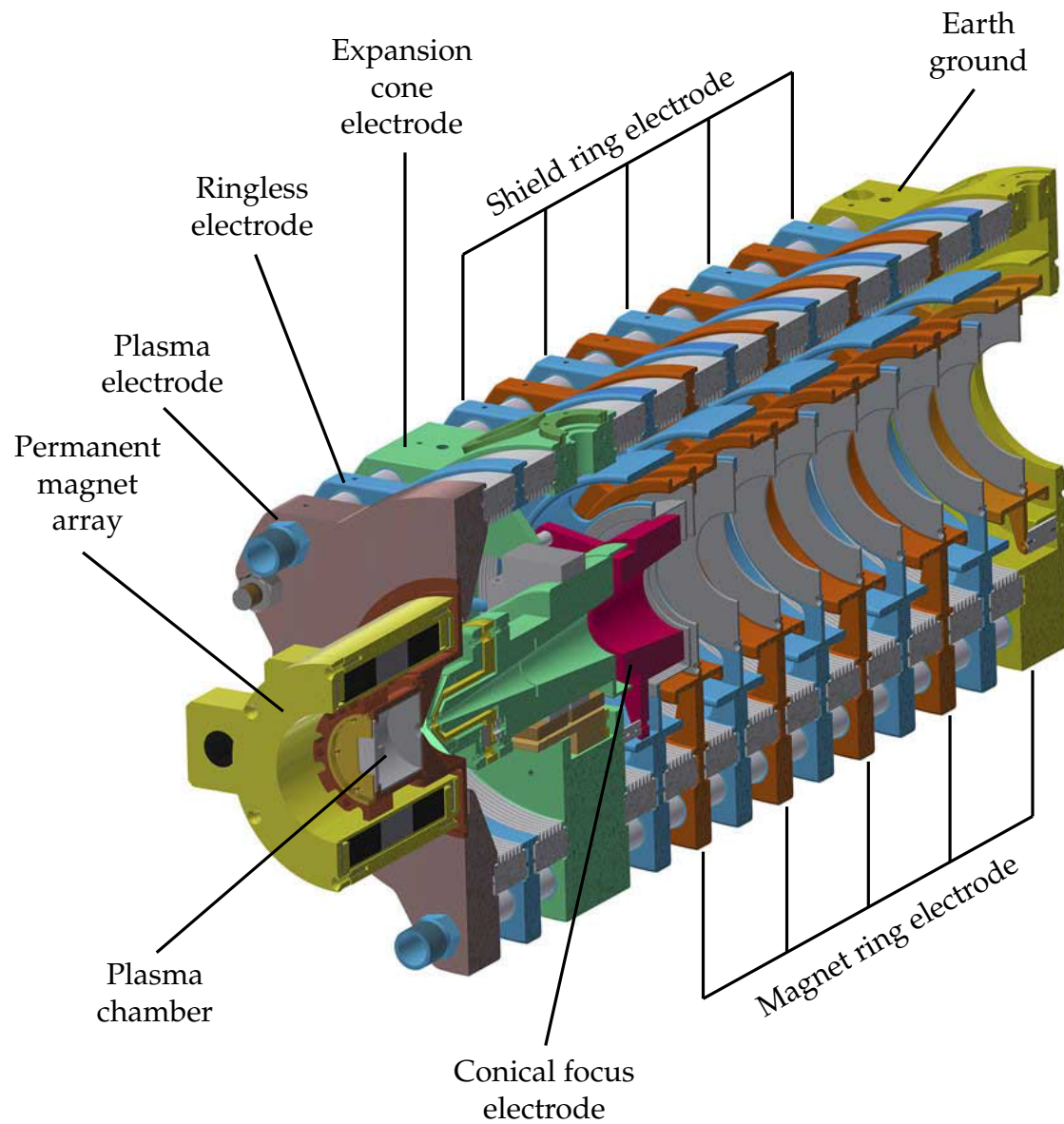


Figure 4.4: A cutaway diagram of the LENA II ion source and acceleration column from [Cooper *et al.* \(2018\)](#).

altered the electrical properties of the acceleration column, caused numerous vacuum leaks, and reduced the voltage gradient (and beam energy) the accelerator was capable of safely sustaining. Consequently, considerable steps were taken to address issues with the previous design as well as build upon the accelerator's initial capabilities.

Inspired by innovations put into practice on the Neutron Therapeutics' Hyperion

accelerator (Ryding *et al.*, 2012), the fruitful efforts of Cooper *et al.* (2018) greatly improved the performance and utility of the LENA II on three major fronts: electrostatic stability, beam optics and transmission, and reduction of beam-induced bremsstrahlung radiation.

To improve electrostatic stability, new acceleration column configurations were extensively simulated in order to determine an ideal design for the experiments performed at LENA. This significantly improved beam transport over the previous acceleration column, which was purchased from HVEC and modified to suit experimental needs. Furthermore, the new column employed water cooling to mitigate the heating effects that hastened the vacuum failure of the previous acceleration column, and the electrical resistance of the cooling water provided the tunable resistance down the length of the column.

To extract and transmit higher proton currents, a new microwave system was installed on the LENA II source. Optics and transmission were also improved by incorporating axial adjustment into the extraction electrode assembly to control the divergence of the proton beam better during transit through the acceleration column.

In order to reduce beam-induced bremsstrahlung radiation, an open electrode geometry was included in the new acceleration column design to better allow the evacuation of residual gases from the region, reducing the production of electrons from proton-hydrogen collisions. In addition, permanent magnets were arranged along the acceleration column to produce a transverse magnetic field, suppressing secondary electrons from generating appreciable bremsstrahlung radiation. Figure 4.4 shows features of the new LENA II design. For further detail and discussion on this accelerator redesign, refer to Cooper *et al.* (2018).

The improvements described here facilitated the first direct study of the $^{29}\text{Si}(p,\gamma)^{30}\text{P}$ $E_r^{lab} = 221$ keV resonance detailed later in this dissertation (Section 7.4).

Beam Pulsing

The intense proton current described above is incredibly useful for sensitive measurements, but it can also cause the rapid degradation of targets. Thankfully, nuclear targets can sustain high, instantaneous beam current if the beam is pulsed, and the new LENA II microwave system has the necessary capabilities to produce pulsed proton beam. Effectively, the microwave system was powered on and off at the desired interval, extinguishing and striking a proton plasma with a given frequency and duty cycle. Advantageously, this method of pulsing requires no adjustment of the high voltage during operation, but it required some adjustments to the microwave tuning used for normal DC operation. As will be discussed later, no target degradation was observed during the course of the experiments described in this dissertation. It seems likely that beam pulsing is at least partially responsible for this success when a comparison is made to the target degradation experienced during previous experiments (see, for example, [Buckner *et al.*, 2015](#)).

It should also be mentioned the data acquisition system has also been modified to allow gating on the “on-pulse” periods, excluding the data collected with no beam incident on the nuclear target from the resulting spectra. Because environmental background dominates the radiation landscape when no beam is present, this technique can be very useful where this type of radiation is responsible for obscuring the signal of interest ([Cooper *et al.*, 2018](#)). However, it will be discussed later that beam-induced contaminant reactions are the most significant contributors to the $E_r^{lab} = 221$ keV resonance spectra, and as a result, no gating on the pulsed signal was employed for this work.

4.2 Target Station

The proton beam ends its journey at the target station. Figure 4.5 shows a simplified, not-to-scale diagram of this region.

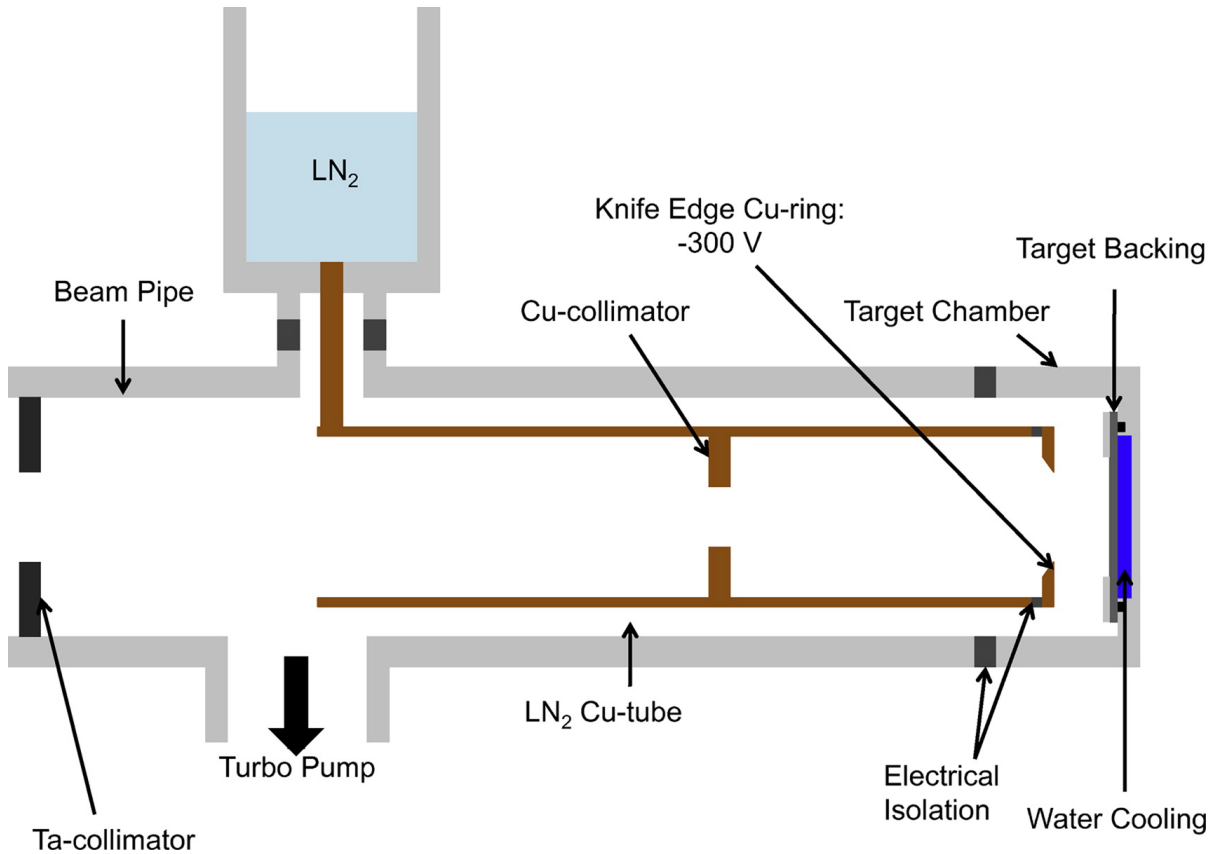


Figure 4.5: Diagram of LENA target station from [Cesaratto *et al.* \(2010\)](#). This diagram shows all of the major components of the target station. The target station is held at a high vacuum ($\sim 10^{-7}$ Torr) via a turbomolecular pump, and carbon in the target station is kept to a minimum using a LN₂-cooled copper tube. Tantalum and copper collimators shape and limit the beam cross section to the implanted area of the target. The knife-edge copper ring, in close proximity to the target, is biased to -300 V, thereby suppressing secondary electrons and facilitating accurate charge integration. Heating effects from the incident particle fluence are mitigated by water cooling the back face of the target.

The proton beam enters the target station through a wide tantalum collimator before going into a copper shroud, which is held at liquid nitrogen temperature by a vertical, insulated liquid nitrogen reservoir. The target station is held at a high vacuum

($\sim 10^{-7}$ Torr) by a turbomolecular pump, and any remaining contaminants condense on the copper shroud, preventing them from propagating through the station and contaminating the target surface.

A copper collimator inside the copper shroud allows for beam current readings to be taken before the beam is incident on the target. This current reading, in conjunction with the current reading taken at the target chamber, is a crucial parameter to aid in optimizing beam transportation to target. Generally, current is minimized on the copper collimator and maximized on target.

After passing through the copper collimator, the beam travels through the remaining length of the copper shroud before exiting through an electrically isolated, knife edge copper ring in close proximity to the target chamber. This ring is held at a -300 V potential which produces an electric field capable of suppressing secondary electrons produced at the target surface. Secondary electrons are a significant source of uncertainty in the target charge collection, and this setup helps reduce this uncertainty to $\sim 3\%$ (Buckner, 2014). At the end of the target station lies the target chamber. It consists of a machined plate on which the target is mounted and then kept in place with a compression ring. This chamber also acts as a Faraday cup, allowing for the incident proton current and accumulated charge to be measured to a high precision. A posterior water well on the chamber is connected to a chilled water system to directly cool the back of the target. This system is generally sufficient to cool targets and prevent target degradation under LENA I proton current but must be used in conjunction with beam pulsing (Section 4.1.2) under the mA-level proton currents of LENA II operation.

4.3 Detection System

All $^{29}\text{Si}(p,\gamma)^{30}\text{P}$ resonance measurements and associated work were conducted using the LENA $\gamma\gamma$ -coincidence detection system. This key apparatus features a 16-segment, thallium-activated sodium iodide (NaI(Tl)) detector annulus and a central, coaxial high-purity germanium (HPGe) detector. The NaI(Tl) annulus and HPGe detector are contained in an aluminum frame which also supports 10 mm-thick lead shielding and five plastic scintillating panels. This detection system is well studied (Longland *et al.*, 2006; Carson *et al.*, 2010; Howard *et al.*, 2013), leading to a precise set of dimensions (Table 4.1) and a GEANT4 (Allison *et al.*, 2016) model of the system. Figure 4.6 shows a DAWN rendering (Kawaguti and Tanaka, 1997) of the GEANT4-simulated $\gamma\gamma$ -coincidence detector with the scintillator panels and aluminum frame removed for visibility.

The variety of detectors in this unique configuration grants remarkable advantages in detecting and isolating γ -rays of interest. Foremost, nesting the HPGe detector inside a NaI(Tl) annulus allows for selection of γ -rays coincident in both systems, effectively isolating γ -ray cascades of reactions of interest from environmental background and beam-induced contaminant γ -rays (Section 4.3.4). Additionally, the five plastic scintillating panels acting in anticoincidence reduce background from cosmic-ray induced muons (Section 4.3.3). The HPGe is located at 0° relative to the incident proton beam and as close to the nuclear target as the target chamber geometry allows in order to compensate for the relatively low efficiency of the germanium detector. The overall arrangement results in a detection sensitivity in a sea-level laboratory that is competitive with that of underground facilities.

Table 4.1. Specifications of the LENA Detection System

Detector	Component	Dimension (mm)
HPGe	End cap outer diameter	107.95 ± 0.02
	Distance end cap-crystal	6.2 ± 0.5
	Crystal length	91.6 ± 1.0
	Crystal diameter	89.0 ± 0.5
	Bulletizing radius	7.1 ± 0.5
	Central hole diameter	8.5 ± 1.0
	Central hole length	79.1^{\dagger}
	Central hole bottom radius	4.7^{\dagger}
	Vertical crystal displacement	-1.5 ± 0.5
	Contact pin diameter	6.9 ± 0.5
	Contact layer thickness	1.5^{\ddagger}
NaI(Tl): Segment	End cap outer diameter	116.92 ± 0.02
	Crystal diameter	115.53 ± 0.02
	Crystal length	177.0 ± 0.1
NaI(Tl): Annulus	Inner radius	118.0 ± 0.5
	Outer radius	357.0 ± 0.5
	Crystal length	330.0 ± 0.5
	Segment spanning angle	43.0 ± 0.5

Note. — These dimensions were used to build and simulate the LENA detection system in GEANT4. All dimensions from [Carson *et al.* \(2010\)](#) or [Howard *et al.* \(2013\)](#) unless otherwise indicated.

[†]Measurements from original manufacturer’s specifications. No tolerances were provided.

[‡]Measurements and simulations recently performed by David Little.

4.3.1 HPGe Detector

The HPGe detector is the core of the LENA detection system, both metaphorically and geometrically. It is a p-type, closed-end, bulletized germanium detector manufactured by EG&G Ortec. The manufacturer specified the HPGe's efficiency as 140% (as compared to that of a 3" x 3" NaI(Tl) at 1333 keV) though this has likely declined slightly in the two decades since the manufacture of the detector. Measured at 1333 keV, this detector has an energy resolution of less than 3 keV and produces highly resolved "singles" spectra (i.e. spectra produced without gating on additional detector signals).

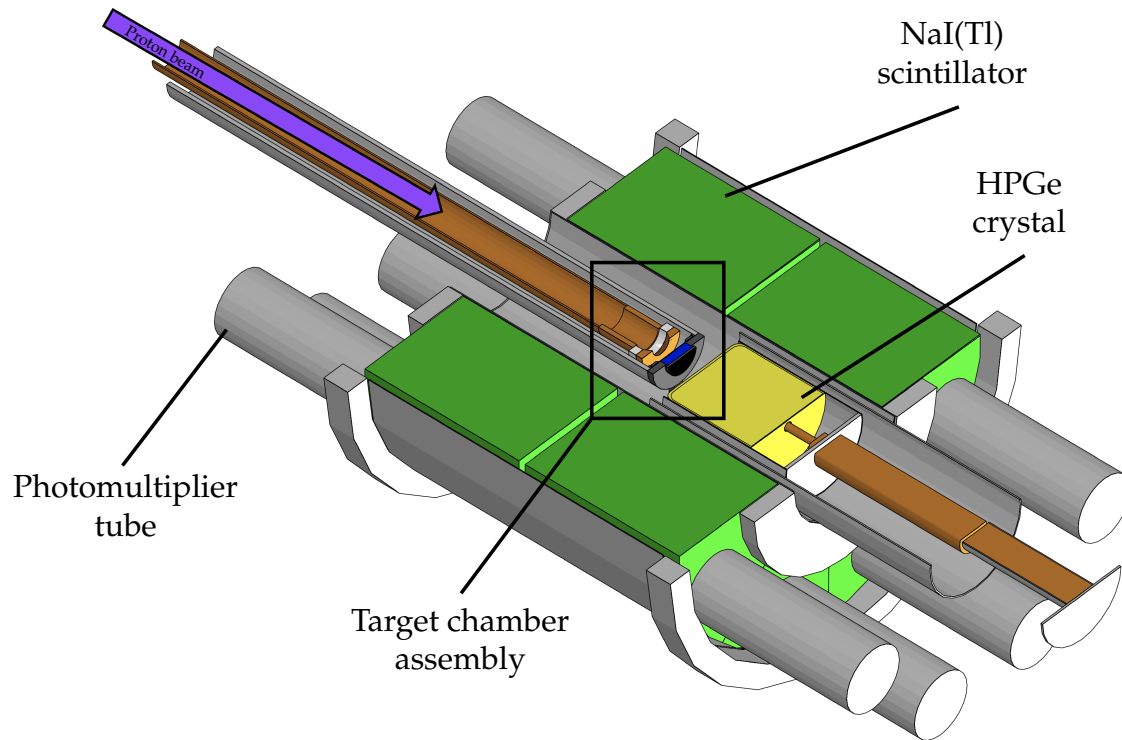


Figure 4.6: A DAWN rendering of the GEANT4-simulated $\gamma\gamma$ -coincidence detection system. The major components of this system—135% HPGe detector (yellow), 16-segment NaI(Tl) annulus (green) and corresponding photomultiplier tubes (grey)—are labeled on the figure. For clarity, the surrounding scintillator panels are not shown. The incoming proton beam (purple) and target chamber assembly (window) are also indicated on the figure. Figure courtesy of Chris Howard.

Detector Efficiency

As will be described in further detail in Chapters 6 and 7, a precise understanding of the LENA detection system and its efficiency in detecting γ -rays was pivotal for the analysis of resonances of interest in $^{29}\text{Si}(p,\gamma)^{30}\text{P}$. While this efficiency is implicitly included in the innovative analysis method employed for the study of all four resonances of interest (Chapter 6), the HPGe detector efficiencies were also determined explicitly to verify the validity of the GEANT4 simulations of the detection system.

To accomplish this, first a series of GEANT4 simulations were performed involving the emission of monoenergetic γ -rays from a 0.47'' diameter beamspot located on the surface of tantalum target backing. These simulations involved 50 different energies from 100 keV to 12000 keV. A second set of GEANT4 simulations were carried out over the same set of energies to model the emission of monoenergetic γ -rays from the center of a 1''-diameter, 0.25''-thick radioactive source puck placed on the target surface.

Next, three different γ -ray sources and two independent analytical methods were used to verify the efficiencies derived from the GEANT4 simulations and quantify the systematic uncertainty in the simulated detector geometry.

The first method of analysis, the *sum peak method*, is detailed in Iliadis (2015). This method relies upon the use of a ^{60}Co source and, through a few approximations, allows the determination of the absolute detector efficiencies of the two ^{60}Co characteristic peaks, 1173 keV and 1333 keV, without the need for a calibrated source. The dominant decay in a ^{60}Co source, $^{60}\text{Co}(\beta^-\bar{\nu}_e)^{60}\text{Ni}$, primarily proceeds through the release of a 1173 keV primary γ -ray to the 1333 keV level in the ^{60}Ni nucleus. This level decays directly to the ground state, releasing a 1333 keV secondary γ -ray. As a result, the $^{60}\text{Co}(\beta^-\bar{\nu}_e)^{60}\text{Ni}$ decay can be approximated as a simple, two γ -ray cascade, $2\rightarrow 1\rightarrow 0$, where γ_{21} is the primary γ -ray of energy 1173 keV and γ_{10} is the secondary γ -ray of energy 1333 keV. See the lefthand panel of Figure 4.8 for an example decay

scheme. For this type of cascade, the intensities of the individual γ -rays are

$$\begin{aligned}
\mathcal{N}_{21} &= \mathcal{N} \eta_{21}^P (1 - W(\theta) \eta_{10}^T) \\
\mathcal{N}_{10} &= \mathcal{N} \eta_{10}^P (1 - W(\theta) \eta_{21}^T) \\
\mathcal{N}_{20} &= \mathcal{N} \eta_{21}^P \eta_{10}^P W(\theta) \\
\mathcal{N}_t &= \mathcal{N} (\eta_{21}^T + \eta_{10}^T - \eta_{21}^T \eta_{10}^T W(\theta)) ,
\end{aligned} \tag{4.1}$$

where \mathcal{N}_{ji} are the measured intensities of the ^{60}Co full-energy and sum peaks, \mathcal{N}_t is the total intensity of the spectrum (which has been corrected for background radiation counts and extrapolated to zero-pulse height), \mathcal{N} is the total number of decaying nuclei, η_{ji}^P are the absolute peak efficiencies for the full-energy peaks, η_{ji}^T are the absolute total efficiencies for the full-energy and sum peaks, and $W(\theta)$ is the angular correlation factor between the primary and secondary γ -rays. If no further approximations were made, this set of equations would need to be solved iteratively to find the absolute efficiencies, but since the primary and secondary transitions are close in energy, the equations can be further simplified by approximating the primary and secondary γ -ray total efficiencies as an average value,

$$\eta_{21}^T \approx \eta_{10}^T \rightarrow \eta^T \approx \frac{(\eta_{21}^T + \eta_{10}^T)}{2}. \tag{4.2}$$

The efficiencies can then be solved with simple algebraic manipulation, yielding the following relationships:

$$\begin{aligned}
\eta_{21}^P &= \frac{1}{W(\theta)} \sqrt{\frac{\mathcal{N}_{21} \mathcal{N}_{20}^2}{\mathcal{N}_{10} \mathcal{N}_{20} \mathcal{N}_t + \mathcal{N}_{21} \mathcal{N}_{10}^2}} \\
\eta_{10}^P &= \frac{1}{W(\theta)} \sqrt{\frac{\mathcal{N}_{10} \mathcal{N}_{20}^2}{\mathcal{N}_{21} \mathcal{N}_{20} \mathcal{N}_t + \mathcal{N}_{10} \mathcal{N}_{21}^2}} \\
\eta^T &= \frac{1}{W(\theta)} \left(1 - \sqrt{\frac{\mathcal{N}_{21} \mathcal{N}_{10}}{\mathcal{N}_{20} \mathcal{N}_t + \mathcal{N}_{21} \mathcal{N}_{10}}} \right).
\end{aligned} \tag{4.3}$$

One final approximation was made in the treatment of the solid angle attenuation factors in the angular correlation factor calculation. This angular correlation factor for the ^{60}Co γ -ray cascade is given as

$$W(\theta) = 1 + \frac{5}{49}Q_2^{21}Q_2^{10}P_2(\cos\theta) + \frac{4}{441}Q_4^{21}Q_4^{10}P_4(\cos\theta), \quad (4.4)$$

where $P_n(\cos\theta)$ are Legendre polynomials of order n and Q_n^{ji} are the solid angle attenuation coefficients of order n for photon γ_{ji} . The type of Q_n^{ji} factor used, either “peak” or “total” solid angle attenuation coefficient, depends upon the type of event being studied. However, Longland *et al.* (2006), who discussed the method for determining the solid angle attenuation coefficients at length, found that although there is a distinction between Q_n^{ji} values for peak efficiencies and total efficiencies, it has little effect when the detector to source distance is small, as it is in this case. Thus, the peak Q_n^{ji} was used for all instances of Q_n^{ji} .

Finally, Equations 4.3 - 4.4 gave the detector efficiencies and angular correlation factor,

$$\begin{aligned} \eta_{21}^P &= \eta^P(1173 \text{ keV}) = 0.0373 \pm 0.0008 \\ \eta_{21}^P &= \eta^P(1333 \text{ keV}) = 0.0350 \pm 0.0008 \\ \eta^T &= \eta^T(1253 \text{ keV}) = 0.171 \pm 0.004 \\ W(\theta = 0^\circ) &= 1.03505 \pm 0.00064. \end{aligned} \quad (4.5)$$

The peak efficiencies derived using the *sum peak method* differ from those given by the GEANT4 simulations by less than 5%. Therefore, a conservative 5% systematic uncertainty in the peak efficiencies was adopted to account for this discrepancy.

Two other experimental datasets, the first taken with a ^{56}Co radioactive source and the second with a ^{14}N -implanted target and a proton beam produced by the LENA I accelerator (Section 4.1.1), were used to further quantify any discrepancies in the LENAGE simulation. However, neither of these decay processes, $^{56}\text{Co}(\varepsilon)^{56}\text{Fe}$ and the

$E_r^{lab} = 278$ keV resonance in $^{14}\text{N}(\text{p},\gamma)^{15}\text{O}$, share the simplicity of the $^{60}\text{Co}(\beta^-\bar{\nu}_e)^{60}\text{Ni}$ decay. As a result, it is not possible to extract the detector efficiencies from these datasets using the *sum peak method*. An alternative method, the *sum matrix method* presented in [Semkow et al. \(1990\)](#), was employed for this purpose. This method relies upon iteratively solving the relationship

$$\eta_{ji}^P = \frac{S_{ji}}{I_{ji}} - \frac{D_{ji}}{[\mathbf{N}^{(0)}\mathbf{c}]_{ji}}, \quad (4.6)$$

where η_{ji}^P is the HPGe efficiency in detecting γ_{ji} , S_{ji} is the measured γ -ray peak intensity in the presence of coincidence summing in counts per unit time, I_{ji} is the emission rate of γ_{ji} in the presence of coincidence summing, D_{ji} is a component of the coincidence summing correction matrix \mathbf{D} , and $[\mathbf{N}^{(0)}\mathbf{c}]_{ji}$ describes the feeding of branch ji where $\mathbf{N}^{(0)}$ is the feeding fraction matrix and \mathbf{c} is the branching ratio matrix. A simple PYTHON program, written by Jack Dermigny, was used to iteratively solve Equation 4.6 for coincidence summing-corrected peak efficiencies and their uncertainties. Because this method produces relative peak efficiencies rather than the absolute peak efficiencies of the *sum peak method*, the resulting efficiencies then had to be scaled to the appropriate GEANT4-simulated efficiency curve.

Figure 4.7 summarizes the peak efficiencies of the LENA HPGe detector. The raw efficiencies determined from GEANT4 calculations are shown by the solid black and red lines for the beamspot and source puck geometries, respectively. The coincidence summing peak efficiencies derived from source and beamspot data are shown as markers. Solid, purple markers indicate the $^{14}\text{N}(\text{p},\gamma)^{15}\text{O}$ efficiencies corresponding to the beamspot geometry, and outlined markers refer to the ^{60}Co (green) and ^{56}Co (blue) efficiencies from the source puck geometry.

The excellent agreement between the experimentally determined, absolute peak efficiencies from the ^{60}Co source and the simulated peak efficiencies shown in this

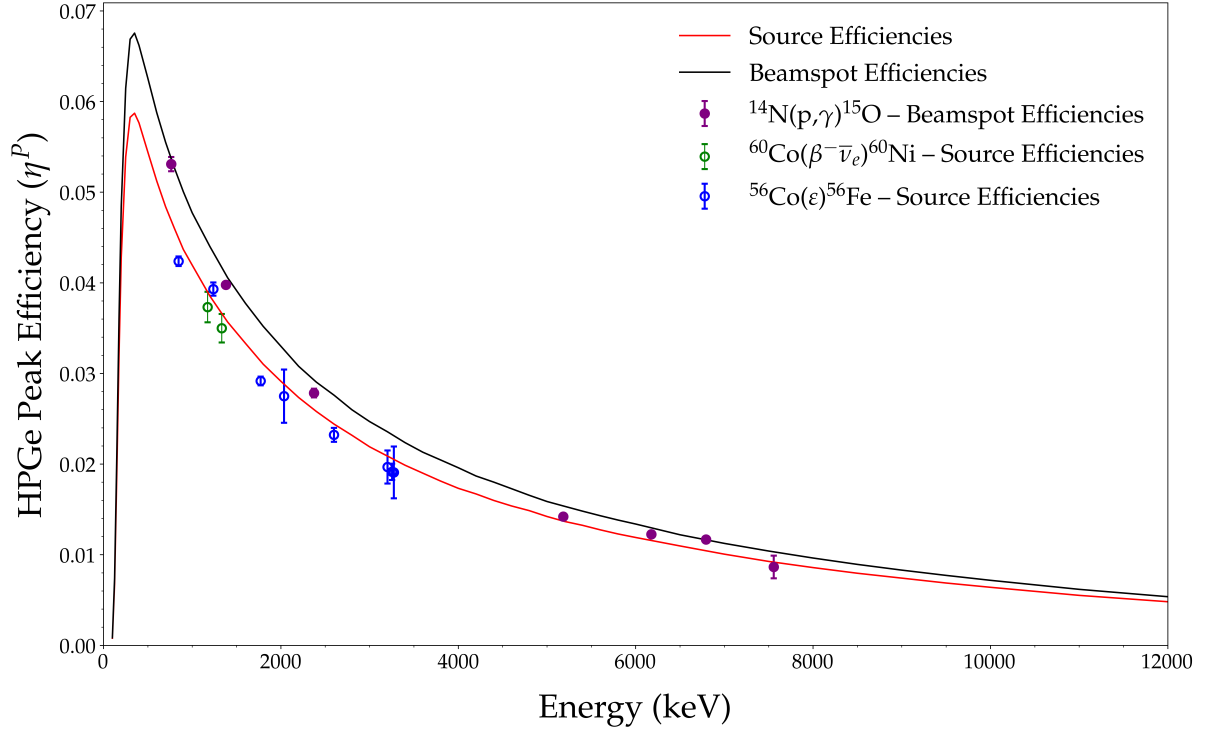


Figure 4.7: The GEANT4-simulated and experimentally determined peak efficiencies of the LENA HPGe detector. The raw efficiencies, as determined by GEANT4 simulations of the HPGe detector (Table 4.1), are shown as solid black and red lines for the beamspot and source puck configurations, respectively. The *sum peak method* was used to derive absolute peak efficiencies from the ^{60}Co source data. The *sum matrix method* was applied to the ^{56}Co source data and the $^{14}\text{N}(\text{p},\gamma)^{15}\text{O}$ data to find relative peak efficiencies. These efficiencies were then scaled to the simulated data using the appropriate efficiency curve.

figure indicate that the GEANT4 simulation of the detection system is accurate. Because only relative peak efficiencies can be derived from the $^{14}\text{N}(\text{p},\gamma)^{15}\text{O}$ and $^{56}\text{Co}(\epsilon)^{56}\text{Fe}$ data, their results are of limited utility in quantifying agreement with the LENA_{Ge} simulation. Regardless, these results were scaled to the appropriate simulated peak efficiency curve in Figure 4.7. Given that the scaled efficiencies follow the general trend of the simulated efficiencies curves, they do indicate agreement with the simulated efficiencies.

4.3.2 NaI(Tl) Annulus

The NaI(Tl) annulus is the second detection element of the $\gamma\gamma$ -coincidence system. The annulus is composed of 16 optically isolated NaI(Tl) scintillating segments, each connected to a photomultiplier tube (PMT), arranged in a coaxial fashion relative to the HPGe detector. The dimensions of the annulus are given in Table 4.1. When the system is arranged in running geometry, the target lies in the center of the system, further optimizing detection (Longland *et al.*, 2006).

As with the HPGe described earlier, the detection efficiencies of the NaI(Tl) did not need to be determined explicitly for the analysis method used in this dissertation. However, past characterizations of the annulus (Longland *et al.*, 2006; Buckner, 2014) make clear that its capabilities are well understood and show the validity of this analytical approach.

4.3.3 Muon Veto Shield

While not shown in Figure 4.6, another important detection array is included in the LENA $\gamma\gamma$ -coincidence spectrometer: the muon veto shield. The HPGe and NaI(Tl) detectors sit inside an aluminum box thinly lined with lead shielding, and the muon-veto system surrounds this box. This system is made up of five, 50 mm-thick plastic scintillator panels on the top and sides of the box. The signals from these panels are gated in anticoincidence, meaning that events coincident in the muon panels and the HPGe or NaI(Tl) annulus can be excluded from the observed spectra. In this way, events caused by cosmic muon background are significantly reduced in the resultant data.

4.3.4 Coincidence Counting System

When a particularly low-strength resonance is to be studied, the large volume HPGe by itself is not always sufficient to make the required measurement. It is in exactly this scenario that the utility and strength of the LENA $\gamma\gamma$ -coincidence detection system become clear.

Imagine, for example, a two γ -ray cascade produced by the resonance of a theoretical reaction, $A(a,\gamma)B$. A sample decay scheme for this cascade is shown in the lefthand panel of Figure 4.8. In some cases, both γ -rays from the decay of interest would be absorbed by either the germanium detector or the NaI(Tl) annulus. Other times, each of the γ -rays could deposit their energy in different detectors, as illustrated by the righthand panel in Figure 4.8. It becomes advantageous to focus on this type of event—where γ -rays are coincidently observed in multiple parts of the LENA detection system—as a means of reducing the presence of environmental and

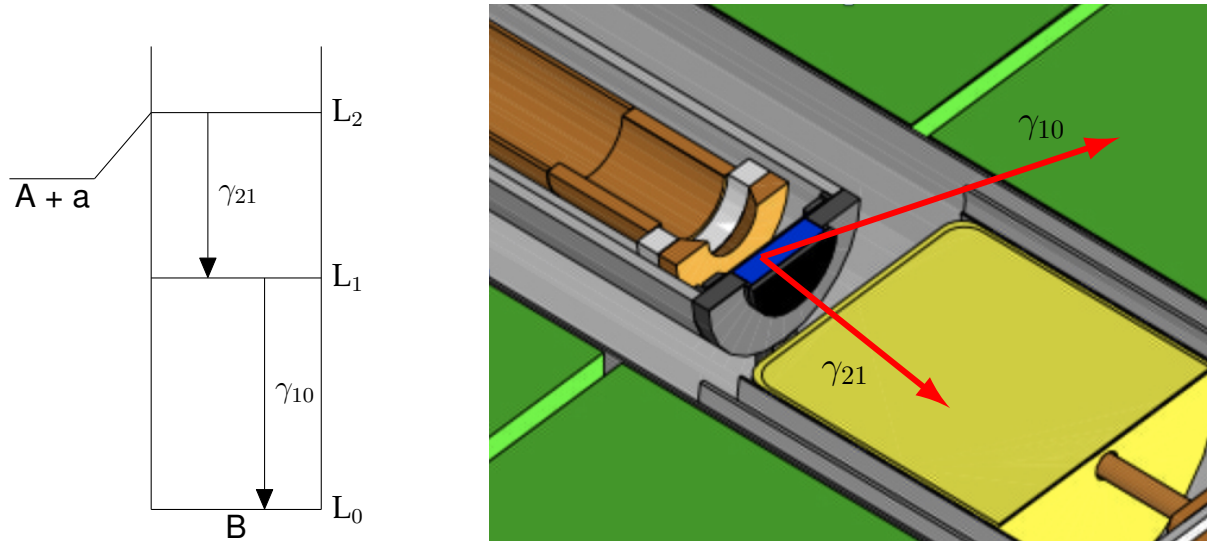


Figure 4.8: An illustration of the LENA $\gamma\gamma$ -coincidence detector operation. The left-hand panel shows a simple, two-step γ -ray cascade produced by a theoretical reaction, $A(a,\gamma)B$. The righthand panel exhibits how the two γ -rays in the cascade, γ_{21} and γ_{10} , could be absorbed by different detectors, the HPGe (yellow) and the NaI(Tl) annulus (green), respectively, in the LENA detection system. In this scenario, it becomes advantageous to gate on these coincident events as a method of focusing on the reaction of interest and minimizing the interference of contaminant reactions.

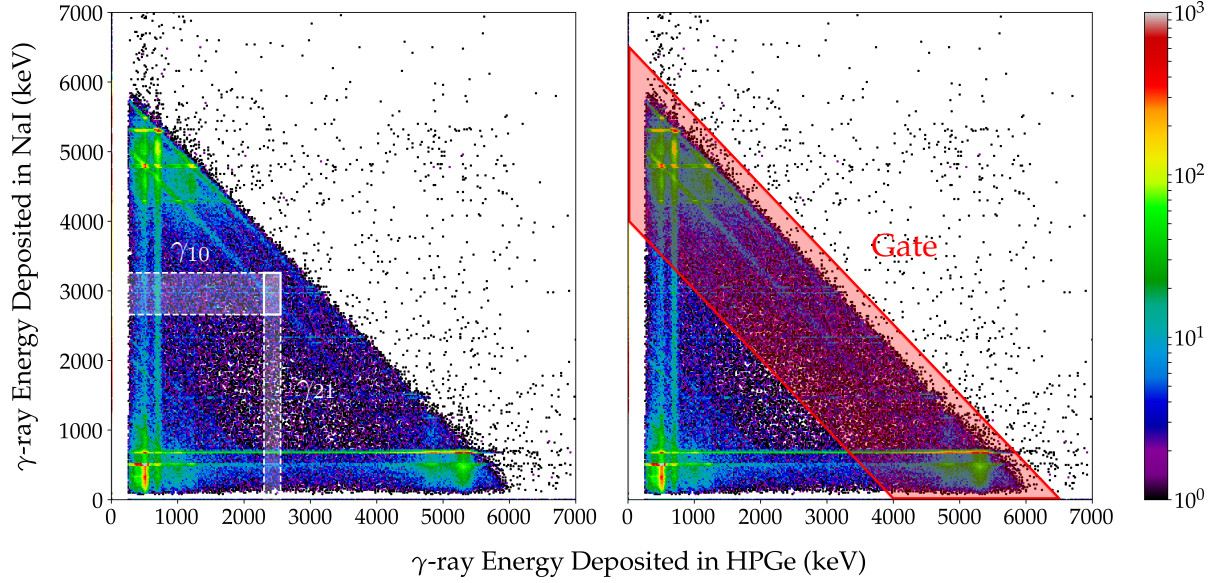


Figure 4.9: An example $\gamma\gamma$ -coincidence 2D histogram and gating scheme. Both the left and righthand panels of the figure show the 2D histogram of γ -ray energies observed by the HPGe (x-axis) and the NaI(Tl) annulus (y-axis). On the left panel, two bands, representing the γ -rays from the two-part cascade shown in Figure 4.8, are superimposed on the histogram. The width of each band shows the relative energy resolution of the two types of detectors, though this is not shown to scale for visibility reasons. The coincidence gate, given by the energy condition of Equation 4.7, is shown in red on the right panel.

beam-induced contaminant background in the resulting spectrum.

With reasonable time and energy gating, the reduction of unwanted background can be significant. Figure 4.9 shows how energy gating between the HPGe and the sum of the NaI(Tl) signals is accomplished. In the lefthand panel, the two-dimensional histogram of events observed coincidently in the HPGe and the NaI(Tl) annulus is shown. The x-axis gives the energy of the γ -rays observed in the HPGe detector, while the y-axis provides the same information for the NaI(Tl) annulus. The color of each data point indicates the frequency with which a particular combination of γ -ray energies is observed.

Two intersecting, white bands, representing the two γ -rays shown in Figure 4.8, are superimposed on this panel as well. The width of each band indicates the energy resolution of the detector upon which the γ -ray was incident: γ_{21} on the HPGe and γ_{10}

on the NaI(Tl) annulus. However, these bands are not shown to scale for visibility reasons. Note that the two bands overlap on a region containing part of a diagonal band with higher occurrence frequency relative to the surrounding region. This band corresponds to the sum of the two γ -ray energies and, in this case, the excitation energy of the theoretical resonance of interest.

If one were to gate only on the region of overlap between the two bands, the presence of environmental and contaminant background would be dramatically reduced. However, the severe accepted-energy restriction imposed by such a gate would greatly reduce the efficiency in measuring an event of interest as well. However, a trapezoidal gate, such as the one shown in the righthand panel of Figure 4.9, would also capture Compton-scattered γ_{10} 's, reducing the effect of background radiation without a significant loss of efficiency compared to HPGe singles data collection.

Then, it is easy to see that a trapezoidal gate on the sum of the HPGe and NaI(Tl) energies,

$$E_{\min} \leq E^{\text{HPGe}} + E^{\text{NaI}} \leq E_{\max}, \quad (4.7)$$

could be effective in isolating the signal from the resonance of interest where its excitation energy lies somewhere between the lower threshold of the gate, E_{\min} , and its upper bound, E_{\max} . An example of this type of energy gate is shown in red on the right panel of Figure 4.9. The major sources of environmental background at LENA, U-Th chains and ^{40}K , have energy signatures at 3 MeV or lower, while the excitation energy of the resonance of interest is often significantly higher. However, beam-induced contaminant reactions often produce higher energy γ -rays, but generally, a carefully chosen upper limit on the coincident gate can still reduce the impact of contaminants in the resulting coincidence spectrum.

The power of $\gamma\gamma$ -coincidence gating is on full display in Figure 4.10. This figure shows a section of the singles and coincidence spectra from the $^{29}\text{Si}(\text{p},\gamma)^{30}\text{P}$ $E_r^{\text{lab}} = 314$

keV resonance measurement (Section 7.3). The singles spectrum is given in black. The coincidence spectrum, produced using a trapezoidal energy gate (Equation 7.1) and muon veto application, is shown in red. The spectra include a number of peaks from various sources as indicated on the figure.

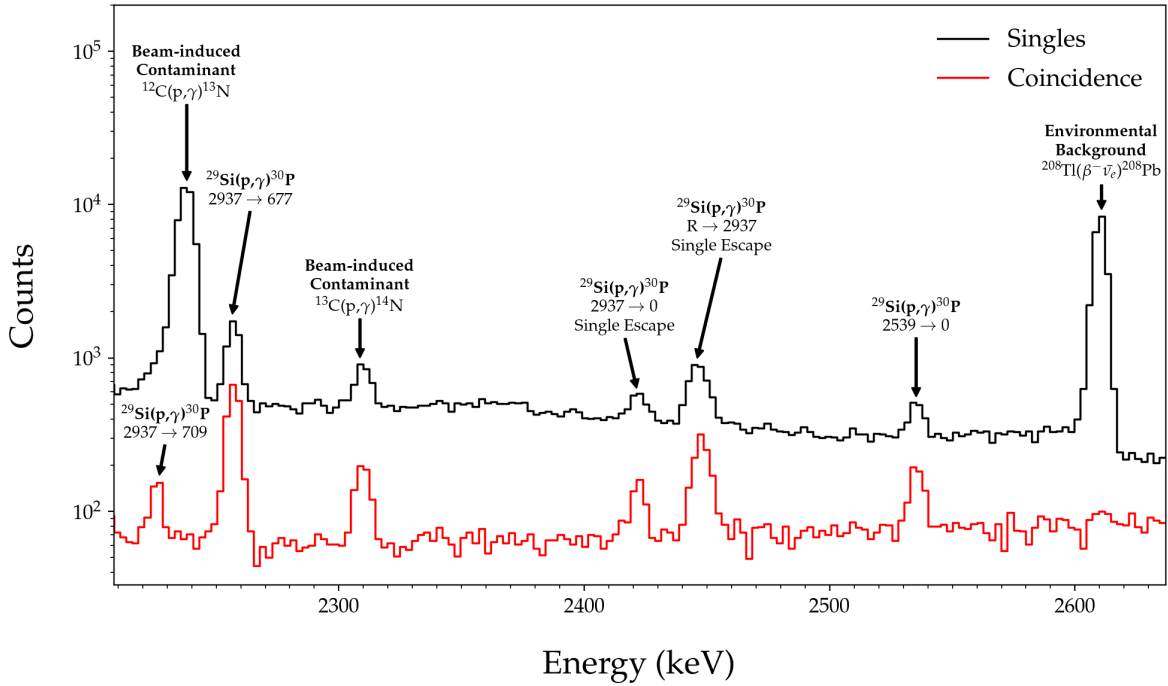


Figure 4.10: A comparison of the HPGe singles & $\gamma\gamma$ -coincidence spectra from the $^{29}\text{Si}(p,\gamma)^{30}\text{P}$ $E_r^{\text{lab}} = 314$ keV measurement. The singles and coincidence spectra are given in black and red, respectively. The coincidence spectrum was produced with a trapezoidal energy gate (Equation 4.7) and muon veto condition applied. Each peak and its source is indicated on the figure with arrows and labels. $^{29}\text{Si}(p,\gamma)^{30}\text{P}$ peaks have labels of the form $R \rightarrow E_f$ for primary transitions or $E_i \rightarrow E_f$ for secondary transitions. All energies are given in keV.

There are several differences between the spectra worthy of note. First, the environmental background peak produced by $^{208}\text{Tl}(\beta^-\bar{\nu}_e)^{208}\text{Pb}$ is prominent in the singles spectrum but not visible in the coincidence spectrum, indicating that the application of the coincidence gate very effectively reduced the presence of environmental background in the coincidence spectrum. Next, note the prominent peak at 2.2 MeV, produced by the direct capture of protons by ^{12}C , in the singles spectrum. A

cursory inspection of this region in the coincidence spectrum reveals that not only is this peak essentially absent in the coincidence spectrum but its absence also reveals a $^{29}\text{Si}(\text{p},\gamma)^{30}\text{P}$ secondary transition peak not visible in the singles spectrum. In fact, all $^{29}\text{Si}(\text{p},\gamma)^{30}\text{P}$ peaks in the coincidence spectrum appear more intense, relative to the background level, than the equivalent peaks in the singles spectrum.

Thus, the $\gamma\gamma$ -coincidence technique can be a powerful tool for the challenging study of low-strength resonances. The analysis of data acquired with this technique will be thoroughly discussed in Chapter 7.

CHAPTER 5: SILICON-29 ENRICHED TARGETS

In addition to the innovative beam production and γ -ray detection techniques described in the previous chapter, highly enriched, minimally contaminated nuclear targets are required to carry out nuclear reaction measurements efficiently. The production and characterization of such targets, however, can be quite complicated. In Section 5.1, a short discussion of targetry methods will be followed by descriptions of target backing preparation (Sections 5.1.1–5.1.2), implantation (Section 5.1.3), and surface restoration (Section 5.1.4). Section 5.2 will then detail target characterization.

5.1 Target Preparation & Maintenance

First, a backing material must be chosen to serve as the inactive portion of the nuclear target. While backing-free targets such as self-supporting transmission targets and gas targets do exist, these targets are limited to certain nuclear species and can be quite delicate under high intensity beam, so the use of backing material is often the favorable option (Iliadis, 2015). Thus, beamstop target backings made of tantalum are typically used in experiments performed at LENA.

Tantalum has a few properties that make it advantageous for this application. Most importantly, the high atomic number of tantalum ($Z = 73$) ensures that the relatively low bombarding energies produced at LENA (Section 4.1) cannot initiate incidental nuclear reactions on tantalum nuclei. Tantalum also has a high melting point, well above even the temperatures expected to be produced in a target under LENA II bombardment (Section 4.1.2), and proves stable under intense proton beam as a result.

When produced as a thin sheet, tantalum captures very few γ -rays produced by proton capture reactions, allowing for the efficient detection of the produced reaction to take place (Iliadis, 2015). A backing of this form also allows for direct water cooling of the target which increases the longevity of the target under intense beam (Section 4.2).

For these reasons, 0.5 mm-thick tantalum sheet was chosen to serve as the backing material for the study of $^{29}\text{Si}(p,\gamma)^{30}\text{P}$. The sheet was machined into 1.5" squares each with a small hole outside the implantation region to allow for careful handling.

5.1.1 Chemical Etching

While the tantalum sheet was of high purity, contaminants can be introduced during machining, and it becomes necessary to remove any such deposits before target material can be introduced to the backing. In truth, the first step in the preparing the target backing—chemical etching—has less to do with decontaminating the backing surface than it does with removing the surface layer of the backing altogether. The efficacy of this technique has been documented by Longland *et al.* (2009). On that account, this process guarantees that the target nuclei will be implanted into pristine tantalum free of contamination from storage, machining, and the like.

Chemical etching was carried out using a well-established recipe (Vermilyea, 1953) involving an acid bath of 95% sulfuric acid (H_2SO_4), 70% nitric acid (HNO_3), and 50% hydrofluoric acid (HF) with a 5:2:2 ratio. The acids were carefully mixed together in a Teflon beaker under a chemical fume hood, and the chemical reaction was slowed and stabilized by placing the beaker in an ice bath. The backing to be etched was secured to highly acid-resistant plastic tongs and fully immersed in the acid bath for 20 seconds (as pictured in the left panel of Figure 5.1), followed by submersion in distilled water. The process was then repeated twice so that each backing was exposed to the acid for a total of 60 seconds. Typically, three to four backings could be etched in this manner before the acid bath became ineffective. The fully etched backings were

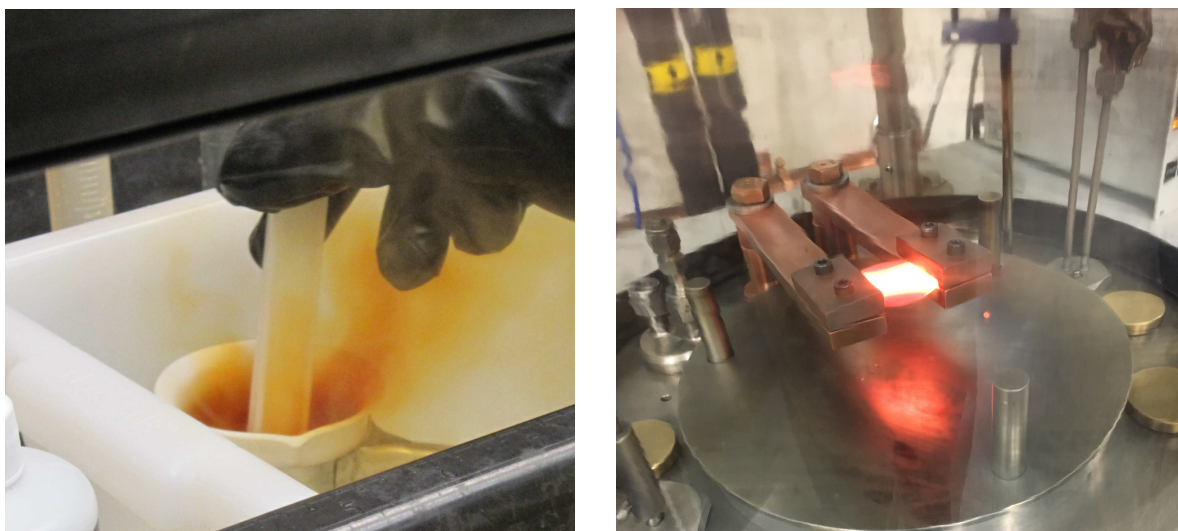


Figure 5.1: Images of the preparation of a target backing prior to implantation. **Left:** The tantalum target backings were wet etched in an acid bath of H_2SO_4 , HNO_3 , and HF with a 5:2:2 ratio. Each backing was submerged in the acid bath for a total of 60 seconds. Image courtesy of Matthew Buckner. **Right:** After the tantalum backing underwent acid etching, the backing was resistively heated under high vacuum to facilitate the outgassing of any remaining contaminants from the backing surface.

finally cleaned with ethanol and set aside to dry.

After acid etching, the backings were covered in clean aluminum foil and stored in a plastic bag until the next stage of target preparation commenced.

5.1.2 Resistive Heating

In order to remove any remaining contaminants, the backing underwent another decontamination process—resistive heating under high vacuum. The evaporation chamber used in this process is described in [Cesaratto \(2011\)](#).

First, the etched backing was placed between two water-cooled copper electrodes in the evaporation chamber. The electrodes were tightened onto the backing to ensure good electrical contact. A glass bell jar was placed over the electrodes, and the system was evacuated to roughly 10^{-6} Torr using a combination of oil-free pumps. After the desired vacuum was achieved, an electric current was applied across the backing and

slowly increased until the backing glowed bright red (as shown in the right panel of Figure 5.1), typically occurring in the range of 200–300 A. The initial heating of the backing was accompanied by a factor 10 increase in the pressure of the vacuum chamber, indicating that contaminants were in the process of boiling off the backing. After about 15 minutes of resistive heating, the target was thoroughly outgassed and the contaminants evacuated from the system. This would coincide with the return of the chamber vacuum to its baseline pressure. Afterward, the current would be gradually decreased to 0 A. The backing was then allowed to cool in vacuo for at least an hour before being stored as described in the preceding section.

As with the acid etching technique described earlier, the efficacy of resistive heating in reducing surface contaminants was explored by Longland *et al.* (2009). Their work determined that resistive heating was particularly effective at reducing contamination from fluorine. As will be detailed in Chapter 7, $^{19}\text{F}(\text{p},\alpha\gamma)^{16}\text{O}$ is a potent contaminant reaction at the low energies used in the study of $^{29}\text{Si}(\text{p},\gamma)^{30}\text{P}$, and this reduction is of critical importance as a result.

5.1.3 Implantation

While there exist several methods of introducing target material to a target backing, silicon targets have generally been produced by either evaporation or implantation.

The production of evaporated targets is relatively easy, benefiting from minimal equipment and time requirements (Holland, 1956). As noted by Iliadis (2015) however, it is possible for evaporated targets to become unstable under high intensity ion beam leading to unpredictable changes to the target stoichiometry and complicating the analysis of the experimental data.

Implanted targets are markedly stable in comparison. Implantation involves the

production of target ions which are then mass separated, accelerated, and finally implanted into a target backing. The target ions can be produced from a variety of compounds depending on the type of ion source and the target species of interest. Typically, LENA researchers have produced implanted targets in-house using a Eaton 3204 positive ion implanter housed at the University of North Carolina at Chapel Hill. This Freeman-type ion implanter was capable of producing ions from gaseous and solid sources (Chivers, 1992) and was used extensively in past experiments (see, for example, Longland *et al.*, 2010a; Cesaratto *et al.*, 2013; Howard *et al.*, 2015; Daigle *et al.*, 2016; Kelly *et al.*, 2017). Unfortunately, silicon source materials for this type of ion implanter are limited to vapors of room-temperature liquids and toxic or corrosive gases (Wielunski *et al.*, 2004), and it was not productive to make the necessary improvements to an implanter at the end of its service life.

Accordingly, a different method of producing target ions, the Source of Negative Ions by Cesium Sputtering (SNICS), was pursued for the $^{29}\text{Si}(p,\gamma)^{30}\text{P}$ study. As the name implies, this type of ion source uses cesium ions to sputter source material. An illustration of this process is shown in Figure 5.2. First, cesium vapor is produced in an oven and then directed to a chamber containing the cathode and the spherical ionizer. While some cesium condenses on the relatively cool surface of the cathode, the remaining cesium is ionized by the heated surface of the spherical ionizer. The positively charged cesium ions (Cs^+) are electrically accelerated toward the cathode, sputtering off source material and producing a beam of negatively charged source ions to be implanted into a target backing (Middleton, 1983).

When the $^{29}\text{Si}(p,\gamma)^{30}\text{P}$ study began, TUNL did not have an operational SNICS source, so the ^{29}Si targets were produced offsite. More specifically, three ^{29}Si targets were produced using the SNICS source at the Centre de Spectrométrie Nucléaire et de Spectrométrie de Masse (CSNSM) in Orsay, France under the direction of Alain Coc. This SNICS source is connected to the ARAMIS, a custom 2-MV Tandem/Van

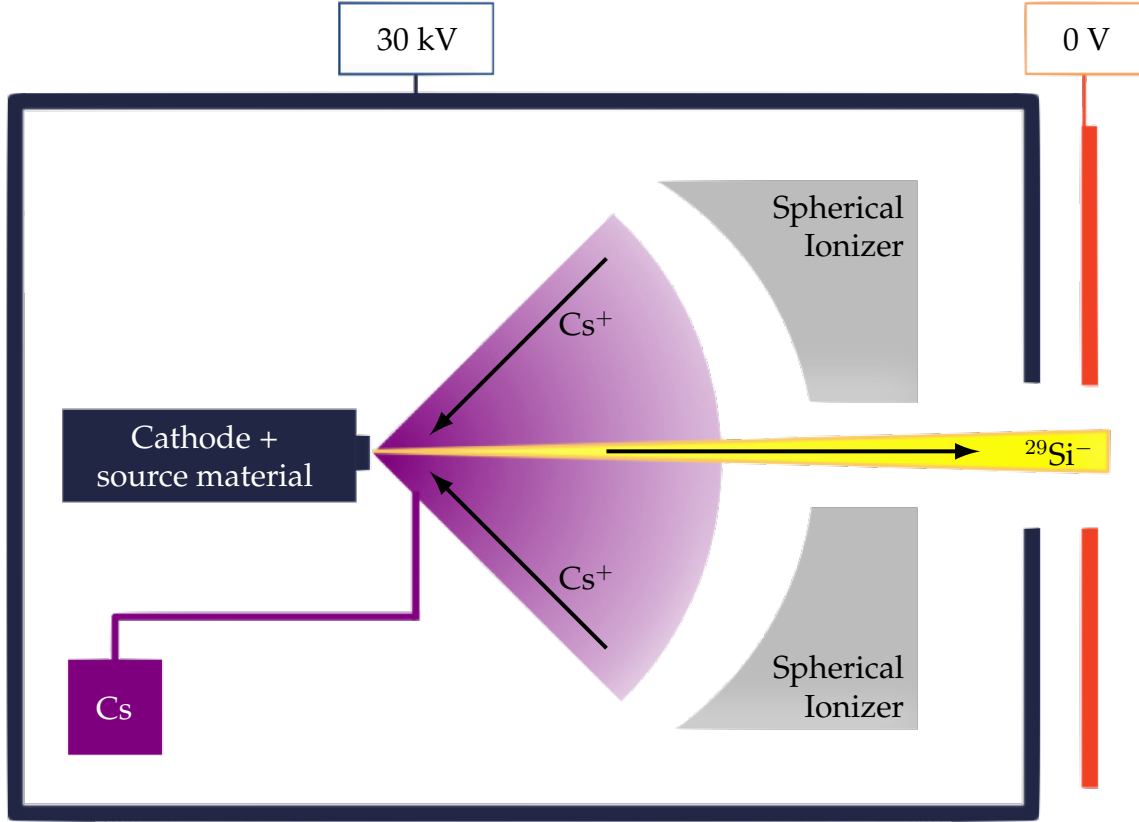


Figure 5.2: A diagram of SNICS source operation. A cesium oven produces cesium vapor which is then ionized by a spherical ionizer. The Cs^+ beam is then used to sputter source material in the cathode. The negatively charged source ions are then magnetically separated, accelerated, and implanted into a target backing. Figure courtesy of CSNSM.

de Graaff accelerator, and has been used to produce ion beams of over 40 different elements with energies up to 10 MeV (Bacri *et al.*, 2017). For the targets used for this dissertation, the $^{29}\text{Si}^-$ beam was produced from natural silicon metal and implanted at 80 keV into etched, outgassed Ta backings. The implantation dose for each target was roughly 200 mC/cm^2 . A photograph of Target #1, taken shortly after it was implanted and before proton beam was applied, is shown in the left panel of Figure 5.3.

While three targets were produced for the $^{29}\text{Si}(p,\gamma)^{30}\text{P}$ study discussed in this dissertation, production difficulties resulted in the heterogenous and off-center implantation in Target #2 and Target #3, respectively. The first target produced, Target #1,

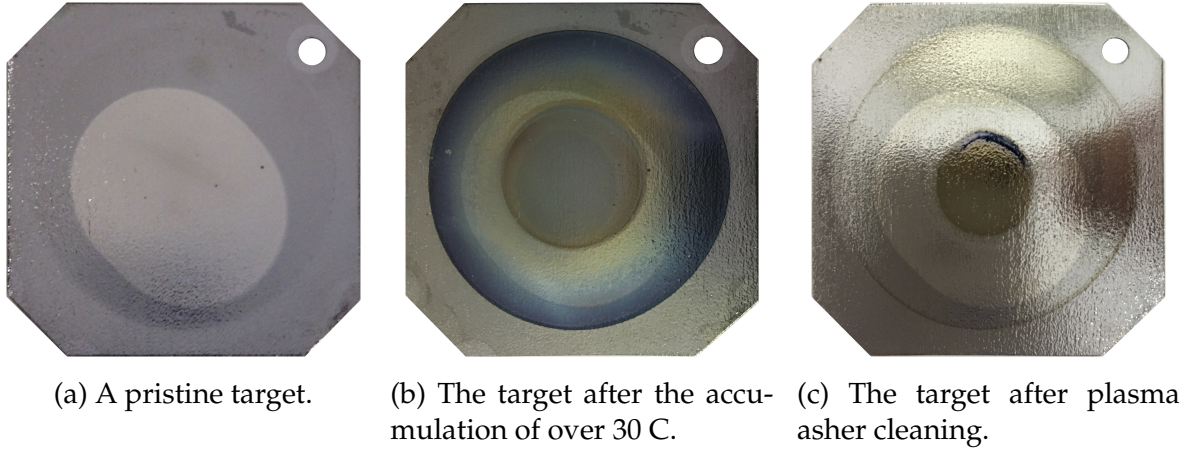


Figure 5.3: Photographs of a ^{29}Si -implanted target at several points during the $^{29}\text{Si}(\text{p},\gamma)^{30}\text{P}$ study. The target was produced using the ARAMIS SNICS source at CSNSM (see text for details). The implanted region is the light silver, slightly off-center area of the target. The dark central region shows where proton beam was incident on the target surface.

did not have these issues. As will be discussed in a later section (Section 5.2), Target #1 proved exceptionally stable, and this made it possible to use only this target for the entire $^{29}\text{Si}(\text{p},\gamma)^{30}\text{P}$ study described in this dissertation.

5.1.4 Target Restoration

Despite the pains taken to ensure a high vacuum and a clean target, the accumulation of contaminants on the target surface inevitably follows the accumulation of charge. After ~ 12 C was accumulated on Target #1 with the LENA I accelerator and ~ 20 C with LENA II, the surface of Target #1 was notably discolored by contaminants (as shown in the center panel of Figure 5.3). This accumulation, made primarily of carbon, typically occurs gradually over the course of an experiment due to the outgassing of vacuum o-rings in the beamline.

Nevertheless, an investigation of acquired data showed that, while the contaminant layer had been slowly developing during LENA I data collection, the accumulation of contaminants accelerated during LENA II data collection. It is hard to say why

the use of the LENA II accelerator caused the contamination accumulation to increase in this way. It is important to realize that this accelerator produced beam currents well above those produced at LENA in the past, and this improvement necessitated significant upgrades to the vacuum and beam transport systems that were not completed before the initial 20 C of LENA II data was taken. Regardless, the work detailed in [Cooper *et al.* \(2018\)](#) eliminated the contaminant issue once completed.

Still, the contaminant layer on Target #1 needed to be removed before the $^{29}\text{Si}(p,\gamma)^{30}\text{P}$ study could be continued. This was accomplished using the Emitech K-1050X Plasma Asher in the Duke University Shared Materials Instrument Facility. This device produces an oxygen plasma that reacts with the carbon in the contaminant layer to form carbon monoxide and carbon dioxide. These byproducts are then removed from the plasma chamber via a rough vacuum ([Dermigny, 2018](#)). As can be seen in the right panel of Figure 5.3, the contaminant layer was visibly reduced after cleaning. Yield curve tests confirmed that target concentrations of ^{12}C and ^{19}F were significantly reduced while the ^{29}Si concentration remained unchanged.

5.2 Yield Curve Target Studies

While some target properties can be estimated based on implantation parameters and the like, it is crucial to quantify key properties of nuclear targets and other experimental parameters as the basis for an accurate nuclear study. To this end, target yield curves were employed to study the ^{29}Si target used in this dissertation. The aptly named yield curve involves mapping the experimental “yield” of a nuclear reaction—the number of times a reaction’s characteristic γ -ray is observed versus the number of incident particles—over a range of bombarding energies.

The top panel of Figure 5.4 shows the cross section of an idealized resonance. The resonance energy is indicated by a dashed line through the center of the resonance

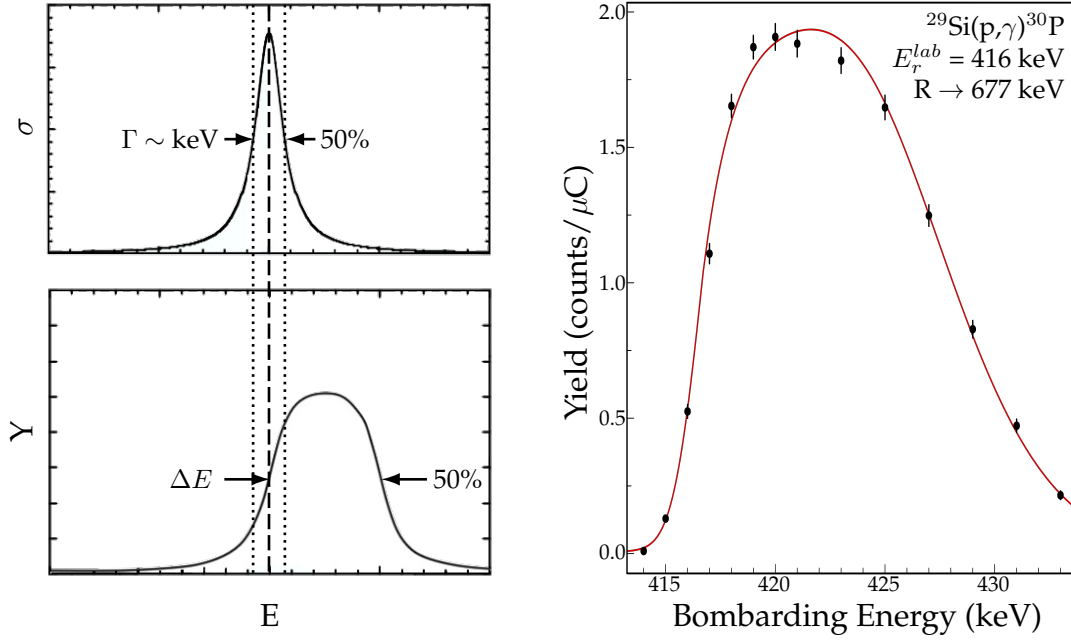


Figure 5.4: **Top:** The cross section of an idealized resonance is shown here. The dashed line indicates the energy of the resonance. The width of the resonance, Γ , is measured at the FWHM of the peak. **Bottom:** This is the yield curve corresponding to the resonance shown in the top panel. Using the dashed line from the top panel, it is clear that the inflection point on the front edge of the yield curve, corresponding to the 50% yield, occurs at the resonance energy. The FWHM, shown with arrows in this panel, gives the width of the target in energy units at the resonance energy. **Right:** A yield curve of the $R \rightarrow 677 \text{ keV}$ primary transition of the $E_r^{\text{lab}} = 416 \text{ keV}$ standard resonance in $^{29}\text{Si}(p,\gamma)^{30}\text{P}$. The data points indicate the experimentally measured yield while the red line indicates the fit to the data performed using the YCurveFit program. See text for details.

peak, and the width of the resonance, Γ , is the full-width half-maximum (FWHM) of the peak as indicated by the dotted lines. For a target of width ΔE where $\Delta E > \Gamma$, the resonant yield curve takes the form shown in the bottom panel of Figure 5.4. As indicated by the dashed line, the inflection point of the yield curve's front edge corresponds to the resonance energy. The FWHM of the yield curve gives the target thickness in energy units at the resonance energy.

Many yield curve measurements were made over the course of the $^{29}\text{Si}(p,\gamma)^{30}\text{P}$ study as these measurements can serve several purposes. For one, a properly understood yield curve can be used to derive a number of different target and experimental

properties. Yield curves can show an experimenter at what energy the maximum yield of a resonance occurs, and performing a measurement at this energy makes for an efficient experiment. This use becomes even more important when the measurement of two closely spaced resonances is undertaken (see Section 7.2.1). Lastly and perhaps most importantly, yield curves are crucial for monitoring target stability because the maximum yield of a target yield curve decreases as a target degrades.

To measure the yield curve of the ^{29}Si target, the LENA I accelerator was employed to generate protons in the range of 400–430 keV to find the experimental yield of the $E_r^{\text{lab}} = 416$ keV standard resonance in $^{29}\text{Si}(p,\gamma)^{30}\text{P}$ (Table 7.3). The beam current was maintained at $\leq 2 \mu\text{A}$ in order to minimize dead time. The intensity of the strongest primary transition, $R \rightarrow 677$ keV, was tracked over this energy range with the HPGe detector operated in singles mode. The background-subtracted, dead time-corrected yield from one such measurement is shown by the data points in the right panel of Figure 5.4. To monitor target stability, the yield of the ^{29}Si target was measured every 1.5–5 C accumulated on target.

While the yield is relatively simple to measure and the idealized yield curve is easy to interpret, it can be quite complicated to account for experimental factors (beam resolution and straggling, target heterogeneities, etc.) in order to extract the desired properties. For resonance yield curves specifically, several reasonable assumptions can be made to simplify matters (for a complete discussion, see Iliadis, 2015). The resulting expression for the experimental yield of a resonance is

$$Y(E_0) = \frac{1}{\varepsilon_r} \int_{E_0 - \Delta E}^{E_0} dE' \int_{E_i=0}^{\infty} dE_i \int_{E=0}^{E_i} \sigma(E) g(E_0 - E_i) f(E_i - E, E') dE \quad (5.1)$$

where E_0 is the mean bombarding energy, ε_r is the constant stopping power of the target over the width of the resonance, ΔE is the target thickness, and $\sigma(E)$ is the energy-dependent resonant cross section. The function $g(E_0 - E_i)$ gives the incident

Table 5.1. $^{29}\text{Si}(\text{p},\gamma)^{30}\text{P}$ $E_r^{\text{lab}} = 416$ keV Yield Curve Analysis

Parameter	Value
Maximum Yield	1.98 ± 0.05 counts/ μC
Yield Area	23.0 ± 0.3 counts $\cdot\text{keV}/\mu\text{C}$
Resonance Energy	416.61 ± 0.09 keV
Target Thickness	11.39 ± 0.26 keV
Beam Width	2.39 ± 0.15 keV
Beam Straggling	2.69 ± 0.31 keV

Note. — These are the results of a fit to a yield curve measured shortly before the $E_r^{\text{lab}} = 221$ keV measurement commenced (Section 7.4).

beam width independent of the mean bombarding energy, while $f(E_i - E, E')$ governs the beam straggling in the target, which is independent of the incident energy.

A R program designed to fit experimental yield curves, `YCurveFit`, was written by Richard Longland. This program uses Markov Chain Monte Carlo (MCMC) to fit the experimental yield, and from the fit, parameters in Equation 5.1 could be extracted. The red curve in the right panel of Figure 5.4 shows a fit found using `YCurveFit`, and Table 5.1 presents the parameter values determined from this fit. The yield curve shown in this figure was taken and analyzed shortly before the $E_r^{\text{lab}} = 221$ keV study (Section 7.4) began. Given the stability of the ^{29}Si target, all yield curves taken during the course of the $^{29}\text{Si}(\text{p},\gamma)^{30}\text{P}$ study strongly resemble that of Figure 5.4.

Between the resonance studies performed using the LENA I accelerator ($E_r^{\text{lab}} = 416$ keV, 324 keV, and 314 keV) and the $E_r^{\text{lab}} = 221$ keV study with the LENA II accelerator, the LENA I bombarding energy was recalibrated for improved accuracy (for details, see [Dermigny, 2018](#)). It should be noted that the yield curves (and corresponding bombarding energies) presented in Sections 7.1–7.3 were affected by the previous

LENA I energy calibration which resulted in an underestimate in the bombarding energy. As this was only a calibration issue, there was no effect on the data presented in these sections, but the ostensible discrepancy could prove confusing to an uninformed reader.

CHAPTER 6: DATA ANALYSIS METHODS

For nuclear capture experiments, the ultimate desire is to further the understanding of both the decay dynamics and the frequency of the reaction. Experimentally, this translates to determining the primary γ -ray branching ratios as well as the total number of nuclear reactions originating from the reaction of interest. Traditional “peak-by-peak” analysis, involving the measurement of net intensities for all full-energy primary transition peaks with corrections applied for detector efficiency, has been successfully used in the past for relatively simple spectral analysis. Nevertheless, the efficacy of this method breaks down when any number of complications—coincidence summing, angular correlations, compound peaks, and the like—are encountered en masse.

Furthermore, the “peak-by-peak” analysis method is challenging to apply to $\gamma\gamma$ -coincidence spectroscopy used in the current $^{29}\text{Si}(\text{p},\gamma)^{30}\text{P}$ study. This data acquisition method involves the roughly simultaneous detection of γ -rays across multiple detectors. The observed data can then be refined using timing and energy gates to focus on the events of interest and reduce the impact of background sources (see Section 4.3.4). As the result of this gating, the likelihood of observing an event of interest is significantly improved, but the detection efficiency is now dependent on multiple factors in addition to the efficiency of the employed detectors. This added complexity means that it is substantially more difficult to correct full-energy primary peak intensities for detection efficiency.

In light of these complications, the binned likelihood approach of [Dermigny et al.](#)

(2016) was adopted instead of a traditional “peak-by-peak” method for the spectral analysis of the $^{29}\text{Si}(\text{p},\gamma)^{30}\text{P}$ study. This method has been successfully applied to $^{17}\text{O}(\text{p},\gamma)^{18}\text{F}$ and $^{22}\text{Ne}(\text{p},\gamma)^{23}\text{Na}$ direct studies by Buckner *et al.* (2015) and Kelly *et al.* (2017), respectively. In this technique, a binned likelihood function is used to produce Monte Carlo-simulated *templates* extending across the entirety of the observed spectrum. Singles or $\gamma\gamma$ -coincidence spectra can be easily produced with this method. A Bayesian approach is then applied to determine the fraction each template contributes to the observed spectrum. One can choose to fit only full-energy peaks, similar to the “peak-by-peak” approach, or the entirety of the experimental spectrum. Because the effects of complicating experimental factors (angular correlations, coincidence summing, etc.) are implicitly included in the simulated templates, no corrections to the resulting fit are required, and the primary γ -ray branching ratios and total number of reactions for the reaction of interest can be easily calculated from the template fractions. With these advantages in mind, a binned likelihood approach is clearly the best analysis method for the current work.

In this chapter, the binned likelihood approach and its application to the present $^{29}\text{Si}(\text{p},\gamma)^{30}\text{P}$ study will be discussed. Section 6.1 will present the analysis method in detail, followed by a discussion of simulated template generation (Section 6.2). Section 6.3 will discuss the method chosen to determine the goodness of fit. Lastly, a summary of the adopted analysis method will be presented in Section 6.4.

6.1 Methodology

Despite any researcher’s best efforts, a measured pulse height spectrum rarely consists of only the reaction of interest. Far more often the γ -ray spectrum resembles that of Figure 4.10 with contributions from various sources including environmental background, beam-induced contaminant reactions, and, hopefully, the reaction of interest

itself. In order to determine the fractional contribution of each source of radiation to the experimental spectrum, each must be modeled and included in the spectral fit in the form of templates.

To this end, the extended binned likelihood function described by [Barlow \(1990\)](#) was adopted. This likelihood function essentially describes the probability, P , of obtaining the data, \mathbf{D} , from the fractions, \mathbf{F} , of m number of templates across n bins. Using the notation of [Dermigny *et al.* \(2016\)](#), the expression for this function is given by [Barlow and Beeston \(1993\)](#) as

$$P(\mathbf{D}|\mathbf{F}) = \left[\sum_{i=1}^n D_i \ln f_i - f_i \right] + \left[\sum_{i=1}^n \sum_{j=1}^m a_{ji} \ln A_{ji} - A_{ji} \right]. \quad (6.1)$$

For a single bin i in template j , a_{ji} is the observed number of events and A_{ji} is the predicted mean number of events. The total number of events contributed by all templates for a given bin is

$$f_i = \sum_{j=1}^m \frac{A_j^{data}}{A_j^{sim}} F_j A_{ji} \quad (6.2)$$

where A_j^{data} and A_j^{sim} are the total areas, within the fitted region, of the observed spectrum and template j , respectively.

Whereas the $^{17}\text{O}(\text{p},\gamma)^{18}\text{F}$ and $^{22}\text{Ne}(\text{p},\gamma)^{23}\text{Na}$ studies mentioned in the previous section used likelihood maximization to estimate the template fractions, the template fractions in the $^{29}\text{Si}(\text{p},\gamma)^{30}\text{P}$ analysis were found using the Bayesian approach presented by [Dermigny *et al.* \(2016\)](#). The primary advantage of embracing a Bayesian strategy is the ability to derive probability density functions for the template fractions, which can then be used to calculate meaningful uncertainties as well as establish upper limit values when necessary.

In this method, inferences are made using the multivariate joint posterior distribution defined as

$$P(\mathbf{F}|\mathbf{D}) = \frac{P(\mathbf{D}|\mathbf{F}) P(\mathbf{F})}{\int_{\mathbf{F}} P(\mathbf{D}|\mathbf{F}) P(\mathbf{F})} \quad (6.3)$$

where $P(\mathbf{D}|\mathbf{F})$ is the likelihood function given in Equation 6.1 and $P(\mathbf{F})$ is the joint prior probability function. For the latter term, a Jeffreys prior (Jeffreys, 1946),

$$P(\mathbf{F}) = \prod_{j=0}^m \left[\frac{1}{F_j} \right], \quad (6.4)$$

was chosen.

The posterior distributions of individual source fractions were determined using this framework. First, the template fractions F_j were sampled from the joint posterior distribution (Equation 6.3) using a Metropolis-Hastings algorithm (Hastings, 1970). For the $^{29}\text{Si}(\text{p},\gamma)^{30}\text{P}$ analysis presented in this dissertation, 80,000 iterations with a 20,000 sample burn-in period and a thinning interval of 5 were used to minimize autocorrelation in the combined posterior distribution (Hilbe *et al.*, 2017). Template fractions and uncertainties were then determined from the median and 68% highest density interval of the corresponding marginal posterior distributions, respectively. For template distributions with nontrivial density at zero probability, the fractional contribution is reported as an upper limit value defined by a 97.5% coverage interval. This analysis method is illustrated in Figure 6.1 which shows how the fractional contributions from each template combines to reproduce the observed data spectrum.

Of course, the template fractions are not the desired final product of the $^{29}\text{Si}(\text{p},\gamma)^{30}\text{P}$ data analysis. They can however be used to extract the sought-after information: the total number of reactions (\mathcal{N}_R) and primary γ -ray branching ratios (B_j) of the reaction of interest. To find these quantities, first one must use the sampled template fractions to find the number of events that a given template contributes to the measured

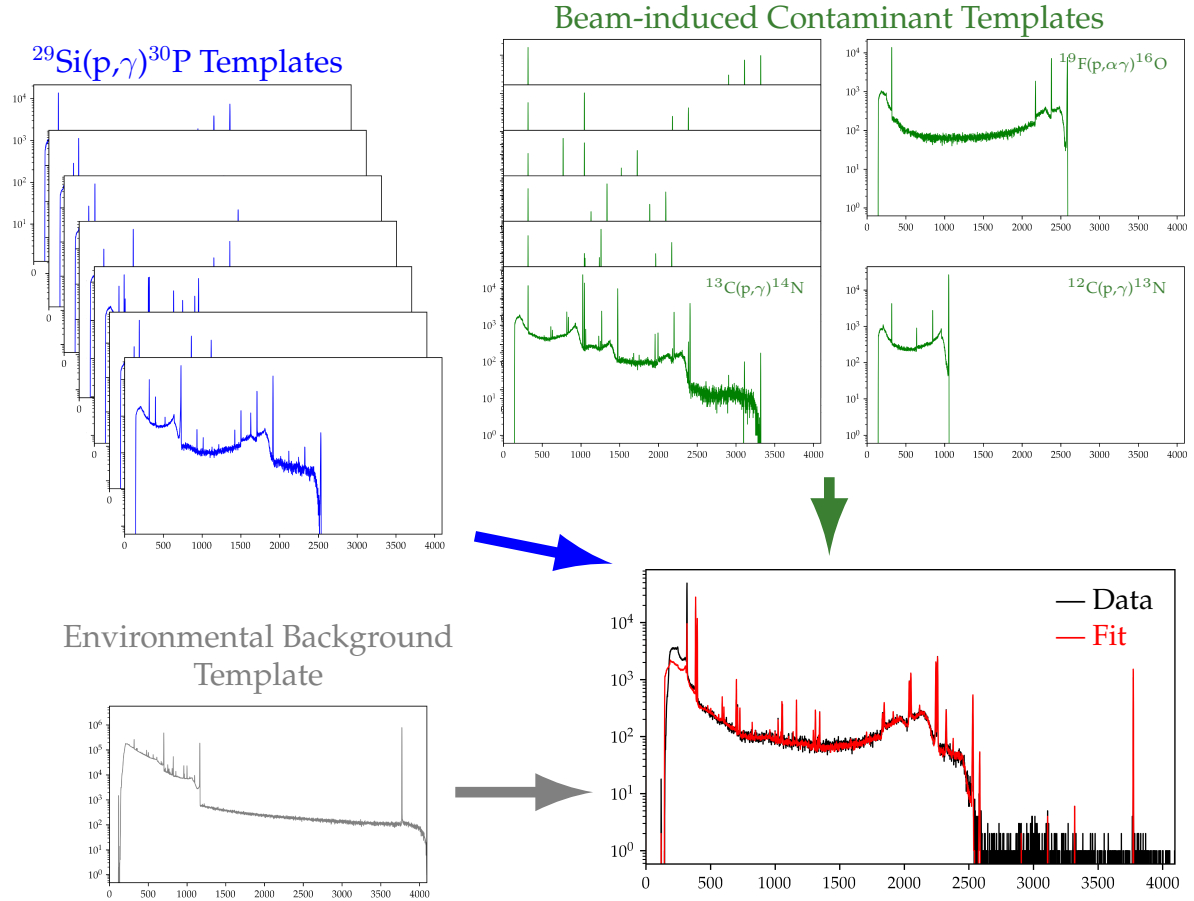


Figure 6.1: Illustration of the fraction fitting data analysis method. An extended binned likelihood function is combined with a detailed GEANT4 model of the LENA detector system to simulate every source of radiation observed in the experimental spectrum. The product of these simulations is two groups of templates: $^{29}\text{Si}(p,\gamma)^{30}\text{P}$ templates (shown in blue) and beam-induced contaminant reactions (green). Additionally, environmental background, measured when no beam is present, is then converted to a template (grey). A Bayesian strategy is used to determine the fractional contribution of each template, and the fractional contributions combine to give an overall fit to the data spectrum. In the bottom right of this figure, the data spectrum (black) and the resulting fit (red) are displayed.

spectrum. This quantity is given by the expression

$$\mathcal{N}_j = \frac{A_j^{data}}{A_j^{sim}} F_j \mathcal{N}_j^{sim} \quad (6.5)$$

where \mathcal{N}_j^{sim} is the simulated number of events used to produce template j . Typically, only one template is generated for each source of contaminant radiation meaning that \mathcal{N}_j is equivalent to the total number of reactions from a particular source. This is not the case for the reaction of interest because we are interested in its primary decay structure, and one template is produced for each purported primary branch as a result. Consequently, the total number of reactions from the reaction of interest, \mathcal{N}_R , is found by summing the number of reactions originating from all relevant templates,

$$\mathcal{N}_R = \sum_j \mathcal{N}_j = \sum_j \frac{A_j^{data}}{A_j^{sim}} F_j \mathcal{N}_j^{sim}. \quad (6.6)$$

As will be shown later, the resonance strength can be derived from the total number of reactions, making this a particularly useful quantity to determine. Lastly, the branching ratio for a given primary transition is then easily found from Equations 6.5–6.6:

$$B_j = \frac{\mathcal{N}_j}{\mathcal{N}_R}. \quad (6.7)$$

The analysis method presented in this chapter, unlike traditional analysis, does not require explicit corrections for various experimental factors such as detector efficiencies and coincidence summing. As will be discussed in the next section, these effects are implicitly included in the GEANT4-simulated templates instead.

6.2 Template Generation

In order to account for the data spectrum accurately, the source of every peak—resonance of interest, beam-induced contaminants, or environmental background—must be identified and then reproduced via simulation. First, recall the deexcitation of a compound nucleus via γ -ray emission during a nuclear reaction. Figure 6.2 (Dermigny *et al.*, 2016) helps illustrate how this can occur. For a theoretical reaction $A(p,\gamma)B$, the deexcitation to the ground state, E_0 , begins at the compound level, E_x , and can occur through a single γ -ray or a complex γ -ray cascade. Transitions originating from the compound level are called primary transitions. If the compound nucleus decays to the ground state via a single γ -ray, the corresponding transition, $E_x \rightarrow E_0$, is often referred to as the ground state transition. All other primary transitions must decay to a secondary state, e.g. E_2 , and emit a γ -ray with a characteristic energy given by the energy difference between levels, $E_x - E_2$ in this example. From here, the decay continues to the ground state, either through one additional transition ($E_2 \rightarrow E_0$) or a γ -ray cascade ($E_2 \rightarrow E_1$ followed by $E_1 \rightarrow E_0$). All γ -rays that originate from a state other than the compound level are known as secondary γ -rays.

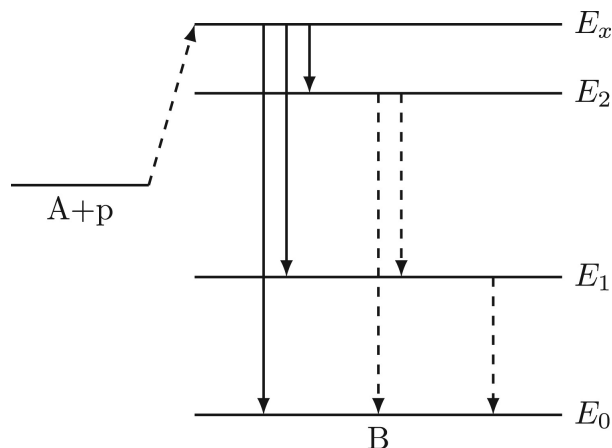


Figure 6.2: The decay scheme of a theoretical reaction, $A(p,\gamma)B$, from Dermigny *et al.* (2016). Primary transitions, originating from the compound state E_x , are shown as solid black lines. Secondary transitions are shown as dashed black lines.

To simulate the deexcitation of compound nuclei via γ -ray emission, a GEANT4 framework, incorporating the precise models of the LENA $\gamma\gamma$ -ray spectrometer (Section 4.3) and target station (Section 4.2) detailed earlier, was employed. For a simulated compound nucleus decay, all γ -rays emerge from the ion beamspot on the nuclear target, and secondary decays are simulated by randomly sampling literature decay branchings. Interactions with the detection system and environment are tracked throughout the simulated event. To account for the number of counts one would see in the experimental spectrum, the energy deposition in the detection system is recorded for every event. This process is repeated many times to simulate a large number of decays, and the resulting simulated data set is processed as it would be in the laboratory. The ultimate result of this process is a template histogram, representing a particular contribution to the observed data, that is directly comparable to the experimentally measured pulse height spectrum.

For the analysis of the reaction of interest—or, more specifically, the resonance of interest—we seek primary branching ratios as well as the overall number of reactions. As a result, a template is generated for each potential primary branch of the reaction, each with an assumed branching ratio of 100%. This allows the fractional contribution from a given template to indicate the primary branching ratio as shown in Equation 6.7.

Template generation for beam-induced reactions is achieved in a similar manner, but the focus is on quantifying the overall contribution each of these reactions makes to the spectrum. Thus, each contaminant reaction is usually accounted for with a single template derived from literature branching ratios because gaining an understanding of its decay structure is unnecessary. In the case of direct capture contaminant reactions such as $^{12}\text{C}(\text{p},\gamma)^{13}\text{N}$, the level energy of the compound nucleus is adjusted as required for the experimental proton bombarding energy.

Radiation from cosmic rays and unstable species in the environment contribute

to the experimental spectrum and must be included in the simulated spectra accordingly. However, the simulation of all sources of environmental background would be a laborious undertaking, and given that this type of background occurs regardless of whether an experiment is being conducted, the simpler approach was to measure the environmental background directly. Environmental background is comparatively weak and can change with meteorological conditions, so background measurements were usually taken on a daily basis after the $^{29}\text{Si}(p,\gamma)^{30}\text{P}$ data acquisition had ended. The resulting data was combined into one data set from which the required template was extracted.

6.2.1 Template Corrections

While simulated templates do an adequate job of reproducing the experimental spectra, there are a few instances in which corrections to the templates are required to account for physics not included in the GEANT4 simulation. These corrections include adjustments to the position of peaks, the overall width and shape of peaks, and the effect of angular correlations.

Peak Position Adjustment

Literature values are used to determine the energies at which γ -ray peaks occur in the spectra, and while these energies are usually known to a high precision, they do not account for other particle kinematics. For example, it can be assumed that γ -decay as a result of radiative capture reactions occurs on a short time scale such that the recoiling compound nucleus does not come to rest before γ -emission ([Iliadis, 2015](#)). The energy of the emitted γ -rays are fully Doppler shifted, but the GEANT4 simulation does not account for this effect. However, this usually results in an energy shift of only a few keV and can be easily adjusted without altering the bins surrounding the

affected peak.

Peak Width Adjustment

Template peak widths also require adjustment. These adjustments can require global or local adjustments to the templates.

First, it should be noted that the HPGe detector has a finite, energy-dependent energy resolution. It has a broadening effect on all peaks in a measured spectrum (for an example, see Figure 4.10), so this effect must be reproduced in the simulated templates as well. To achieve this, each raw simulated spectrum is convolved with a Gaussian function of width $\sigma(E)$. This width is found by measuring the FWHM of environmental and secondary transition full-energy peaks across a large energy range. Both of these types of peaks should be free of kinematic effects (e.g. Doppler shifts) that would impact peak widths. The energy resolution of the HPGe is roughly linear, so σ for a given peak is

$$\sigma(E) = \frac{\text{FWHM}}{2\sqrt{2\ln 2}} \approx \frac{\text{FWHM}}{2.35} \quad (6.8)$$

(Knoll, 2010). From the measured values of σ for a variety of peaks, the linear $\sigma(E)$ function can be found and the entirety of the simulated spectra broadened accordingly.

Two situations exist in which templates would require broadening local to particular peaks. First, additional adjustment is occasionally required to account for Doppler broadening in full-energy primary transition peaks. This effect results in both broadening of the peak and the appearance of a tail on the low-energy side of the peak. To produce these effects in the required peaks, the γ -ray peak fitting algorithm developed by MacMullin (2015), which allows for both peak broadening and a low-energy tail, was applied.

Additionally, the width of peaks produced by direct capture are often dependent on the target thickness which is not included in the GEANT4 simulation. Thus, any broadening of direct capture peaks seen in the data spectrum must be applied to the appropriate templates as well.

Angular Correlations

Sometimes, two radiations are angularly correlated because of the alignment of a particular nuclear level. This coupling can occur between two consecutive, outgoing γ -rays, but for the purposes of this work, the coupling of the incident radiation (in this case, proton bombardment) and primary transition γ -rays is of interest. In this scenario, the aligned nuclear level is populated unequally so that the subsequent decay of this level will result in an anisotropic γ -ray emission, or angular correlation. The angular distribution of the γ -ray emission is described by the angular correlation factor,

$$W(\theta) \approx 1 + a_2 P_2(\cos \theta) + a_4 P_4(\cos \theta). \quad (6.9)$$

In this expression, θ refers to the emission angle with respect to the incident beam direction in the center-of-mass frame, P_2 and P_4 are Legendre polynomials, and a_2 and a_4 are angular correlation coefficients of the second and fourth orders, respectively. For $^{29}\text{Si}(p,\gamma)^{30}\text{P}$ primary transitions where published angular correlation coefficients were available, the primary transition γ -ray distribution was simulated with a weighted probability for emittance given by

$$P(\Omega)d\Omega = W(\theta)d\Omega \quad (6.10)$$

where $d\Omega$ is the solid angle ([Iliadis, 2015](#)).

6.3 Goodness of Fit Test

While the fraction fitting method of analyzing spectral data is a powerful technique, the statistical nature of the data makes ascertaining the goodness of fit rather challenging. The likelihood function given in Equation 6.1 assumes that the data and simulated templates obey Poisson statistics, and while this is generally true, any deviation from this statistical model, such as overdispersion, precipitates a disproportionately large effect in most goodness-of-fit measures.

This effect has been studied in detail by [Dermigny \(2018\)](#) for the fraction fitting of $^{30}\text{Si}(p,\gamma)^{31}\text{P}$ data. For their work, they tested three likelihood models—the Poisson likelihood function, the negative binomial likelihood function, and the scaled Poisson likelihood function—for their suitability in describing the relatively large statistical fluctuations seen in high count areas of the data spectrum. Using a toy model and calculating the reduced likelihood ratio for each likelihood function, they found that the negative binomial and scaled Poisson models best fit the overdispersed data. If one recalls that the ultimate product of a fractionally fit data spectrum is a collection of template fractions which sum to unity, it is clear that the outcome of the data analysis would not be affected by the scaling required by the adoption of the scaled Poisson likelihood function. Therefore, this likelihood model was chosen for the $^{29}\text{Si}(p,\gamma)^{30}\text{P}$ study presented in this dissertation.

While used to evaluate the three likelihood models described above, the likelihood ratio test is somewhat incomplete in that it assesses the adequacy of a fit based solely on the magnitude of deviations between the data and the fit. One can imagine a scenario in which data exhibits a number of changes in direction such as in an oscillating function. If these oscillations are relatively small in amplitude and the data is naively fit with a linear function, the likelihood ratio test, based solely on the magnitude of the deviation between the data and the fit, would indicate a good fit and miss the

larger trend (for illustration, see Figure 5.4 in [Dermigny, 2018](#)).

On the other hand, the run test evaluates fit based on the sign of the discrepancies between the data and fit and serves as an excellent complement to the likelihood ratio test ([Bradley, 1968](#); [James, 2006](#)). A run is defined as a sequence of deviations between the data and the fit of the same sign. A new run begins when the sign of the deviation changes. As one might expect, the total number of runs in a data set is given by

$$N \equiv N_+ + N_- \quad (6.11)$$

where N_+ and N_- are the number of positive and negative deviation runs, respectively. The expected number of runs, $\langle r \rangle$, is

$$\langle r \rangle = 1 + \frac{2N_+N_-}{N} \quad (6.12)$$

with a variance of

$$V[r] = \frac{2N_+N_-(2N_+N_- - N)}{N^2(N - 1)} \quad (6.13)$$

([James, 2006](#)). The test statistic, Z , is then derived from these two parameters to find

$$Z = \frac{r - \langle r \rangle}{\sigma} \quad (6.14)$$

where r is the observed number of runs in a data set and σ is the standard deviation of r ([NIS, 2002](#)).

To assess the success or failure of a given fit to the experimental data, a hypothesis test was carried out. In this type of test, the null hypothesis, H_0 , is tested against some alternative hypothesis, H_1 . In the case of fraction fitting, the null hypothesis is that the run test indicates that the probability distribution of the data is adequately produced by the fraction fit and that any deviations between the data and the fit can be

ascribed to random statistical fluctuations. The alternative hypothesis supposes that these fluctuations are not random, meaning that the fraction fit does not adequately represent the data.

Based on the deviations between the data and the fit, the test statistic was calculated. It should be noted that the fit was evaluated on a bin-by-bin basis, and for large-sample run tests such as these, the value of the test statistic (Equation 6.14) can be compared to a standard normal table to determine if the null hypothesis is accepted or rejected within the desired confidence level, α . As an example, consider a test statistic value of $Z = -1.645$ for a single-tailed test. When compared to a standard normal table, this value indicates that discrepancies between the data and the fit can be considered random to a significance level of 5%.

6.4 Summary

In this chapter, the fraction fitting method for the analysis of the $^{29}\text{Si}(\text{p},\gamma)^{30}\text{P}$ spectra data was presented. This method has a number of advantages over the more traditional “peak-by-peak” approach and has been used successfully in studies similar to the present work (Buckner *et al.*, 2015; Kelly *et al.*, 2017).

In the presented method, the extended binned likelihood approach was combined with a detailed GEANT4 simulation of the experimental setup to produce Monte-Carlo simulated templates for every source of radiation present in the data. Each template was generated with the same time and energy gating as the experimental data and spanned the full length of the data spectrum. Unlike the traditional approach, this analysis method did not require any explicit corrections to the templates or fit to account for experimental factors such as detector efficiency and coincidence summing, but occasionally templates required adjustments after their generation in order to represent physics not included in the GEANT4 simulation. To determine what fraction

each template contributes to the experimental spectrum, a Bayesian strategy, which produced probability density functions for each template fraction, was employed. Relevant experimental information such as the branching ratios and number of reactions from the resonance of interest were derived from the fit. Crucially, the fraction probability density functions allowed for statistically meaningful upper limit values to be extracted from the fit where necessary, and it will be shown that this aspect greatly impacts the analysis of the $E_r^{lab} = 221$ keV resonance in the current $^{29}\text{Si}(p,\gamma)^{30}\text{P}$ study (Section 7.4). Finally, the validity of each fit was then accessed using a run test and the significance level formalism.

In the next chapter, this methodology will be applied for the analysis of the $E_r^{lab} = 221$ keV, 314 keV, 324 keV, and 416 keV resonances in $^{29}\text{Si}(p,\gamma)^{30}\text{P}$.

CHAPTER 7: $^{29}\text{Si}(\text{p},\gamma)^{30}\text{P}$ PROTON CAPTURE

The earliest notable work on the $^{29}\text{Si}(\text{p},\gamma)^{30}\text{P}$ reaction was undertaken by [Endt *et al.* \(1954\)](#) over 65 years ago. Their farsighted interest was sparked by the intriguing properties of self-conjugate odd-odd nuclei such as ^{30}P . For their work, targets, prepared by magnetically separating $^{29}\text{SiO}_2$ and evaporating the material onto a 0.5 mm copper backing, were bombarded with a 6 μA proton current produced using a 700 keV Cockroft-Walton generator. The gamma-ray cascades of the (p,γ) resonances at $E_r^{\text{lab}} = 324$ keV and $E_r^{\text{lab}} = 416$ keV were observed using a NaI(Tl) detector, and this data was used a short number of years later to derive a variety of useful information about $^{29}\text{Si}(\text{p},\gamma)^{30}\text{P}$ with a focus on properties of the first excited state in the ^{30}P nucleus. [Broude *et al.* \(1956a\)](#) used the $^{29}\text{Si}(\text{p},\gamma)^{30}\text{P}$ reaction to find five additional levels in the ^{30}P nucleus. While both of these studies were direct measurements of the $^{29}\text{Si}(\text{p},\gamma)^{30}\text{P}$ reaction, perhaps some of the most significant advances were made by [Endt and Paris \(1958\)](#) using the $^{32}\text{S}(d,\alpha)^{30}\text{P}$ reaction. This group added substantially to the field of knowledge by mapping an impressive 26 new levels in ^{30}P and discovering that the first excited state in this nucleus was in fact a doublet.

This flurry of work continued for over three decades (see, for example, [Harris and Hyder, 1966](#); [Kennedy *et al.*, 1967](#); [Vermette *et al.*, 1968](#); [Harris *et al.*, 1969](#); [Din, 1970](#); [Poirier *et al.*, 1970](#)), culminating in the work presented in [Riihonen *et al.* \(1979\)](#). By this time, the $E_r^{\text{lab}} = 416$ keV resonance in $^{29}\text{Si}(\text{p},\gamma)^{30}\text{P}$ was already in frequent use as a standard for other resonance measurements, despite significant discrepancies among previous absolute strength measurements of this resonance. Thus, [Riihonen *et al.* \(1979\)](#) focussed on carefully determining absolute resonance strengths for

Table 7.1. Summary of $^{29}\text{Si}(\text{p},\gamma)^{30}\text{P}$ Resonance Data Collection

Property	Resonance (E_r^{lab} in keV)			
	416	324	314	221
Bombarding Energy (keV)	417	327	317	227
Accumulated Charge (C)	0.005217	2.2745	4.7043	9.97289
Average Beam Intensity (μA)	1.9	40.4	51.2	637.4 ^a
Running Time (s)	2716	56352	91917	15647
Average Dead Time (%)	2.5	4.2	1.0	1.2

^aPulsed proton beam was used for this resonance measurement, but the value given here represents the proton current averaged over the entire length of the experiment. See Section 7.4.1 for details.

the $^{28-30}\text{Si}(\text{p},\gamma)^{29-31}\text{P}$ reactions by comparison to the well-known $E_r^{lab} = 992$ keV resonance in $^{27}\text{Al}(\text{p},\gamma)^{28}\text{Si}$. Their work also included several improvements over previous experiments including the use of a Ge(Li) detector, updated γ -ray intensity standards, and improved proton stopping powers. This work formed a solid foundation upon which other $^{29}\text{Si}(\text{p},\gamma)^{30}\text{P}$ resonance strengths could be determined with confidence.

All told, $^{29}\text{Si}(\text{p},\gamma)^{30}\text{P}$ resonance strengths, decay schemes, and spin-parity assignments of over 50 resonances in the proton bombarding energy range of 0.32–3.3 MeV have been determined. The atomic reaction Q-value, $Q = 5594.75 \pm 0.07$ keV, is known precisely thanks to the work of Wang *et al.* (2017). Indirect studies, like the ones mentioned above, mapped the ^{30}P nucleus, resulting in the energy level diagram and spin-parity assignments summarized in Figure 7.1. The known resonances, level structure, decay of bound states, spin-parities, and more are comprehensively presented in Endt (1990), Endt (1998), and Grossmann *et al.* (2000).

This is not to say that no open questions about $^{29}\text{Si}(\text{p},\gamma)^{30}\text{P}$ remain, particularly concerning low-energy resonances. For one, while the lowest energy resonance studied (excluding the work presented in this dissertation), $E_r^{lab} = 324$ keV, was measured

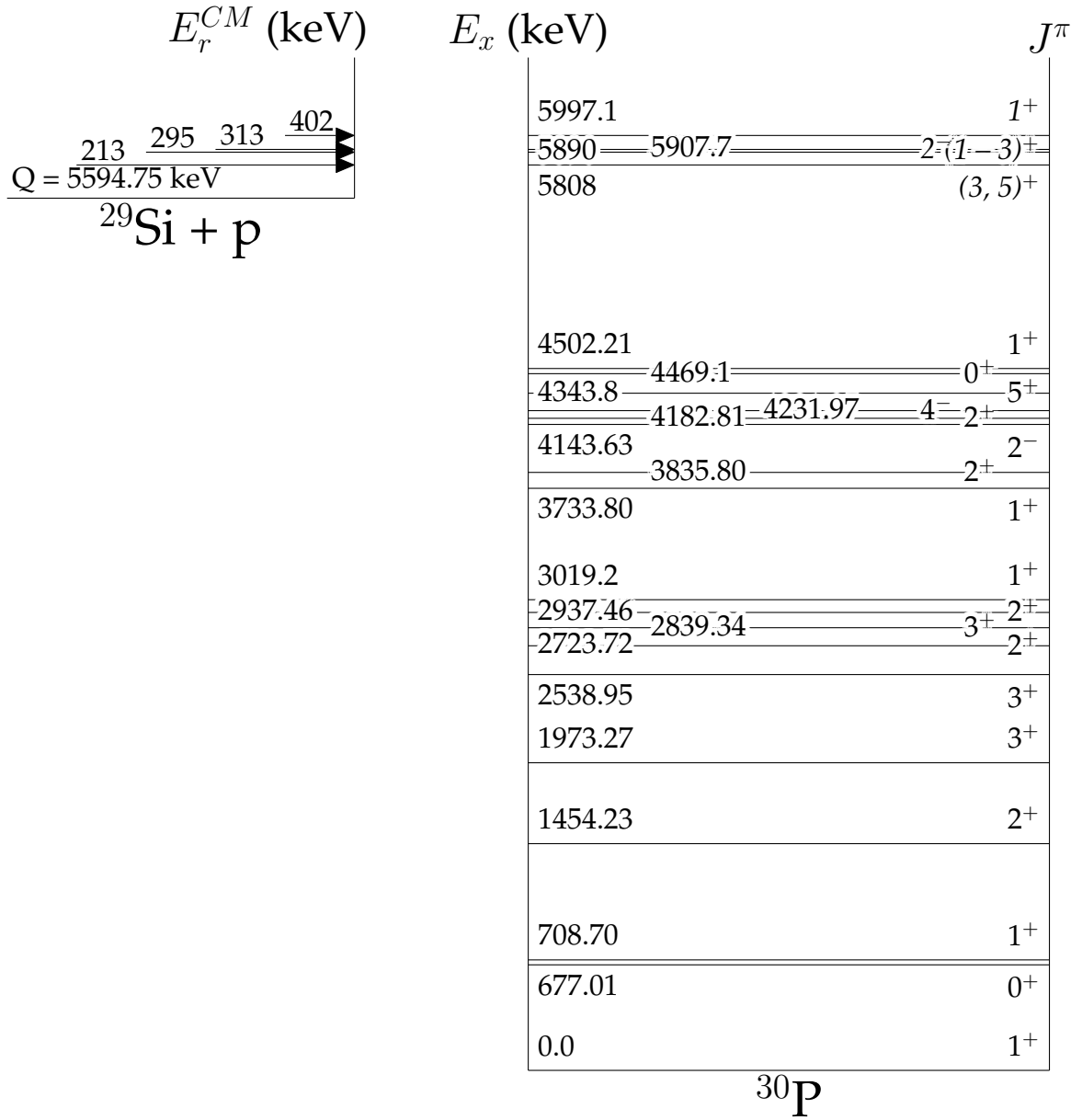


Figure 7.1: Energy level diagram for ^{30}P with an emphasis on the $^{29}\text{Si}(\text{p},\gamma)^{30}\text{P}$ resonances of interest. Some levels have been omitted for clarity. All level energies are given by [Grossmann *et al.* \(2000\)](#). All spin-parities adopted from [Endt \(1998\)](#). Resonant level spin-parities have been restricted to the italicized values. The atomic Q-value is given by [Wang *et al.* \(2017\)](#).

Table 7.2. Systematic Uncertainties of the $^{29}\text{Si}(\text{p},\gamma)^{30}\text{P}$ Resonance Study

Source	Uncertainty (%)
GEANT4 ¹	1.3
Charge integration ²	3.0
Stopping Powers ³	5.0
Detector Geometry	5.0

References. — ¹Howard *et al.* (2013); ²Buckner (2014) and references therein; ³Ziegler *et al.* (2015)

by Reinecke *et al.* (1985) and others, their resonance strength determinations include significant ($\sim 30\%$) uncertainties, limited agreement with one another, and reliance on different $E_r^{\text{lab}} = 416$ keV resonance strength standards. Reinecke *et al.* (1985) provides a fairly detailed decay scheme for the 324 keV resonance but neglected to give uncertainties for their primary branching ratios. The two lowest potential resonances explored in this dissertation, $E_r^{\text{lab}} = 314$ keV and 221 keV, have not measured previously, so our knowledge is limited to the compound state energies and theoretical upper limits to the resonance strengths. Furthermore, the compound state spin-parity assignments of the resonances studied here are tentative at best.

Consequently, the study of the $E_r^{\text{lab}} = 416$ keV, 324 keV, 314 keV, and 221 keV resonances in $^{29}\text{Si}(\text{p},\gamma)^{30}\text{P}$ was undertaken at LENA and will be presented in this chapter. Table 7.1 summarizes the data collection for each of the four resonances studied for this dissertation, and Table 7.2 detailed the systematic uncertainties involved in the measurements and subsequent calculations. Measurement and analysis techniques are comprehensively presented for each measurement. The efforts to benchmark the $E_r^{\text{lab}} = 416$ keV resonance, which was used as a standard for the following measurements, are described in Section 7.1. The study of the remaining three resonances— $E_r^{\text{lab}} = 324$ keV, 314 keV, and 221 keV—is reported in Sections 7.2, 7.3, and 7.4, respectively.

7.1 416 keV Resonance

Because the ^{30}P nucleus garnered interest in the early 1950s, a fair amount of work has gone into studying it, and, by extension, reactions involving this nucleus in the intervening years. Many of these efforts were directed at finding new levels in ^{30}P , but several experiments focussed on mapping the resonances in $^{29}\text{Si}(\text{p},\gamma)^{30}\text{P}$ as well. In order to understand the importance of these resonances to the overall $^{29}\text{Si}(\text{p},\gamma)^{30}\text{P}$ reaction rate, absolute resonance strengths needed to be determined. The $E_r^{\text{lab}} = 416$ keV resonance was identified early on as a convenient standard to compare to other $^{29}\text{Si}(\text{p},\gamma)^{30}\text{P}$ resonance strengths. Thus, several absolute strength measurements, summarized in Table 7.3, have concentrated on this resonance.

The first absolute resonance strength was reported by [van der Leun and Endt \(1958\)](#), only a few short years after the first explorations of the ^{30}P nucleus. In this work, a 10 μA proton beam, produced by a 800-keV Cockcroft-Walton generator, was used to bombard a $^{29}\text{SiO}_2$ target. Two NaI(Tl) detectors, oriented at 0° , 55° , or 90° from the proton beam, were used to determine the thick-target yield on resonance, decay scheme, and γ -ray anisotropies. These parameters were then used to calculate the number of γ -rays decaying from the resonant level per incident proton, a quantity proportional to the resonance strength, $\omega\gamma$. It must be noted that [van der Leun and Endt \(1958\)](#) also presents the measurements discussed in [Broude *et al.* \(1956b\)](#), but these results do not appear to be otherwise published.

Several years later, [Engelbertink and Endt \(1966\)](#) remeasured this resonance strength, and while they used the same type of accelerator as and a similar detector to [van der Leun and Endt \(1958\)](#), their targetry methods were quite different. They measured resonances in several (p,γ) reactions and, as a result, chose to produce evaporated targets of 17 different chemical compounds of natural isotropic composition. For

Table 7.3. $^{29}\text{Si}(\text{p},\gamma)^{30}\text{P}$ $E_r^{lab} = 416$ keV Resonance Strength Measurements

Reference	Resonance Strength, $\omega\gamma$ (eV)
Broude <i>et al.</i> (1956b)	0.0575 ^a
van der Leun and Endt (1958)	0.0585 ± 0.015
Engelbertink and Endt (1966)	0.175 ± 0.025^b
Riihonen <i>et al.</i> (1979)	0.26 ± 0.025
Present (adopted)	0.244 ± 0.038^c

Note. — Literature values for the $E_r^{lab} = 416$ keV resonance strength. The adopted value in the present work is adapted from the strength determined by [Riihonen *et al.* \(1979\)](#).

^aAs reported by [van der Leun and Endt \(1958\)](#).

^bCorrected with $\omega\gamma = 1.55 \pm 0.13$ eV for $E_r^{lab} = 620$ keV in $^{30}\text{Si}(\text{p},\gamma)^{31}\text{P}$ ([Smith and Endt, 1958](#)).

^cCorrected for recent stopping power adjustments ([Ziegler *et al.*, 2015](#)) and an adjustment to the strength of the $E_r^{lab} = 992$ keV resonance in $^{27}\text{Al}(\text{p},\gamma)^{28}\text{Si}$ recommended by [Iliadis *et al.* \(2010a\)](#).

their measured $^{29}\text{Si}(\text{p},\gamma)^{30}\text{P}$ resonances, natural silicon metal and sodium metasilicate (Na_2SiO_3) targets were used, though in the case of Na_2SiO_3 , evaporation was an unsuitable method for target preparation, and the target was produced by painting a thin layer of the powdered compound onto a target backing. They were able to measure relative resonance strength ratios between multiple species of different elements as well as between isotopes of the same element. All relative strength measurements were converted to absolute strengths using the $^{30}\text{Si}(\text{p},\gamma)^{31}\text{P}$ $E_r^{lab} = 620$ keV resonance strength determined by [Smith and Endt \(1958\)](#).

The most recent measurement of the $^{29}\text{Si}(\text{p},\gamma)^{30}\text{P}$ $E_r^{lab} = 416$ keV absolute resonance strength, and the one adopted for this dissertation, was performed by [Riihonen *et al.* \(1979\)](#). They noted that measurements of the $^{30}\text{Si}(\text{p},\gamma)^{31}\text{P}$ $E_r^{lab} = 620$ keV resonance strength ([Hough *et al.*, 1968](#); [Lyons *et al.*, 1969](#)) undertaken after that of [Smith](#)

and Endt (1958) produced significantly different values. These discrepancies led to a 30% variation in stellar reaction rates of hydrogen burning depending on which resonance strength was used. Their goal was to precisely remeasure the relative strengths of frequently used standard resonances in $^{28-30}\text{Si}(p,\gamma)^{29-31}\text{P}$ and convert the relative strengths to absolute strengths using the well-known $^{27}\text{Al}(p,\gamma)^{28}\text{Si}$ $E_r^{lab} = 992$ keV absolute resonance strength. Their work also benefited from access to a large volume Ge(Li) detector, updated γ -ray intensity standards, and improved proton stopping power values. This new result, $\omega\gamma = 0.26 \pm 0.025$ eV (or, in the form of an absolute strength as given in the publication, $S = (1 + \delta_{01})\omega\gamma / (2j_0 + 1)(2j_1 + 1) = 1.04 \pm 0.10$ eV), is a factor of 1.5 larger than the Engelbertink and Endt (1966) result; however, this discrepancy could easily be explained by the use of $E_r^{lab} = 620$ keV $^{30}\text{Si}(p,\gamma)^{31}\text{P}$ absolute resonance strength from Smith and Endt (1958). As a result of their careful considerations, the Riihonen *et al.* (1979) $^{29}\text{Si}(p,\gamma)^{30}\text{P}$ $E_r^{lab} = 416$ keV resonance strength value was universally adopted as the standard. A few updates to stopping power evaluations (Ziegler *et al.*, 2015) and the recommended strength of the $E_r^{lab} = 992$ keV $^{27}\text{Al}(p,\gamma)^{28}\text{Si}$ resonance have been made since this measurement, and the present work adopts the Riihonen *et al.* (1979) value with these corrections applied accordingly (see Table 7.3).

The $E_r^{lab} = 416$ keV resonance is a superb choice for a standard on several fronts. As detailed above, the meticulous work of Riihonen *et al.* (1979) in determining the strength of this resonance allows one to make measurements relative to this resonance with confidence. The state at $E_r^{lab} = 416$ keV is also a strong resonance, meaning that a minimum of accumulated charge and beam time is required to check target degradation using it. It is also somewhat isolated in energy from other $^{29}\text{Si}(p,\gamma)^{30}\text{P}$ resonances. Because this resonance has been studied many times, its decay structure is well known also (see, for example, Harris *et al.*, 1969; Riihonen *et al.*, 1979; Reinecke *et al.*, 1985). Perhaps the only drawback of using the $E_r^{lab} = 416$ keV state for this purpose lies in

the uncertainty of its spin-parity assignment. The work of [Ramstein *et al.* \(1981\)](#) found that this resonant state is in fact a doublet of two states with opposite parities. The angular distribution measurements performed by [Reinecke *et al.* \(1985\)](#) determined that the resonant state has spin $J = 1$, but because of the presence of the doublet, they cannot conclude that the state they measured is the same as that measured by various indirect studies (see, for example, [Dykoski and Dehnhard, 1976](#), which assigned a negative parity to the state they measured). Finally, [Grossmann *et al.* \(2000\)](#) used the results of their exhaustive study of the ^{30}P nucleus and the empirical, recommended upper limit (RUL) method to assign the resonant state a spin-parity of $J^\pi = 1^+$ (see [Endt, 1993](#)). All of this is to say that numerous efforts have culminated in a wealth of knowledge regarding the $E_r^{lab} = 416$ keV resonance in $^{29}\text{Si}(p,\gamma)^{30}\text{P}$, making it an ideal standard on which to base the measurements of this dissertation.

7.1.1 Measurement

Because this resonance has been well studied and its strength is known to a high accuracy, the goal of its measurement becomes the establishment of a benchmark by which other resonance strengths can be determined. This is accomplished by finding the maximum yield of the standard resonance and then using it to determine the stoichiometry of the target.

An initial yield curve was taken (as described in Section 5.2) to determine the energy at which the maximum yield occurs. A low-intensity, 417 keV proton beam was generated with the LENA I JN Van de Graaff accelerator (Section 4.1.1) and used to bombard the ^{29}Si implanted target. The proton beam was rastered over the target surface to minimize the effects of any local target irregularities and prevent inhomogeneous degradation of the target. The $\gamma\gamma$ -coincidence spectrometer (Section 4.3) was positioned in close geometry to the target chamber to optimize detection of the decay. Given the strength of the resonance and the proximity of the detection apparatus, the

HPGe detector dead time required close monitoring and was kept to less than 5% during data acquisition. The ^{29}Si target used in this project proved extraordinarily robust, and no loss of target material was observed during the course of this measurement, meaning the yield was unchanged over the course of data acquisition. The data collection of this resonance measurement is summarized in Table 7.1. A small amount of off-resonance data, roughly 10 keV below E_p , was also accumulated in order to facilitate the identification of contaminant peaks in the on-resonance spectrum.

The data acquired by the detection apparatus—the HPGe, the NaI(Tl) annulus, and the muon veto panels—was sorted into pulse height spectra by the data acquisition software JAM (Swartz *et al.*, 2001). No corrections or gating of any kind were applied to the singles spectrum. The coincidence spectrum, however, was produced with the following energy condition:

$$4.0 \text{ MeV} \leq E^{\text{HPGe}} + E^{\text{NaI}} \leq 6.5 \text{ MeV}. \quad (7.1)$$

This condition allows for the efficient observation of decays from the compound state located at $5997.1 \pm 0.8 \text{ keV}$ (Grossmann *et al.*, 2000), while minimizing the effect of environmental and beam-induced background sources. Additionally, all events coincident with the muon-veto panels were disregarded. These spectra are displayed in Figure 7.2, where the singles spectrum is shown in black and the coincidence spectrum in red. Full-energy primary peaks are indicated by arrows and labels of the form $R \rightarrow E_f$, where R is the resonant state and E_f is the energy of the bound state to which the compound state decays. The escape peaks of the primary transitions are also indicated when they are easily identified in the spectra. As can be seen in this figure, all primary transitions reported by the most recent measurement (Reinecke *et al.*, 1985) were observed in this work.

The background-subtracted, full-energy primary peak energies and intensities for

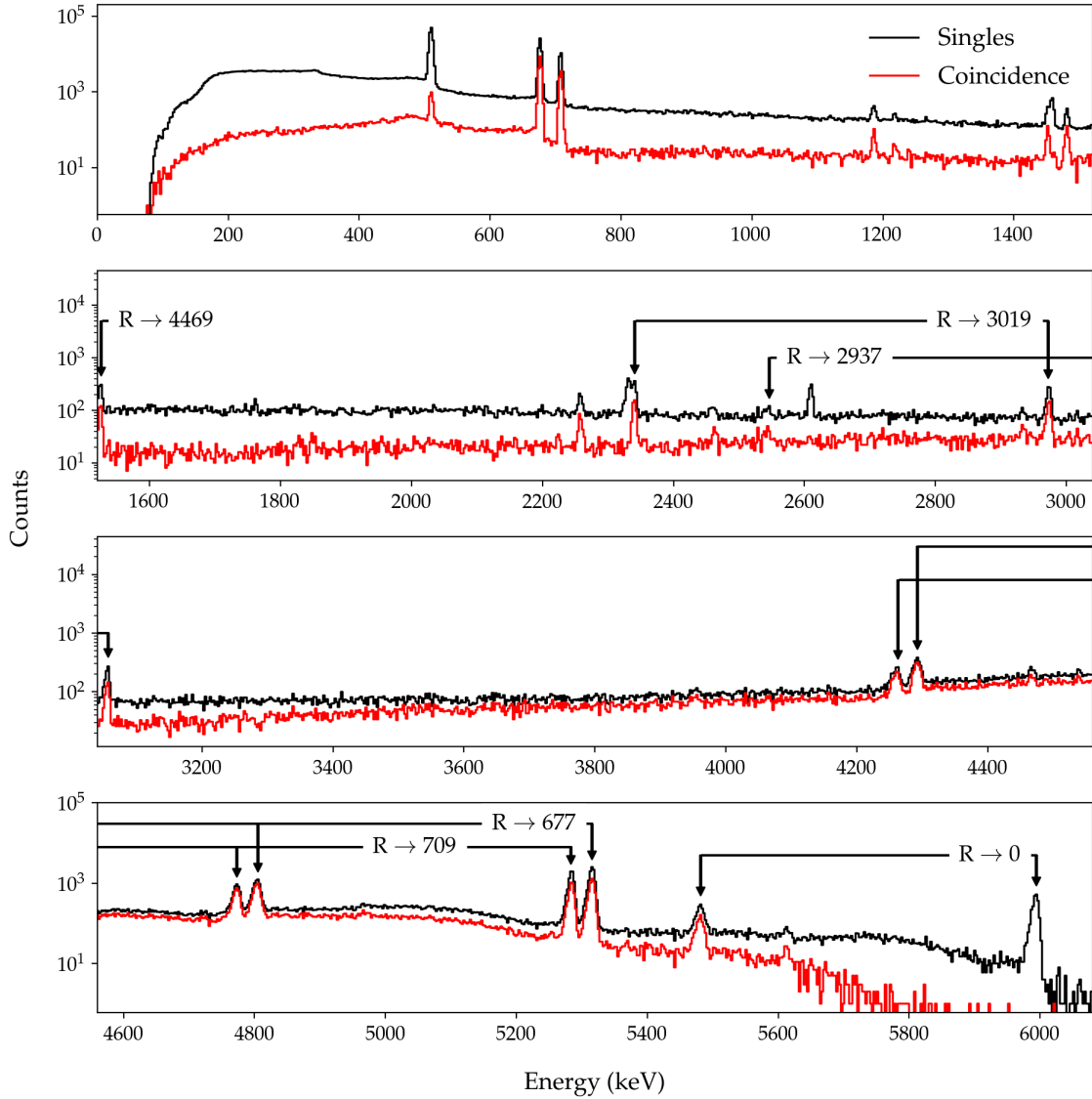


Figure 7.2: HPGe singles and $\gamma\gamma$ -coincidence pulse-height spectra of the $^{29}\text{Si}(p,\gamma)^{30}\text{P}$ $E_r^{\text{lab}} = 416$ keV resonance. The singles spectrum is shown in black, while the coincidence spectrum is shown in red. The full-energy primary peaks are denoted by labeled arrows of the form $R \rightarrow E_f$, where R is the resonant state and E_f is the bound state to which the compound state decays. Prominent escape peaks of primary transitions are similarly indicated where they are clearly visible in the spectra.

Table 7.4. Energies & Decay Intensities for the $E_r^{lab} = 416$ keV Resonance

Primary Transition	J^π	E_γ (keV)	Intensity	
			Singles	Coincidence
$R \rightarrow 4469.1$	0^+	1528.55 ± 1.56	527 ± 45	260 ± 22
$R \rightarrow 3019.2$	1^+	2977.24 ± 1.85	600 ± 49	343 ± 33
$R \rightarrow 2937.46$	2^+	3059.50 ± 1.99	607 ± 46	353 ± 31
$R \rightarrow 1454.23^a$	2^+	...	< 54	< 47
$R \rightarrow 708.70$	1^+	5290.18 ± 1.48	7699 ± 100	4005 ± 72
$R \rightarrow 677.01$	0^+	5321.53 ± 1.47	10239 ± 112	5321 ± 80
$R \rightarrow 0$	1^+	5999.56 ± 1.39	2189 ± 49	664 ± 35

Note. — The resonant state has been assigned a spin and tentative parity of 1^+ (see discussion in [Reinecke *et al.*, 1985](#); [Grossmann *et al.*, 2000](#)). For all other spin-parity assignments, see [Endt \(1998\)](#). Presented intensities are based on 5217 μC accumulated on target. Coincidence intensities are determined using a 4.0 - 6.5 MeV coincidence gate where the reported $R \rightarrow 0$ keV intensity corresponds to the single-escape peak intensity for this transition. No observed energies are presented for transitions with upper limit intensities.

^aThe measured peak intensities for this primary transition should be considered upper limit values, estimated as $\sqrt{2 \times \text{BG}}$, where BG indicates the number of background counts in the region of interest.

the singles and coincidence spectra are given in Table 7.4. No correction for coincidence summing effects was applied to the presented intensities. Also note that while the weak primary $R \rightarrow 1454$ keV was observed by [Reinecke *et al.* \(1985\)](#), the decay to this level could not be determined unambiguously in this work, and its intensity is presented as an upper limit value as a result.

7.1.2 Analysis

The benefits of using the $E_r^{lab} = 416$ keV resonance as a standard also make its analysis straightforward and an excellent illustrative example of the analysis method used for all other resonances of interest in this work. Technical aspects of the analysis

methodology were addressed in Chapter 6 and will not be repeated here. However, a presentation of methodology is perhaps not the optimal way to elucidate the steps required over the course of analysis. Instead, this section presents a “roadmap” of sorts describing the individual steps taken on the path to ascertain the partial reaction numbers, branching ratios, and, ultimately, the resonance strength.

First, aspects of the expected decay were simulated. This was accomplished by synthesizing previous research into input for LENAGE, the GEANT4 simulation of the $\gamma\gamma$ -coincidence detection system. Individual templates were generated for each $^{29}\text{Si}(p,\gamma)^{30}\text{P}$ primary transition observed in Reinecke *et al.* (1985). Angular correlation coefficients given by Riihonen *et al.* (1979) were used to simulate the primary transitions where available. Literature bound state branching ratios, presented in Table A.1, were used to simulate the secondary decays. Beam-induced contaminant sources— $^{11}\text{B}(p,\gamma)^{12}\text{C}$, $^{12}\text{C}(p,\gamma)^{13}\text{N}$, $^{13}\text{C}(p,\gamma)^{14}\text{N}$, and $^{19}\text{F}(p,\alpha\gamma)^{16}\text{O}$ —were modeled as templates in a similar manner. Ambient background sources present a number of simulation challenges, however, so the same approach was not directly applicable. As a result, the ambient background template was measured directly using the detection apparatus in running geometry when no beam-induced sources of radiation were present. The resulting full-spectrum templates were then abridged so as to only include the channels containing the primary transitions (or prominent signature peaks, in the case of contaminant templates). The $^{29}\text{Si}(p,\gamma)^{30}\text{P}$ ground-state primary peak is not visible in the coincidence spectrum; as a result, the single-escape peak of this transition is included in the coincidence fit instead.

These templates were then used to fit the data with the techniques described in Chapter 6. Essentially, the contribution of each template (both resonance of interest and background sources) to the total spectrum is varied until a high confidence fit is achieved. The fit is determined using the PYTHON package `pymc` (Patil *et al.*, 2010). This software combines Markov Chain Monte Carlo (MCMC) sampling with

the Metropolis-Hastings algorithm to establish the combined posterior distribution of the model. The combined posterior distribution is composed of the posterior distributions of the individual templates. In total, 80,000 iterations were performed. This includes a 20,000 sample burn-in period that excludes preconvergence samples from the fit. A thinning interval of 5 was also used in order to minimize autocorrelation in the combined posterior distribution (Hilbe *et al.*, 2017). Template posterior distributions and data projections were produced using the PYTHON package `corner` (Foreman-Mackey, 2016). The resulting fit provides the fractional contribution of each template to the overall spectrum. From this information, the partial number of reactions, branching ratios, and eventually, the resonance strength can be derived.

The template posterior distributions and data projections of the singles fit are shown in Figure 7.3. Each template posterior distribution is labeled according to which primary branch of the $E_r^{lab} = 416$ keV resonance it represents. The 16th, 50th, and 84th percentiles are indicated by the dashed lines on each posterior distribution. Note that the Gaussian shape of the posteriors indicates that the spectrum fit converged on a solution. The $R \rightarrow 1454$ keV primary branch fraction was treated as an upper limit value (see later discussion) as indicated by the \dagger superscript.

Figure 7.4 displays a second method of visualizing the fit. The measured pulse-height spectrum is shown in black. The median fractional contribution of each template was used to determine the simulated pulse-height spectrum of each template. The sum of these pulse-height spectra are shown as the red “fit” line in this figure. The dotted lines indicate breaks in the pulse-height spectrum, since featureless sections of the spectrum were not included in the fit. These excluded regions sometimes result in sharp boundaries between the included (displayed) regions of the spectrum. The source of the spectral peaks— $^{29}\text{Si}(p,\gamma)^{30}\text{P}$, contaminant reactions, or environmental background—is marked on the figure with labeled arrows. As in Figure 7.3, $^{29}\text{Si}(p,\gamma)^{30}\text{P}$ branches treated as upper limits are indicated by a superscripted

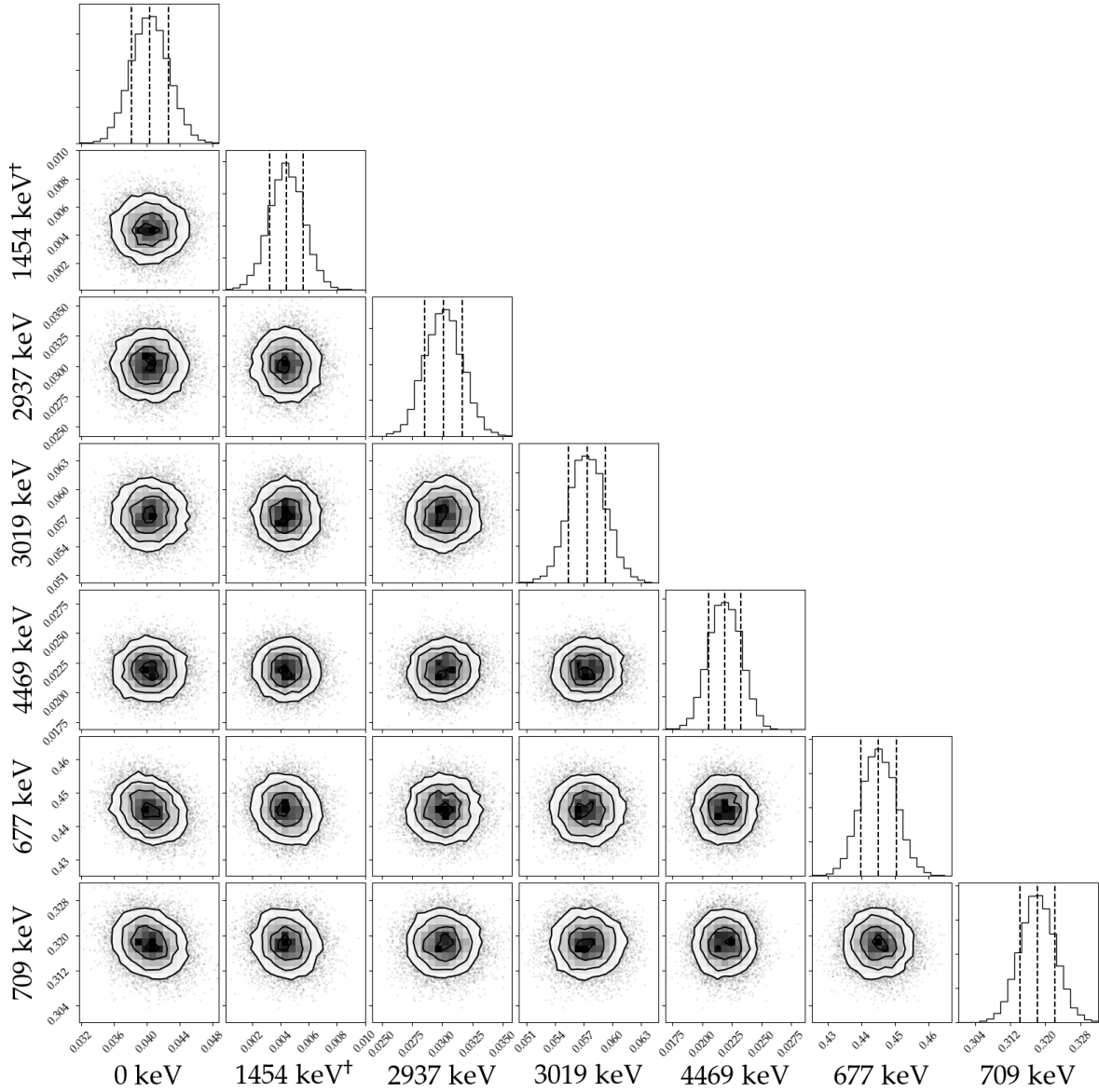


Figure 7.3: Template posterior distributions and two-dimensional pairwise posterior projections from the MCMC fraction fit of the $^{29}\text{Si}(p,\gamma)^{30}\text{P}$ $E_r^{\text{lab}} = 416$ keV singles abridged spectrum. Each posterior distribution refers to the fractional contribution a $^{29}\text{Si}(p,\gamma)^{30}\text{P}$ primary transition makes to the overall spectrum. The axis labels indicate the bound state to which the compound state decays for the represented primary transition. The 16th, 50th, and 84th percentiles are indicated by the dashed lines on each one-dimensional posterior distribution. † denotes a branch of the reaction of interest that is treated as an upper limit.

† symbol. The good agreement between the measured and simulated spectra is easily seen in this figure.

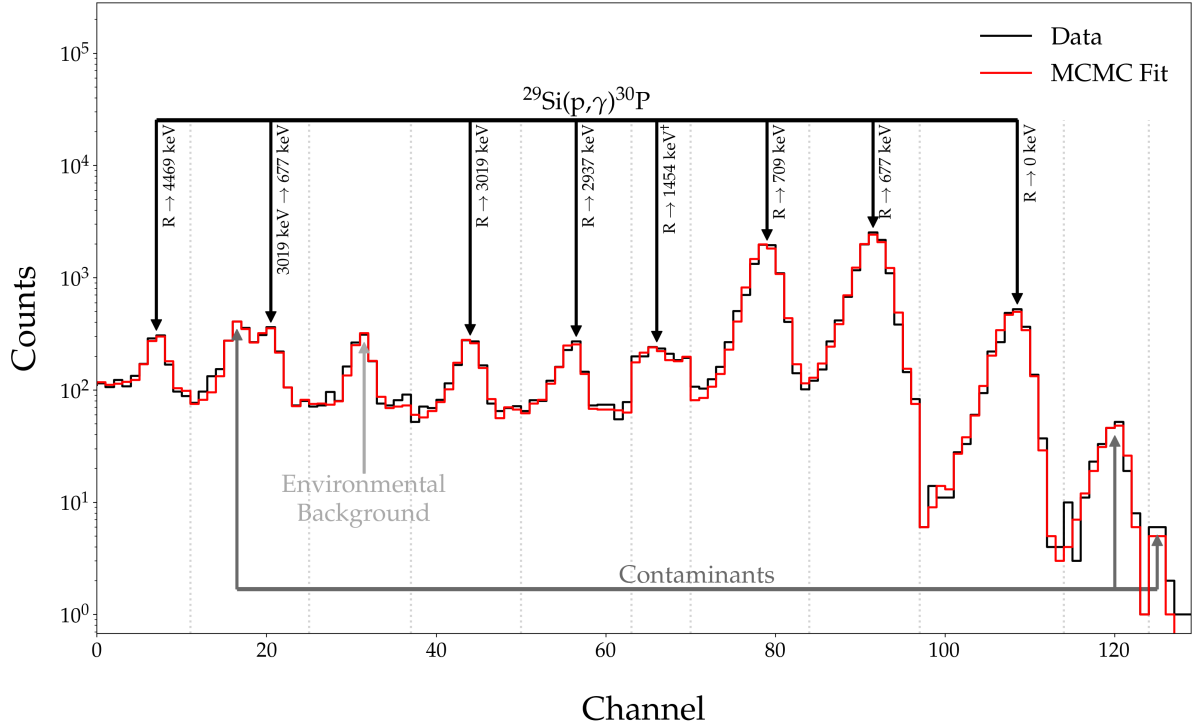


Figure 7.4: Measured (black) and simulated (red) pulse-height spectra for the $^{29}\text{Si}(p,\gamma)^{30}\text{P}$ $E_r^{\text{lab}} = 416$ keV abridged singles analysis. The full spectrum and templates were abridged to only include the regions containing the peaks of interest from $^{29}\text{Si}(p,\gamma)^{30}\text{P}$, beam-induced contaminant reactions, and environmental background sources. Each feature of the spectrum indicates the presence of the reaction of interest, various contaminant reactions, or environmental background, as indicated in the figure. The dotted lines denote breaks in the spectrum where featureless sections of the spectrum were excluded from the fit. These breaks can result in sharp boundaries, as seen above. The † superscript denotes a branch of the reaction of interest that is treated as an upper limit.

The analysis of the $E_r^{\text{lab}} = 416$ keV coincidence abridged spectrum is similarly shown in Figures 7.5 (template posteriors) and 7.6 (data and fit spectra comparison). It must be noted that the posterior distribution corresponding to the $R \rightarrow 1454$ keV template does not display the typical Gaussian form seen in the other distributions. Upon further inspection, it is clear that a nontrivial density exists at zero probability for this template, and as a result, the fractional contribution of this template must be treated as an upper limit. It was decided that this branch, while it appears to be well-fit in the singles data, would be conservatively presented as an upper limit in both

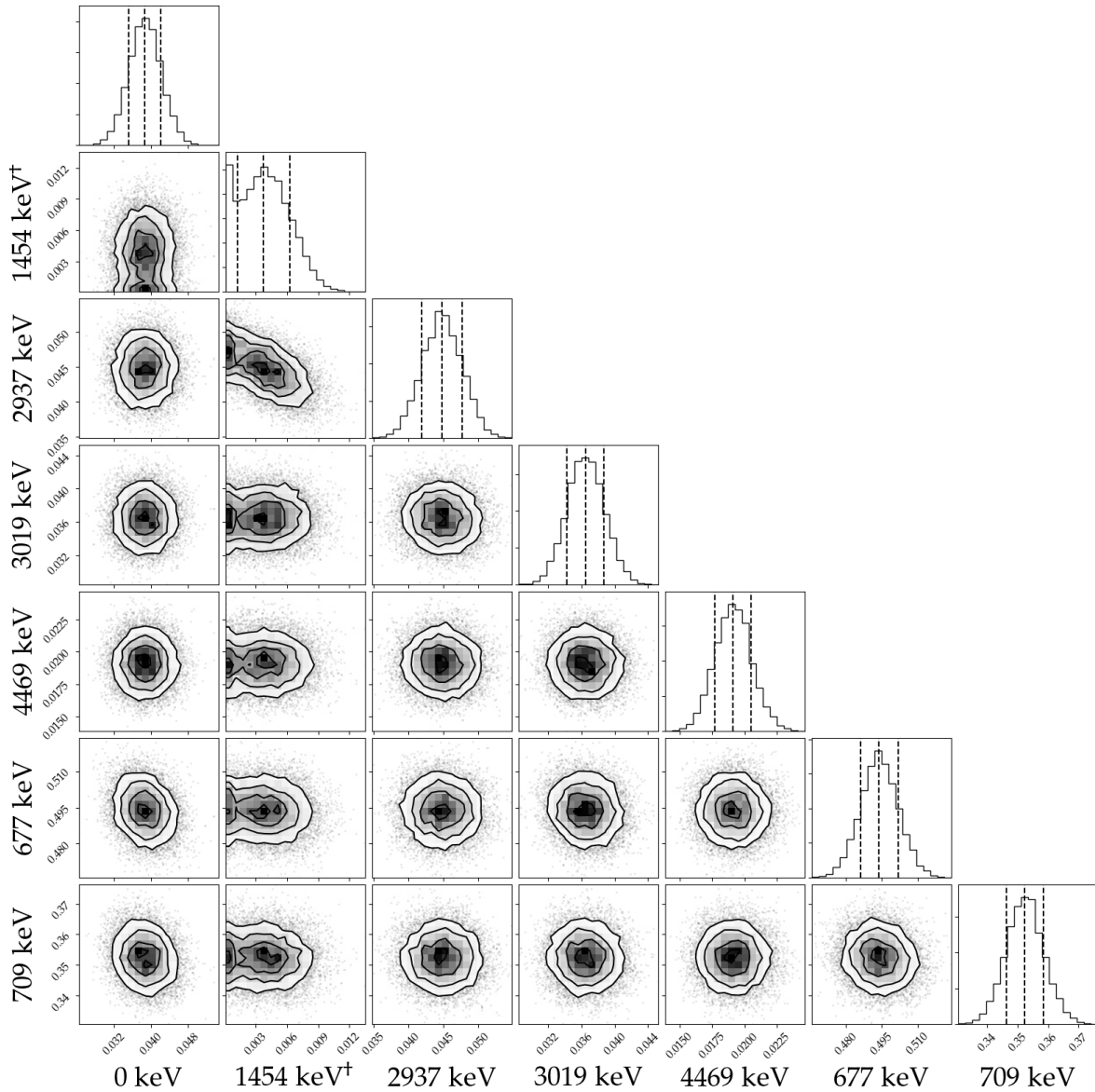


Figure 7.5: Template posterior distributions and two-dimensional pairwise posterior projections from the MCMC fraction fit of the $^{29}\text{Si}(p,\gamma)^{30}\text{P}$ $E_r^{\text{lab}} = 416$ keV coincidence abridged spectrum. The coincidence spectrum was found using a 4.0 - 6.5 MeV trapezoidal gate. For more information, see Figure 7.3.

singles and coincidence analyses. As mentioned in Section 7.1.1, this branch was not detected by Riihonen *et al.* (1979) and was by far the weakest branch presented in the Reinecke *et al.* (1985) measurement, both of which lend further credence to a cautious treatment of its contribution.

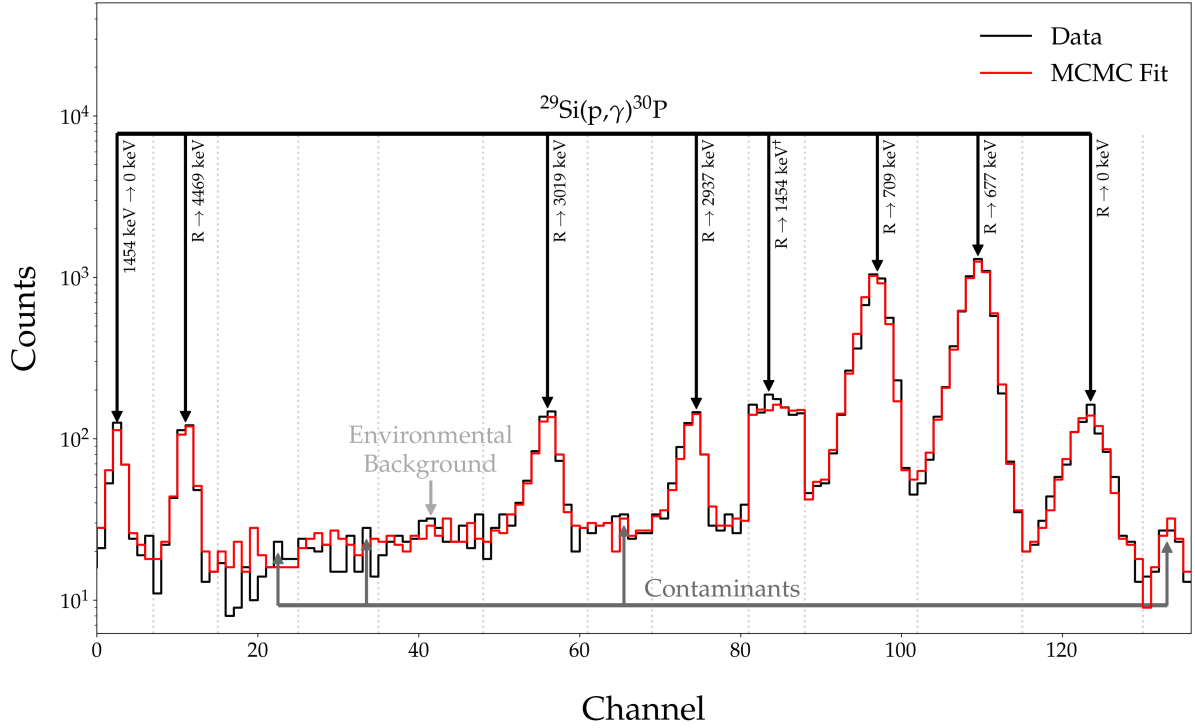


Figure 7.6: Measured (black) and simulated (red) pulse-height spectra for the $^{29}\text{Si}(p,\gamma)^{30}\text{P}$ $E_r^{\text{lab}} = 416$ keV abridged coincidence analysis. The coincidence spectrum was determined using a 4.0 - 6.5 MeV trapezoidal gate. See Figure 7.4 for details.

Both quantitative singles and coincidence analyses, along with a comparison to literature branching ratios from the previous measurements, are presented in Table 7.5. First of all, it must be noted that the goodness of fit for singles and coincidence analyses was determined (as described in Section 6.3). The test statistic, Z , communicates the significance level to which the data supports the null hypothesis. In this situation, the null hypothesis is that any discrepancies between the data and fraction fit results are produced by random fluctuations. A Z -value of -2.326 corresponds to a significance level of 1% in a single-tailed test. The test statistic for the $E_r^{\text{lab}} = 416$ keV analyses was determined to be -0.365 and -0.870 for the singles and coincidence data, respectively. Consequently, the singles and coincidence Z -values indicate that the discrepancies are largely random, and both fits to the observed data were successful. The template fractional contributions were used to determine the partial

number of reactions ($\mathcal{N}_R^{Partial}$) and primary branching ratios (B_γ) using Equations 6.5 and 6.7, respectively. The total $^{29}\text{Si}(p,\gamma)^{30}\text{P}$ number of reactions for each analysis was determined by summing the individual $^{29}\text{Si}(p,\gamma)^{30}\text{P}$ partial reaction numbers (Equation 6.6). It is clear that the $^{29}\text{Si}(p,\gamma)^{30}\text{P}$ total number of reactions and branching ratio determinations are consistent across both the singles and coincidence analyses. This agreement is crucial because demonstrates the internal consistency of the singles and coincidence analyses. Furthermore, it shows that the analyses are founded on a good understanding of the experimental parameters such as detector geometry and efficiency, γ -ray absorption, and so on. These branching ratios largely appear to agree with the literature values as well. Nevertheless, the agreement with the [Reinecke et al. \(1985\)](#) values cannot be quantified because no errors were presented in the previous work.

7.1.3 Resonance Energy

It is useful to determine the observed resonance energy and check agreement with the literature value. This calculation is performed by using the observed energies of the $^{29}\text{Si}(p,\gamma)^{30}\text{P}$ primary peaks in conjunction with knowledge of the reaction kinematics. Equation C.14 in [Iliadis \(2015\)](#) presents the relationship between these quantities and the lab frame resonance energy while taking Doppler and recoil shifts into account. This relationship is

$$E_\gamma = \frac{Q(m_a c^2 + m_A c^2 + m_B c^2)/2 + m_A c^2 E_a}{m_a c^2 + m_A c^2 + E_a - \cos\theta \sqrt{E_a(2m_a c^2 + E_a)}}, \quad (7.2)$$

where E_γ is the energy of the full-energy primary peak; Q is the nuclear Q-value of the reaction less the final state energy of the primary transition of interest; m_a , m_A , and m_B refer to the projectile, target, and daughter masses, respectively; E_a is the projectile energy in the laboratory frame; and θ represents the photon emission

Table 7.5. $E_r^{lab} = 416$ keV Fit Results

Primary Transition	Literature B_γ (%)		Singles ^a		Coincidence ^b	
	Rii79 ¹	Rei85 ²	$\mathcal{N}_R^{Partial}$	B_γ (%)	$\mathcal{N}_R^{Partial}$	B_γ (%)
R \rightarrow 4469.1	1.0 ± 0.3	1.0	21550 ± 1746	1.16 ± 0.10	17240 ± 1551	0.91 ± 0.09
R \rightarrow 3019.20	2.1 ± 0.3	1.8	43125 ± 2675	2.33 ± 0.17	39893 ± 3209	2.12 ± 0.19
R \rightarrow 2937.46	2.2 ± 0.3	1.9	40000 ± 2952	2.16 ± 0.18	34528 ± 2871	1.83 ± 0.17
R \rightarrow 1454.23 ^c	...	0.4	< 12619	< 0.68	< 5236	< 0.28
R \rightarrow 708.70	33 ± 1	30	544873 ± 29234	29.45 ± 1.48	552414 ± 30595	29.30 ± 1.53
R \rightarrow 677.01	57 ± 1	60	1130480 ± 60568	61.10 ± 1.61	1172568 ± 64707	62.19 ± 1.67
R \rightarrow 0	4.7 ± 0.3	4.9	70197 ± 5398	3.79 ± 0.31	68856 ± 7175	3.65 ± 0.39

Note. — The resonant state has been assigned a spin and tentative parity of 1^+ (see discussion in [Reinecke *et al.*, 1985](#); [Grossmann *et al.*, 2000](#)). The results displayed in this table are based on the GEANT4 simulation of 2.5×10^6 events for each primary transition. Coincidence simulated fit is determined using a 4 - 6.5 MeV coincidence gate. Singles and coincidence analyses make use of the angular coefficients for the R \rightarrow 677.01 keV and R \rightarrow 708.70 keV primaries reported by [Riihonen *et al.* \(1979\)](#). Calculated values (partial reaction numbers and branching ratios) are determined using a 68% credible interval from an abridged spectrum fit unless otherwise noted. Uncertainties associated with detector geometry (5%) and GEANT4 usage (1.3%) are included in the calculation of the partial reaction numbers and propagated through the following calculations.

$$^a Z = -0.365. \mathcal{N}_R^{29Si} = 1850225 \pm 67610.$$

$$^b Z = -0.870. \mathcal{N}_R^{29Si} = 1885499 \pm 72080.$$

^cThe partial numbers of reactions and branching ratios for this primary transition represent upper limits given by a 97.5% coverage interval.

References. — ¹[Riihonen *et al.* \(1979\)](#); ²[Reinecke *et al.* \(1985\)](#).

angle. The mean, energy-dependent value of $\cos \theta$ is given by the first-order peak attenuation coefficient, Q_1^P , which was found by simulating the detector geometry (see Section 4.3.1 for details). It should be noted that Equation 7.2 is only valid if one assumes that the resonant state decays on a relatively short timescale ($\lesssim 10$ fs), resulting in negligible recoil energy losses in the target and the full Doppler energy shift of the emitted photon.

The laboratory projectile energy was found numerically for each value of E_γ given in Table 7.4. A weighted average of these results gave a average, laboratory-frame proton energy of $E_r^{lab} = 416.8 \pm 0.7$ keV. This value is in excellent agreement with that of Endt (1998), 416.6 ± 0.7 keV, and that of the yield curve analysis (Section 5.2).

7.1.4 Target Stoichiometry Determination

Target yield curves (described in Section 5.2) of standard resonances are typically used to study the properties of nuclear targets. This type of measurement involves bombarding the nuclear target with protons across an energy region in order to map the yield of the resonance of interest. From the features of the resulting curve, a variety of information can be derived—the laboratory-frame resonance energy, implantation depth, proton beam width, beam straggling constant, and most importantly, target stoichiometry.

First, one must define the experimental yield as Iliadis (2015) does in Equation 4.123,

$$Y = \frac{\mathcal{N}_R}{\mathcal{N}_b} = \frac{\mathcal{N}}{\mathcal{N}_b B_\gamma \eta W}, \quad (7.3)$$

where \mathcal{N}_R is the total number of reactions and \mathcal{N}_b is the total number of incident particles. The parameters on the far righthand side of the equation refer to a specific nuclear transition where \mathcal{N} , B_γ , η , and W are the total number of detected photons, branching ratio, detector efficiency, and angular correlation, respectively. For the thick

targets used in most LENA experiments, the measured yield can then be related to the strength of the measured resonance as shown in Equation 4.125,

$$\omega\gamma = \frac{2\varepsilon_r}{\lambda_r^2} Y_{max, \Delta E \rightarrow \infty} = \frac{2\varepsilon_r}{\lambda_r^2} \frac{\mathcal{N}_{max, \Delta E \rightarrow \infty}}{\mathcal{N}_b B_\gamma \eta W}, \quad (7.4)$$

where ε_r is the stopping power at the resonance energy, λ_r is the de Broglie wavelength at the resonance energy, and all remaining quantities were defined previously. It should be noted that all dynamic quantities (stopping powers and the de Broglie wavelength) in this expression are center-of-mass values.

For the traditional yield curve analysis applied in past experiments, all parameters in Equation 7.4 were determined explicitly through a combination of measurement, calculation, and correction (see, for example, Kelly *et al.*, 2017). The fraction fitting analysis presented earlier can also be used here however. In fact, there are a number of advantages to this approach, primarily the implicit inclusion of detector geometry and decay kinematics in the GEANT4-simulated fit. Equation 7.4 can then be simplified to

$$\omega\gamma = \frac{2\varepsilon_r}{\lambda_r^2} Y_{max, \Delta E \rightarrow \infty} = \frac{2\varepsilon_r}{\lambda_r^2} \frac{\mathcal{N}_{R, max}}{\mathcal{N}_b} \quad (7.5)$$

where $\mathcal{N}_{R, max}$ is the total number of reactions determined at the maximum of the yield curve and B_γ , η , and W are implicitly included in this value. It is important to realize that $\mathcal{N}_{R, max}$ has already been determined since the analysis of the $E_r^{lab} = 416$ keV standard resonance was carried out at peak yield. Thus, the total number of reactions for the $E_r^{lab} = 416$ keV resonance is given by the unweighted average of the results from the singles and coincidence analyses (Table 7.5),

$$\mathcal{N}_{R, max} = 1867862 \pm 49413. \quad (7.6)$$

If the experimental yield is carefully measured and the resonance strength well

known, Equation 7.5 can be used to determine the stopping power at the resonance energy which is closely related to the target stoichiometry. The remaining quantities in this equation are already in hand or can easily be calculated. The systematic uncertainties included in the calculations are given in Table 7.2. The literature resonance strength was presented earlier in this chapter, $\omega\gamma = 0.244 \pm 0.038$ eV (Table 7.3). The total incident charge, Q (Table 7.1), can be used to derive the number of incident protons,

$$\mathcal{N}_b = \frac{Q}{qe} = \frac{(5.2 \pm 0.2) \times 10^{-3} \text{ C}}{1 \cdot (1.6 \times 10^{-19}) \text{ C}} = (3.3 \pm 0.1) \times 10^{16} \text{ protons}, \quad (7.7)$$

where q is the charge of incident particle ($q = 1$ for protons) and e is a single unit of charge. The de Broglie wavelength is given by Equation 4.107 in Iliadis (2015),

$$\begin{aligned} \frac{\lambda_r^2}{2} &= 2\pi^2 \frac{\hbar^2}{2m_{01}E_r} = \left(\frac{M_0 + M_1}{M_1} \right)^2 \frac{4.125 \times 10^{-18}}{M_0 E_r^{lab}} \text{ (cm}^2\text{)} \\ &= (1.05213 \pm 0.00170071) \times 10^{-23} \text{ cm}^2, \end{aligned} \quad (7.8)$$

where m_{01} , M_0 , and M_1 refer to the reduced mass of the system, projectile mass, and target mass, respectively. All masses were given by Wang *et al.* (2017) in atomic mass units. The laboratory-frame resonance energy, E_r^{lab} , was found in the previous section. Finally, inverting Equation 7.5 and solving for the resonance-energy stopping power finds

$$\varepsilon_r = \frac{\lambda_r^2}{2} \frac{\omega\gamma\mathcal{N}_b}{\mathcal{N}_{R,max}} = (44.8 \pm 7.5) \text{ eV} \cdot \text{cm}^2 / 10^{15} \text{ atoms} \quad (7.9)$$

where the resonance-energy stopping power, ε_r , is sometimes referred to as the effective stopping power in the center-of-mass frame, ε_{eff}^{CM} . It is advantageous to find the effective stopping power in the laboratory frame,

$$\varepsilon_{eff}^{lab} = \left(\frac{M_0 + M_1}{M_1} \right) \varepsilon_{eff}^{CM} = (46.4 \pm 7.5) \text{ eV} \cdot \text{cm}^2 / 10^{15} \text{ atoms}. \quad (7.10)$$

For a compound $X_a Y_b$, the relationship between the target stopping powers and the

stoichiometry is given by Iliadis (2015) in Equation 4.94 as

$$\varepsilon_{eff} = \varepsilon_X + \frac{n_Y}{n_X} \varepsilon_Y \quad (7.11)$$

where n is the number of nuclei per square centimeter and X and Y refer to the active and inactive nuclei, respectively. The ratio of the nuclei per square centimeter, n_Y/n_X , is equivalent to the target stoichiometry, b/a . Stopping powers for the active (^{29}Si) and inactive (^{nat}Ta) nuclei in the laboratory frame were found by linear interpolation of values provided by Ziegler *et al.* (2015),

$$\begin{aligned} \varepsilon_{Si} &= (13.1 \pm 0.7) \text{ eV} \cdot \text{cm}^2 / 10^{15} \text{ atoms} \\ \varepsilon_{Ta} &= (28.6 \pm 1.4) \text{ eV} \cdot \text{cm}^2 / 10^{15} \text{ atoms.} \end{aligned} \quad (7.12)$$

Altogether, Equation 7.11 can be solved to find the target stoichiometry,

$$\frac{b}{a} = \frac{n_{Ta}}{n_{Si}} = \frac{\varepsilon_{eff}^{lab} - \varepsilon_{Si}}{\varepsilon_{Ta}} = 1.17 \pm 0.27, \quad (7.13)$$

indicating that the ^{29}Si -implanted nuclear target used in this dissertation has a stoichiometry of roughly $^{29}\text{Si}_1\text{Ta}_1$.

7.2 324 keV Resonance

While $^{29}\text{Si}(p,\gamma)^{30}\text{P}$ and the $E_r^{lab} = 416$ keV resonance specifically garnered a significant amount of interest over the years, the $E_r^{lab} = 324$ keV resonance was studied somewhat less frequently. A few studies, such as Baart *et al.* (1962), determined sundry structural information about this resonance but often neglected to present a $E_r^{lab} = 324$ keV resonance strength in the literature. van der Leun and Endt (1958), which was responsible for reporting the first $E_r^{lab} = 416$ keV resonance strength, was also the first to report an absolute strength for the $E_r^{lab} = 324$ keV resonance. Their

experimental details are summarized in Section 7.1 and will not be repeated here.

The next measurement of this resonance strength was not conducted until a decade later by Harris *et al.* (1969) as part of their 24 resonance study of $^{29}\text{Si}(p,\gamma)^{30}\text{P}$ and an extension of their earlier work, Harris and Hyder (1967). They prepared silver-backed, SiO_2 targets enriched with 95% ^{29}Si using an electron-gun evaporator. A 2-MV Van de Graaff accelerator was then used to bombard the targets, mounted at 45° relative to the beam, with proton currents of typically 20–40 μA . A combination of two NaI(Tl) detectors, the first 5" x 5" and the second 8" x 8" in size, were used to find preliminary angular distribution measurements, excitation curves, and triple-correlation curves for the studied resonances. A 40-cm³ Ge(Li) detector was used for more precise measurements, including final angular distribution measurements, decay schemes, and lifetime measurements. Relative resonance strengths were converted to absolute resonance strengths using the $^{29}\text{Si}(p,\gamma)^{30}\text{P}$ $E_r^{\text{lab}} = 416$ keV resonance strength reported by Engelbertink and Endt (1966) (see Table 7.3 for renormalized value).

Reinecke *et al.* (1985) is responsible for the most recent measurement of this resonance. In total, their work involved the measurement of 32 $^{29}\text{Si}(p,\gamma)^{30}\text{P}$ resonances and the properties of 30 ^{30}P bound states. They utilized a 2.5-MV Van de Graaff accelerator to produce 30–60 μA proton currents of $E_p \leq 2.3$ MeV. The targets, similar to those of Harris *et al.* (1969), used were produced by evaporating highly enriched (95% ^{29}Si) SiO_2 on thin tantalum backings. The reaction was then observed by a combination of Ge(Li) and NaI detectors at an angle of 55° with respect to the proton beam. Unlike the previous strength measurements of the $E_r^{\text{lab}} = 324$ keV resonance, Reinecke *et al.* (1985) used the $^{29}\text{Si}(p,\gamma)^{30}\text{P}$ $E_r^{\text{lab}} = 416$ keV strength reported by Riihonen *et al.* (1979) to convert their relative strengths to absolute resonance strengths.

The previous $E_r^{\text{lab}} = 324$ keV resonance strengths are summarized in Table 7.6. It should be noted that while several of these measurements agree with each other, this is in large part due to the substantial (~ 20 – 35%) uncertainties on each measurement.

Table 7.6. $^{29}\text{Si}(\text{p},\gamma)^{30}\text{P}$ $E_r^{lab} = 324$ keV Resonance Strength Measurements

Reference	Resonance Strength, $\omega\gamma$ (eV)
van der Leun and Endt (1958)	0.0175 ± 0.0050
Harris <i>et al.</i> (1969)	0.0275 ± 0.0050^a
Reinecke <i>et al.</i> (1985)	0.015 ± 0.005

Note. — Literature values for the $E_r^{lab} = 324$ keV resonance strength.

^aCorrected with $\omega\gamma = 0.260 \pm 0.025$ eV for $E_r^{lab} = 416$ keV (Riihonen *et al.*, 1979) by Reinecke *et al.* (1985).

The absolute resonance strength measured by van der Leun and Endt (1958) is in good agreement with the strength measurement Reinecke *et al.* (1985), but it barely falls within the range of agreement with the Harris *et al.* (1969) value. The Harris *et al.* (1969) value was originally determined relative to the Engelbertink and Endt (1966) $^{29}\text{Si}(\text{p},\gamma)^{30}\text{P}$ $E_r^{lab} = 416$ keV strength but was renormalized to the more recent Riihonen *et al.* (1979) $E_r^{lab} = 416$ keV strength for this comparison. This new value does not agree with the most recent $E_r^{lab} = 324$ keV strength (Reinecke *et al.*, 1985). The lack of consensus in the previous measurements makes a new study of the $E_r^{lab} = 324$ keV resonance a worthwhile undertaking.

Some ambiguity also remains in the spin-parity assignment of this resonance as well. The angular correlation data of Harris *et al.* (1969) indicated that J^π should be restricted to $(1, 2^-)$. Similarly, the $^{29}\text{Si}(\text{}^3\text{He},\text{d})^{30}\text{P}$ experiment of Hertzog *et al.* (1974) restricted compound state spin-parity to $(0,1,2)^-$. Ramstein *et al.* (1981), using the $^{30}\text{Si}(\text{}^3\text{He},\text{t})^{30}\text{P}$ reaction and the angular distribution “fingerprint method,” further restricted the state spin-parity to $J^\pi = 2^-$.

7.2.1 Measurement

The measurement of the $E_r^{lab} = 324$ keV resonance was performed in the same manner described in Section 7.1.1. In short, an initial yield curve (Figure 7.7) was taken using the LENA I accelerator in order to ascertain the proton bombarding energy resulting in the maximum yield. Because of the close proximity of this resonance to the $E_r^{lab} = 314$ keV resonance (to be discussed later in Section 7.3), an excitation curve spanning the energy region of both resonances was measured. This work is shown in Figure 7.8. The yield of the strongest primary in the 314 keV resonance, $R \rightarrow 2937$ keV, is shown in red, while the yield of the dominant primary in the 324 keV resonance, $R \rightarrow 0$ keV, is displayed in blue. Figure 7.8 shows that $E_r^{lab} = 324$ keV data taken at a bombarding energy of $E_p = 327$ keV should result in the maximum yield and be free of interference from the $E_r^{lab} = 314$ keV resonance. Thus, the bombarding energy of $E_p = 327$ keV was chosen to take the remaining 2.2745 C of data needed to study this resonance precisely. This data was acquired over 56352 s with an average proton current and dead time of 40.4 μ A and 4.2%, respectively (see Table 7.1). The proximity of the $E_r^{lab} = 314$ keV resonance somewhat complicated the acquisition of off-resonance data as well; thus, the $E_r^{lab} = 314$ keV data was also used as off-resonance data for the $E_r^{lab} = 324$ keV study. The use of this off-resonance data aided in identifying contaminants in the $E_r^{lab} = 324$ keV spectra and $E_r^{lab} = 314$ keV peaks that could potentially contaminate the $E_r^{lab} = 324$ keV data.

Both singles and coincidence spectra of the $E_r^{lab} = 324$ keV resonance were generated at maximum yield. The coincidence pulse-height spectrum was generated using the energy condition given by Equation 7.1 and by disregarding events coincident with the muon-veto panels. These spectra are shown in Figure 7.9, where the singles spectrum is given in black and the coincidence spectrum in red. In this figure it is easily seen that all of the primary transitions observed in the [Reinecke et al. \(1985\)](#) measurement were observed here as well. Additionally, minor primary transitions to

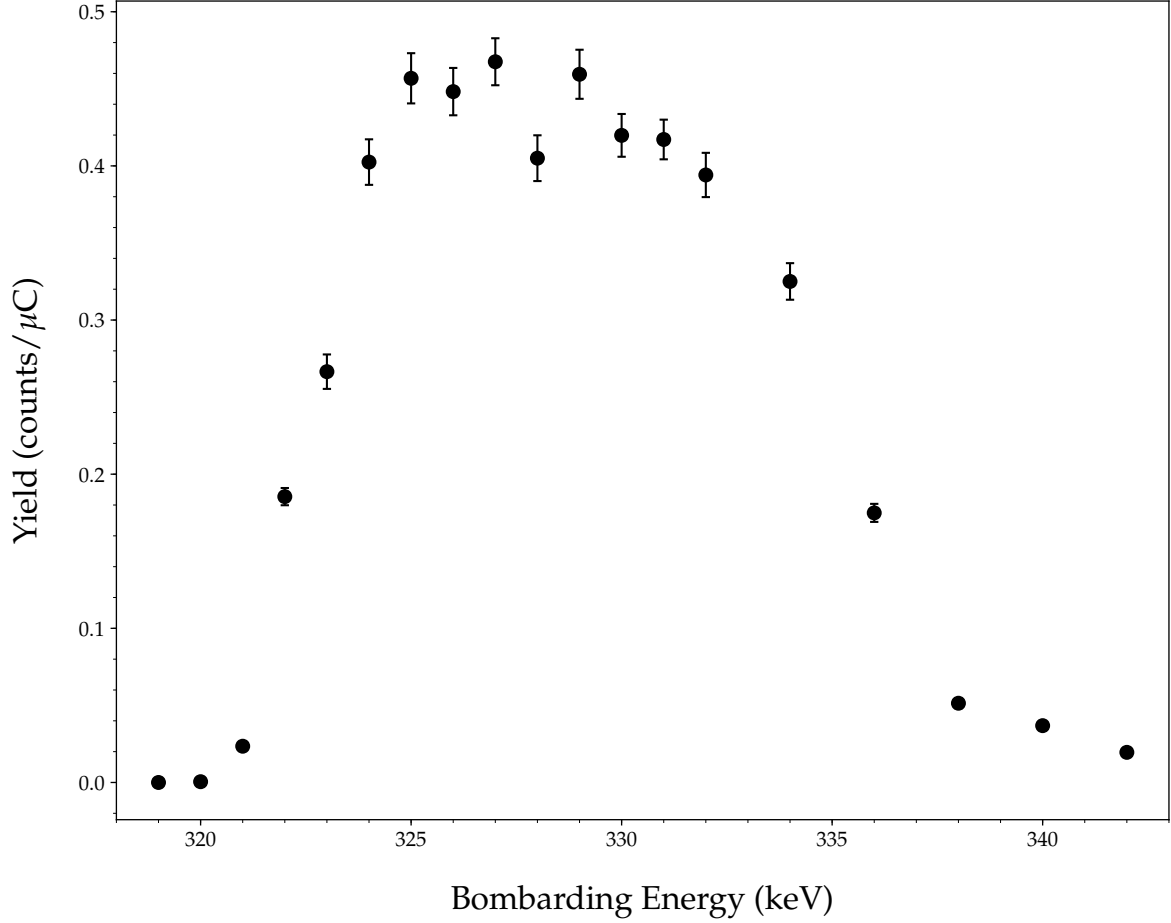


Figure 7.7: The yield of the $E_r^{lab} = 324$ keV resonance mapped over a 23-keV region. The strongest transition in this resonance, $R \rightarrow 0$ keV, was used to determine the net yield shown. The yield was also corrected for the observed dead time in each data-point.

the 3734 keV, 3836 keV, 4144 keV, 4232 keV, and 4502 keV levels were observed in the present work. Note that while these new primaries are weakly visible in the singles spectrum, they are significantly more defined in the coincidence spectrum.

Table 7.7 gives the background-subtracted, full-energy primary peak energies and intensities observed in the singles and coincidence spectra. In accordance with the work of Reinecke *et al.* (1985), primary intensities to the 677 keV, 1973 keV, and 2539 keV levels are treated as upper limits here. This table also presents the energies and intensities of five newly discovered primaries in the $E_r^{lab} = 324$ keV resonance: $R \rightarrow$

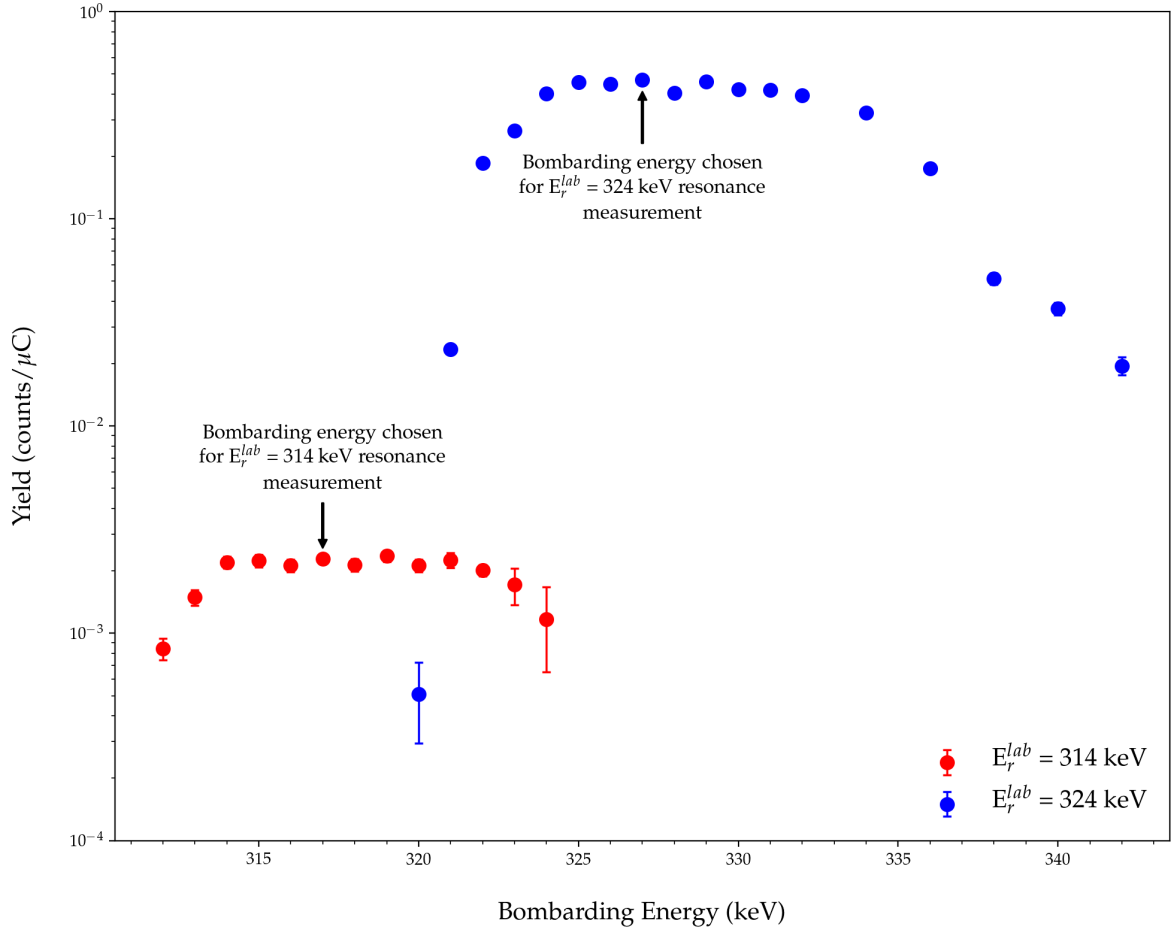


Figure 7.8: The yield of the $^{29}\text{Si}(p,\gamma)^{30}\text{P}$ $E_r^{lab} = 314$ keV and 324 keV resonances mapped over a 34-keV region. The strongest transition of the $E_r^{lab} = 314$ keV resonance, $R \rightarrow 2937$ keV, was used to determine the net yield shown in red. The $E_r^{lab} = 324$ keV yield, shown in blue, was determined using the prominent $R \rightarrow 0$ keV decay. These yields make clear that the $E_r^{lab} = 314$ keV and $E_r^{lab} = 324$ keV datasets taken at their respective bombarding energies, $E_p = 317$ keV and $E_p = 327$ keV, are independent and free of the other's influence.

3734 keV, $R \rightarrow 3836$ keV, $R \rightarrow 4144$ keV, $R \rightarrow 4232$ keV, and $R \rightarrow 4502$ keV. The analysis of this resonance follows in the next section.

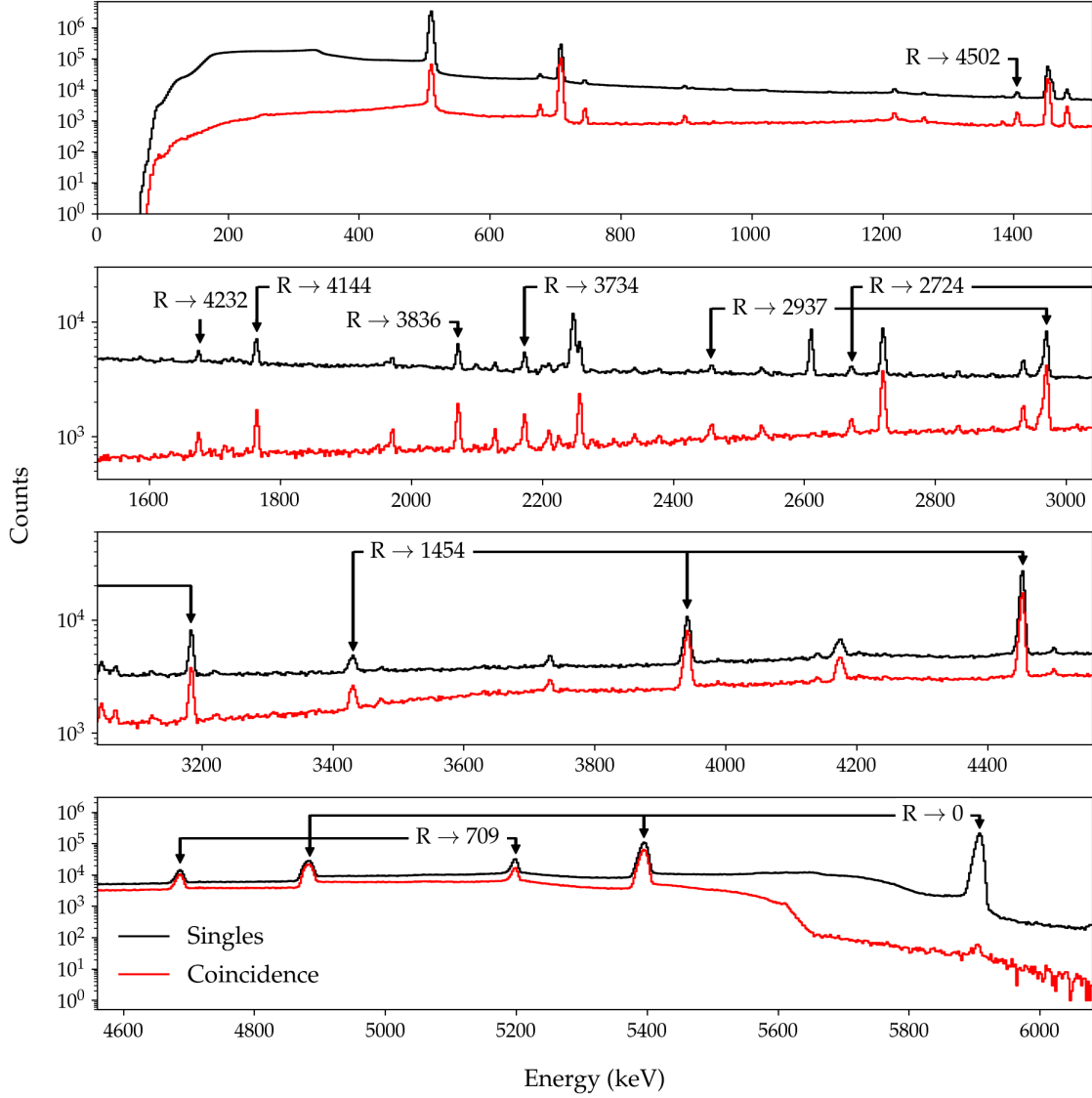


Figure 7.9: HPGe singles and $\gamma\gamma$ -coincidence pulse-height spectra of the $^{29}\text{Si}(p,\gamma)^{30}\text{P}$ $E_r^{\text{lab}} = 324$ keV resonance. The singles spectrum is shown in black, while the coincidence spectrum is shown in red. Primary transitions to the 3734 keV, 3836 keV, 4144 keV, 4232 keV, and 4502 keV levels have been observed for the first time in the present work.

Table 7.7. Energies & Decay Intensities for the $E_r^{lab} = 324$ keV Resonance

Primary Transition	J^π	E_γ (keV)	Intensity	
			Singles	Coincidence
$R \rightarrow 4502.21$	1^+	1408.24 ± 1.76	6763 ± 293	2725 ± 113
$R \rightarrow 4231.97$	4^-	1678.23 ± 1.82	2530 ± 273	876 ± 110
$R \rightarrow 4143.63$	2^-	1766.19 ± 1.85	6527 ± 278	2143 ± 117
$R \rightarrow 3835.80$	2^+	2074.54 ± 1.99	6083 ± 276	2957 ± 130
$R \rightarrow 3733.80$	1^+	2176.07 ± 1.77	4346 ± 238	2133 ± 115
$R \rightarrow 2937.46$	2^+	2969.50 ± 2.31	15966 ± 320	9671 ± 200
$R \rightarrow 2839.34$	3^+	3070.27 ± 1.83	2173 ± 219	1200 ± 135
$R \rightarrow 2723.72$	2^+	3185.82 ± 2.37	14486 ± 271	7620 ± 176
$R \rightarrow 2538.95^a$	3^+	...	< 309	< 146
$R \rightarrow 1973.27^a$	3^+	...	< 444	< 365
$R \rightarrow 1454.23$	2^+	4455.42 ± 1.90	79192 ± 458	49654 ± 364
$R \rightarrow 708.70$	1^+	5199.00 ± 2.21	97907 ± 670	50146 ± 497
$R \rightarrow 677.01^a$	0^+	...	< 723	< 381
$R \rightarrow 0$	1^+	5909.79 ± 1.25	934366 ± 990	332919 ± 696

Note. — The resonant state spin-parity has been restricted to 2^- . See [Hertzog et al. \(1974\)](#) and [Ramstein et al. \(1981\)](#) for details. For all other spin-parity assignments, see [Endt \(1998\)](#). Presented intensities are based on a proton beam charge of 2.274474 C accumulated on target. Coincidence intensities are determined using a 4.0 - 6.5 MeV coincidence gate where the reported $R \rightarrow 0$ keV intensity corresponds to the single-escape peak intensity for this transition. No observed energies are presented for transitions with upper limit intensities.

^aThe measured peak intensities for this primary transition should be considered upper limit values, estimated as $\sqrt{2 \times BG}$, where BG indicates the number of background counts in the region of interest.

7.2.2 Analysis

The substantial uncertainties in previously determined resonance strengths and the discovery of five additional primary transitions make the analysis of this resonance particularly interesting. The analysis methods used with this resonance are largely the same as those described for the $E_r^{lab} = 416$ keV analysis (Section 7.1.2), but extra complications arise as results of the dominant ground state decay and the large number of substantially weaker primary branches. In brief, the expected decay was modeled using the LENAGe detection simulation, resulting in full-spectrum templates for each primary branch in the $^{29}\text{Si}(p,\gamma)^{30}\text{P}$ $E_r^{lab} = 324$ keV resonance as well as beam-induced contaminant reactions. The γ -ray distribution from this resonance was treated as anisotropic since the angular correlation coefficients are provided for one primary transition, $R \rightarrow 709$ keV, by the literature (Reinecke *et al.*, 1985). Ambient background sources were accounted for by direct measurement with the detection apparatus in running geometry. The full-spectrum templates were then truncated to only include regions containing $E_r^{lab} = 324$ keV primaries and other prominent transitions from this resonance, beam-induced contaminants, and environmental background contributions.

The techniques described in Chapter 6 were used to fit the templates to the singles and coincidence spectra. The resultant fit gives the fractional contribution of each template to the overall spectrum from which other information—such as the partial number of reactions, branching ratios, and resonance strength—can be derived.

The analysis of the $E_r^{lab} = 324$ keV singles spectrum is shown in Figures 7.10 and 7.11. Qualitatively, Figure 7.10 illustrates the agreement between the fit and $E_r^{lab} = 324$ keV singles data. Figure 7.11 displays the posterior distributions and two-dimensional pairwise posterior projections of each $^{29}\text{Si}(p,\gamma)^{30}\text{P}$ template included in the fit. All template distributions appear roughly Gaussian in shape, indicating that the spectrum fit converged on a reasonable solution. Despite this, several of these

template contributions were treated as upper limits as will be discussed later on.

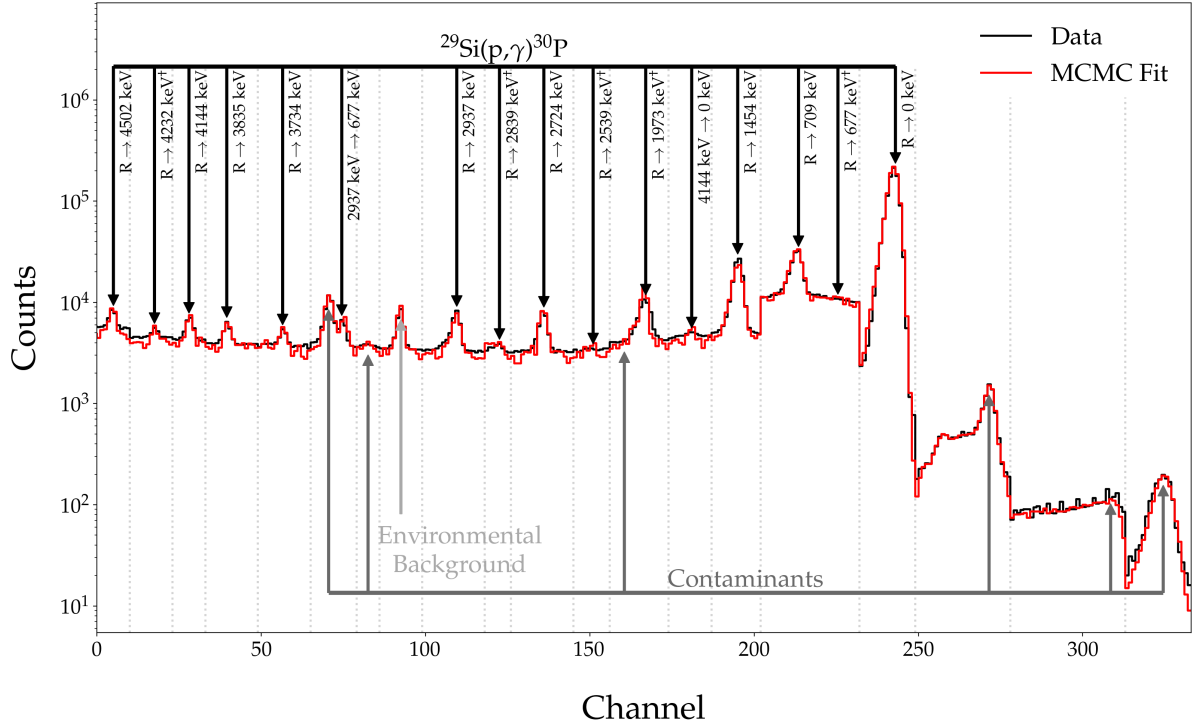


Figure 7.10: Measured (black) and simulated (red) pulse-height spectra for the $^{29}\text{Si}(p,\gamma)^{30}\text{P}$ $E_r^{\text{lab}} = 324$ keV abridged singles analysis. See Figure 7.4 for details.

Figures 7.12 and 7.13 express the agreement between the coincidence dataset and its fraction fitting analysis. In Figure 7.12, it is clear that, unlike the near-gaussian posterior distributions of the singles analysis, several of the template posteriors of the coincidence fit appear irregular in shape with nontrivial densities at zero probability, indicating a lack of clear agreement between these simulated templates and the observed data. Thus, the fractional contributions of these primary transitions— $R \rightarrow 677$ keV, $R \rightarrow 1973$ keV, $R \rightarrow 2539$ keV, $R \rightarrow 2839$ keV, and $R \rightarrow 4232$ keV—must be presented as upper limits. Not surprisingly, the first four of these upper limit primary transitions are presented as upper limit branching ratios in the Reinecke *et al.* (1985) analysis. The last upper limit primary identified in the current work, $R \rightarrow 4232$ keV, is a newly discovered but weak branch. For consistency, these primary transitions are also presented as upper limits in the singles analysis.

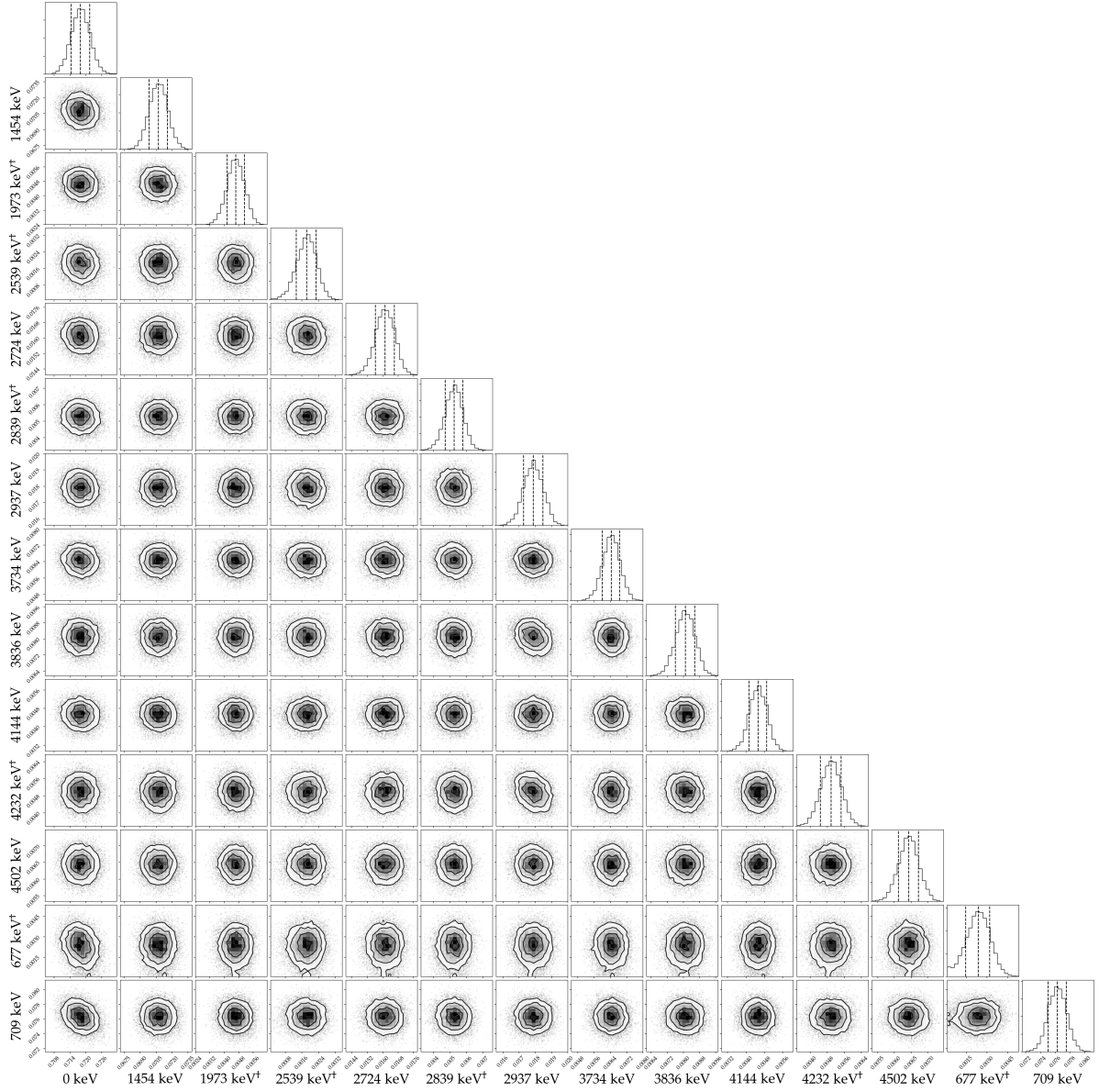


Figure 7.11: Template posterior distributions and two-dimensional pairwise posterior projections from the MCMC fraction fit of the $^{29}\text{Si}(p,\gamma)^{30}\text{P}$ $E_r^{\text{lab}} = 324$ keV singles abridged spectrum. For more information, see Figure 7.3.

Table 7.8 summarizes the analysis of the $E_r^{\text{lab}} = 324$ keV resonance and provides a comparison to the Reinecke *et al.* (1985) measurement. To begin with, it should be noted that the test statistic, Z , was found to be -3.787 and -3.349 for the singles and coincidence analyses, respectively, indicating superb agreement between the simulated fit and the observed spectra. The partial number of reactions and branching ratios for

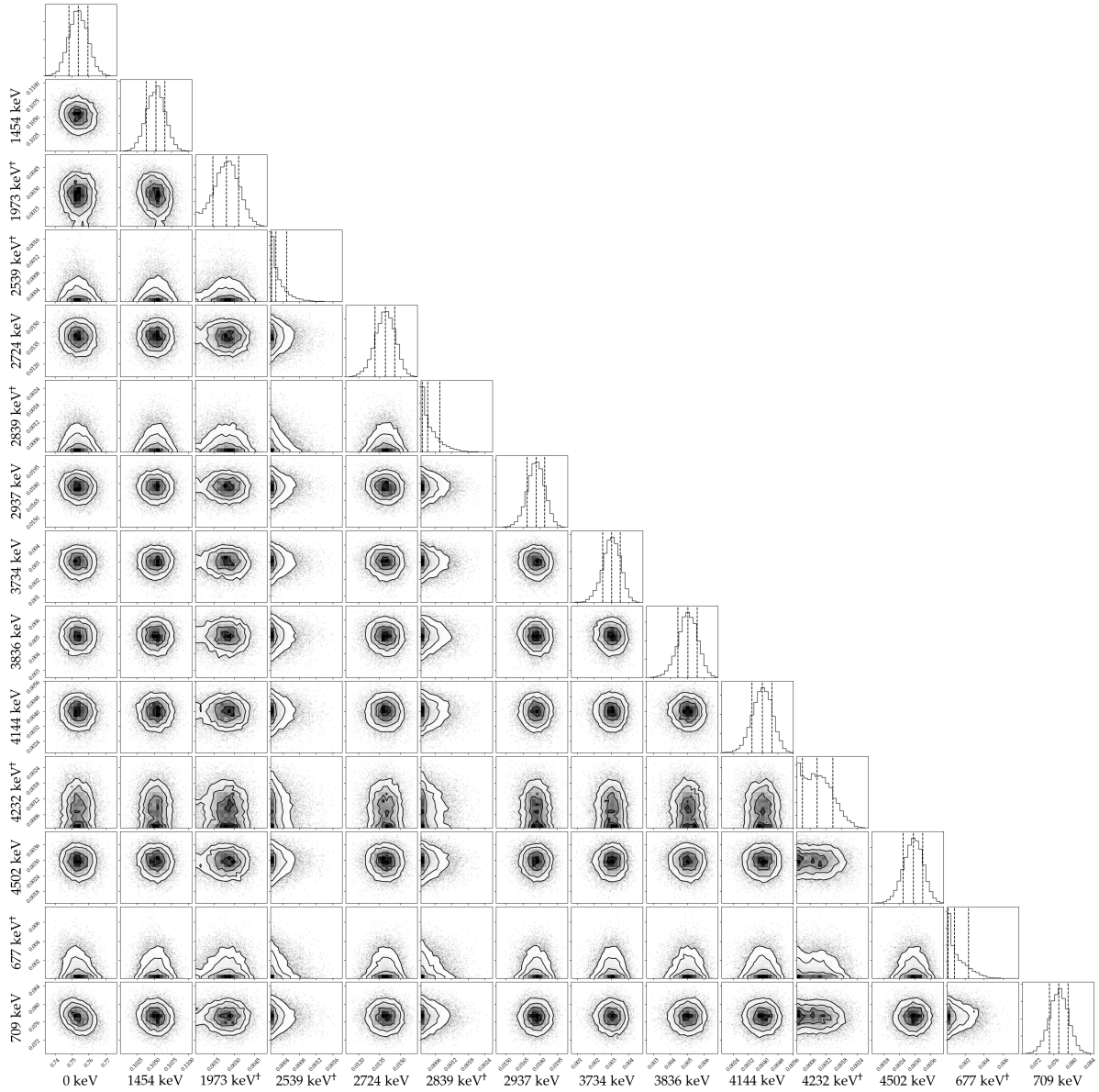


Figure 7.12: Template posterior distributions and two-dimensional pairwise posterior projections from the MCMC fraction fit of the $^{29}\text{Si}(p,\gamma)^{30}\text{P}$ $E_r^{\text{lab}} = 324$ keV coincidence abridged spectrum. The coincidence spectrum was found using a 4.0 - 6.5 MeV trapezoidal gate. For more information, see Figure 7.3.

the singles and coincidence resonance analyses are also shown. It is clear that these results broadly agree with that of [Reinecke *et al.* \(1985\)](#), though the level of agreement is difficult to ascertain because of the lack of uncertainties given in the literature.

There are a few discrepancies to note though. Perhaps the foremost issue is the

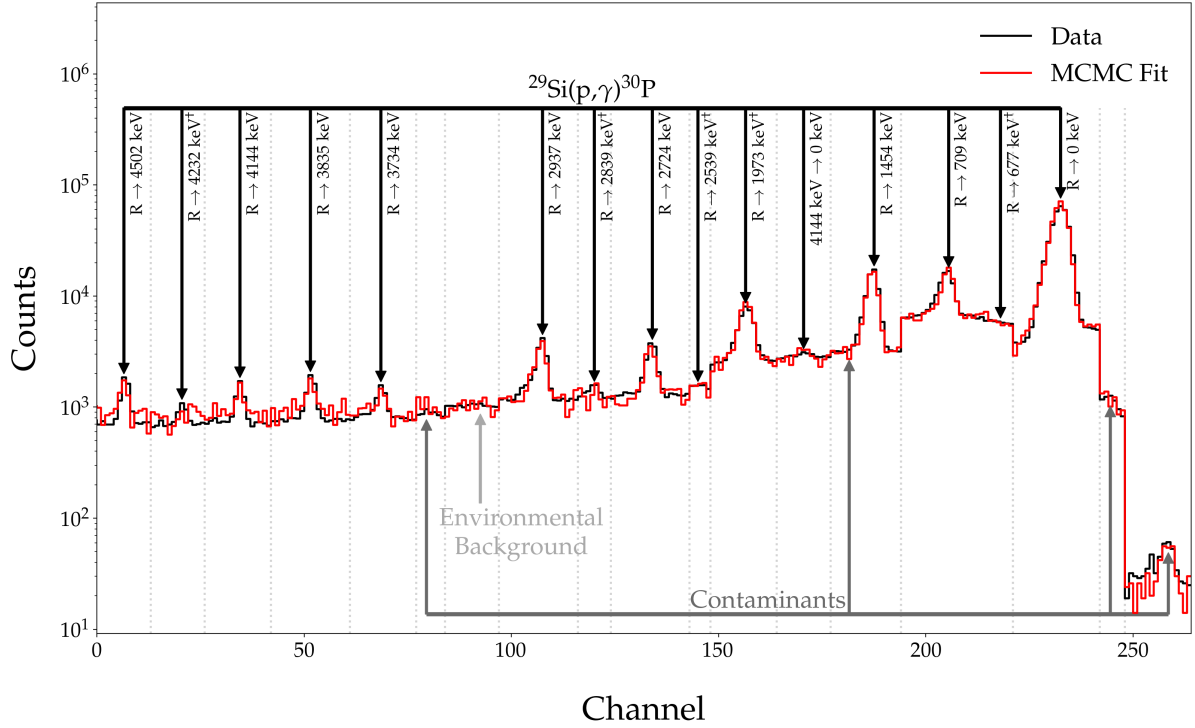


Figure 7.13: Measured (black) and simulated (red) pulse-height spectra for the $^{29}\text{Si}(p,\gamma)^{30}\text{P}$ $E_r^{\text{lab}} = 324$ keV abridged coincidence analysis. The coincidence spectrum was determined using a 4.0 - 6.5 MeV trapezoidal gate. See Figure 7.4 for details.

slight conflict (2.9%) in the ground-state branching ratios of the singles and coincidence analyses. Similar but more significant disagreements were seen in the fraction fitting analysis of [Dermigny \(2018\)](#). As discussed in their work, the single-escape peak of ground-state transitions does not appear to be accurately reproduced by the GEANT4 LENA_{Ge} simulation. This peak, while excluded from the singles spectral fit, is used as the principal determinant of the ground-state fractional contribution in the coincidence fit. Thus, this issue should be addressed in future work. Furthermore, the agreement between the total number of $^{29}\text{Si}(p,\gamma)^{30}\text{P}$ reactions in the singles and coincidence analyses shows that this issue with the coincidence ground-state branching ratio will not affect the calculation of the resonance strength.

Of lesser importance are discrepancies between the literature branching ratios and those of this work for the $R \rightarrow 0$ keV, $R \rightarrow 709$ keV, and $R \rightarrow 1454$ keV primaries.

Table 7.8. $E_r^{lab} = 324$ keV Fit Results

Primary Transition	Literature B_γ (%) ¹	Singles ^a		Coincidence ^b	
		$\mathcal{N}_R^{Partial}$	B_γ (%)	$\mathcal{N}_R^{Partial}$	B_γ (%)
R \rightarrow 4502.21	...	345692 ± 24228	0.38 ± 0.03	145009 ± 19945	0.16 ± 0.02
R \rightarrow 4231.97 ^c	...	< 235747	< 0.26	< 100975	< 0.11
R \rightarrow 4143.63	...	186121 ± 18294	0.20 ± 0.02	133657 ± 19142	0.15 ± 0.02
R \rightarrow 3835.80	...	421168 ± 33073	0.46 ± 0.04	259589 ± 32518	0.29 ± 0.04
R \rightarrow 3733.80	...	339863 ± 28446	0.37 ± 0.03	139683 ± 24900	0.16 ± 0.03
R \rightarrow 2937.46	0.6	972153 ± 59976	1.06 ± 0.08	894516 ± 60409	1.00 ± 0.08
R \rightarrow 2839.34 ^c	< 0.1	< 434708	< 0.47	< 68507	< 0.08
R \rightarrow 2723.72	0.5	903095 ± 54162	0.98 ± 0.07	676716 ± 49296	0.75 ± 0.06
R \rightarrow 2538.95 ^c	< 0.1	< 144482	< 0.16	< 41733	< 0.05
R \rightarrow 1973.27 ^c	< 0.2	< 427274	< 0.47	< 223317	< 0.25
R \rightarrow 1454.23	3.4	5211623 ± 277297	5.68 ± 0.37	5272206 ± 281670	5.89 ± 0.39
R \rightarrow 708.70	9.5	9843840 ± 534312	10.74 ± 0.69	8187142 ± 478305	9.15 ± 0.63
R \rightarrow 677.01 ^c	< 0.7	< 426743	< 0.47	< 345975	< 0.39
R \rightarrow 0	86	73472631 ± 3824986	80.13 ± 0.99	73790225 ± 3878923	82.45 ± 0.92

Note. — The resonant state spin-parity has been restricted to 2^- . See [Hertzog *et al.* \(1974\)](#) and [Ramstein *et al.* \(1981\)](#) for details. These results are based on the simulation of 2.5×10^6 events for each potential primary transition. Coincidence simulated fit is determined using a 4 - 6.5 MeV coincidence gate. Singles and coincidence analyses make use of the angular coefficients for the R \rightarrow 709 keV primary reported by [Reinecke *et al.* \(1985\)](#). Calculated values (partial reaction numbers and branching ratios) are determined using a 68% credible interval from an abridged spectrum fit unless otherwise noted. Uncertainties associated with detector geometry (5%) and GEANT usage (1.3%) are included in the calculation of the partial reaction numbers and propagated through the following calculations.

$$^a Z = -3.59. \mathcal{N}_R^{29Si} = 91696186 \pm 3873275.$$

$$^b Z = -3.60. \mathcal{N}_R^{29Si} = 89498743 \pm 3919525.$$

^cThe partial numbers of reactions and branching ratios for this primary transition represent upper limits given by a 97.5% coverage interval.

References. — ¹[Reinecke *et al.* \(1985\)](#).

Singles and coincidence analyses of these branches are consistent with each other but perhaps inconsistent with the [Reinecke *et al.* \(1985\)](#) values. It is difficult to state this with any certainty, however, due to the lack of error analysis in [Reinecke *et al.* \(1985\)](#).

7.2.3 Resonance Energy

Following the procedure outlined in Section [7.1.3](#), the observed primary peak energies (Table [7.7](#)) were used to determine the laboratory frame resonance energy. This was found to be $E_r^{lab} = 325.8 \pm 0.6$ keV. It should be noted that this value does not agree with that of [Reinecke *et al.* \(1985\)](#), $E_r^{lab} = 324.1 \pm 0.7$ keV, within uncertainties, though the disagreement only amounts to a difference of 0.4 keV. The method used to calculate the resonance energy in this dissertation makes use of the nuclear Q-value, 5593.33 ± 0.07 keV, rather than the more commonly but erroneously used atomic Q-value ([Iliadis, 2019](#)), 5594.75 ± 0.07 keV ([Wang *et al.*, 2017](#)). The difference between these values readily accounts for the minor discrepancy between these resonance energy determinations.

7.2.4 Resonance Strength

Earlier, Table [7.6](#) made clear that the previously measured values for the $E_r^{lab} = 324$ keV resonance strength had not converged on an indisputable value. With this in mind and all of the necessary particulars—resonance energy, partial reaction numbers, etc.—at hand, the $E_r^{lab} = 324$ keV resonance strength, $\omega\gamma$, can be determined relative to the well known $E_r^{lab} = 416$ keV strength. Equation 4.128 in [Iliadis \(2015\)](#) gives the relationship between resonance strengths for the maximum yield in an infinitely thick target as

$$\frac{\omega\gamma_1}{\omega\gamma_2} = \frac{\varepsilon_{r,1}}{\varepsilon_{r,2}} \frac{\lambda_{r,2}^2}{\lambda_{r,1}^2} \frac{\Upsilon_{max,\Delta E \rightarrow \infty,1}}{\Upsilon_{max,\Delta E \rightarrow \infty,2}} = \frac{\varepsilon_{r,1}}{\varepsilon_{r,2}} \frac{\lambda_{r,2}^2}{\lambda_{r,1}^2} \frac{\mathcal{N}_{R,1}}{\mathcal{N}_{R,2}} \frac{\mathcal{N}_{p,2}}{\mathcal{N}_{p,1}} \quad (7.14)$$

where ε_r is the target stopping power, λ_r^2 is de Broglie wavelength, $\mathcal{Y}_{max, \Delta E \rightarrow \infty}$ is the maximum resonant yield in an infinitely thick target, \mathcal{N}_R is the total number of reactions from each $^{29}\text{Si}(p, \gamma)^{30}\text{P}$ resonance, and \mathcal{N}_p is the total number of incident protons. The subscripts 1 and 2 refer to the resonance of interest and the standard resonance, respectively. This can be rewritten for the specific application of this dissertation,

$$\omega\gamma_{ROI} = \frac{\varepsilon_{r,ROI}}{\varepsilon_{r,416}} \frac{\lambda_{r,416}^2}{\lambda_{r,ROI}^2} \frac{\mathcal{N}_{R,ROI}}{\mathcal{N}_{R,416}} \frac{\mathcal{N}_{p,416}}{\mathcal{N}_{p,ROI}} \omega\gamma_{416}, \quad (7.15)$$

where the 416 subscript refers to quantities of the standard resonance and ROI refers to those of the resonance of interest. This particular expression for the relative resonance strength has a few notable advantages over similar formulae. The most obvious benefit is its lack of explicit dependence on previous knowledge of the decay of the resonance of interest (i.e. primary branching ratios and angular correlation coefficients). Detector efficiencies and summing corrections are not explicitly included in this formula either. Instead, these parameters are implicitly included in the total number of reactions from the $^{29}\text{Si}(p, \gamma)^{30}\text{P}$ resonance calculated from the fractional contributions given in Tables 7.5 and 7.8, and Table 7.2 gives the systematic uncertainties adopted for the resonance calculations.

Even so, this formulation does rely on the target stoichiometry through the target stopping power, ε_r . This parameter is also given by Iliadis (2015) in Equation 4.94,

$$\varepsilon_r = \varepsilon_{eff} \equiv \varepsilon_X + \frac{n_Y}{n_X} \varepsilon_Y = (5.03 \pm 0.84) \times 10^{-15} \text{ eV cm}^2/\text{atom}, \quad (7.16)$$

where X refers to the target material (in this case, ^{29}Si) and Y the backing material (^{nat}Ta). The ratio n_Y/n_X is equivalent to the target stoichiometry which was found in Section 5.2, and material stopping powers are provided by the recent evaluations of Ziegler *et al.* (2015). Additionally, the de Broglie wavelengths rely upon the resonance energies determined in Sections 7.1.3 and 7.2.3. The adopted $E_r^{lab} = 416$ keV resonance

strength, $\omega\gamma_{416}$, was presented in Table 7.3. Altogether, Equation 7.15 yields the $E_r^{lab} = 324$ keV resonance strength,

$$\omega\gamma = 0.023 \pm 0.004 \text{ eV}. \quad (7.17)$$

Figure 7.14 illustrates the relationship between the resonance strength of this work and that of previous experiments. Past measurements of the resonance strength are shown with their uncertainties in black. The resonance strength determined in this dissertation is shown in red. Dashed lines indicate the error band of the current measurement, making clear that the current measurement agrees with all three previous

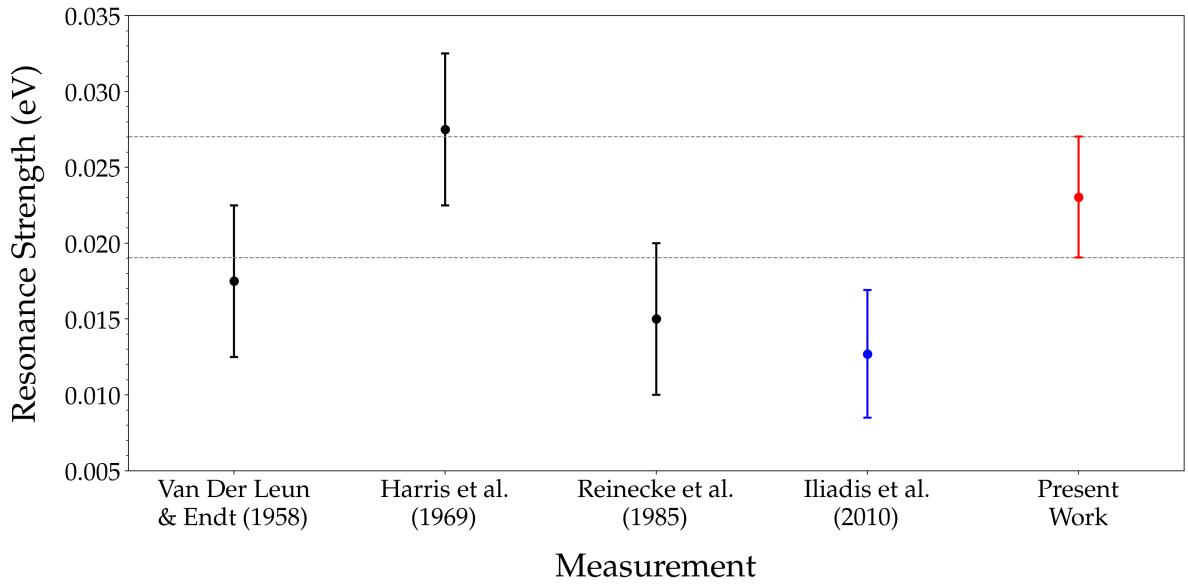


Figure 7.14: A comparison of past $E_r^{lab} = 324$ keV resonance strength measurements with that of the current work. The previous measurements are shown in black while the measurement of the current work is shown in red. The Iliadis *et al.* (2010a) derived value, obtained from the Reinecke *et al.* (1985) strength renormalized to a $E_r^{lab} = 416$ keV resonance strength of $\omega\gamma = 0.22 \pm 0.021$ eV, was used as the nuclear physics input for the STARLIB reaction rate library (Sallaska *et al.*, 2013) and provides another useful comparison to the current work. Dashed lines indicate the error band of the current measurement and help guide the eye. It should be noted that the Harris *et al.* (1969) strength was renormalized using the $E_r^{lab} = 416$ keV strength given by Riihonen *et al.* (1979).

measurements though this is partially caused by the large uncertainties on these previous resonance strengths. The present measurement also represents an improvement to the uncertainty of previous measurements. More importantly, the present work is significantly less prone to systematic uncertainties arising from the use of a large-volume HPGe detector, and the observation of five new primary transitions indicates that the current work represents an increase in sensitivity over the [Reinecke *et al.* \(1985\)](#) experiment.

The STARLIB ([Sallaska *et al.*, 2013](#)) nuclear physics input for this resonance ([Iliadis *et al.*, 2010a](#)) is shown in blue. This value, which is roughly a factor of two less than this dissertation's strength, helps illustrate the significant effect the current work's measurement will have on a recalculated $^{29}\text{Si}(p,\gamma)^{30}\text{P}$ reaction rate. This impact will be explored later in this text (Chapter 8).

7.3 314 keV Resonance

Following the study of the $E_r^{lab} = 416$ keV and $E_r^{lab} = 324$ keV resonances, the study of the $E_r^{lab} = 314$ keV resonance presents a new challenge: it does not appear to have been detected in the past. Previous indirect measurements of the ^{30}P level structure provide the only available information on this resonance.

The resonant level in ^{30}P , $E_x = 5890 \pm 12$ keV, was discovered by [Van Gasteren *et al.* \(1974\)](#). These authors used the $^{31}\text{P}(t,\alpha)^{30}\text{P}$ reaction primarily to determine the spectroscopic factors of ^{30}P levels above 3 MeV. They employed two different types of ^{31}P targets (Zn_3P_2 and natural red phosphorus) along with a split-pole magnetic spectrograph and position sensitive detectors. Their measurements were carried out at 23 different angles between 15° and 125° . Because they did not observe the energy level corresponding to the $E_r^{lab} = 324$ keV resonance, $E_x = 5907.7 \pm 0.8$ keV (as given by [Grossmann *et al.*, 2000](#)), they were able to observe the energy level corresponding

to the $E_r^{lab} = 314$ keV resonance even with their detector's somewhat limited energy resolution (15-20 keV at full-width half-maximum). The authors also posit that this state is an analogue to the 5.23 MeV state in ^{30}Si which has spin-parity $J^\pi = 3^+$, implying that the $E_x = 5890 \pm 12$ keV state also has a spin-parity of $J^\pi = 3^+$. Endt and van der Leun (1978) provides a more conservative spin-parity restriction of $J^\pi = (1 - 3)^+$, but they do not provide further details on their reasoning. Ramstein *et al.* (1981), whose $^{30}\text{Si}(^3\text{He}, t)^{30}\text{P}$ study was described earlier in Section 7.2, determined a spin-parity of 3^+ , in agreement with the Van Gasteren *et al.* (1974) findings. Beyond one resonant energy level measurement and a few speculative spin-parity assignments, nothing further is known about a potential $^{29}\text{Si}(p, \gamma)^{30}\text{P}$ resonance at 314 keV, making the exploratory study detailed in the following pages a trying but intriguing task.

7.3.1 Measurement

The first ever direct measurement of the $E_r^{lab} = 314$ keV resonance was undertaken using the same methods described in Section 7.1.1 with the added complication of its proximity to the $E_r^{lab} = 324$ keV resonance. However, the excitation curve of the energy region (Figure 7.8) shows that it was possible to measure the maximum yield of the $E_r^{lab} = 314$ keV resonance at a proton energy of $E_p = 317$ keV without the interference of the significantly stronger $E_r^{lab} = 324$ keV resonance. The $E_r^{lab} = 314$ keV data collection is summarized in Table 7.1. In order to better distinguish peaks of the resonance of interest from those of contaminants, off-resonance data was taken at 10 keV below the bombarding energy.

Singles and coincidence spectra were obtained for the maximum yield measurement of the $E_r^{lab} = 314$ keV resonance. The coincidence spectrum was produced using the Equation 7.1 energy condition and by disregarding events coincident with the muon-veto panels. The resultant spectra are shown in Figure 7.15. The singles spectrum is displayed here in black and the $\gamma\gamma$ -coincidence spectrum in red. Prominent

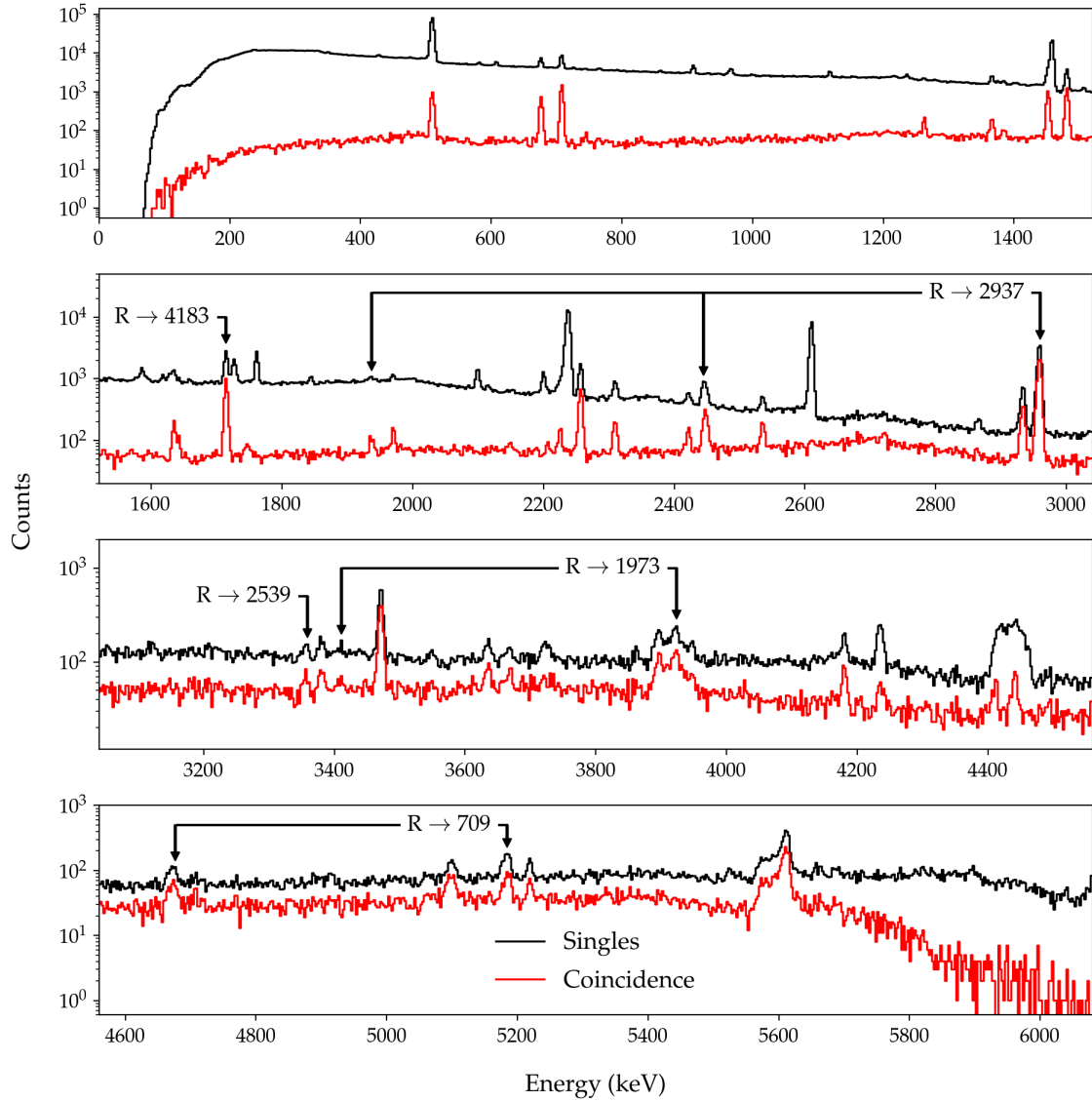


Figure 7.15: HPGe singles and $\gamma\gamma$ -coincidence pulse-height spectra of the $^{29}\text{Si}(p,\gamma)^{30}\text{P}$ $E_r^{\text{lab}} = 314$ keV resonance. The singles spectrum is shown in black, while the coincidence spectrum is shown in red. The full-energy primary peaks are denoted by arrows and labels of the form $R \rightarrow E_f$, where R is the resonant excitation energy and E_f is the bound state to which the compound state decays. Prominent escape peaks of primary transitions are similarly indicated where they are clearly visible in the spectra.

Table 7.9. Energies & Decay Intensities for the $E_r^{lab} = 314$ keV Resonance

Primary Transition	J^π	E_γ (keV)	Intensity	
			Singles	Coincidence
$R \rightarrow 4182.81$	2^+	1717.44 ± 1.68	5121.58 ± 130.90	2142 ± 54
$R \rightarrow 2937.46$	2^+	2962.24 ± 1.20	10492.65 ± 116.42	6376 ± 87
$R \rightarrow 2538.95$	3^+	3356.79 ± 2.33	149.61 ± 46.74	80 ± 31
$R \rightarrow 1973.27^a$	3^+	...	< 59	< 44
$R \rightarrow 1454.23^a$	2^+	...	< 73	188 ± 28
$R \rightarrow 708.70$	1^+	5184.37 ± 2.41	580.37 ± 56.87	253 ± 39
$R \rightarrow 677.01$	0^+	5221.71 ± 2.01	188.03 ± 43.93	94 ± 30
$R \rightarrow 0^a$	1^+	...	< 50	< 34

Note. — The resonant state spin-parity has been restricted to $(1-3)^+$ (see [Van Gasteren *et al.*, 1974](#); [Ramstein *et al.*, 1981](#); [Endt, 1998](#)). For all other spin-parity assignments, see [Endt \(1998\)](#). Presented intensities are based on 4.704253 C accumulated on target. Coincidence intensities are determined using a 4.0 - 6.5 MeV coincidence gate where the reported $R \rightarrow 0$ keV intensity corresponds to the single-escape peak intensity for this transition. No observed energies are presented for transitions with upper limit intensities.

^aThe measured peak intensities for this primary transition should be considered upper limit values, estimated as $\sqrt{2 \times BG}$, where BG indicates the number of background counts in the region of interest. In the case of the $R \rightarrow 1454$ keV primary transition in the singles spectrum, any peak that may be present cannot be distinguished due to broad structure from $^{11}\text{B}(p,\gamma)^{12}\text{C}$ at 4.4 MeV. Coincidence gating excludes this $^{11}\text{B}(p,\gamma)^{12}\text{C}$ contribution, and the primary transition is visible in this spectrum as a result.

escape peaks of the primary transitions are also indicated where clearly visible in the spectra. Primaries to which upper limit intensities have been assigned are not labeled in this figure. Five full-energy primary peaks—to the 677 keV, 709, keV, 2539 keV, 2937 keV, and 4183 keV bound states—were plainly visible in the spectra. Additionally, three weaker primaries—to the 0 keV, 1454 keV, and 1973 keV states—are suggested by the observed spectra.

The background-subtracted full-energy primary peak energies and intensities for

both spectra are given in Table 7.9. Note that because coincidence summing effects will be handled implicitly in the analysis (see Section 7.3.2), no summing correction to these intensities was required. Upper limit intensities for three potential primaries are provided in this table, but their full-energy peaks are not pronounced enough to allow for peak energy measurements. It should be noted that in the singles spectrum a broad structure produced by $^{11}\text{B}(\text{p},\gamma)^{12}\text{C}$ obscures any sign of a $\text{R} \rightarrow 1454 \text{ keV}$ in the 4.4 MeV region. As such only an upper limit intensity is reported for this primary in the singles analysis. Coincidence gating proved quite successful in reducing the interference of the $^{11}\text{B}(\text{p},\gamma)^{12}\text{C}$ contamination in this region though. Consequently, a full-energy peak intensity is reported for this primary in the coincidence spectrum.

7.3.2 Analysis

As can be expected, the analysis of the $E_r^{lab} = 314 \text{ keV}$ resonance is significantly more challenging than the resonances presented earlier in this dissertation. For one, the lack of previously determined decay scheme means that extra care must be taken to correctly identify peaks produced by the resonance of interest. At first glance this resonance also appears to be at least two orders of magnitude weaker than the $E_r^{lab} = 324 \text{ keV}$ resonance, meaning that not only are signals from the resonance of interest more difficult to observe but the level of interference from beam-induced contaminant reactions is substantially greater than encountered in the prior measurements of this dissertation. Additionally, no information regarding the angular distribution of its γ -decay is available, and the decay must be assumed to be isotropic as a result.

Nevertheless, analysis of this resonance was commenced in the fashion described earlier (Section 7.1.2). With all spectral contributions gathered and necessary templates produced and condensed, the fitting process was carried out as described in Chapter 6 for both the singles and $\gamma\gamma$ -coincidence data. The resulting fits provide

the fraction each $E_r^{lab} = 314$ keV primary or beam-induced contaminant reaction contributes to the spectrum. The partial number of reactions, branching ratios, and resonance strength are then derived from these fractional contributions.

The successful fit of the $E_r^{lab} = 314$ keV singles spectrum is shown in Figures 7.16 and 7.17. Figure 7.16 displays the qualitative agreement between the observed singles data and fit of this spectrum. The observed pulse-height spectrum is shown in black. The red line represents the fit and was produced using the median fractional contribution of each template.

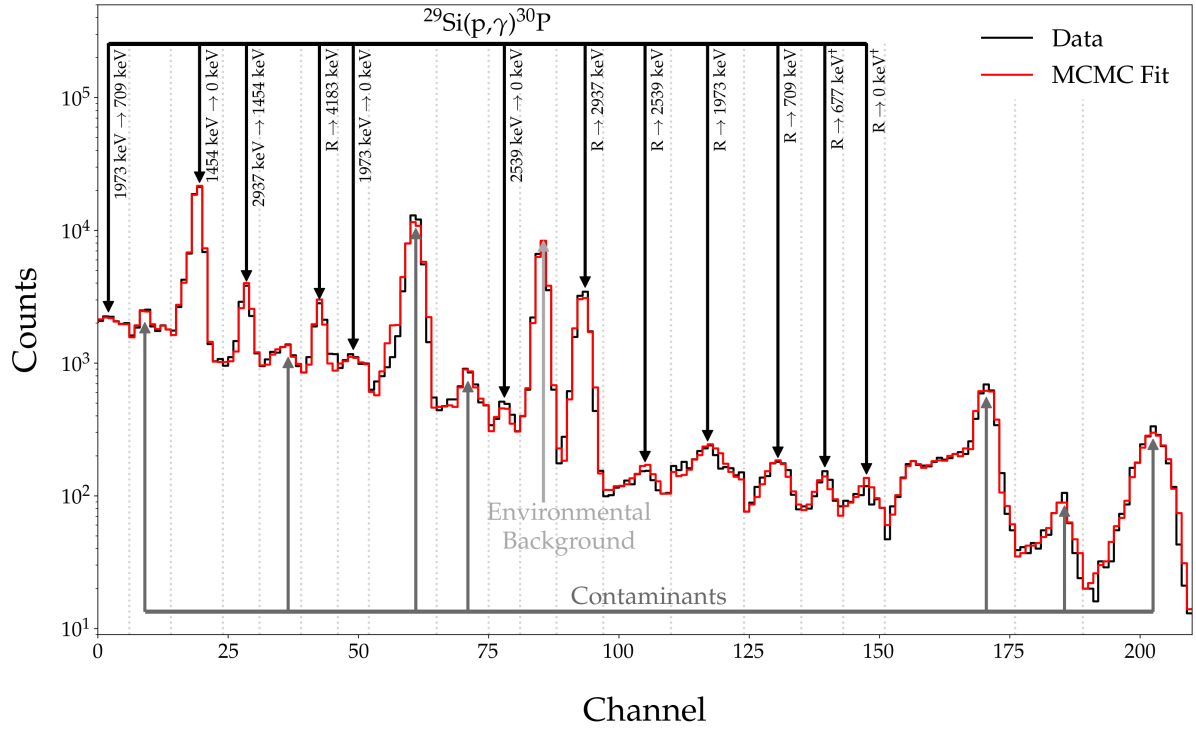


Figure 7.16: Measured (black) and simulated (red) pulse-height spectra for the $^{29}\text{Si}(p,\gamma)^{30}\text{P}$ $E_r^{lab} = 314$ keV abridged singles analysis. See Figure 7.4 for details.

The posterior distributions and data projections of Figure 7.17 indicate how well each primary from the resonance of interest is reproduced by the fit. With the exception of the $R \rightarrow 0$ keV and $R \rightarrow 1454$ keV primaries, the Gaussian shape of the template posteriors indicate that the observed spectrum is satisfactorily reproduced by the fit. The $R \rightarrow 677$ keV primary, while sufficiently modeled by the singles fit

shown in this figure, will be treated as an upper limit and will be discussed shortly. In both Figures 7.16 and 7.17 the \dagger superscript indicates a $^{29}\text{Si}(p,\gamma)^{30}\text{P}$ primary handled as an upper limit contribution.

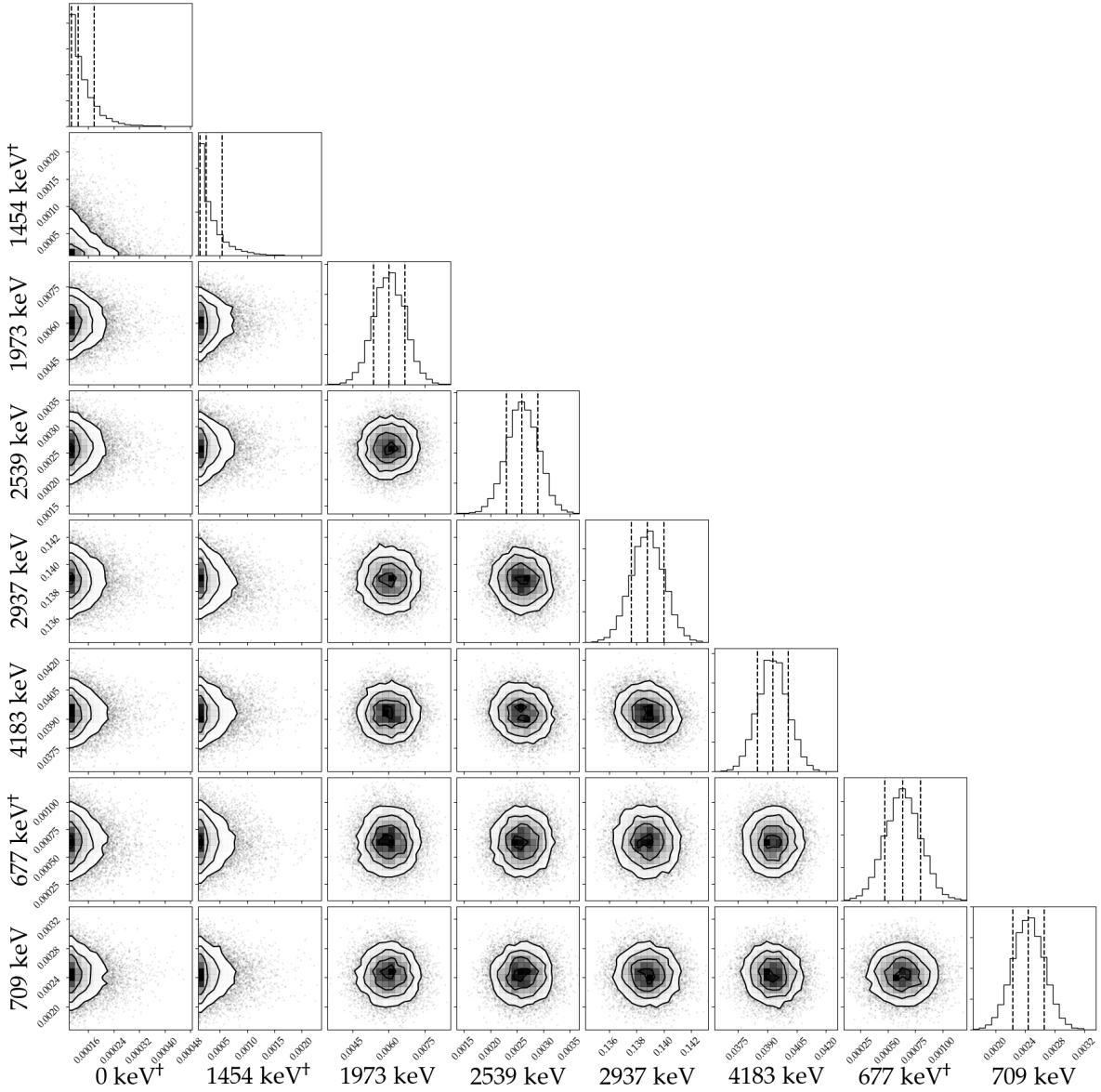


Figure 7.17: Template posterior distributions and two-dimensional pairwise posterior projections from the MCMC fraction fit of the $^{29}\text{Si}(p,\gamma)^{30}\text{P}$ $E_r^{\text{lab}} = 314$ keV singles abridged spectrum. For more information, see Figure 7.3.

To demonstrate the effective fit of the $E_r^{\text{lab}} = 314$ keV coincidence spectrum, Figures 7.18 and 7.19 were produced. The posterior distributions of Figure 7.18, similar to

those of Figure 7.17 of the singles fit, indicate that the $R \rightarrow 709$ keV, $R \rightarrow 1973$ keV, $R \rightarrow 2539$ keV, $R \rightarrow 2937$ keV, and $R \rightarrow 4183$ keV primary transitions are acceptably reproduced by the Metropolis Hastings MCMC fit. The posteriors of the three remaining primaries are not adequately emulated by the fit however. Thus, median fractional contributions as well as median partial reaction numbers and branching ratios cannot be presented for these branches. In accordance with the upper limit designation of the $R \rightarrow 677$ keV branch in the coincidence fit shown here, this branch is also treated as an upper limit in the singles fit presented earlier.

Figure 7.19 demonstrates the MCMC fit to the coincidence spectrum in another way. In this figure, the observed, abridged pulse-height spectrum is shown in black, and the fit to the data, based on the median fractional contribution of each template, is shown in red. It is clear from this figure that, if some allowance is made for statistical fluctuations, the fit tracks with the observed spectrum quite well. It should also be noted that the coincidence gating reduced the presence of beam-induced contaminant peaks substantially so only two contaminant peaks are included in this abridged spectrum as opposed to the seven contaminant peaks in the abridged singles spectrum. The environmental background (represented in this figure by the $^{208}\text{Tl}(\beta^- \bar{\nu}_e)^{208}\text{Pb}$ peak at 2614 keV) appears to be underpredicted by the coincidence fit. This is likely caused by the way the environmental template for the coincidence spectrum is produced, but coincidence gating reduces the impact of the environmental background to the point where it is of little concern.

The singles and coincidence fit results presented in these four figures are summarized in Table 7.10. The primary partial number of reactions and branching ratios for each analysis are given in this table. The test statistic, Z , was found to be -0.971 and -0.329 for the singles and coincidence analyses, respectively, indicating that both spectra are reasonably recreated by the MCMC fit. Because this is the very first measurement of this resonance, the only comparison to be made with this data is between

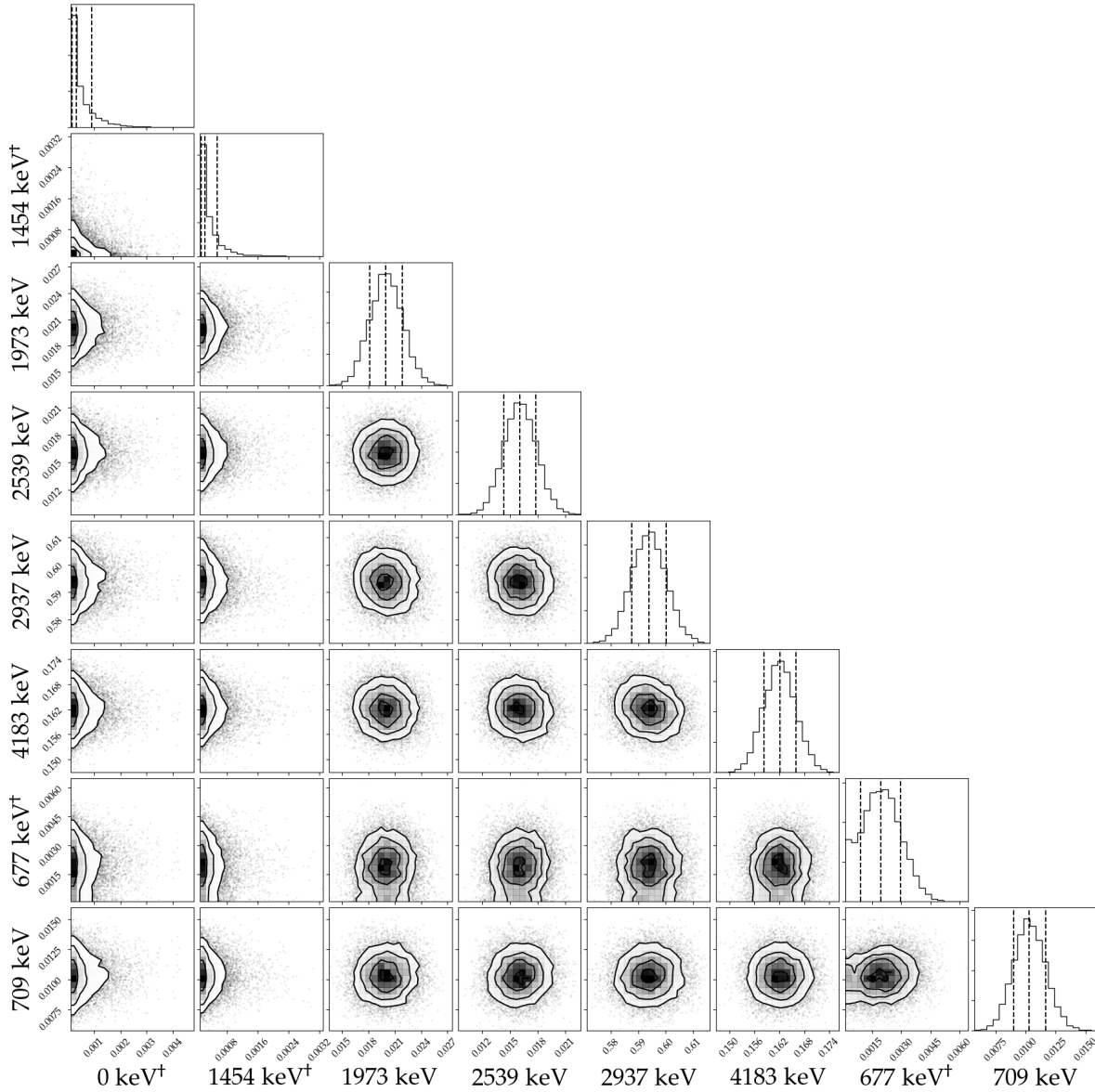


Figure 7.18: Template posterior distributions and data projections from the MCMC fraction fit of the $^{29}\text{Si}(p,\gamma)^{30}\text{P}$ $E_r^{\text{lab}} = 314$ keV coincidence abridged spectrum. The coincidence spectrum was found using a 4.0 - 6.5 MeV trapezoidal gate. For more information, see Figure 7.3.

the singles and coincidence fit results. Fortuitously, the agreement between the two analyses is excellent. The total number of reactions from $^{29}\text{Si}(p,\gamma)^{30}\text{P}$ from the singles and the coincidence analyses are in good agreement with each other. All primary branching ratios and partial reaction numbers agree within their uncertainties with

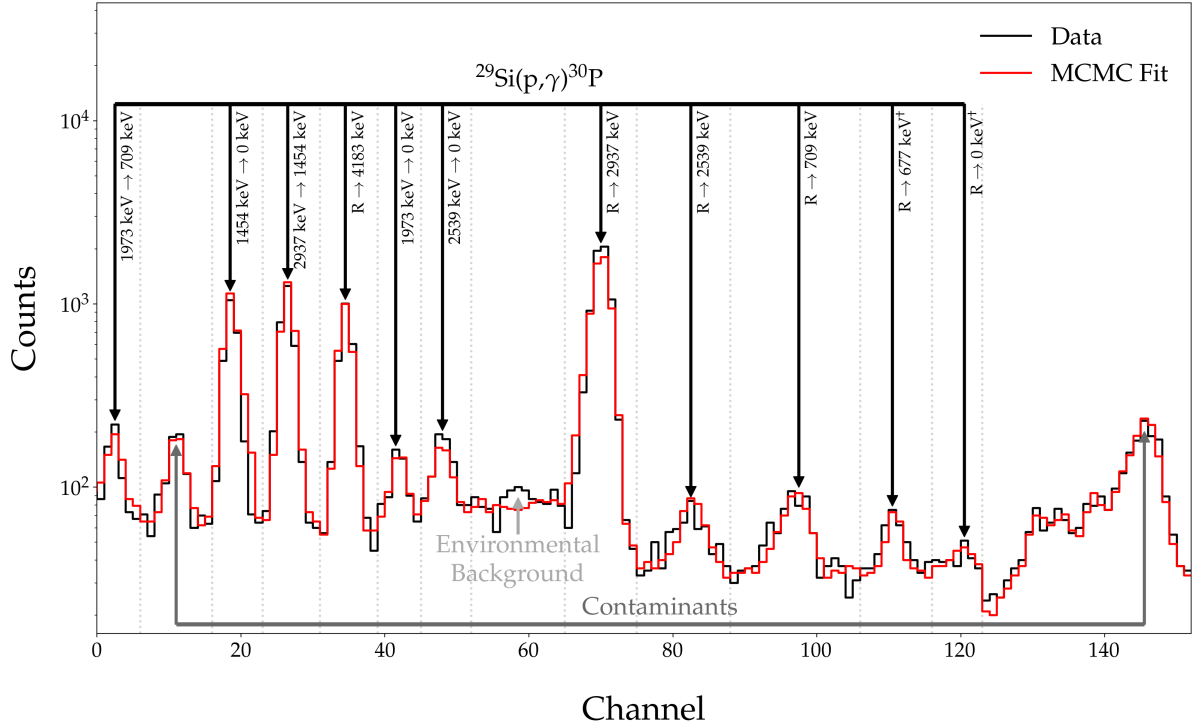


Figure 7.19: Measured (black) and simulated (red) pulse-height spectra for the $^{29}\text{Si}(p,\gamma)^{30}\text{P}$ $E_r^{\text{lab}} = 314$ keV abridged coincidence analysis. The coincidence spectrum was determined using a 4.0 - 6.5 MeV trapezoidal gate. See Figure 7.4 for details.

the minor exception of the $R \rightarrow 2539$ keV branch which falls very slightly outside the range of agreement. Though this branch is not presented as an upper limit, it is weak, and this disagreement is negligible as a result.

7.3.3 Resonance Energy

As mentioned earlier, the indirect measurement of the excitation energy level, E_x , was restricted to $E_x = 5890 \pm 12$ keV by [Van Gasteren *et al.* \(1974\)](#). This value can be used to give the approximate laboratory frame resonance energy by adapting Equation C.31 in [Iliadis \(2015\)](#),

$$E_x = E'_a + Q_{nu} = E_a \frac{m_A}{m_a + m_A} + Q_{nu}, \quad (7.18)$$

Table 7.10. $E_r^{lab} = 314$ keV Fit Results

Primary Transition	Singles ^a		Coincidence ^b	
	$\mathcal{N}_R^{Partial}$	B_γ (%)	$\mathcal{N}_R^{Partial}$	B_γ (%)
R \rightarrow 4182.81	196706 ± 10899	23.18 ± 1.30	189369 ± 10863	23.08 ± 1.33
R \rightarrow 2937.46	581837 ± 30547	68.55 ± 1.49	558360 ± 29750	68.05 ± 1.54
R \rightarrow 2538.95	10923 ± 1375	1.29 ± 0.17	14763 ± 1784	1.80 ± 0.23
R \rightarrow 1973.27	26253 ± 3155	3.09 ± 0.38	27109 ± 2888	3.30 ± 0.36
R \rightarrow 1454.23 ^c	< 5618	< 0.66	< 1582	< 0.19
R \rightarrow 708.70	33063 ± 3368	3.89 ± 0.41	30904 ± 4286	3.77 ± 0.52
R \rightarrow 677.01 ^c	< 12950	< 1.53	< 11929	< 1.45
R \rightarrow 0 ^c	< 3325	< 0.39	< 5773	< 0.70

Note. — The resonant state spin-parity has been restricted to $(1-3)^+$ (Van Gasteren *et al.*, 1974; Ramstein *et al.*, 1981; Endt, 1998). The results displayed in this table are based on the GEANT4 simulation of 2.5×10^6 events for each primary transition. Coincidence simulated fit is determined using a 4 - 6.5 MeV coincidence gate. Calculated values (partial reaction numbers and branching ratios) are determined using a 68% credible interval from an abridged spectrum fit unless otherwise noted. Uncertainties associated with detector geometry (5%) and GEANT4 usage (1.3%) are included in the calculation of the partial reaction numbers and propagated through the following calculations.

$$^a Z = -0.971. \mathcal{N}_R^{29Si} = 848782 \pm 32789.$$

$$^b Z = -0.329. \mathcal{N}_R^{29Si} = 820505 \pm 32140.$$

^cThe partial numbers of reactions and branching ratios for this primary transition represent upper limits given by a 97.5% coverage interval.

where E'_a is the projectile energy in the center-of-mass frame, E_a is the projectile energy (or, in this case, the resonance energy) in the laboratory frame, Q_{nu} is the nuclear Q-value for $^{29}\text{Si}(p,\gamma)^{30}\text{P}$, and m_a and m_A are the masses of the projectile and target, respectively. This gives the literature-derived resonance energy, E_r^{lab} of 307 ± 12 keV.

Next, the observed primary peak energies in Table 7.9 were employed in order to determine the experimental laboratory frame resonance energy of the current work. This was accomplished using the procedure laid out in Section 7.1.3. The laboratory frame resonance energy was found to be $E_r^{lab} = 314.4 \pm 0.8$ keV. This value is in agreement with the literature value and also provides a vast improvement on the uncertainty of this resonance energy.

7.3.4 Resonance Strength

Finally, the first ever $E_r^{lab} = 314$ keV strength was calculated. This calculation followed the procedure described by Equations 7.15 - 7.16 in Section 7.2.4. To summarize, the effective stopping power for the resonance energy, ε_r , was calculated using material stopping powers from SRIM (Ziegler *et al.*, 2015), the experimentally determined laboratory frame resonance energy (Section 7.3.3), and the target stoichiometry (Section 5.2) according to Equation 7.16. The total number of reactions from the $E_r^{lab} = 314$ keV resonance was determined by calculating the unweighted average of the values from the singles and coincidence fits. The total number of incident protons for the measurement and the de Broglie wavelength were easily derived from the total accumulated charge at $E_p = 317$ keV and the experimental laboratory frame resonance energy, respectively. Combining these values with that of the standard resonance, $E_r^{lab} = 416$ keV, the $E_r^{lab} = 314$ keV resonance strength was found to be

$$\omega\gamma = (1.0 \pm 0.2) \times 10^{-4} \text{ eV}. \quad (7.19)$$

This is a significant result, not just because it marks the first direct measurement of the $E_r^{lab} = 314$ keV resonance strength but also because it indicates that this resonance may make a more significant contribution to the $^{29}\text{Si}(p,\gamma)^{30}\text{P}$ reaction rate than originally imagined. In fact, the STARLIB nuclear physics input for this resonance results in an estimated $\omega\gamma$ upper limit of 4.0×10^{-5} eV, 2.5 times smaller than the resonance strength measured in this dissertation. The impact of this resonance strength measurement will be discussed further in Chapter 8.

7.4 221 keV Resonance

As was mentioned in the introduction to this chapter, the wide-ranging and exhaustive work of [Endt and Paris \(1958\)](#) involved the high resolution analysis of the $^{32}\text{S}(d, \alpha)^{30}\text{P}$ reaction to learn more about the structure of the ^{30}P nucleus. Chief among their accomplishments was their success at resolving the ^{30}P first- and second-excited state doublet for the first time. This doublet was thought to be a single level based on past measurements. They also precisely measured 28 additional energy levels in the ^{30}P nucleus up to 5.8 MeV, and it was in this group of level measurements that the nascent signs of a potential $^{29}\text{Si}(p,\gamma)^{30}\text{P}$ resonance at $E_r^{lab} = 221$ keV emerged.

[Endt and Paris \(1958\)](#) found a level in ^{30}P at $E_x = 5790 \pm 10$ keV, and this level wasn't remeasured until 16 years later by [Hafner and Duhm \(1974\)](#). Their work concerned another indirect measurement of the ^{30}P nucleus, this time employing the $^{28}\text{Si}(^3\text{He}, p)^{30}\text{P}$ reaction at incident energies of 16 MeV and 28 MeV. They observed the resultant proton spectrum via a magnetic spectrograph and observed this level at $E_x = 5807 \pm 15$ keV. Their observed energy level was supported by the work of [Boerma *et al.* \(1975\)](#) ($^{32}\text{S}(\vec{d}, \alpha)^{30}\text{P}$) and [Dykoski and Dehnard \(1976\)](#) ($^{29}\text{Si}(^3\text{He}, d)^{30}\text{P}$) who found excitation energies of $E_x = 5810 \pm 5$ keV and 5808 ± 5 keV, respectively.

These two papers also provided the first restrictions to the spin-parity of this state—unnatural parity (Boerma *et al.*, 1975) and $(1^+, 2^+, 3^+)$ (Dykoski and Dehnhard, 1976). Ramstein *et al.* (1981) went on to restrict the spin-parity to 3^+ by applying the “fingerprint” method to their observed $^{30}\text{Si}(^3\text{He}, t)^{30}\text{P}$ angular distributions. This restriction is in conflict with that of shell model calculations (Grossmann *et al.*, 2000, and references therein), which indicate a spin-parity of 5^+ .

Unfortunately, this information—a somewhat imprecise excitation energy and a few contradictory spin-parity restrictions—completes the summary of available information on a potential $^{29}\text{Si}(p, \gamma)^{30}\text{P}$ resonance at $E_r^{lab} = 221$ keV. The deexcitation branching ratios and resonance strength are unknown, though Iliadis *et al.* (2010a) provides an upper limit resonance strength estimate, $\omega\gamma < 3.1 \times 10^{-7}$ eV, based on spectroscopic factor upper limits obtained in the transfer study of Dykoski and Dehnhard (1976). Altogether, these factors combine to make attempting a $E_r^{lab} = 221$ keV study an intriguing if trying endeavor.

7.4.1 Measurement

Because of the low predicted resonance strength discussed earlier, the measurement of the $E_r^{lab} = 221$ keV resonance required a substantially different approach than that of the other resonances studied in this work. First, the LENA II 240 kV Electron Cyclotron Resonance (ECR) accelerator (Section 4.1.2) was used to produce the necessary proton beam in favor of the LENA I JN Van de Graaff accelerator used for the other resonant measurements. The superior utility of the LENA II accelerator was discussed earlier. To summarize, this accelerator is capable of proton currents at energies below the range of LENA I and with intensities unmatched by the vast majority of accelerators in its class (including the LENA I). The LENA II also makes use of a beam pulsing system that helps mitigate target damage caused by high currents and can

be used in tandem with the data acquisition system to eliminate the “beam-off” periods from the resultant spectra (see Section 4.1.2 for details), though the latter feature was not used in this work. The pulsed beam was also rastered over the implanted target surface to prevent inhomogeneous target degradation and average the effect of any local target irregularities. As was the case for the measurement of the three other $^{29}\text{Si}(\text{p},\gamma)^{30}\text{P}$ resonances, the $\gamma\gamma$ -coincidence spectrometer was arranged in close geometry to the target chamber to optimize detection of the $E_r^{lab} = 221$ keV resonance.

Owing to the potential for target damage at high current and charge accumulation, it was decided that it would be best to forgo the initial yield curve performed at the start of the other resonant measurements to help determine the best bombarding energy. A bombarding energy of 227 keV was chosen by considering the expected resonance energy, target thickness measurements from the other $^{29}\text{Si}(\text{p},\gamma)^{30}\text{P}$ resonances in this work and accelerator stability limitations. Thus, a high-intensity, pulsed $E_p = 227$ keV proton beam was generated with the LENA II ECR accelerator and used to bombard the ^{29}Si implanted target. As summarized in Table 7.1, 9.972895 C were accumulated on target over a period of 15647 s. The proton beam was pulsed with a frequency of 10 Hz and a duty cycle of 30%. While the proton beam was incident on the nuclear target (or “on-pulse”), the average current was 2.125 mA, though this only represents 30% of the total running time of the experiment. Thus, the average proton current over the entire running time of the experiment, including both on- and off-pulse periods, was actually 637.4 μA . The average dead time was kept to a minimum, 1.2% over the course of the experiment.

The data acquisition was carried out in largely the same manner described in Section 7.1.1 with one exception. While no corrections or gating were applied to the singles spectrum, the coincidence spectrum was produced with an energy condition that differs from the one used for the analysis of the other three $^{29}\text{Si}(\text{p},\gamma)^{30}\text{P}$ resonances

presented in this dissertation. This energy condition,

$$\begin{aligned} 2.9 \text{ MeV} &\leq E^{\text{HPGe}} + E^{\text{NaI}} \leq 5.9 \text{ MeV} \\ E^{\text{NaI}} &\geq 0.64 \text{ MeV} \end{aligned} \quad (7.20)$$

serves two purposes. First, it facilitates the efficient observation of decays from the compound state energy, $E_x = 5808 \pm 3 \text{ keV}$ (adopted by [Endt, 1998](#)), or in the absence of observed decay peaks, it allows for the establishment of strict upper limits on potential primary peak intensities. Second, it dramatically reduces the presence of contaminant reactions, primarily the $E_r^{\text{lab}} = 224 \text{ keV}$ resonance in $^{19}\text{F}(\text{p}, \alpha\gamma)^{16}\text{O}$ ([Tilley et al., 1998](#)), in the spectrum. Events coincident with the muon-veto panels were also disregarded in the coincidence data acquisition.

The resulting singles and coincidence spectra are displayed in Figure 7.20. The singles spectrum is shown in black, while the coincidence spectrum is shown in red. No $^{29}\text{Si}(\text{p}, \gamma)^{30}\text{P}$ peaks were observed in this measurement, so the peaks visible in these spectra are the result of environmental background reactions ($E \leq 2.6 \text{ MeV}$) or beam-induced contaminant reactions (mainly $E > 2.0 \text{ MeV}$). A cursory comparison between the two spectra reveals the success of the coincidence energy gate at reducing the impact of environmental background and beam-induced contaminants. In particular, note the reduction of the single- and double-escape intensities of the $^{19}\text{F}(\text{p}, \alpha\gamma)^{16}\text{O}$ characteristic peak at 6130 keV.

Upper limit intensity values for the potential primary peaks in the $E_r^{\text{lab}} = 221 \text{ keV}$ are presented in Table 7.11. Because no decay scheme has been measured in the past and the resonance was not observed in the current work, one must speculate as to what bound levels the compound state may decay. As a result, the potential primary decays included in Table 7.11 were chosen based two criteria: the “dipole or E2” rule given in [Endt \(1990\)](#) and the decay structure of other $^{29}\text{Si}(\text{p}, \gamma)^{30}\text{P}$ resonances that share their spin-parity with the resonance of interest (restricted to 3^+ or 5^+ by [Endt, 1990](#)).

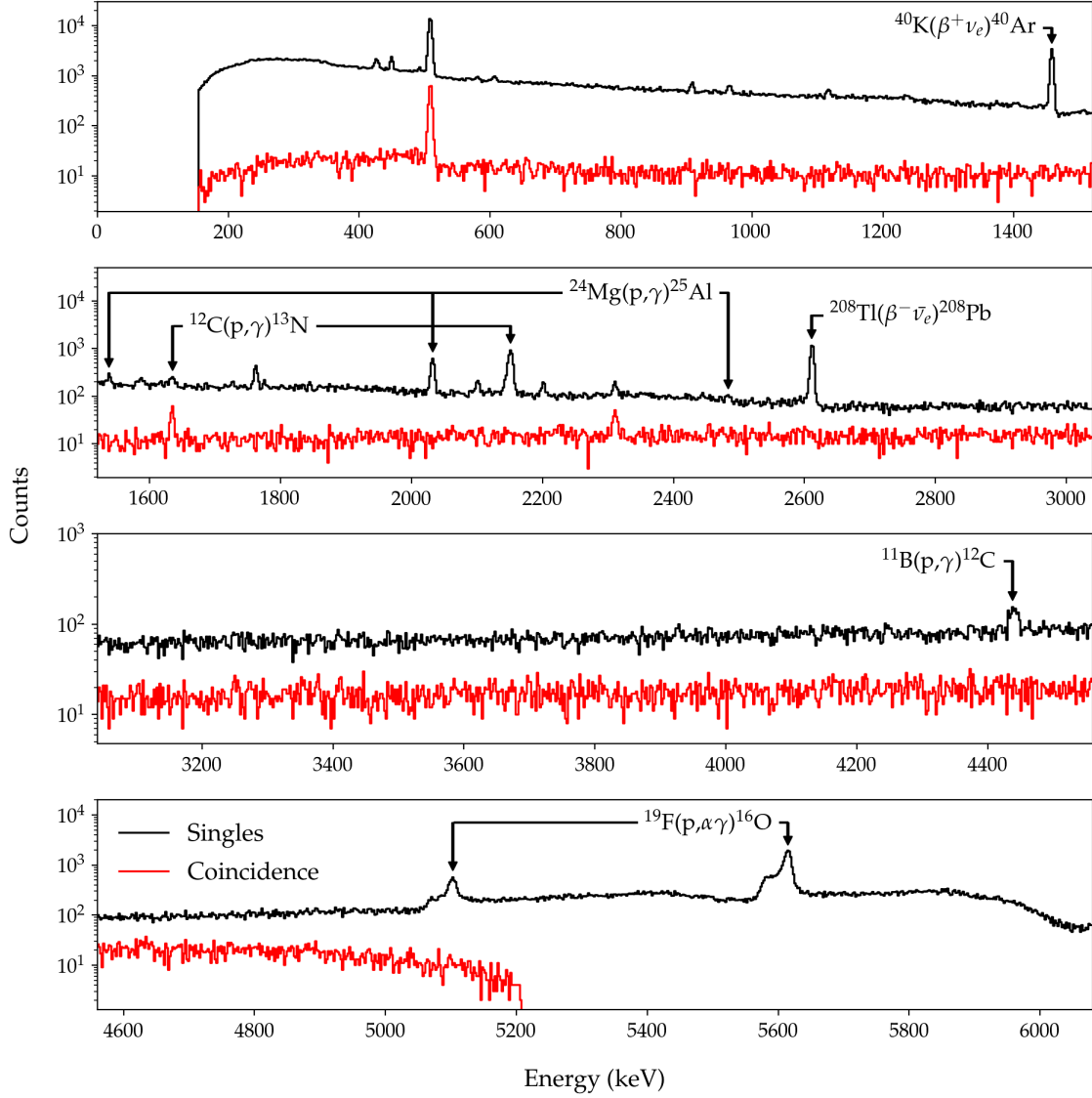


Figure 7.20: HPGe singles and $\gamma\gamma$ -coincidence pulse-height spectra of the $^{29}\text{Si}(p,\gamma)^{30}\text{P}$ $E_r^{\text{lab}} = 221$ keV resonance. The singles spectrum is shown in black, while the coincidence spectrum is shown in red. No $^{29}\text{Si}(p,\gamma)^{30}\text{P}$ peaks were observed, but several observed contaminant and environmental background peaks are noted on the figure.

Table 7.11. Energies & Decay Intensities for the $E_r^{lab} = 221$ keV Resonance

Primary Transition	J^π	Intensity	
		Singles	Coincidence
$R \rightarrow 4343.80$	5^+	< 141	< 14
$R \rightarrow 2937.46$	2^+	< 33	< 18
$R \rightarrow 2839.34$	3^+	< 34	< 17
$R \rightarrow 2723.72$	2^+	< 33	< 17
$R \rightarrow 2538.95$	3^+	< 35	< 17
$R \rightarrow 1973.27$	3^+	< 36	< 17
$R \rightarrow 1454.23$	2^+	< 43	< 21
$R \rightarrow 708.70$	1^+	< 90	< 15
$R \rightarrow 0$	1^+	< 80	< 19

Note. — The resonant state spin-parity has been restricted to $(3, 5)^+$ by (Endt, 1990). For all other spin-parity assignments, see Endt (1998). Presented intensities are upper limit values (estimated as $\sqrt{2 \times \text{BG}}$ where BG indicates the number of background counts in the region of interest) based on 9.97289 C accumulated on target. Coincidence intensities are determined using a 2.9–5.9 MeV coincidence gate where the reported $R \rightarrow 0$ keV intensity upper limit corresponds to the double-escape peak intensity upper limit for this transition.

As evidenced by the low primary peak intensities given in this table, the coincidence gating was quite valuable in reducing the effect of background reactions.

7.4.2 Analysis

Though the $E_r^{lab} = 221$ keV resonance was not observed, its analysis was not as different from the analysis of the preceding resonances as one might expect. The argument could be made that this application shows the versatility of the fraction fitting methodology actually.

The template posteriors and data projections of each $^{29}\text{Si}(p,\gamma)^{30}\text{P}$ template included in the singles fit are given in Figure 7.21. The vertical dashed line on each posterior

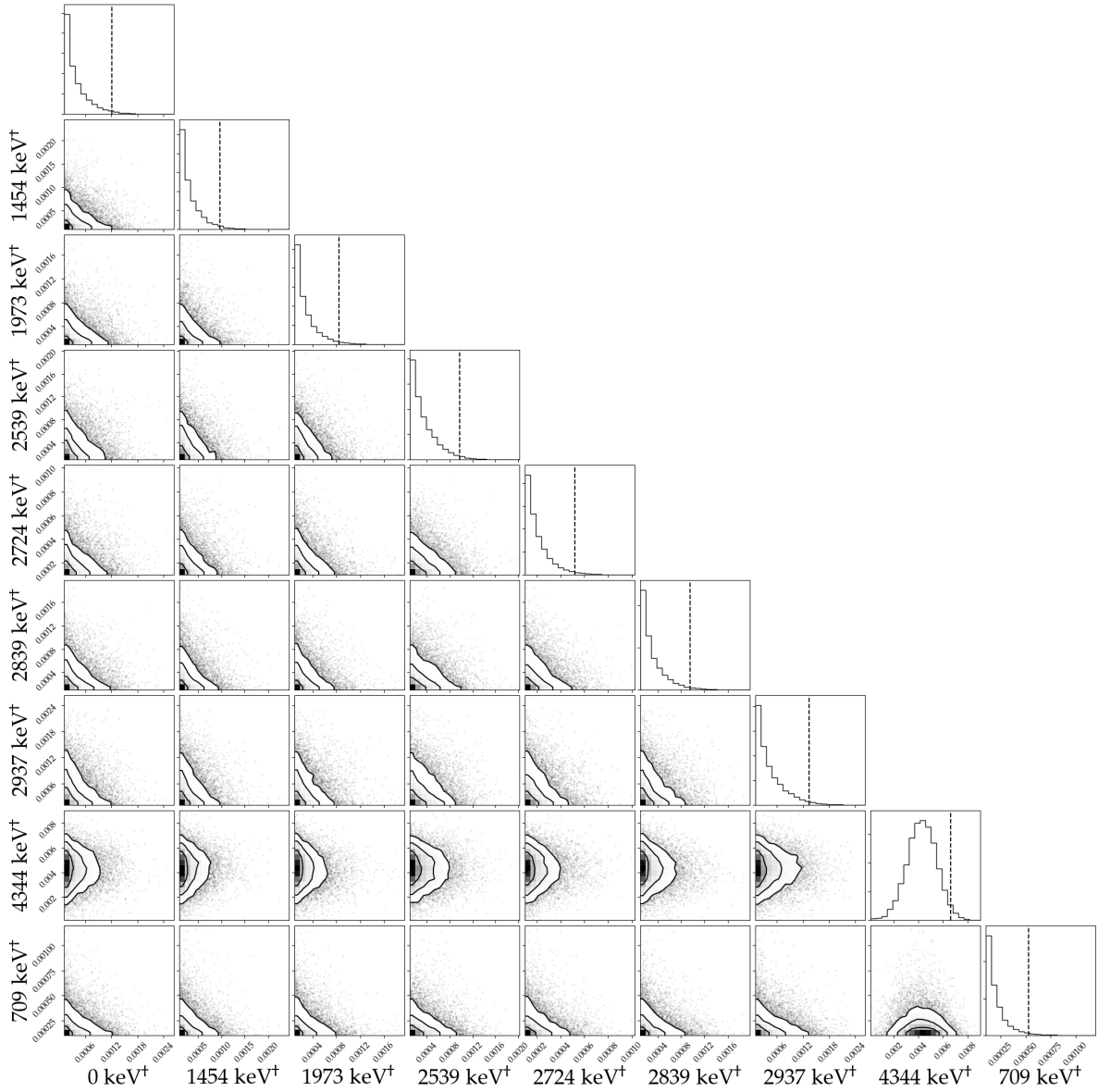


Figure 7.21: Template posterior distributions and two-dimensional pairwise posterior projections from the MCMC fraction fit of the $^{29}\text{Si}(p,\gamma)^{30}\text{P}$ $E_r^{lab} = 221$ keV singles abridged spectrum. Each posterior distribution refers to the fractional contribution a $^{29}\text{Si}(p,\gamma)^{30}\text{P}$ primary transition makes to the overall spectrum. The axis labels indicate the bound state to which the compound state decays for the represented primary transition. The 97.5th percentile is indicated by the dashed line on each posterior distribution. † denotes a branch of the reaction of interest that is treated as an upper limit.

indicates the 97.5th percentile. Typically, the template posteriors take on a near-Gaussian shape with negligible density at zero probability if a template contributes to the spectrum and its contribution is adequately reproduced by the fit. All $^{29}\text{Si}(p,\gamma)^{30}\text{P}$ template contributions for this resonance were treated as upper limit values a priori because their primary peaks were not visible in the data (see Figure 7.20), but the substantial probability density at zero fractional contribution of each template distribution supports this assumption.

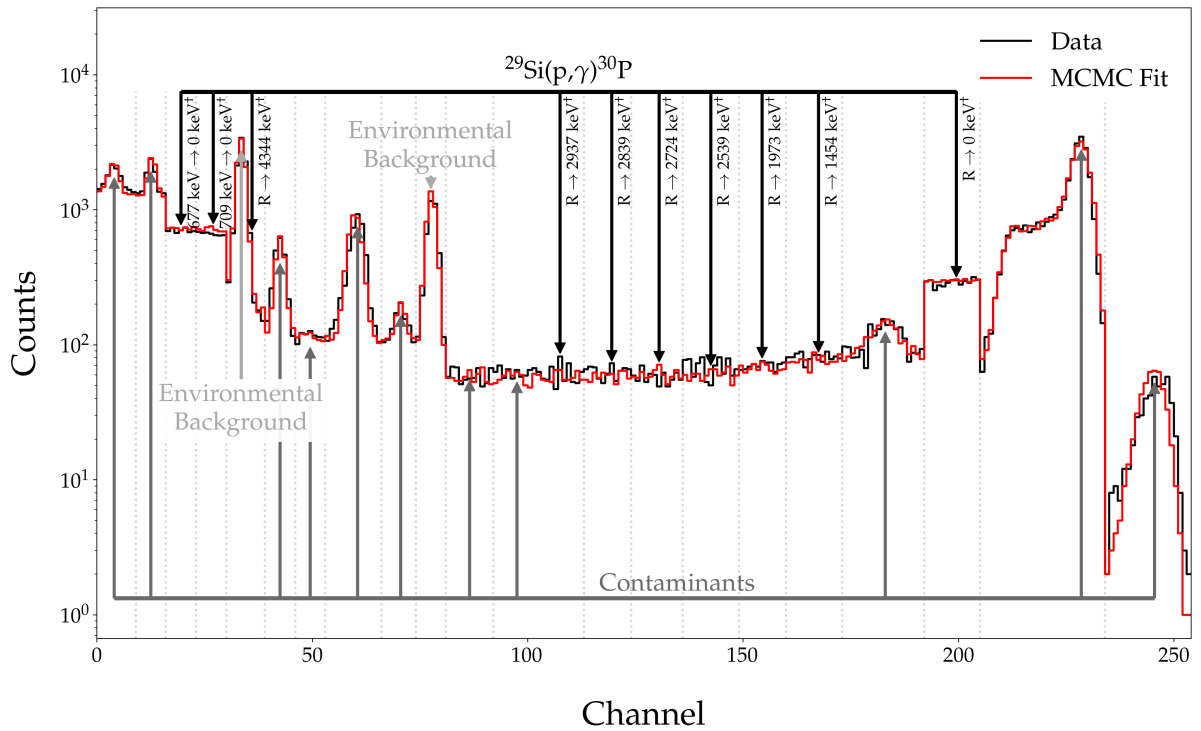


Figure 7.22: Measured (black) and simulated (red) pulse-height spectra for the $^{29}\text{Si}(p,\gamma)^{30}\text{P}$ $E_r^{\text{lab}} = 221$ keV abridged singles analysis. See Figure 7.4 for details.

Since Figure 7.21 only includes information on $^{29}\text{Si}(p,\gamma)^{30}\text{P}$ templates, it does not give any indication as to how well contaminant and ambient background sources are reproduced by the fitting procedure. However, understanding these other contributions is critical to correctly deriving the $^{29}\text{Si}(p,\gamma)^{30}\text{P}$ upper limits, and Figure 7.22 helps demonstrate that non- $^{29}\text{Si}(p,\gamma)^{30}\text{P}$ sources are well modeled too. The location of

the potential, unobserved primaries from the $E_r^{lab} = 221$ keV resonance are also indicated on the figure. Figure 7.22 makes it clear that environmental and beam-induced background sources are the significant contributors to the singles spectrum and are reproduced nicely by the MCMC fit.

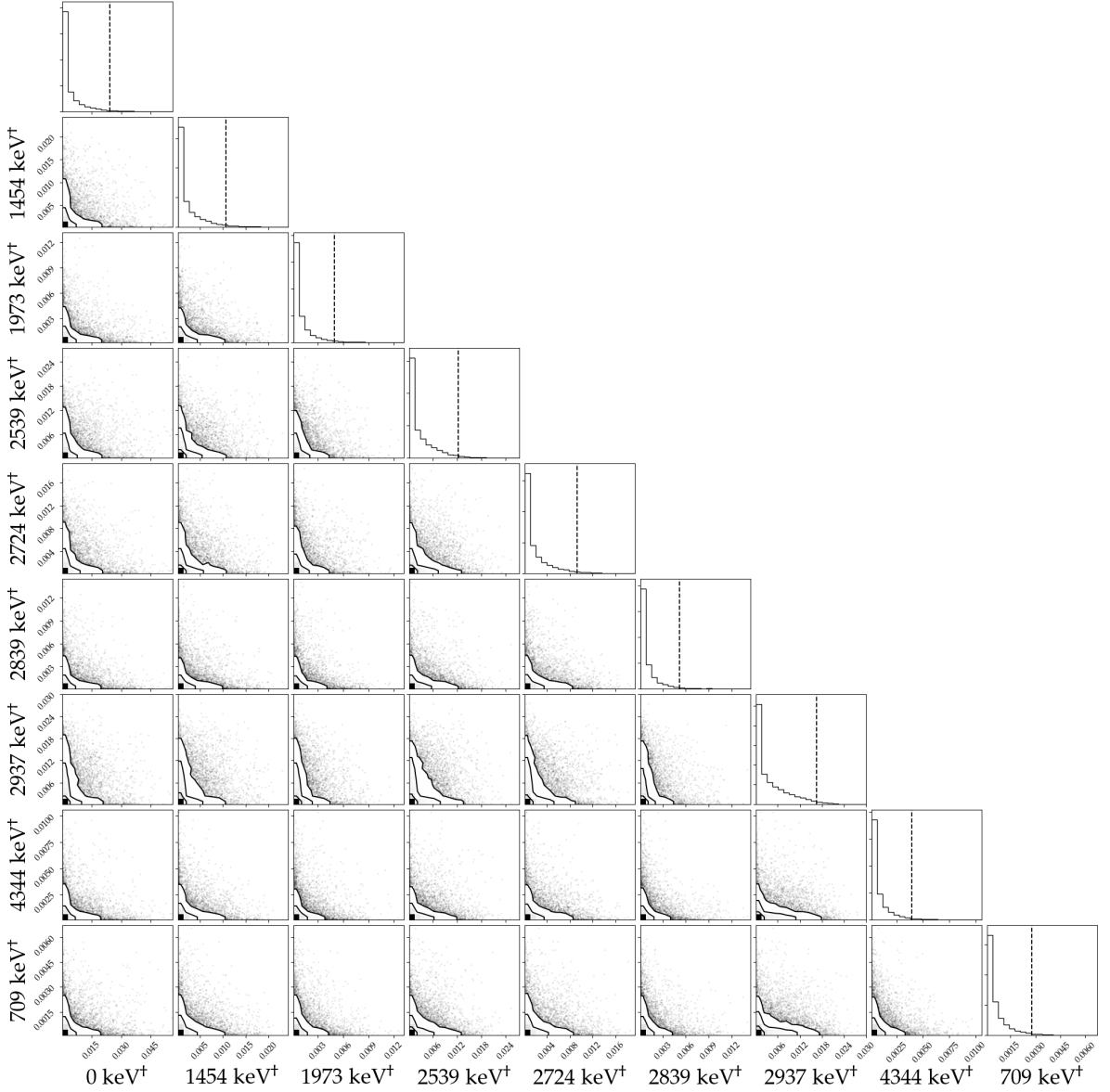


Figure 7.23: Template posterior distributions and two-dimensional pairwise posterior projections from the MCMC fraction fit of the $^{29}\text{Si}(p,\gamma)^{30}\text{P}$ $E_r^{lab} = 221$ keV coincidence abridged spectrum. The coincidence fit was determined using a 2.9 - 5.9 MeV trapezoidal gate. See Figure 7.21 for details.

The results of the coincidence fit, displayed in Figures 7.23 and 7.24, confirm the results of the singles fit. It can be seen in Figure 7.23 that all $^{29}\text{Si}(p,\gamma)^{30}\text{P}$ template posteriors have nontrivial density at zero probability, meaning that only their upper limit fractional contributions should be considered. With some consideration for statistical fluctuations, the abridged spectrum shown in Figure 7.24 also supports the argument that the observed coincidence spectrum is sufficiently reproduced by the simulated templates and the MCMC fit.

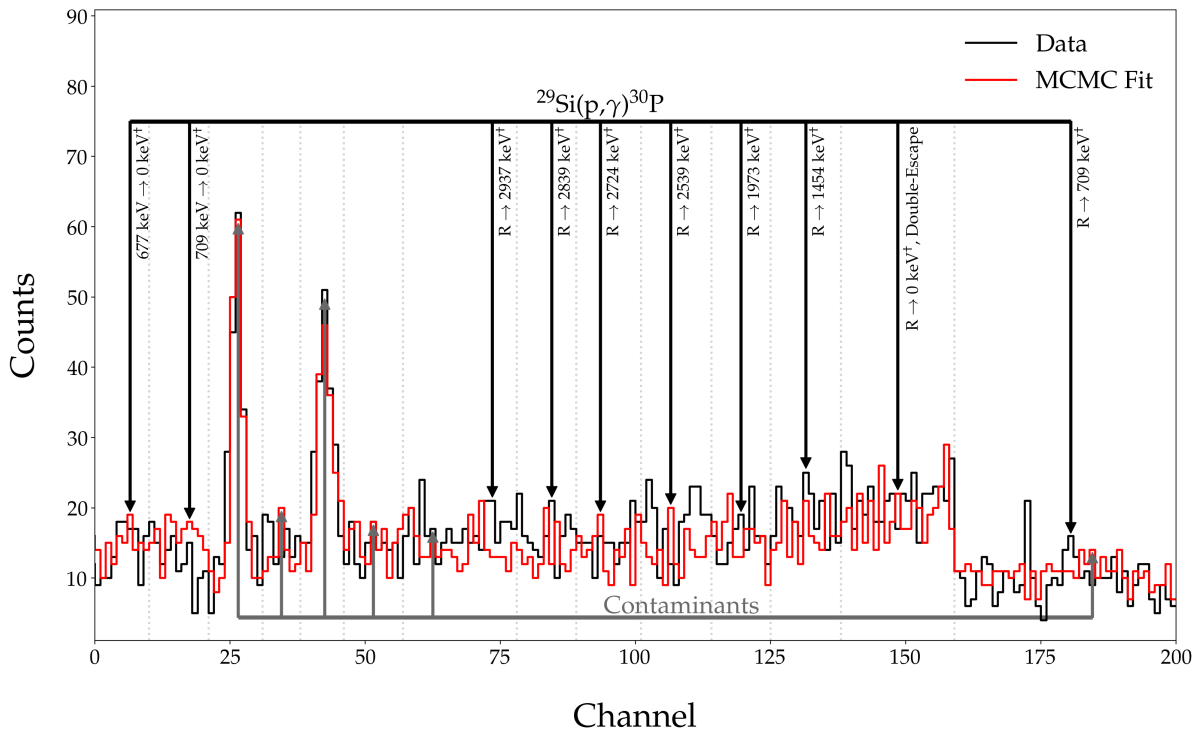


Figure 7.24: Measured (black) and simulated (red) pulse-height spectra for the $^{29}\text{Si}(p,\gamma)^{30}\text{P}$ $E_r^{\text{lab}} = 221 \text{ keV}$ abridged coincidence analysis. The coincidence spectrum was determined using a 2.9 - 5.9 MeV trapezoidal gate. See Figure 7.4 for details.

The quantitative analyses of the singles and coincidence data are provided in Table 7.12. The goodness of fit for each data set is indicated by the test statistic: -2.159 and -1.571 for the singles and coincidence fits, respectively. These values prove that the fits were successful and most divergences from the observed spectra were statistical in nature. Because no indications of the $E_r^{\text{lab}} = 221 \text{ keV}$ resonance were observed,

Table 7.12. $E_r^{lab} = 221$ keV Fit Results

Primary Transition	$\mathcal{N}_R^{Partial}$	
	Singles ^a	Coincidence ^b
R \rightarrow 4343.8	< 9864	< 630
R \rightarrow 2937.46	< 2004	< 1791
R \rightarrow 2839.34	< 1343	< 490
R \rightarrow 2723.72	< 1234	< 1490
R \rightarrow 2538.95	< 2210	< 1922
R \rightarrow 1973.27	< 1510	< 576
R \rightarrow 1454.23	< 1504	< 2172
R \rightarrow 708.70	< 846	< 281
R \rightarrow 0	< 5758	< 21621

Note. — The resonant state spin-parity has been restricted to $(3, 5)^+$ by (Endt, 1990). Coincidence intensities and simulated fit are determined using a 2.9 - 5.9 MeV coincidence gate. The results displayed in this table are based on the GEANT4 simulation of 2.5×10^6 events for each primary transition. Calculated values (partial reaction numbers) represent upper limits determined using a 97.5% credible interval from an abridged spectrum fit.

$$^a Z = -2.16. \mathcal{N}_R^{29Si} < 26273.$$

$$^b Z = -1.57. \mathcal{N}_R^{29Si} < 30973.$$

all $^{29}\text{Si}(p, \gamma)^{30}\text{P}$ template fractional contributions were calculated as upper limit values, meaning that the 97.5% coverage interval was determined from the template posterior, and partial reaction numbers were derived from these fractions in the usual manner.

It is clear that for most primary transitions the coincidence fit provides similar or reduced upper limit partial reaction numbers compared to that of the singles analysis. The main exception to this norm is the partial reaction number upper limit corresponding to the ground-state transition. As mentioned earlier, neither the full-energy peak of ground-state transition nor its single-escape peak are clearly visible with the

energy gating condition in Equation 7.20, so the second-escape peak of this transition must be fit in order to establish an upper limit value for the primary's contribution to the coincidence spectrum. However, the ability of the GEANT4 LENAGE simulation to reproduce escape peaks is somewhat lacking. This deficiency results in a coincidence upper limit that is significantly larger than that of the singles fit.

7.4.3 Resonance Strength

In the absence of an observation of the resonance of interest, it is desirable to set as low of an upper limit on the resonance strength as supported by the data. Furthermore, the relationship given in Equation 7.15 shows that the total number of reactions from the resonance of interest is directly proportional to the resonance strength, meaning that it is advantageous to use low partial reaction values to calculate the resonance strength upper limit. The results presented in Table 7.12 make clear that, with the exception of the $R \rightarrow 0$ keV primary transition, the upper limits on the $^{29}\text{Si}(p,\gamma)^{30}\text{P}$ partial number of reactions from the $E_r^{lab} = 221$ keV coincidence analysis are significantly lower than that of the singles analysis. Thus, rather than taking an unweighted average of the singles and coincidence $^{29}\text{Si}(p,\gamma)^{30}\text{P}$ total number of reactions (as was the case for the $E_r^{lab} = 314$ and 324 keV strength calculations presented earlier), it was necessary to combine the $^{29}\text{Si}(p,\gamma)^{30}\text{P}$ number of reactions from the coincidence analysis, excluding the $R \rightarrow 0$ keV contribution, with the $R \rightarrow 0$ keV contribution from the singles analysis.

The temptation to merely sum the the upper limit partial number of reactions from these transitions is significant, but it is not the best plan in this situation. By determining the upper limit partial number of reactions from each $^{29}\text{Si}(p,\gamma)^{30}\text{P}$ template, these contributions are in effect being treated independently of each other. While this approach was sufficient in the resonance analyses where only a few primary transitions were treated as upper limits that did not factor into the resonance strength calculation,

this approach would lead to a serious overestimation of the total number of reactions and, consequently, the resonance strength upper limit.

A more sound approach would involve calculating the $^{29}\text{Si}(\text{p},\gamma)^{30}\text{P}$ number of reactions for every iteration of the MCMC fit, finding the posterior for this parameter, and determining the 97.5% coverage interval on the posterior. Because it is clear that the $R \rightarrow 0$ keV partial number of reactions from the coincidence analysis is problematic, the partial number of reactions for this branch from the singles analysis could be used to determine the $^{29}\text{Si}(\text{p},\gamma)^{30}\text{P}$ number of reactions at every iteration instead. The $^{29}\text{Si}(\text{p},\gamma)^{30}\text{P}$ total number of reactions could then be adopted and used to determine the resonance strength upper limit. In this way, the effect of the flawed $R \rightarrow 0$ keV contribution was mitigated and the singles and coincidence analyses were combined to determine an appropriate upper limit on the $^{29}\text{Si}(\text{p},\gamma)^{30}\text{P}$ total number of reactions,

$$\mathcal{N}_R^{29\text{Si}} < 8250. \quad (7.21)$$

Figure 7.25 shows three posteriors illustrating this approach. The lefthand panel shows the posterior distribution of the $R \rightarrow 0$ keV partial number of reactions from the singles analysis. The center panel shows the posterior of the $^{29}\text{Si}(\text{p},\gamma)^{30}\text{P}$ number of reactions, with the exclusion of the $R \rightarrow 0$ keV contribution, from the coincidence analysis. The righthand panel contains the posterior distribution of the $^{29}\text{Si}(\text{p},\gamma)^{30}\text{P}$ total number of reactions, given by the $R \rightarrow 0$ keV singles contribution and the all other $^{29}\text{Si}(\text{p},\gamma)^{30}\text{P}$ contributions from the coincidence analysis. The 97.5% coverage interval is indicated by a dashed line on each posterior.

While the spectra in Figure 7.20 already supports the assertion that the $E_r^{\text{lab}} = 221$ keV resonance was not detected, the $^{29}\text{Si}(\text{p},\gamma)^{30}\text{P}$ total number of reactions posterior distribution (righthand panel in Figure 7.25) was used to further quantify the lack of

detection. To this end, the mean,

$$\mu(\mathcal{N}_R^{29Si}) = 3921 \quad (7.22)$$

and standard deviation of this distribution were determined. The standard deviation of the distribution was convolved with additional uncertainties due to the detector geometry (5%) and the HPGe dimensions (1.3%), giving

$$\sigma(\mathcal{N}_R^{29Si}) = 1807. \quad (7.23)$$

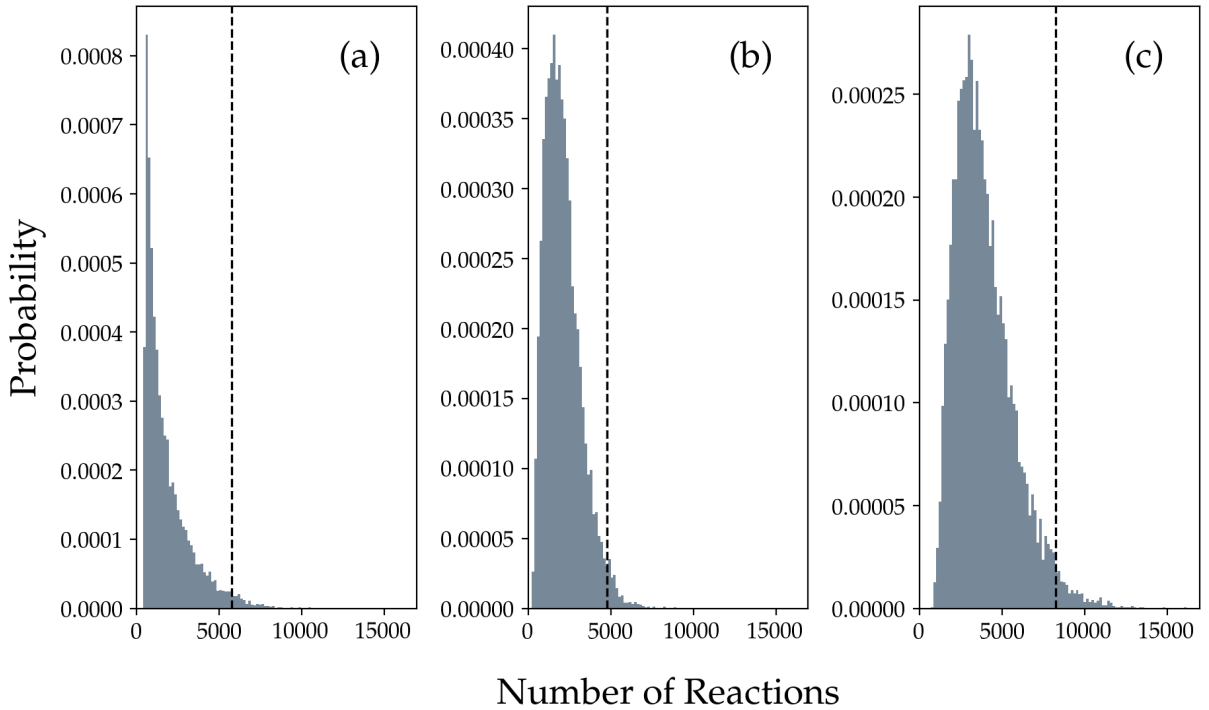


Figure 7.25: A collection of posterior distributions of the number of reactions from the $E_r^{lab} = 221$ keV resonance. The dashed lines indicate the 97.5% coverage interval of each posterior. (a) The number of reactions posterior of the $R \rightarrow 0$ keV branch from the singles analysis. (b) The posterior of all $^{29}\text{Si}(p,\gamma)^{30}\text{P}$ number of reactions, excluding the $R \rightarrow 0$ keV contribution, from the coincidence analysis. (c) The $^{29}\text{Si}(p,\gamma)^{30}\text{P}$ total number of reactions, derived using the $R \rightarrow 0$ keV contribution from the singles fit and all other $^{29}\text{Si}(p,\gamma)^{30}\text{P}$ contributions from the coincidence analysis. See the text for details.

Thus, it was concluded that the $E_r^{lab} = 221$ keV resonance was not detected within three σ .

From this point forward, the upper limit resonance strength calculation follows the procedure laid out in Equations 7.15 - 7.16 in Section 7.2.4. With the total number of reactions from the resonance of interest in hand (Equation 7.21), the effective stopping power was determined using SRIM material stopping powers (Ziegler *et al.*, 2015), the target stoichiometry, and the theoretical laboratory frame resonance energy. Using the absolute resonance strength and a few other input values from the $^{29}\text{Si}(p,\gamma)^{30}\text{P}$ $E_r^{lab} = 416$ keV resonance, the $E_r^{lab} = 221$ keV resonance strength upper limit was found to be

$$\omega\gamma < 3.69 \times 10^{-7} \text{ eV}. \quad (7.24)$$

The impact of this upper limit on the $^{29}\text{Si}(p,\gamma)^{30}\text{P}$ reaction rate will be explored in the following chapter.

7.5 Summary

A summary of the available literature information and the results of the $^{29}\text{Si}(p,\gamma)^{30}\text{P}$ study presented in this dissertation is given in Table 7.13. Bold values refer to the results of the current study while unbolded values indicate values that were pulled from previous studies.

Generally speaking, this information conveys the success of the current work in determining key values about $^{29}\text{Si}(p,\gamma)^{30}\text{P}$ relevant to classical nova nucleosynthesis. Specifically, the $E_r^{lab} = 314$ keV and $E_r^{lab} = 221$ keV resonances were studied for the first time. Where only theoretical resonance strength upper limits were available for these resonances in the past, now an experimentally determined resonance strength and resonance strength upper limit exists for $E_r^{lab} = 314$ keV and $E_r^{lab} = 221$ keV, respectively. An improved $E_r^{lab} = 324$ keV resonance strength, in agreement with previous

Table 7.13. Summary of the $^{29}\text{Si}(\text{p},\gamma)^{30}\text{P}$ Resonance Study Results

Property	Resonance (E_r^{lab} in keV)			
	416	324	314	221
E_x^a	5997.1 ± 0.8	5907.7 ± 0.8	5890 ± 12	5808 ± 3
$J^\pi{}^a$	1^+	2^-	$(1-3)^+$	$(3, 5)^+$
E_r^{CM}	402.76 ± 0.65	314.85 ± 0.56	303.80 ± 0.78	...
E_r^{lab}	416.76 ± 0.67	325.79 ± 0.58	314.36 ± 0.81	...
	416.6 ± 0.7	324.1 ± 0.7
ε_r^{lab}	46.4 ± 7.5	50.3 ± 8.5	50.9 ± 8.5	56.8 ± 9.3
$\omega\gamma$...	0.023 ± 0.004	$(1.0 \pm 0.2) \times 10^{-4}$	$< 3.69 \times 10^{-7}$
	0.244 ± 0.038^b	0.015 ± 0.005^c	4.0×10^{-5d}	$< 3.1 \times 10^{-7e}$

Note. — Bold values are from the present work. Resonance strengths are given in units of eV. All other energies given in keV. Stopping powers presented in units of $\text{eV}\cdot\text{cm}^2/10^{15}$ atoms. Resonance strengths derived indirectly should be regarded as order-of-magnitude estimates, and rigorous uncertainties cannot be obtained from this type of method.

^aFrom [Endt \(1998\)](#).

^bRenormalized from the directly measured value of [Riihonen *et al.* \(1979\)](#). See Table 7.3 for details.

^cDirectly measured value from [Reinecke *et al.* \(1985\)](#).

^dFrom [Sallaska *et al.* \(2013\)](#) derived indirectly from dimensionless single-particle reduced width calculations ([Iliadis, 1997](#)).

^eDerived indirectly from spectroscopic factor upper limits obtained in the transfer study of [Dykoski and Dehnard \(1976\)](#).

measurements, was also established, and an renormalized $E_r^{lab} = 416$ keV strength was also presented. Additionally, resonance energies were presented for $E_r^{lab} = 416$ keV, $E_r^{lab} = 324$ keV, and $E_r^{lab} = 314$ keV. The impact of this study will be explored in the Chapter 8.

CHAPTER 8: REACTION RATE EVALUATION

Above all, the primary goal of this dissertation was to advance the understanding of classical nova nucleosynthesis by refining the $^{29}\text{Si}(\text{p},\gamma)^{30}\text{P}$ thermonuclear reaction rate. As discussed in Section 2.3, reaction rates depend on contributions from resonant and nonresonant processes, so an accurate understanding of both processes is crucial to fulfilling this objective.

However, resonances falling within the Gamow window of the astrophysical phenomenon of interest can have a potent effect on thermonuclear reaction rates. Thus far, new strengths for three such $^{29}\text{Si}(\text{p},\gamma)^{30}\text{P}$ resonances have been presented in the current study. In this chapter, the Monte Carlo calculation of the thermonuclear reaction rate, using the `RatesMC` framework of Longland *et al.* (2010b), will be discussed (Section 8.1). Next, the nuclear input required for these calculations will be summarized in Sections 8.2–8.3. Finally, the new $^{29}\text{Si}(\text{p},\gamma)^{30}\text{P}$ thermonuclear reaction rate will be presented (Section 8.4) followed by a brief comparison to the reaction rate evaluation presented in Iliadis *et al.* (2010a) (Section 8.5).

8.1 Monte Carlo Sampling and Rate Calculations

At its most basic level, Monte Carlo sampling involves the generation of a random value for each input parameter, and for a given sample, these values are used to calculate the reaction rate (Cowan, 1998). The sampling process is repeated many, many times in order to determine the reaction rate. Typically, the number of samples is limited to the number required to achieve the desired statistical precision. In order

Table 8.1. Probability Density Functions of Nuclear Properties

Distribution	Nuclear Property
Gaussian	Resonance energy
Lognormal	Resonance strength
	Partial width
	Nonresonant S-factor
Porter-Thomas	Partial width upper limit

Note. — For descriptions of these distributions, see Appendix B.

to determine a reaction rate with meaningful uncertainties, each input parameter—or in this case, nuclear property—must be assigned an appropriate probability density function (Table 8.1), and these in turn determine the probability density function of the reaction rate from which the rate uncertainties can be extracted.

8.1.1 Rate Calculations

To understand how these calculations are carried out, first recall the general expression for the reaction rate in a stellar plasma (Equation 2.14),

$$\begin{aligned}
 N_A \langle \sigma v \rangle &= N_A \left(\frac{8}{\pi m_{01}} \right)^{1/2} \frac{1}{(kT)^{3/2}} \int_0^\infty E \sigma(E) e^{-E/kT} dE \\
 &= \frac{3.7318 \times 10^{10}}{T_9^{3/2}} \sqrt{\frac{M_0 + M_1}{M_0 M_1}} \int_0^\infty E \sigma(E) e^{-11.605 E/T_9} dE \left(\frac{\text{cm}^3}{\text{mol} \cdot \text{s}} \right), \quad (8.1)
 \end{aligned}$$

where N_A is Avogadro's number, k is the Boltzmann constant, T is the stellar temperature, and m_{01} is the reduced mass of the interacting particles. The total reaction rate includes contributions from multiple interaction processes; therefore, it is often

convenient to express Equation 8.1 as a composite expression,

$$N_A \langle \sigma v \rangle_{\text{total}} = \sum_i [N_A \langle \sigma v \rangle]_i = N_A \langle \sigma v \rangle_{\text{nonresonant}} + N_A \langle \sigma v \rangle_{\text{resonant}}. \quad (8.2)$$

Because $^{29}\text{Si}(p,\gamma)^{30}\text{P}$ does not involve broad or interfering resonances, the nonresonant and resonant components of the reaction rate correspond to the direct capture and narrow resonance rates, respectively. Thus, the total reaction rate expression reduces to

$$N_A \langle \sigma v \rangle_{\text{total}} = N_A \langle \sigma v \rangle_{\text{direct capture}} + N_A \langle \sigma v \rangle_{\text{narrow resonance}}. \quad (8.3)$$

The reaction rate contributions from direct capture and narrow resonances can then be addressed separately.

8.1.2 Direct Capture Reaction Rate Calculations

Recall from Equation 2.16 that the nonresonant cross section can be given as

$$\sigma(E)_{\text{nonresonant}} \equiv \frac{1}{E} e^{-2\pi\eta} S(E). \quad (8.4)$$

In this equation, $S(E)$ is the astrophysical S-factor, and the Gamow factor is the exponential term which also contains the Sommerfeld parameter, η . Expressing the nonresonant cross section in this way allows the astrophysical S-factor to be free of the $1/E$ dependence of the underlying s-wave Coulomb barrier transmission probability.

Direct radiative capture, the nonresonant process of consequence for the study of $^{29}\text{Si}(p,\gamma)^{30}\text{P}$, is infrequently observed in experiments, so it becomes necessary to estimate its impact on the reaction rate using nuclear structure information. The relationship between the direct capture cross section and nuclear structure is given

by

$$\sigma(E)_{\text{direct capture}} = \sum_j \sum_{\ell_i, \ell_f} C^2 S_j(\ell_f) \sigma_{\text{calc},j}(\ell_i, \ell_f) \quad (8.5)$$

where $C^2 S_j(\ell_f)$ is the experimental spectroscopic factor for state j and $\sigma_{\text{calc},j}$ is the cross section for a specific transition calculated using a single-particle potential model (Iliadis and Wiescher, 2004). These terms are incoherently summed over the orbital angular momentum of the initial state (ℓ_i), the orbital angular momentum of the final state (ℓ_f), and all final bound states (j).

From here, the result of Equation 8.5 could be substituted directly into Equation 8.1 to find the direct capture contribution to the total reaction rate. It was shown in Section 2.3.1, however, that the cross section can be converted to the astrophysical S-factor (Equation 2.16), which can often be replaced by the effective astrophysical S-factor (Equations 2.23–2.26). The `RatesMC` program makes use of the latter method, and the direct capture reaction rate is calculated accordingly. The specifics of the $^{29}\text{Si}(p,\gamma)^{30}\text{P}$ direct capture rate calculation will be addressed in Section 8.2.

8.1.3 Narrow Resonance Reaction Rate Calculations

While `RatesMC` is capable of integrating the second expression in Equation 8.1 for a given resonance, this method is computationally intensive and only worthwhile if the partial widths of a resonance are well known. Consequently, the resonant reaction rate is usually determined analytically instead. Barring any interferences between resonances, the reaction rate solely arising from a collection of narrow resonances is the sum of the individual contributions. Furthermore, the individual contributions can be approximated as shown in Equation 2.33. Thus, the total reaction rate due to narrow resonances is

$$N_A \langle \sigma v \rangle_{\text{narrow resonance}} = \sum_i \left[N_A \langle \sigma v \rangle_{\text{narrow resonance}} \right]_i \quad (8.6)$$

$$\approx N_A \hbar^2 \left(\frac{2\pi}{m_{01} kT} \right)^{3/2} \sum_i [(\omega\gamma)_i e^{-(E_r)_i/kT}]. \quad (8.7)$$

The resonance strengths used in the calculation of the $^{29}\text{Si}(p,\gamma)^{30}\text{P}$ reaction rate are summarized in Section 8.3 and Table 8.4.

8.1.4 Reaction Rate Calculations Involving Unobserved Resonances

Occasionally, a direct resonance search will not result in a successful observation but instead a sea of undesirable background counts in the spectral region of interest. Through careful analysis, an upper limit on the number of counts originating from the resonance of interest can be determined from the total number of observed counts. This count upper limit can then be used to determine an upper limit resonance strength, $\omega\gamma_{ul}$. However, unobserved resonances are included in the `RatesMC` rate calculation using particle partial width upper limits rather than resonance strength upper limits. Thus, the strategy described by Longland *et al.* (2010b) was adopted to convert resonance strength upper limits into partial width upper limits.

First, it must be assumed that a resonance strength upper limit is related to the upper limit of the particle partial width for the entrance channel, Γ_a^{ul} . In reactions with only two open channels, $\Gamma_a \ll \Gamma_b$ generally holds true for upper limit resonance strengths determined from direct searches of low-energy resonances, supporting the required assumption. Equations 2.31 and 2.34 were used to cast $\omega\gamma_{ul}$ in terms of Γ_a^{ul} , giving

$$\Gamma_a^{ul} = \frac{(2j_0 + 1)(2j_1 + 1)}{2J + 1} \frac{\Gamma}{\Gamma_b} \omega\gamma_{ul} \approx \frac{(2j_0 + 1)(2j_1 + 1)}{2J + 1} \omega\gamma_{ul}. \quad (8.8)$$

The particle partial width for a given level λ and channel c can also be expressed in terms of the dimensionless reduced width such that

$$\Gamma_{\lambda c} \equiv 2P_c \gamma_{\lambda c}^2 = \frac{2\hbar^2}{mR^2} P_c \theta_{\lambda c}^2 \quad (8.9)$$

where P_c is the penetration factor, $\gamma_{\lambda c}^2$ is the reduced width, m is the reduced mass of the system, R is the channel radius, and $\theta_{\lambda c}^2$ is the dimensionless reduced width for a single-particle channel (Iliadis, 1997). This can be taken one step further by parameterizing the dimensionless reduced width as

$$\theta_{\lambda c}^2 = C^2 S \theta_{pc}^2 \quad (8.10)$$

where C and θ_{pc}^2 are the isospin Clebsch-Gordan coefficient and the dimensionless single-particle reduced width, respectively. Finally, a Porter-Thomas distribution (Section B.3) of the form

$$f(\theta_p^2) = \frac{c}{\sqrt{\theta_p^2}} e^{-\theta_p^2 / (2\langle \theta_p^2 \rangle)} \quad (8.11)$$

was assigned as the probability density function of the proton dimensionless reduced width, θ_p^2 . Here, c denotes a normalization constant rather than a reaction channel.

8.2 Nonresonant Contributions

Like that of many other reactions, the nonresonant cross section of the $^{29}\text{Si}(p,\gamma)^{30}\text{P}$ reaction has yet to be measured experimentally, even though direct capture is expected to dominate the $^{29}\text{Si}(p,\gamma)^{30}\text{P}$ reaction rate below $T = 0.03$ GK (Iliadis *et al.*, 2001). Consequently, it was necessary to estimate the total direct capture cross section using the single-particle potential model as shown in Equation 8.5.

First, the DIRCAP program was used to calculate the direct capture cross section for each ^{30}P bound state, $\sigma_{\text{calc},j}$, by integrating the radial wave function given by a Woods-Saxon potential. In accordance with Iliadis and Wiescher (2004), the Woods-Saxon potential was defined with a well radius and diffuseness of $r_0 = 1.25$ fm and $a = 0.65$ fm, respectively. The nuclear masses and Q-value for the cross section calculation were derived from Wang *et al.* (2017) and Tanabashi *et al.* (2018), and the level energies

Table 8.2. Astrophysical S-factor Approximation Parameters

$S(0)$ (keV·b)	$S'(0)$ (b)	$S''(0)$ (keV ⁻¹ ·b)
107.2	-1.262×10^{-2}	1.114×10^{-6}

Note. — Parameters of the second-order S-factor approximation (Equation 2.23) used to calculate the direct capture contribution to the total $^{29}\text{Si}(p,\gamma)^{30}\text{P}$ reaction rate. The resulting fit is shown in Figure 8.1.

and spins of the ^{30}P bound states were taken from Endt (1990) and Grossmann *et al.* (2000) (see Table A.1 for details). This calculation was performed over a range of bombarding energies from 0.05 MeV to 1 MeV in the center-of-mass frame.

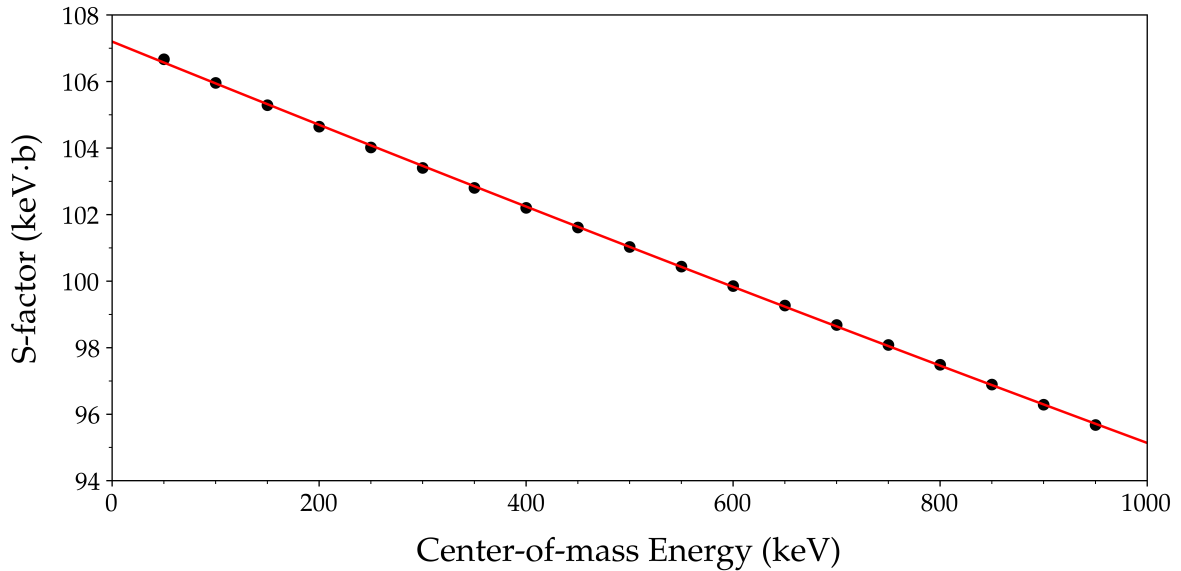


Figure 8.1: Estimate of the nonresonant astrophysical S-factor from the present $^{29}\text{Si}(p,\gamma)^{30}\text{P}$ study. The black data points indicate the S-factor values calculated using the DIRCAP program. The red curve shows the second-order S-factor approximation used in the present $^{29}\text{Si}(p,\gamma)^{30}\text{P}$ rate evaluation.

Next, the results of the DIRCAP calculations were combined with the spectroscopic factors of the ^{30}P bound states (from Dykoski and Dehnard, 1976) to compute

Equation 8.5. The nonresonant cross section can be converted to an astrophysical S-factor (Equation 8.4) and then approximated by a second-order Taylor series (Equation 2.23) as described earlier. Thus, a second-order polynomial fit for the calculated S-factor, given in Table 8.2, was determined. The resulting approximation, shown in Figure 8.1, was included in the `RatesMC` reaction rate calculation to estimate the nonresonant contribution to the $^{29}\text{Si}(p,\gamma)^{30}\text{P}$ total reaction rate below an energy of 1 MeV. Above 1 MeV, the total reaction rate is dominated by narrow resonances rather than by nonresonant processes.

8.3 Resonant Contributions

This section details the adoption of resonance measurements from this work as well as literature sources over three energy ranges. The center-of-mass resonance energies and strengths adopted for the current evaluation of the $^{29}\text{Si}(p,\gamma)^{30}\text{P}$ reaction rate are tabulated in Tables 8.4–8.3.

8.3.1 $E_r^{CM} < 300 \text{ keV}$

In the energy range below 300 keV, three potential resonances have been theorized but remain unobserved to date. It is, however, important to include any possible contribution from these resonances in the reaction rate calculation.

Generally, any reaction rate contribution from unobserved resonances must be estimated using nuclear parameters such as entrance and exit channel partial widths for $^{29}\text{Si}(p,\gamma)^{30}\text{P}$ (Γ_p and Γ_γ , respectively). Such is the case for the two lowest lying $^{29}\text{Si}(p,\gamma)^{30}\text{P}$ resonances, $E_r^{CM} = 108 \text{ keV}$ and $E_r^{CM} = 121 \text{ keV}$. The entrance channel partial width upper limits for these resonances were derived indirectly from the spectroscopic factor upper limits in [Dykoski and Dehnhard \(1976\)](#). The partial widths of the exit channel were adopted from [Iliadis *et al.* \(2010a\)](#).

Table 8.3. Unobserved Resonance Parameters

E_r^{CM} (keV)	J^π	ℓ_p	$\omega\gamma_{ul}$ (eV)	Γ_p^{ul} (eV)	Γ_γ (eV)	$\langle\theta_p\rangle$
108.4 ± 4.0	1^+	0	4.3×10^{-11}	5.7×10^{-11}	0.041 ± 0.021	0.005
120.7 ± 3.0	5^+	4	1.2×10^{-14}	4.2×10^{-15}	≈ 0.1	0.005
214.7 ± 3.0	3^+	2	3.69×10^{-7}	2.106×10^{-7}	≈ 0.1	0.005

Note. — These are the parameters used to include unobserved resonances in the $^{29}\text{Si}(p,\gamma)^{30}\text{P}$ reaction rate calculation using RatesMC. Bold values refer to the results of the current study.

The last unobserved resonance in this energy region, $E_r^{CM} = 215$ keV ($E_r^{lab} = 221$ keV), was studied in the current work. While it remains unobserved, an upper limit strength of $\omega\gamma_{ul} = 3.69 \times 10^{-7}$ eV was determined for this resonance based on the current $^{29}\text{Si}(p,\gamma)^{30}\text{P}$ study. The resonance strength was converted to an upper limit particle partial width using the procedure described in Section 8.1.4. For the reaction rate evaluation presented in this thesis, a value of $\langle\theta_p^2\rangle = 0.005$ was adopted for the mean value of the dimensionless reduced width based on the work of Pogrebnyak *et al.* (2013). A value of $\Gamma_\gamma \approx 0.1$ eV was assumed for the exit channel partial width, but this assumption is inconsequential as $\Gamma_p \ll \Gamma_\gamma$ usually holds true for low-energy resonances.

Another aspect that sets $E_r^{CM} = 215$ keV apart from the other resonances in this region is its ambiguous spin assignment. As described in Section 7.4, the $^{30}\text{Si}(^3\text{He}, t)^{30}\text{P}$ experiment of Ramstein *et al.* (1981) indicated a spin-parity of 3^+ ($\ell = 2$) for the resonant level. Shell model calculations (Grossmann *et al.*, 2000, and others) support a spin-parity designation of 5^+ ($\ell = 4$) however. For the purposes of the present rate evaluation, $J^\pi = 3^+$ was assumed as it is the more conservative choice.

The parameters used to include the unobserved resonances in the current $^{29}\text{Si}(p,\gamma)^{30}\text{P}$ reaction rate evaluation are summarized in Table 8.3.

8.3.2 $E_r^{CM} = 300 \text{ keV} - 500 \text{ keV}$

The three $^{29}\text{Si}(p,\gamma)^{30}\text{P}$ resonances in the $E_r^{CM} = 300 \text{ keV} - 500 \text{ keV}$ range have not been studied as frequently as their higher lying brethren. A measurement of the $E_r^{CM} = 304 \text{ keV}$ resonance had not been attempted prior to the efforts presented in this dissertation. On a similar note, the most recent measurement of the $E_r^{CM} = 315 \text{ keV}$ resonance was performed nearly 35 years ago (see Table 7.6). The current work was intended to ameliorate the lack of study surrounding the low lying resonances in $^{29}\text{Si}(p,\gamma)^{30}\text{P}$, and as such, the resonance energies and strengths measured in this work (Table 7.13) were used as input for the RatesMC rate calculation. The center-of-mass energies and strengths of these resonances and others used in the current rate evaluation are summarized in Table 8.4.

8.3.3 $E_r^{CM} > 500 \text{ keV}$

A number of resonance studies have concentrated their efforts on the $E_r^{CM} > 500 \text{ keV}$ region in $^{29}\text{Si}(p,\gamma)^{30}\text{P}$. The two most recent and expansive studies were performed by Reinecke *et al.* (1985) and Frankle *et al.* (1992) in the $E_r^{CM} < 2200 \text{ keV}$ and $E_r^{CM} = 1965 - 3076 \text{ keV}$ energy regions, respectively. Their results are compiled and tabulated in Endt (1998), making for a straightforward inclusion in the present $^{29}\text{Si}(p,\gamma)^{30}\text{P}$ reaction rate evaluation. However, there are two points of caution that must be addressed in order to responsibly adopt these literature results.

The first point pertains to the determination of center-of-mass resonance energies. As recently presented in Iliadis (2019), the use of atomic Q-values to calculate center-of-mass resonance energies is pervasive in the literature. However, one must realize that nuclei in stellar plasmas are fully ionized, meaning that the nuclear Q-value should be used to determine resonance energies for this application. Failure to use the nuclear Q-value when calculating resonance energies for thermonuclear reaction

Table 8.4. Resonance Strengths for the $^{29}\text{Si}(p,\gamma)^{30}\text{P}$ Reaction Rate Calculation

E_r^{CM} (keV)	$\omega\gamma$ (eV)	$\sigma(\omega\gamma)$ (eV)	E_r^{CM} (keV)	$\omega\gamma$ (eV)	$\sigma(\omega\gamma)$ (eV)	E_r^{CM} (keV)	$\omega\gamma$ (eV)	$\sigma(\omega\gamma)$ (eV)
303.8(8)	1.0×10^{-4}	2×10^{-5}	1790.1(5)	0.089	0.028	2594(3)	0.073	0.052
314.9(6)	0.023	0.004	1900.8(7) ^a	0.300	0.088	2613(3)	0.444	0.138
402.8(7)	0.244	0.038	1967.2(5)	0.141	0.044	2678(3)	0.367	0.114
675.1(7) ^a	0.305	0.090	1969.2(5)	0.422	0.131	2683(3)	0.078	0.025
704.8(4) ^a	0.111	0.030	1986.6(5)	0.108	0.033	2685(3)	3.110	0.964
886.9(4) ^a	0.103	0.028	2011.7(5)	0.753	0.234	2726(3)	0.722	0.222
924.9(4) ^a	0.047	0.013	2042.7(5)	0.400	0.124	2757(3)	0.033	0.011
1004.4(5)	0.007	0.003	2051.0(5)	0.744	0.233	2758(3)	0.074	0.023
1073.4(6) ^a	0.042	0.012	2094.9(5)	0.061	0.019	2759(3)	0.278	0.087
1258.8(4) ^a	0.377	0.098	2156.0(5)	0.255	0.080	2793(3)	0.278	0.087
1280.1(5)	0.164	0.076	2159.4(5)	0.047	0.015	2805(3)	0.093	0.029
1282.3(6) ^a	0.564	0.235	2165.7(5)	1.077	0.332	2816(3)	0.144	0.045
1327.0(4) ^a	0.800	0.257	2193.1(5)	0.057	0.018	2833(3)	0.031	0.010
1385.0(5)	0.007	0.003	2233.0(5)	0.053	0.017	2839(3)	0.911	0.287
1421.7(4) ^a	0.211	0.061	2290.5(5)	0.111	0.034	2858(3)	0.522	0.164
1451.7(5)	0.021	0.008	2327.6(5)	0.322	0.100	2891(3)	0.167	0.052
1455.7(4) ^a	0.659	0.169	2328.5(5)	0.422	0.131	2933(3)	0.567	0.178
1525.8(5)	0.014	0.005	2403.4(5)	0.822	0.255	2937(3)	0.087	0.027
1582.6(6) ^a	0.941	0.327	2408(1)	0.122	0.038	2989(3)	0.111	0.039
1609.7(5)	0.211	0.061	2414.1(5)	0.489	0.152	3026(3)	0.467	0.149
1614.2(5)	0.111	0.029	2421.0(5)	0.084	0.026	3039(3)	0.178	0.055
1629.1(4) ^a	1.294	0.409	2502(3)	0.700	0.219	3049(3)	0.567	0.178
1688.7(5)	0.444	0.185	2513(3)	0.300	0.093	3054(3)	0.355	0.110
1689.2(4) ^a	1.105	0.390	2558(3)	0.444	0.138	3069(3)	1.011	0.316
1711.6(5)	0.188	0.078	2572(3)	0.167	0.052	3076(3)	0.633	0.194
1713.0(5)	0.164	0.076						

Note. — Bold values were adopted from the present work. The center-of-mass energies are derived from the excitation energies reported by [Endt \(1998\)](#) unless otherwise noted. The resonance strengths were renormalized to the adopted resonance strength standard, $\omega\gamma(E_r^{CM} = 403 \text{ keV}) = 0.244 \pm 0.038 \text{ eV}$ (Table 7.3).

^aThe center-of-mass resonance energies are derived from the bombarding energies reported by [Reinecke et al. \(1985\)](#).

rates can lead to a significant, erroneous increase in a given rate.

To avoid this bias in the calculation of the $^{29}\text{Si}(p,\gamma)^{30}\text{P}$ rate, the literature center-of-mass resonance energies were handled carefully. Some center-of-mass resonance energies, particularly $E_p < 2000$ keV, were derived from proton bombarding energies reported by [Reinecke *et al.* \(1985\)](#). These values were free from the Q-value bias discussed in [Iliadis \(2019\)](#) and merely required conversion to the center-of-mass frame using the target and projectile nuclear masses.

The remaining resonance energies were determined using excitation energies from [Endt \(1998\)](#) and references therein. First, the total electron binding energy of an atom can be approximated using Equation 5 in [Iliadis \(2019\)](#),

$$B_e(Z) \approx 14.4381Z^{2.39} + 1.55468 \times 10^{-6}Z^{5.35} \quad (8.12)$$

where Z is the atomic number. For the $^{29}\text{Si}(p,\gamma)^{30}\text{P}$ reaction, the total electron binding energy difference is then

$$\Delta B_e \equiv \sum B_e^i - \sum B_e^f = -1.42 \text{ keV}. \quad (8.13)$$

The binding energy difference can be used to find the nuclear Q-value, Q_{nu} , from the atomic Q-value, Q_{at} . It was found that the nuclear Q-value for $^{29}\text{Si}(p,\gamma)^{30}\text{P}$ was

$$Q_{nu} = Q_{at} + \Delta B_e = 5593.33 \pm 0.07 \text{ keV} \quad (8.14)$$

where the atomic Q-value, $Q_{at} = 5594.75 \pm 0.07$ keV, was tabulated by [Wang *et al.* \(2017\)](#). Finally, the center-of-mass resonance energies were derived from the [Endt \(1998\)](#) excitation energies using Equation 6 in [Iliadis \(2019\)](#),

$$E_{r,nu}^{CM} = E_x - Q_{nu} = E_x - (Q_{at} + \Delta B_e) \quad (8.15)$$

where $E_{r,nu}^{CM}$ represents the center-of-mass resonance energy based on the nuclear mass difference and E_x is the excitation energy of the resonance.

The second issue arises from the common use of resonance strength standards to convert relative resonance strength measurements to absolute values. The [Reinecke et al. \(1985\)](#) study uses the strength of the $E_r^{lab} = 416$ keV resonance in $^{29}\text{Si}(p,\gamma)^{30}\text{P}$, as measured by [Riihonen et al. \(1979\)](#), as the standard for their resonance strength conversion. The [Frankle et al. \(1992\)](#) study did not involve bombarding energies as low as $E_p \approx 416$ keV, so this resonance could not be used as a standard directly. Instead, [Frankle et al. \(1992\)](#) obtained absolute resonance strengths by normalizing eight of their resonance measurements to that of [Reinecke et al. \(1985\)](#), and in this way their strengths are dependent on the [Riihonen et al. \(1979\)](#) $E_r^{lab} = 416$ keV standard as well.

Conveniently, the [Riihonen et al. \(1979\)](#) standard was also adopted for the measurements presented in this dissertation, but while it is the most rigorous determination to date, the [Riihonen et al. \(1979\)](#) value is dependent on resonance strength and stopping power values that have been revised in the years since its publication.

First, the [Riihonen et al. \(1979\)](#) $E_r^{lab} = 416$ keV strength was measured relative to an often used standard resonance: $E_r^{lab} = 992$ keV in $^{27}\text{Al}(p,\gamma)^{28}\text{Si}$. Their adopted strength for this resonance, $\omega\gamma = 2.0 \pm 0.2$ eV, originated from the measurements of [Switkowski et al. \(1975\)](#), [Keinonen and Anttila \(1976\)](#), and [Lyons et al. \(1969\)](#). More recent work by [Iliadis et al. \(2001\)](#) suggests a resonance strength of $\omega\gamma = 1.9 \pm 0.1$ eV based on the renormalization of the strength presented by [Paine and Sargood \(1979\)](#).

Secondly, silicon stopping powers from [Andersen and Ziegler \(1977\)](#) were not experimentally well known at the time of the [Riihonen et al. \(1979\)](#) study. Knowledge of the adjacent aluminum stopping powers allowed for a reasonably accurate approximation. However, a recent evaluation ([Ziegler et al., 2015](#)) indicates that the [Riihonen et al. \(1979\)](#) stopping power, $\varepsilon_{29\text{Si}}(416 \text{ keV}) = 13.3 \pm 0.7 \text{ eV}\cdot\text{cm}^2/10^{15} \text{ atoms}$, should be updated to $\varepsilon_{29\text{Si}}(416 \text{ keV}) = 13.1 \pm 0.7 \text{ eV}\cdot\text{cm}^2/10^{15} \text{ atoms}$.

In light of these improved values, the $^{29}\text{Si}(p,\gamma)^{30}\text{P}$ $E_r^{lab} = 416$ keV resonance strength reported by [Riihonen *et al.* \(1979\)](#), $\omega\gamma = 0.26 \pm 0.025$ eV, was renormalized to $\omega\gamma = 0.244 \pm 0.038$ eV. This strength value was adopted for the entirety of the work detailed in this dissertation, and all $^{29}\text{Si}(p,\gamma)^{30}\text{P}$ literature resonance strengths were normalized to this value.

It should be noted that this adoption differs from that of the [Iliadis *et al.* \(2010c\)](#) reaction rate evaluation. In their study, they chose to use the $E_r^{lab} = 416$ keV resonance strength presented by [Sargood \(1982\)](#). [Sargood \(1982\)](#), however, did not measure $^{29}\text{Si}(p,\gamma)^{30}\text{P}$ directly. Instead, their value relies on the $E_r^{lab} = 416$ keV measurement of [Engelbertink and Endt \(1966\)](#) which they renormalized to the strength of the $^{30}\text{Si}(p,\gamma)^{31}\text{P}$ $E_r^{lab} = 620$ keV resonance given by [Paine and Sargood \(1979\)](#). As [Paine and Sargood \(1979\)](#) states, the [Engelbertink and Endt \(1966\)](#) results largely disagreed with that of independent absolute measurements, and a second study ([Paine *et al.*, 1978](#)) conducted using the methods of [Engelbertink and Endt \(1966\)](#) was unable to reproduce their results. With this knowledge in mind, adopting the [Riihonen *et al.* \(1979\)](#) strength in favor of the [Sargood \(1982\)](#) value is the natural choice. As a result of adopting the [Riihonen *et al.* \(1979\)](#) strength, the renormalized literature $^{29}\text{Si}(p,\gamma)^{30}\text{P}$ resonance strengths reported in the present work are 10% higher than those of the [Iliadis *et al.* \(2010c\)](#) evaluation.

8.4 The New $^{29}\text{Si}(p,\gamma)^{30}\text{P}$ Reaction Rate

The $^{29}\text{Si}(p,\gamma)^{30}\text{P}$ reaction rate was reevaluated using the presented methodology described in Section 8.1 and the nuclear input detailed in Sections 8.2–8.3. To describe the particle interactions, the nuclear masses and corresponding nuclear Q-value were adopted. In total, 8,000 samples were taken at 51 temperatures in the range of 10 MK–10 GK using the `RatesMC` program ([Longland *et al.*, 2010b](#)).

Table 8.5 presents the results of the present $^{29}\text{Si}(\text{p},\gamma)^{30}\text{P}$ reaction rate evaluation. It provides the low, median, and high reaction rates corresponding to the 0.16, 0.50, and 0.84 quantiles of the reaction rate probability density function, respectively. Additionally, the probability density function of the calculated rate is approximated by a lognormal distribution (Appendix B.2). The lognormal parameters of the approximation, μ and σ , are tabulated in Table 8.5.

In the final column of Table 8.5, the Anderson-Darling test statistic, t_{AD}^* , is given for each temperature. It serves as a quantitative assessment of the lognormal approximation (Iliadis *et al.*, 2010c). For a value of $t_{AD}^* \lesssim 1$, the Anderson-Darling test indicates that the reaction rate probability density function is consistent with a lognormal distribution. This is true for most temperatures in the current $^{29}\text{Si}(\text{p},\gamma)^{30}\text{P}$ rate evaluation. Values of $t_{AD}^* \approx 1\text{--}30$ signify the rejection of the lognormal hypothesis by the test, but generally speaking, a lognormal approximation still tracks the probability density function relatively well in this test statistic range. However, the lognormal approximation visibly diverges from the probability density function for values of $t_{AD}^* \gtrsim 30$, and based on the results of the Anderson-Darling test in the $T = 25\text{ MK--}110\text{ MK}$ range, one can expect the lognormal approximation to deviate from the probability density function of the $^{29}\text{Si}(\text{p},\gamma)^{30}\text{P}$ rate in this region as will be explained below.

The contour plot shown in Figure 8.2 illustrates the probability density function of the $^{29}\text{Si}(\text{p},\gamma)^{30}\text{P}$ reaction rate across the temperature range of study. In this plot, the 8,000 samples performed by RatesMC are normalized to the median rate at each temperature. The thick black lines signify the 1σ (68%) coverage boundary, and the thin black lines mark the edge of the 2σ (95%) coverage region. In a similar fashion, the color mapping indicates the coverage probability percentage. The salient feature of this plot is the three orders of magnitude spanned by the 95% coverage probability between 20 MK and 100 MK.

Table 8.5. $^{29}\text{Si}(p,\gamma)^{30}\text{P}$ Reaction Rates from the Current Study

T (GK)	Monte Carlo Rate			Lognormal Parameters		t_{AD}^*
	Low	Median	High	μ	σ	
0.010	1.437×10^{-39}	2.105×10^{-39}	3.054×10^{-39}	-8.9058×10^1	3.8304×10^{-1}	0.4557
0.011	4.673×10^{-38}	6.911×10^{-38}	1.004×10^{-37}	-8.5573×10^1	3.8521×10^{-1}	0.8126
0.012	1.018×10^{-36}	1.481×10^{-36}	2.140×10^{-36}	-8.2504×10^1	3.7948×10^{-1}	0.3335
0.013	1.613×10^{-35}	2.346×10^{-35}	3.505×10^{-35}	-7.9732×10^1	3.8778×10^{-1}	0.8520
0.014	1.953×10^{-34}	2.846×10^{-34}	4.127×10^{-34}	-7.7242×10^1	3.8107×10^{-1}	0.4687
0.015	1.856×10^{-33}	2.687×10^{-33}	3.946×10^{-33}	-7.4994×10^1	3.8075×10^{-1}	0.3335
0.016	1.482×10^{-32}	2.161×10^{-32}	3.181×10^{-32}	-7.2910×10^1	3.8225×10^{-1}	0.3526
0.018	5.684×10^{-31}	8.312×10^{-31}	1.226×10^{-30}	-6.9262×10^1	3.8877×10^{-1}	0.2565
0.020	1.387×10^{-29}	2.024×10^{-29}	2.981×10^{-29}	-6.6067×10^1	3.8749×10^{-1}	0.7240
0.025	1.557×10^{-26}	5.357×10^{-26}	2.333×10^{-25}	-5.8077×10^1	1.2597×10^0	43.96
0.030	1.577×10^{-23}	1.519×10^{-22}	6.236×10^{-22}	-5.0569×10^1	1.8020×10^0	101.1
0.040	3.740×10^{-19}	3.851×10^{-18}	1.249×10^{-17}	-4.0636×10^1	1.9536×10^0	252.6
0.050	1.457×10^{-16}	1.522×10^{-15}	4.706×10^{-15}	-3.4692×10^1	1.9605×10^0	308.5
0.060	7.568×10^{-15}	7.765×10^{-14}	2.380×10^{-13}	-3.0772×10^1	1.9535×10^0	321.9
0.070	1.204×10^{-13}	1.227×10^{-12}	3.742×10^{-12}	-2.7995×10^1	1.9184×10^0	308.3
0.080	9.438×10^{-13}	9.533×10^{-12}	2.905×10^{-11}	-2.5902×10^1	1.8077×10^0	265.1
0.090	5.419×10^{-12}	4.677×10^{-11}	1.412×10^{-10}	-2.4192×10^1	1.5547×10^0	183.9
0.100	4.168×10^{-11}	1.821×10^{-10}	5.130×10^{-10}	-2.2584×10^1	1.1065×10^0	88.84
0.110	4.993×10^{-10}	8.801×10^{-10}	1.784×10^{-9}	-2.0798×10^1	5.8084×10^{-1}	58.43
0.120	5.489×10^{-9}	6.921×10^{-9}	9.087×10^{-9}	-1.8772×10^1	2.5188×10^{-1}	10.16
0.130	4.485×10^{-8}	5.370×10^{-8}	6.364×10^{-8}	-1.6743×10^1	1.7562×10^{-1}	0.4337
0.140	2.840×10^{-7}	3.380×10^{-7}	4.002×10^{-7}	-1.4901×10^1	1.7132×10^{-1}	0.3000
0.150	1.439×10^{-6}	1.711×10^{-6}	2.027×10^{-6}	-1.3279×10^1	1.7150×10^{-1}	0.2760
0.160	5.988×10^{-6}	7.114×10^{-6}	8.413×10^{-6}	-1.1855×10^1	1.7086×10^{-1}	0.3085
0.180	6.452×10^{-5}	7.621×10^{-5}	9.007×10^{-5}	-9.4816×10^0	1.6776×10^{-1}	0.2892
0.200	4.320×10^{-4}	5.079×10^{-4}	5.979×10^{-4}	-7.5847×10^0	1.6318×10^{-1}	0.2495
0.250	1.343×10^{-2}	1.555×10^{-2}	1.803×10^{-2}	-4.1634×10^0	1.4838×10^{-1}	0.2198
0.300	1.359×10^{-1}	1.553×10^{-1}	1.776×10^{-1}	-1.8621×10^0	1.3392×10^{-1}	0.2770
0.350	7.226×10^{-1}	8.179×10^{-1}	9.252×10^{-1}	-2.0152×10^{-1}	1.2380×10^{-1}	0.2910
0.400	2.541×10^0	2.865×10^0	3.222×10^0	1.0522×10^0	1.1840×10^{-1}	0.3150
0.450	6.768×10^0	7.613×10^0	8.540×10^0	2.0290×10^0	1.1638×10^{-1}	0.3243
0.500	1.477×10^1	1.660×10^1	1.860×10^1	2.8085×10^0	1.1629×10^{-1}	0.2704
0.600	4.690×10^1	5.284×10^1	5.939×10^1	3.9668×10^0	1.1826×10^{-1}	0.2420
0.700	1.054×10^2	1.188×10^2	1.342×10^2	4.7785×10^0	1.2047×10^{-1}	0.2958
0.800	1.907×10^2	2.154×10^2	2.436×10^2	5.3737×10^0	1.2194×10^{-1}	0.3515
0.900	2.996×10^2	3.387×10^2	3.831×10^2	5.8260×10^0	1.2259×10^{-1}	0.4013
1.000	4.268×10^2	4.827×10^2	5.452×10^2	6.1797×10^0	1.2257×10^{-1}	0.4403
1.250	7.913×10^2	8.928×10^2	1.006×10^3	6.7941×10^0	1.2073×10^{-1}	0.4612
1.500	1.175×10^3	1.320×10^3	1.486×10^3	7.1859×10^0	1.1779×10^{-1}	0.4135
1.750	1.548×10^3	1.735×10^3	1.944×10^3	7.4584×10^0	1.1441×10^{-1}	0.2968
2.000	1.904×10^3	2.128×10^3	2.377×10^3	7.6631×10^0	1.1064×10^{-1}	0.3099
2.500	2.607×10^3	2.887×10^3	3.201×10^3	7.9684×10^0	1.0184×10^{-1}	0.4288
3.000	3.340×10^3	3.672×10^3	4.027×10^3	8.2080×10^0	9.2440×10^{-2}	0.4713
3.500	4.139×10^3	4.511×10^3	4.903×10^3	8.4141×10^0	8.4123×10^{-2}	0.4385

Table 8.5 (cont'd)

T (GK)	Monte Carlo Rate			Lognormal Parameters		t_{AD}^*
	Low	Median	High	μ	σ	
4.000	5.000×10^3	5.405×10^3	5.846×10^3	8.5953×10^0	7.7684×10^{-2}	0.3567
5.000	6.791×10^3	7.271×10^3	7.797×10^3	8.8924×10^0	6.9652×10^{-2}	0.5213
6.000	8.514×10^3	9.082×10^3	9.696×10^3	9.1146×10^0	6.5280×10^{-2}	0.6535
7.000	1.005×10^4	1.069×10^4	1.139×10^4	9.2780×10^0	6.2538×10^{-2}	0.8821
8.000	1.135×10^4	1.203×10^4	1.280×10^4	9.3968×10^0	6.0628×10^{-2}	1.072
9.000	1.237×10^4	1.311×10^4	1.392×10^4	9.4825×10^0	5.9228×10^{-2}	1.137
10.000	1.316×10^4	1.394×10^4	1.478×10^4	9.5432×10^0	5.8179×10^{-2}	1.150

Note. — The $^{29}\text{Si}(p,\gamma)^{30}\text{P}$ thermonuclear reaction rates calculated in the present work using the Monte Carlo-based `RatesMC` program (Longland *et al.*, 2010b). The low, median, and high rates correspond to the 0.16, 0.50, and 0.84 quantiles of the reaction rate probability density function, respectively, and are given in units of $\text{cm}^3\text{mol}^{-1}\text{s}^{-1}$. The parameters μ and σ describe the lognormal approximation of the rate probability density function. The Anderson-Darling test statistics, t_{AD}^* , indicate the merit of the lognormal approximation of the probability density function at each temperature.

Similarly, Figure 8.3 shows the probability density function of the reaction rate (shown in red) as well as its agreement with a lognormal distribution (black) at several discrete temperatures. The temperature and Anderson-Darling test statistic of the lognormal distribution corresponding to the displayed probability density function are shown in the upper right corner of each subplot. It is clear that, while the lognormal distribution adequately reproduces the reaction rate probability density function for $T = 20$ MK, 250 MK, 500 MK, and 1 GK, it strongly diverges from the probability density function at $T = 50$ MK and 100 MK.

First, consider the $T = 50$ MK subplot. Upon cursory inspection, it is clear that the reaction rate probability density function at this temperature resembles a Porter-Thomas distribution (Appendix B.3) rather than a lognormal distribution. It comes as no surprise then that the Anderson-Darling test statistic for this temperature, $t_{AD}^* = 308.5$, indicates that this probability density function is poorly reproduced by a lognormal distribution. Now, recall that the probability density functions of resonance strength and partial width upper limits are described by Porter-Thomas distributions

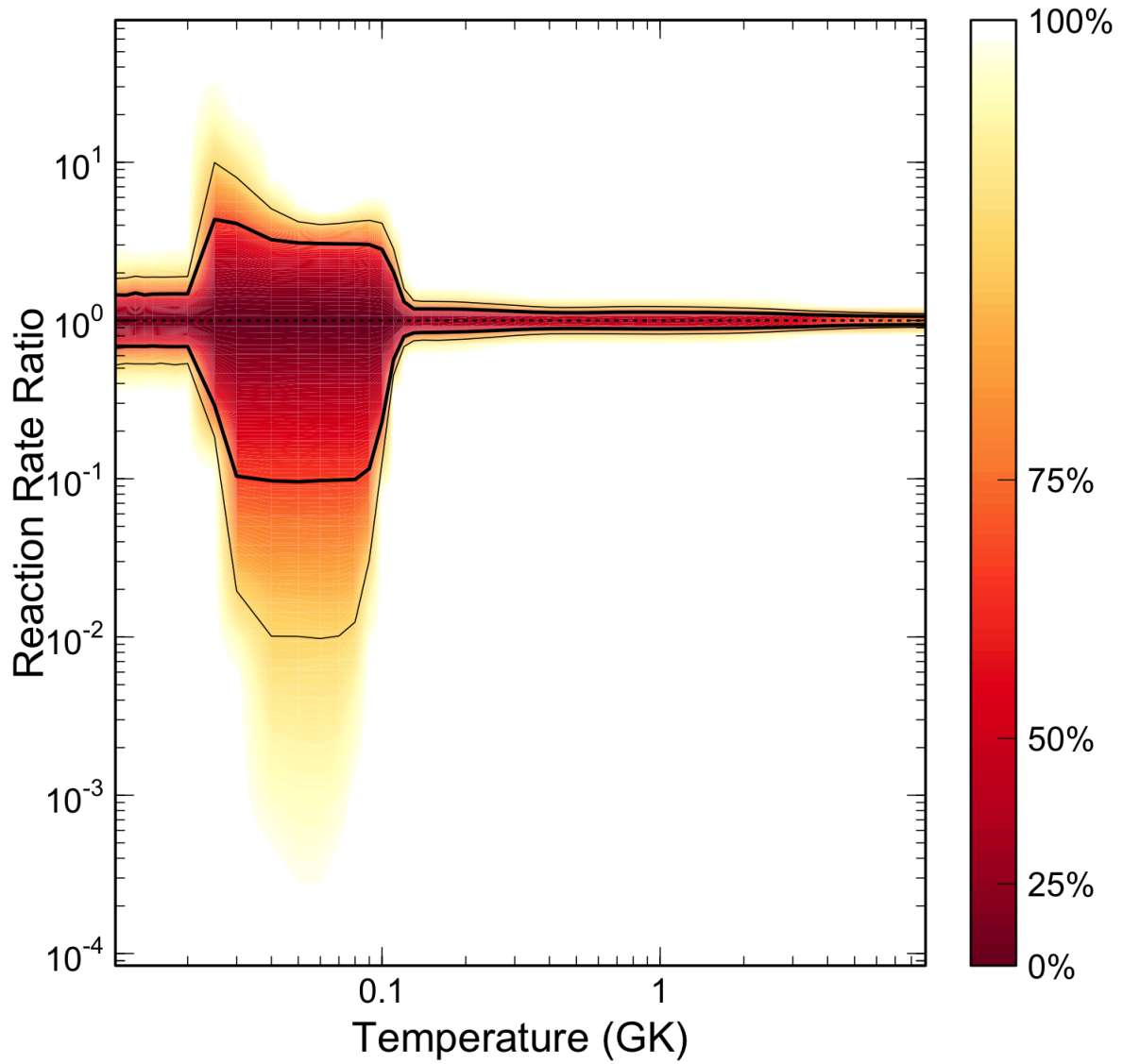


Figure 8.2: The $^{29}\text{Si}(p,\gamma)^{30}\text{P}$ reaction rate probability density as a function of temperature. All RatesMC samples are normalized to the median rate at each temperature. The thick black lines indicate 1σ coverage while the thin black lines mark the edge of the 2σ region. The color indicates the magnitude of the probability density function with the percent coverage marked on the color scale to the right.

(see Table 8.1), so it seems likely that the reaction rate at this temperature is dominated by the effects of a poorly known resonance. Further testing reveals that if the unobserved $E_r^{CM} = 108$ keV resonance (Table 8.3) is excluded from the $^{29}\text{Si}(p,\gamma)^{30}\text{P}$ reaction rate calculation, the rate probability density function at $T = 50$ MK exhibits

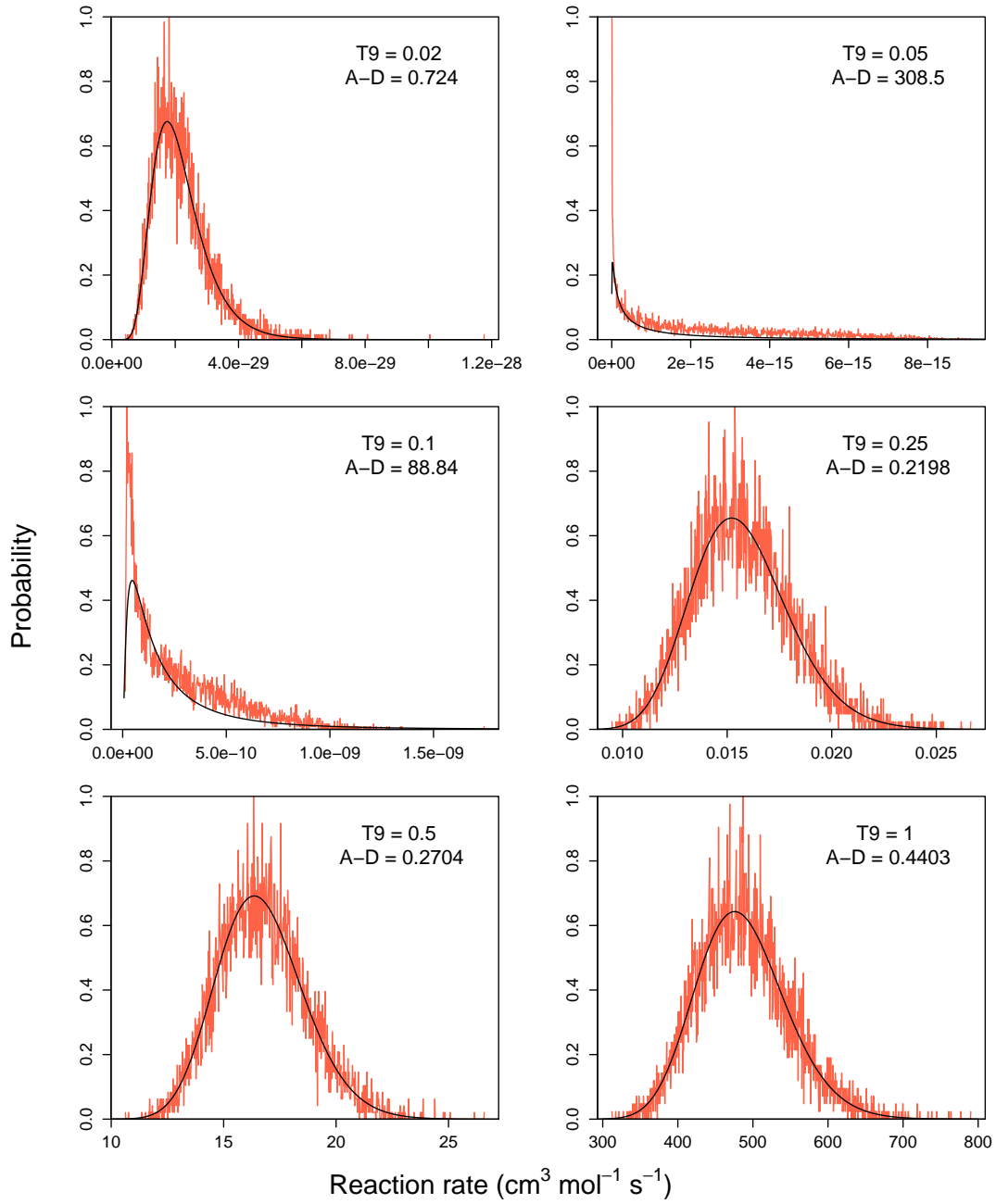


Figure 8.3: $^{29}\text{Si}(p,\gamma)^{30}\text{P}$ reaction rate probability density functions produced by RatesMC (Longland *et al.*, 2010b) for select temperatures. The red lines indicate the reaction rate probability density functions while black lines display the lognormal distributions approximating the reaction rates. The temperature (in GK) and the Anderson-Darling statistic (A-D) is indicated in the upper right corner of each subplot.

lognormal behavior. Therefore, this situation is likely to improve once experimentally determined values are available for the $E_r^{CM} = 108$ keV resonance.

Though it does not appear as dramatic as that of $T = 50$ MK, the $T = 100$ MK probability density function also appears to resemble a Porter-Thomas distribution and is inadequately reproduced by its lognormal approximation as a result. Therefore, the $T = 100$ MK reaction rate likely suffers from the same lack of experimentally determined values for resonances in the $E_r^{CM} < 300$ keV region discussed earlier. The probability density function does, however, exhibit a narrow peak in probability at approximately $1.7 \times 10^{-11} \text{ cm}^3 \text{ mol}^{-1} \text{ s}^{-1}$ rather than the sharp cutoff seen in the $T = 50$ MK function. This indicates that the reaction rate at this temperature likely includes weak contributions from resonances with experimentally known strengths in addition to contributions from unobserved resonances.

These hypotheses are supported by reaction rate contributions charted across the relevant temperature range in Figure 8.4, but the findings displayed in this figure are somewhat cryptic without further commentary. First, note that this figure includes a variety of colored bands. Each of these bands corresponds to a particular resonant or nonresonant source (labeled by center-of-mass frame energies in matching colors at the top of the figure) that contributes to the total $^{29}\text{Si}(p,\gamma)^{30}\text{P}$ thermonuclear reaction rate. Additionally, the fractional contributions vary over the temperature range of interest. The height of each band indicates the source's fractional contribution to the rate, while the thickness of each band corresponds to the uncertainty in the contribution.

Recall that the probability density function shown in Figure 8.3 implied that the reaction rate at $T = 50$ MK was governed by a poorly known resonance. The red band in Figure 8.4, corresponding to the unobserved $E_r^{CM} = 108$ keV resonance, shows that this resonance is the sole contributor to the $^{29}\text{Si}(p,\gamma)^{30}\text{P}$ rate at this temperature and the source of the Porter-Thomas features of the rate's probability density function at

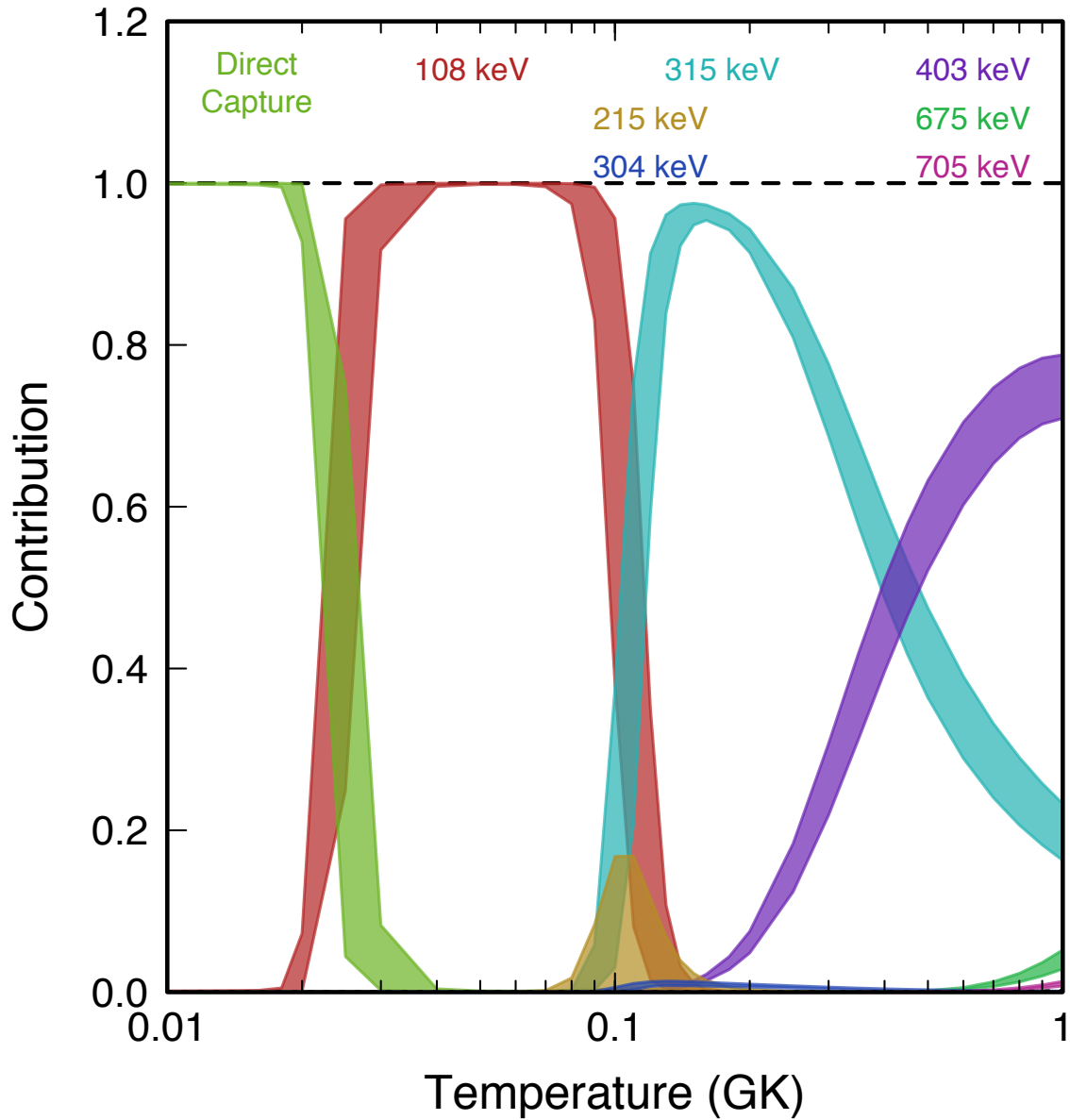


Figure 8.4: The fractional contributions to the total $^{29}\text{Si}(p,\gamma)^{30}\text{P}$ reaction rate. Each colored curve represents a specific contribution to the overall rate. The magnitude of the curve indicates the fraction it contributes to the rate at a given energy while the thickness of the curve signifies the uncertainty of its contribution. All energies refer to the center-of-mass frame. It is clear that in the classical nova Gamow window (0.1–0.4 GK) the resonances studied in these dissertation constitute the majority of contributions to the $^{29}\text{Si}(p,\gamma)^{30}\text{P}$ rate.

this temperature. By the same token, Figure 8.4 reveals that the reaction rate at 100 MK is composed of contributions from both unobserved resonances ($E_r^{CM} = 108$ keV and 215 keV) and an experimentally studied resonance ($E_r^{CM} = 315$ keV) in agreement with the probability density function seen in Figure 8.3 at this temperature.

In addition to supporting the findings of Figure 8.3, Figure 8.4 allows one to consider the improvements made to the understanding of the $^{29}\text{Si}(p,\gamma)^{30}\text{P}$ rate through the efforts described in this dissertation. For the the classical nova Gamow window—roughly 0.1 to 0.4 GK—it is clear that the resonances measured in this dissertation significantly contribute to the $^{29}\text{Si}(p,\gamma)^{30}\text{P}$ reaction rate. Though the unobserved $E_r^{CM} = 215$ keV resonance and the newly measured $E_r^{CM} = 304$ keV resonance each contribute less than 20% to the thermonuclear rate in this region, the $E_r^{CM} = 315$ keV resonance dominates the entirety of the Gamow window. Given that the current work has shown that this resonance is a factor of 1.5 stronger than indicated by previous research and reduced the uncertainty in this measurement by half (see Table 7.13), one can expect notable impact on the total $^{29}\text{Si}(p,\gamma)^{30}\text{P}$ reaction rate. This will be addressed in the following section when the current rate is compared to the rate evaluation of Iliadis *et al.* (2010c).

8.5 Comparison to Previous Rate Evaluation

Lastly, a comparison must be made between the current $^{29}\text{Si}(p,\gamma)^{30}\text{P}$ rate and that of the previous evaluation performed by Iliadis *et al.* (2010c). Figure 8.5 illuminates the differences between the two thermonuclear reaction rates.

In the top panel of this figure, both rates have been normalized to the median reaction rate obtained in the current rate evaluation. The pink region marks the 68% coverage probability of the Iliadis *et al.* (2010c) rate ratio, and the blue region signifies the same for the present rate ratio. The ample overlap between the two regions is

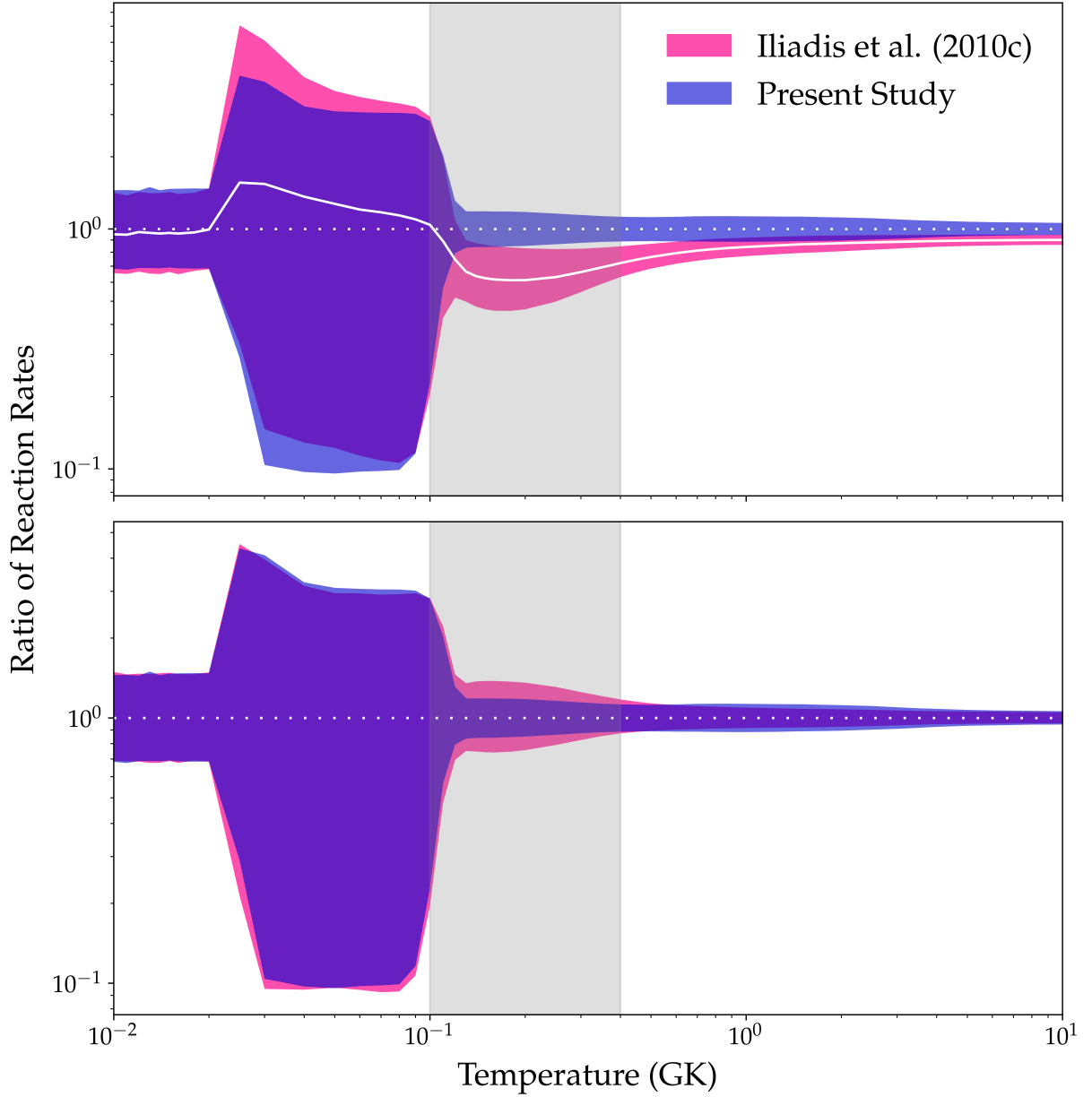


Figure 8.5: Comparison of the present $^{29}\text{Si}(p,\gamma)^{30}\text{P}$ reaction rate (blue) to that of [Iliadis et al. \(2010c\)](#) (pink). The shaded region illustrates the 68% coverage probability of each reaction rate ratio, and the purple regions indicate overlap between the rates. The Gamow window of ONE classical novae ($T = 0.1\text{--}0.4$ GK) is indicated by the grey region. **Top:** Both rates are normalized to the median rate of the current evaluation. The solid white line indicates the ratio of the [Iliadis et al. \(2010c\)](#) median rate to the present median rate. **Bottom:** Each rate is normalized to its respective median value.

shown in purple. The solid white line indicates the ratio of the median rates. A few significant observations can be made from this plot.

First, it should be noted that the two rates visibly deviate from each other in the $T \approx 0.025\text{--}0.1$ GK region. In this region, the [Iliadis *et al.* \(2010c\)](#) rate is larger than the current rate, and from Figure 8.4 it is clear that the $E_r^{CM} = 108$ keV resonance is the only significant contributor to the $^{29}\text{Si}(p,\gamma)^{30}\text{P}$ rate here. In the current rate evaluation, the center-of-mass energy for this resonance was corrected for the erroneous use of the atomic Q-value in the past (see [Iliadis, 2019](#)), and this correction is likely the cause of the discrepancy between the rates in the $T \approx 0.025\text{--}0.1$ GK range.

The two rates also differ from each other between $T \approx 0.1$ GK and $T \approx 1$ GK. Here, the current rate is up to a factor of ~ 1.6 higher than the [Iliadis *et al.* \(2010c\)](#) rate, and it is again useful to refer to Figure 8.4 for rate contributions. While this region includes contributions from multiple resonances between $E_r^{CM} = 200$ keV and $E_r^{CM} = 700$ keV, the outstanding contribution in this region is $E_r^{CM} = 315$ keV resonance. This resonance was found to be a factor of 1.5 stronger than previously reported by [Reinecke *et al.* \(1985\)](#) and likely responsible for the difference between the rates as a result.

The bottom panel of Figure 8.5 provides a slightly different comparison of the past and present reaction rates. In this panel, each rate is normalized to its respective median rate. This tactic allows for a straightforward comparison of the past and present rate uncertainty. Again, there are large regions of overlap between the two rate ratios, but it is clear that the reaction rate uncertainty has been reduced between $T \approx 0.1$ GK and $T \approx 0.5$ GK. This is probably the result of the considerable reduction in the $E_r^{lab} = 324$ keV resonance strength uncertainty produced by the current $^{29}\text{Si}(p,\gamma)^{30}\text{P}$ study.

Lastly, the grey shaded region in each Figure 8.5 subplot indicates the Gamow window for oxygen-neon classical novae—roughly $T = 0.1\text{--}0.4$ GK. In the top panel, it is clear that the increase to the $^{29}\text{Si}(p,\gamma)^{30}\text{P}$ rate caused by the $E_r^{CM} = 315$ keV strength

measured in the present study falls firmly within this Gamow window, meaning that it can be expected to have a notable effect on classical novae nucleosynthesis. The decrease to the rate uncertainty seen in the bottom panel of the figure also falls within the classical nova Gamow window. These and other significant findings in the present $^{29}\text{Si}(p,\gamma)^{30}\text{P}$ study will be reviewed in the following chapter.

CHAPTER 9: CONCLUSIONS

Classical novae are fascinating celestial phenomena that hold important implications for galactic chemical evolution, extragalactic research, and cutting edge astrophysical research. Neon novae, with their enhanced peak burning temperatures and rare variety of underlying white dwarf stars, are of particular interest to the astrophysical community. Nucleosynthesis simulations, presented in [Downen *et al.* \(2013\)](#) and the current work, identified several reactions important to the understanding of neon novae.

In fact, one of these reactions, $^{29}\text{Si}(p,\gamma)^{30}\text{P}$, proved particularly well suited to become the focus of this dissertation. It was shown that uncertainty in this reaction rate has significant ramifications on our understanding of neon novae through presolar grain measurements and computational models. Furthermore, this reaction had not been measured in the classical nova energy range for over three decades, and three $^{29}\text{Si}(p,\gamma)^{30}\text{P}$ resonances in the nova Gamow window were unobserved or uncertain prior to the current work.

Consequently, the present study of the $^{29}\text{Si}(p,\gamma)^{30}\text{P}$ reaction was undertaken at the Laboratory for Experimental Nuclear Astrophysics in Durham, North Carolina. To measure the three resonances of interest, ^{29}Si -enriched tantalum targets were produced in collaboration with Centre de Spectrométrie Nucléaire et de Spectrométrie de Masse, and both the LENA I JN Van de Graaff accelerator and the newly upgraded LENA II electron cyclotron resonance accelerator ([Cooper *et al.*, 2018](#)) were employed to produce proton beams across a range of energies. These efforts proved fruitful,

yielding a number of significant findings. First, a renormalized $E_r^{lab} = 416$ keV resonance strength was presented and used as a standard in the following resonance measurements. The $E_r^{lab} = 324$ keV resonance, last measured by [Reinecke *et al.* \(1985\)](#), was remeasured as part of the present effort, and while the determined resonance strength agreed with previous measurements, the new measurement notably improved upon the resonance strength uncertainty of the [Reinecke *et al.* \(1985\)](#) value. Furthermore, the first successful observation of the $E_r^{lab} = 314$ keV resonance was made. This resonance was found to be a factor of 2.5 stronger than the theoretical upper limit predicted by dimensionless single-particle reduced width calculations. An experimental upper limit resonance strength for the $E_r^{lab} = 221$ keV resonance, comparable to the theoretical upper limit derived from spectroscopic factor upper limits, was also determined.

To explore the significance of this work, the $^{29}\text{Si}(p,\gamma)^{30}\text{P}$ reaction rate was reevaluated. Compared to the thermonuclear rate presented in [Iliadis *et al.* \(2010c\)](#), the new $^{29}\text{Si}(p,\gamma)^{30}\text{P}$ rate is markedly stronger and has a smaller uncertainty, particularly within the confines of the classical nova Gamow window, and it would undoubtedly affect the final ejecta abundances predicted by simulations of classical nova nucleosynthesis. In conclusion, it is my sincere hope that the work presented in this dissertation renews efforts to clarify the relationship between spectroscopic and presolar grain measurements, reaction rate uncertainty, and classical nova nucleosynthesis.

APPENDIX A: BOUND STATE BRANCHING RATIOS

The bound state branching ratios presented in Table A.1 were used for the analysis of the $^{29}\text{Si}(\text{p},\gamma)^{30}\text{P}$ data in dissertation. In particular, these branching ratios were used to simulate the decay of the ^{30}P bound states in the GEANT4 simulation of the $^{29}\text{Si}(\text{p},\gamma)^{30}\text{P}$ decay (Chapter 7). With a few exceptions, the presented branching ratios represent the weighted mean values from Grossmann *et al.* (2000) and Endt (1990) and references therein. Branching ratios where only an upper limit is provided were presented for completeness, but these branchings were not included in the simulation or analysis.

Table A.1. Gamma Decay of ^{30}P Bound States

Bound Levels in ^{30}p		Decay to E_x (%)									Other Levels
E_x (keV) ^a	$J^\pi; \Gamma^b$	0 1 ⁺	677.01 0 ⁺ ; 1	708.70 1 ⁺	1454.23 2 ⁺	1973.27 3 ⁺	2538.95 3 ⁺	2723.72 2 ⁺	2839.34 3 ⁺	2937.46 2 ⁺ ; 1	
677.01	0 ⁺ ; 1	100									
708.70	1 ⁺	99.87 ± 0.02	0.13 ± 0.02								
1454.23	2 ⁺	95.3 ± 0.3	< 0.2	4.7 ± 0.1							
1973.27	3 ⁺	44.2 ± 0.3	< 0.3	55.8 ± 0.3	< 4						
2538.95	3 ⁺	96.2 ± 0.4	< 0.4	3.1 ± 0.1	< 0.4	0.7 ± 0.1					
2723.72	2 ⁺	97.5 ± 0.4	< 0.6	2.5 ± 0.2	< 0.2	< 0.1					
2839.34	3 ⁺	22.4 ± 0.5	< 5	52.1 ± 0.7	25.5 ± 0.5						
2937.46	2 ⁺ ; 1	17.9 ± 0.2	32.3 ± 0.3	5.5 ± 0.1	44.0 ± 0.4	0.3 ± 0.1					
3019.2	1 ⁺	< 1	100	< 0.7	< 0.2						
3733.80	1 ⁺	50.5 ± 1.0	32 ± 1		10 ± 1	< 3	< 2			7.5 ± 0.5	
3835.80	2 ⁺	< 2	< 5	20.0 ± 0.5	9.9 ± 0.4					70.1 ± 0.8	
3928.61	3 ⁺		< 7	< 3	29 ± 1					71 ± 1	
4143.63	2 [−]	86.9 ± 0.9	< 1	4.2 ± 0.3	7.5 ± 0.4	< 1	< 0.9			1.4 ± 0.1	
4182.81	2 ⁺ ; 1	10.7 ± 0.3	1.2 ± 0.1	75.9 ± 0.8	2.6 ± 0.3	3.6 ± 0.2	6.0 ± 0.3				
4231.97	4 [−]	2.5 ± 0.5 ^b	< 0.1		< 0.2	68.5 ± 0.9 ^b	25.9 ± 0.5 ^b		3.1 ± 0.5 ²		
4298.6	4 ⁺				81 ± 5 ^b		19 ± 5 ²				
4343.8	5 ⁺					95 ± 1	5 ± 1				
4422.8	2 ⁺	95.9 ± 0.8		4.1 ± 0.2	< 3	< 0.8	< 0.7				
4469.1	0 ⁺ ; 1	93 ± 1	< 0.9	7 ± 1	< 0.9	< 0.5	< 0.2				
4502.21	1 ⁺ ; 1	40.3 ± 1.0	< 2	3.6 ± 0.3	56.1 ± 1.0	< 4				< 2	
4625.92	3 [−]		< 0.8	< 0.8	56.8 ± 0.9	14.8 ± 0.5	< 1			28.4 ± 0.7	
4736.03	3 ⁺	11.3 ± 0.4		7.4 ± 0.3	12.3 ± 0.5					67.1 ± 0.9	1.9 ± 0.2 → 3019.2
4925.5	5 [−]	< 0.6			10.7 ± 0.4						89.3 ± 0.9 → 4231.97
4937.3	1		82 ± 2							18 ± 1	
4941.4	1 ⁺		91 ± 1			9 ± 1					
5206.8	3 ⁺	76 ± 2		24 ± 1							
5230.1	4 [−]					51.3 ± 3.1	24.2 ± 1.8		24.5 ± 1.8		
5411.1						28 ± 6 ^c			41 ± 6 ^c	31 ± 7 ³	
5506.4	1; 0	1.7 ± 0.3	96 ± 1							2.3 ± 0.2	
5508.55	(2, 3); 1				52 ± 1	48 ± 1					
5576.3	(1, 2) ⁺ ; 1	17 ± 1		61 ± 2	16 ± 1						3 ± 1 → 3733.80 3 ± 1 → 3835.80
5701.3	1 ⁺ ; 0						7 ± 1	5 ± 1		74 ± 3	14 ± 1 → 4182.81
5934.0						31.1 ± 1.0 ^c	2.1 ± 0.4 ^c		11.9 ± 0.7 ^c	12.8 ± 0.7 ^c	42.1 ± 1.0 → 4343.8 ^c

Note. — All branching ratios are weighted mean values from Grossmann *et al.* (2000) and Endt (1990) and references therein unless noted otherwise. All upper limit branching ratios are given by Endt (1990).

^aAll excitation energies are given by Grossmann *et al.* (2000).

^bFrom Endt (1990).

^cFrom Grossmann *et al.* (2000).

APPENDIX B: PROBABILITY DENSITY FUNCTIONS

In order to calculate thermonuclear reaction rates with statistically meaningful uncertainties, all required nuclear properties needed to be assigned appropriate probability density functions. Three different types of distributions—the Gaussian distribution, the lognormal distribution, and the Porter-Thomas distribution—were chosen for this purpose. The following sections, based on the thorough discussion in [Longland *et al.* \(2010b\)](#) and [Pogrebnyak *et al.* \(2013\)](#), detail the distributions and the way in which they describe certain nuclear properties. For a summary of the nuclear property probability density function assignments used in the calculation of the new $^{29}\text{Si}(\text{p},\gamma)^{30}\text{P}$ reaction rate, see Table [8.1](#).

B.1 Gaussian distribution

One of the simplest and most frequently used distributions, the Gaussian probability density function for a continuous random variable is defined as

$$f(x) = \frac{1}{\sigma\sqrt{2\pi}} e^{-(x-\mu)^2/(2\sigma^2)} \quad (\text{B.1})$$

with the parameters μ and σ ([Cowan, 1998](#)). Here, μ is the mean (or expectation value, $E[x]$) and σ is the standard deviation (or square root of the variance, $V[x]$), meaning that

$$E[x] = \int_{-\infty}^{\infty} x f(x) dx = \mu \quad (\text{B.2})$$

$$V[x] = \int_{-\infty}^{\infty} (x - \mu)^2 f(x) dx = \sigma^2. \quad (\text{B.3})$$

The Gaussian distribution is useful for a few reasons. For one, it is easily understood because of its simple, symmetric form. On a more technical note, the central

limit theorem indicates that a Gaussian distribution describes the sum of a large collection of independent variables, and this type of distribution is particularly suitable for describing the measurement uncertainty involving many small contributions as a result. However, it should be noted that the distribution is defined for the region $-\infty < x < \infty$. If improperly used to describe a physical quantity, this can result in an unphysical situation.

Typically, resonance energies are determined using thick-target yield curve or excitation energy measurements (see Sections 5.2 and 7.1.3). Thus, it is easy to imagine that the uncertainty in one of these measurements would be well described by a Gaussian probability density function. In `RatesMC`, the literature-reported or -derived resonance energy is associated with μ , and the 1σ uncertainty is associated with the σ parameter of the Gaussian distribution. Of course, it is possible to sample negative values of E_r . On its face, this may seem unphysical, but `RatesMC` safely treats these values as subthreshold resonances and applies the appropriate treatment.

B.2 Lognormal distribution

The next distribution to be discussed is the lognormal distribution. Like the previously discussed Gaussian distribution, this distribution deals with a continuous random variable, y , that is Gaussian distributed. However, this variable is defined as

$$y \equiv \ln(x) \tag{B.4}$$

resulting in the definition of the lognormal distribution,

$$f(x) = \frac{1}{\sigma x \sqrt{2\pi}} e^{-(\ln x - \mu)^2 / (2\sigma)^2}. \tag{B.5}$$

Again, this distribution is specified using the two parameters, μ and σ . In terms of the expectation value and the variance, these parameters are given by

$$E[x] = e^{(2\mu+\sigma^2)/2} \quad (\text{B.6})$$

$$V[x] = e^{(2\mu+\sigma^2)} \left[e^{\sigma^2} - 1 \right]. \quad (\text{B.7})$$

The geometric mean, μ_g , and the geometric standard deviation, σ_g , are

$$\mu_g = e^\mu \quad (\text{B.8})$$

$$\sigma_g = e^\sigma. \quad (\text{B.9})$$

The median value of the lognormal probability density function is also equivalent to the geometric mean given above. For a 68% coverage probability, a number of properties can be found in terms of the geometric mean and standard deviation:

$$\text{Lower Bound : } \frac{\mu_g}{\sigma_g} = e^{\mu-\sigma} \quad (\text{B.10})$$

$$\text{Upper Bound : } \mu_g \sigma_g = e^{\mu+\sigma} \quad (\text{B.11})$$

$$\text{Factor Uncertainty : } f.u. = e^\sigma. \quad (\text{B.12})$$

It was discussed earlier that Gaussian distributions characterize the *sum* of an infinite number of independent contributions, but while y is Gaussian distributed, it is defined as a function of the independent variable x . Then, it is easy to see that a lognormal distribution describes the *product* of many independent variables, rather than the summation. It should also be noted that the lognormal distribution is only defined in the range of $0 < x < \infty$. This means that it is particularly convenient when used to describe physical quantities that are explicitly positive. Because of these features, lognormal distributions were chosen to represent partial widths, nonresonant

S-factors (Section 2.3.1), and resonance strengths (Section 2.3.2) in `RatesMC` calculations.

B.3 Porter-Thomas distribution

One final type of distribution is required to characterize the nuclear input used by `RatesMC`. This distribution, is a specific form of the chi-squared distribution. A chi-square distribution, as the name implies, describes the summation of the squares of k independent, Gaussian-distributed variables. If the chi-square distribution is limited to one degree of freedom ($k = 1$), it takes the form of

$$f(x) = \frac{1}{\sqrt{2\pi x}} e^{-x/2} \quad (\text{B.13})$$

with expectation value and variance

$$E[x] = k = 1 \quad (\text{B.14})$$

$$V[x] = 2k = 2, \quad (\text{B.15})$$

respectively. This particular form of the chi-square distribution is frequently referred to as the Porter-Thomas distribution. This distribution is defined over the range $0 < x < \infty$.

As shown by [Longland *et al.* \(2010b\)](#), partial widths can be expressed in terms of the dimensionless reduced width, θ^2 , so by extension, the upper limits of these parameters can be found in terms of the dimensionless reduced width upper limit, θ_{ul}^2 . As one might expect, the Porter-Thomas distribution is well suited to describe the probability density function of a squared amplitude such as this. Thus, the Porter-Thomas distribution was used to describe upper limit values of partial widths in `RatesMC`.

REFERENCES

- NIST/SEMATECH e-Handbook of Statistical Methods. NIST, 2002.
- Hertzsprung-Russell Diagram. European Southern Observatory, 2007.
- J. Allison, K. Amako, J. Apostolakis, P. Arce, M. Asai, T. Aso, E. Bagli, A. Bagulya, S. Banerjee, G. Barrand, *et al.* Recent developments in GEANT4. Nuclear Instruments & Methods in Physics Research A, 835:186, 2016.
- L. G. Althaus, A. H. Córscico, J. Isern, and E. García-Berro. Evolutionary and pulsational properties of white dwarf stars. *Astronomy & Astrophysics Review*, 18(4):471, 2010.
- S. I. Amari, X. Gao, L. Nittler, E. Zinner, J. José, M. Hernanz, and R. S. Lewis. Presolar grains from novae. *The Astrophysical Journal*, 551(2):1065, 2001.
- S. I. Amari, E. Zinner, and R. S. Lewis. Interstellar graphite from the Murchison meteorite. In *AIP Conference Proceedings*, pages 581–584. AIP, 1995.
- E. Anders and E. Zinner. Interstellar Grains in Primitive Meteorites: Diamond, Silicon Carbide, and Graphite. *Meteoritics & Planetary Science*, 28:490, 1993.
- H. H. Andersen and J. F. Ziegler. *Hydrogen. Stopping Powers and Ranges in All Elements*. Pergamon Press, New York, 1977.
- J. Andrea, H. Drechsel, and S. G. Starrfield. Element abundances of classical novae. *Astronomy & Astrophysics*, 291:869, 1994.
- C. Angulo, M. Arnould, M. Rayet, P. Descouvemont, D. Baye, C. Leclercq-Willain, A. Coc, S. Barhoumi, P. Aguer, C. Rolfs, *et al.* A compilation of charged-particle induced thermonuclear reaction rates. *Nuclear Physics A*, 656(1):3, 1999.
- R. d. Atkinson and F. G. Houtermans. Zur Frage der Aufbaumöglichkeit der Elemente in Sternen. *Zeitschrift für Physik*, 54(9-10):656, 1929.
- E. E. Baart, L. L. Green, and J. C. Willmott. An Investigation of the $^{29}\text{Si}(p,\gamma)^{30}\text{P}$ Reaction. *Proceedings of the Physical Society*, 79(2):237, 1962.
- C.-O. Bacri, C. Bachelet, C. Baumier, J. Bourçois, L. Delbecq, D. Ledu, N. Pauwels, S. Picard, S. Renouf, and C. Tanguy. SCALP, a platform dedicated to material modifications and characterization under ion beam. *Nuclear Instruments & Methods in Physics Research B*, 406, Part A:48, 2017.

- R. J. Barlow. Extended maximum likelihood. *Nuclear Instruments & Methods in Physics Research A*, 297(3):496, 1990.
- R. J. Barlow and C. Beeston. Fitting using finite Monte Carlo samples. *Computer Physics Communications*, 77(2):219, 1993.
- M. S. Basunia. Nuclear Data Sheets for $A = 30$. *Nuclear Data Sheets*, 111(9):2331, 2010.
- D. O. Boerma, W. Grüebler, V. König, P. A. Schmelzbach, and R. Risler. Spin-parity Combinations in ^{30}P Determined with a t_{20} Polarized Deuteron Beam. *Nuclear Physics A*, 255:275, 1975.
- N. Bohr. Neutron Capture and Nuclear Constitution. *Nature*, 137:344, 1936.
- M. Bose. Private Communication, 2017.
- M. Bose, X. Zhao, C. Floss, F. J. Stadermann, and Y. Lin. Stardust material in the paired enstatite meteorites: SAH 97096 and SAH 97159. In *11th International Symposium on Nuclei in the Cosmos*, page 138. Heidelberg, Germany, 2010.
- J. V. Bradley. *Distribution-Free Statistical Tests*. Prentice-Hall, Englewood Cliffs, NJ, 1st edition edition, 1968.
- C. Broude, L. L. Green, J. J. Singh, and J. C. Willmott. Low-Lying Levels of P^{30} . *Physical Review*, 101(3):1052, 1956a.
- C. Broude, L. L. Green, J. C. Willmott, and J. J. Singh. Levels of ^{26}Al , ^{30}P , and ^{31}P . *Physica*, 22(6):1139, 1956b.
- M. Q. Buckner. *Hydrogen Burning of the Rare Oxygen Isotopes*. Ph.D. thesis, The University of North Carolina at Chapel Hill, 2014.
- M. Q. Buckner, C. Iliadis, K. J. Kelly, L. N. Downen, A. E. Champagne, J. M. Cesaratto, C. Howard, and R. Longland. High-intensity-beam study of $^{17}\text{O}(p,\gamma)^{18}\text{F}$ and thermonuclear reaction rates for $^{17}\text{O} + p$. *Physical Review C*, 91(1):015812, 2015.
- S. Carson, C. Iliadis, J. M. Cesaratto, A. E. Champagne, L. N. Downen, M. Ivanovic, J. H. Kelley, R. Longland, J. R. Newton, G. Rusev, *et al.* Ratio of germanium detector peak efficiencies at photon energies of 4.4 and 11.7 MeV: Experiment versus simulation. *Nuclear Instruments & Methods in Physics Research A*, 618(1-3):190, 2010.
- J. Casanova, J. José, E. García-Berro, S. N. Shore, and A. C. Calder. Kelvin-Helmholtz instabilities as the source of inhomogeneous mixing in nova explosions. *Nature*,

478(7370):490, 2011.

- J. M. Cesaratto. *Resonant Proton Capture on ^{23}Na and Elemental Variations in Globular Cluster Stars*. Ph.D. thesis, The University of North Carolina at Chapel Hill, 2011.
- J. M. Cesaratto, A. E. Champagne, M. Q. Buckner, T. B. Clegg, S. Daigle, C. Howard, C. Iliadis, R. Longland, J. R. Newton, and B. M. Oginni. Measurement of the $E_r^{c.m.} = 138$ keV resonance in the $^{23}\text{Na}(p,\gamma)^{24}\text{Mg}$ reaction and the abundance of sodium in AGB stars. *Physical Review C*, 88(6):065806, 2013.
- J. M. Cesaratto, A. E. Champagne, T. B. Clegg, M. Q. Buckner, R. C. Runkle, and A. Stefan. Nuclear astrophysics studies at LENA: The accelerators. *Nuclear Instruments & Methods in Physics Research A*, 623(3):888, 2010.
- D. J. Chivers. Freeman ion source: An overview (invited). *Review of Scientific Instruments*, 63(4):2501, 1992.
- B.-G. Choi, G. J. Wasserburg, and G. R. Huss. Circumstellar Hibonite and Corundum and Nucleosynthesis in Asymptotic Giant Branch Stars. *The Astrophysical Journal Letters*, 522(2):L133, 1999.
- D. D. Clayton. *Principles of Stellar Evolution and Nucleosynthesis*. The University of Chicago Press, Chicago, 2nd edition, 1983.
- A. Coc, M. Hernanz, J. José, and J.-P. Thibaud. Influence of new reaction rates on ^{18}F production in novae. *Astronomy & Astrophysics*, 357(2):561, 2000.
- A. L. Cooper, K. J. Kelly, E. Machado, I. Pogrebnyak, J. T. Surbrook, C. Tysor, P. Thompson, M. Emamian, B. Walsh, B. P. Carlin, *et al.* Development of a variable-energy, high-intensity, pulsed-mode ion source for low-energy nuclear astrophysics studies. *Review of Scientific Instruments*, 89(8):083301, 2018.
- G. Cowan. *Statistical Data Analysis*. Oxford University Press, New York, 1998.
- S. Daigle, K. J. Kelly, A. E. Champagne, M. Q. Buckner, C. Iliadis, and C. Howard. Measurement of the $E_r^{c.m.} = 259$ keV resonance in the $^{14}\text{N}(p,\gamma)^{15}\text{O}$ reaction. *Physical Review C*, 94(2):025803, 2016.
- J. R. Dermigny. *Investigation of the $^{30}\text{Si}(p,\gamma)^{31}\text{P}$ Reaction*. Ph.D. thesis, The University of North Carolina at Chapel Hill, 2018.
- J. R. Dermigny, C. Iliadis, M. Q. Buckner, and K. J. Kelly. γ -Ray spectroscopy using a binned likelihood approach. *Nuclear Instruments & Methods in Physics Research A*, 830(c):427, 2016.

- G. U. Din. The $^{29}\text{Si}(p,\gamma)^{30}\text{P}$ and $^{29}\text{Si}(p, p'\gamma)^{29}\text{Si}$ Reactions from 1300 to 1850 keV. *Australian Journal of Physics*, 23:261, 1970.
- C. L. Doherty, L. Siess, J. C. Lattanzio, and P. Gil-Pons. Super asymptotic giant branch stars. I – Evolution code comparison. *Monthly Notices of the Royal Astronomical Society*, 401(3):1453, 2010.
- D. T. Doherty, G. Lotay, P. J. Woods, D. Seweryniak, M. P. Carpenter, C. J. Chiara, H. M. David, R. V. F. Janssens, L. Trache, and S. Zhu. Key Resonances in the $^{30}\text{P}(p,\gamma)^{31}\text{S}$ Gateway Reaction for the Production of Heavy Elements in ONe Novae. *Physical Review Letters*, 108(26):262502, 2012.
- L. N. Downen, C. Iliadis, J. José, and S. G. Starrfield. Nuclear Thermometers for Classical Novae. *The Astrophysical Journal*, 762(2):105, 2013.
- L. N. Downen, K. J. Kelly, S. Hunt, J. T. Surbrook, J. R. Dermigny, M. Q. Buckner, B. P. Carlin, R. Longland, A. E. Champagne, A. L. Cooper, *et al.* The LENA JN Van de Graaff Accelerator. TUNL Progress Report, LII:138, 2015.
- H. W. Duerbeck. Novae: an historical perspective. In *Classical Novae*, pages 1–15. Cambridge University Press, 2008.
- W. W. Dykoski and D. Dehnhard. Single proton transfer to $^{29,30}\text{P}$ states. *Physical Review C*, 13:80, 1976.
- P. M. Endt. Energy Levels of $A=21\text{--}44$ Nuclei (VII). *Nuclear Physics A*, 1990.
- P. M. Endt. Strengths of Gamma-Ray Transitions in $A=5\text{--}44$ Nuclei, IV. *Atomic Data and Nuclear Data Tables*, 55:171, 1993.
- P. M. Endt. Supplement to Energy Levels of $A=21\text{--}44$ Nuclei (VII). *Nuclear Physics A*, 633(1):1, 1998.
- P. M. Endt, J. C. Kluyver, and C. van der Leun. Gamma Rays from the $\text{Si}^{29}(p,\gamma)\text{P}^{30}$ Reaction. *Physical Review*, 95(2):580, 1954.
- P. M. Endt and C. H. Paris. Nuclear Levels in P^{30} , S^{33} , and S^{35} . *Physical Review*, 110(1):89, 1958.
- P. M. Endt and C. van der Leun. Energy Levels of $A=21\text{--}44$ Nuclei (VI). *Nuclear Physics A*, 310:1, 1978.
- G. A. P. Engelbertink and P. M. Endt. Measurement of (p,γ) Resonance Strengths in the $s-d$ Shell. *Nuclear Physics*, 88(1):12, 1966.

- G. J. Ferland. Quantitative Spectroscopy of Photoionized Clouds. *Annual Review of Astronomy and Astrophysics*, 41(1):517, 2003.
- D. Foreman-Mackey. corner.py: Scatterplot matrices in Python. *The Journal of Open Source Software*, 1(2):24, 2016.
- W. A. Fowler, G. R. Caughlan, and B. A. Zimmermann. Thermonuclear Reaction Rates. *Annual Review of Astronomy and Astrophysics*, 5:525, 1967.
- S. C. Frankle, G. E. Mitchell, J. F. Shriner, E. G. Bilpuch, and C. R. Westerfeldt. Proton resonances in ^{30}P . *Physical Review C*, 45:2746, 1992.
- G. Gamow. Zur Quantentheorie des Atomkernes. *Zeitschrift für Physik*, 51:204, 1928.
- R. D. Gehrz, T. J. Jones, C. E. Woodward, M. A. Greenhouse, R. M. Wagner, T. E. Harrison, T. L. Hayward, and J. Benson. The Peculiar Infrared Temporal Development of Nova Vulpeculae 1987 (QV Vulpeculae). *The Astrophysical Journal*, 400(2):671, 1992.
- R. D. Gehrz, J. W. Truran, R. E. Williams, and S. G. Starrfield. Nucleosynthesis in Classical Novae and Its Contribution to the Interstellar Medium. *Publications of the Astronomical Society of the Pacific*, 110(743):3, 1998.
- C. A. Grossmann, M. A. Labonte, G. E. Mitchell, J. D. Shriner, J. F. Shriner, G. A. Vavrina, and P. M. Wallace. Complete spectroscopy of ^{30}P . *Physical Review C*, 62(2):24323, 2000.
- R. W. Gurney and E. U. Condon. Quantum Mechanics and Radioactive Disintegration. *Physical Review*, 33(2):127, 1929.
- F. Gyngard, E. Zinner, L. Nittler, A. Morgand, F. J. Stadermann, and K. M. Hynes. Automated NanoSIMS Measurements of Spinel Stardust from the Murray Meteorite. *The Astrophysical Journal*, 717(1):107, 2010.
- P. Haenecour, C. Floss, J. José, S. I. Amari, K. Lodders, M. Jadhav, A. Wang, and F. Gyngard. Coordinated Analysis of Two Graphite Grains from the CO3.0 LAP 031117 Meteorite: First Identification of a CO Nova Graphite and a Presolar Iron Sulfide Subgrain. *The Astrophysical Journal*, 825:88, 2016.
- H. Hafner and H. H. Duhm. The $^{28}\text{Si}(^3\text{He},\text{p})^{30}\text{P}$ Reaction at 16 and 28 MeV. *Nuclear Physics A*, 227:450, 1974.
- G. I. Harris and A. K. Hyder, Jr. The 1505 keV Resonance in $^{29}\text{Si}(\text{p},\gamma)^{30}\text{P}$ and Properties of ^{30}P Levels. *Physics Letters*, 22(2):159, 1966.

- G. I. Harris and A. K. Hyder, Jr. Properties of P^{30} Levels from $Si^{29}(p,\gamma)P^{30}$ Reaction. I. Physical Review, 157(4):958, 1967.
- G. I. Harris, A. K. Hyder, Jr., and J. Walinga. Properties of P^{30} Levels from the Reaction $Si^{29}(p,\gamma)P^{30}$. II. Physical Review, 187(4):1413, 1969.
- W. K. Hastings. Monte Carlo sampling methods using Markov chains and their applications. Biometrika, 57(1):97, 1970.
- L. A. Helton, C. E. Woodward, F. M. Walter, K. M. Vanlandingham, G. J. Schwarz, A. Evans, J.-U. Ness, T. R. Geballe, R. D. Gehrz, M. A. Greenhouse, *et al.* The Dusty Nova V1065 Centauri (Nova Cen 2007): A Spectroscopic Analysis of Abundances and Dust Properties. The Astronomical Journal, 140(5):1347, 2010.
- R. C. Hertzog, L. L. Green, and M. W. Greene. Excited states of ^{30}P investigated through the $^{29}Si(^3He,d)^{30}P$ reaction. Journal of Physics A, 7, 1974.
- J. M. Hilbe, R. S. de Souza, and E. E. O. Ishida. *Bayesian Models for Astrophysical Data*. Cambridge University Press, 2017.
- L. Holland. *Vacuum Deposition of Thin Films*. Chapman and Hall, London, 1956.
- P. Hoppe, M. Pignatari, J. Kodolányi, and E. Gröner. NanoSIMS Isotope Studies of Rare Types of Presolar Silicon Carbide Grains from the Murchison Meteorite: Implications for Supernova Models and the Role of ^{14}C . Geostandards and Geoanalytical Research, 37(2):111, 2017.
- P. Hoppe, M. Pignatari, J. Kodolányi, E. Gröner, and S. I. Amari. NanoSIMS isotope studies of rare types of presolar silicon carbide grains from the Murchison meteorite: Implications for supernova models and the role of ^{14}C . Geochimica et Cosmochimica Acta, 221:182, 2018.
- J. H. Hough, Z. B. du Toit, and W. L. Mouton. Level Widths in ^{31}P . Nuclear Physics A, 109:393, 1968.
- C. Howard, S. Daigle, M. Q. Buckner, L. E. Erikson, R. C. Runkle, S. C. Stave, A. E. Champagne, A. L. Cooper, L. N. Downen, B. D. Glasgow, *et al.* Performance of a compact multi-crystal high-purity germanium detector array for measuring coincident gamma-ray emissions. Nuclear Instruments & Methods in Physics Research A, 783:85, 2015.
- C. Howard, C. Iliadis, and A. E. Champagne. Monte Carlo simulation of the LENA detector system. Nuclear Instruments & Methods in Physics Research A, A729:254, 2013.

- S. Hunt, C. Iliadis, A. E. Champagne, L. N. Downen, and A. L. Cooper. New measurement of the $E_{\alpha}^{lab} = 0.83$ MeV resonance in $^{22}\text{Ne}(\alpha, \gamma)^{26}\text{Mg}$. *Physical Review C*, 99(4):045804, 2019.
- K. M. Hynes and F. Gyngard. The Presolar Grain Database: <http://presolar.wustl.edu.libproxy.lib.unc.edu/~pgd>. In *40th Lunar and Planetary Science Conference*. The Woodlands, Texas, USA, 2009.
- C. Iliadis. Proton single-particle reduced widths for unbound states. *Nuclear Physics A*, 618:166, 1997.
- C. Iliadis. *Nuclear Physics of Stars*. Wiley-VCH Verlag GmbH & Co. KGaA, Hoboken, NJ, 2nd edition edition, 2015.
- C. Iliadis. Calculation of resonance energies from Q values. *Physical Review C*, 99(6):1, 2019.
- C. Iliadis, A. E. Champagne, J. José, S. G. Starrfield, and P. Tupper. The Effects of Thermonuclear Reaction-Rate Variations on Nova Nucleosynthesis: A Sensitivity Study. *The Astrophysical Journal Supplement Series*, 142(astro-ph/0206020):105, 2002.
- C. Iliadis, J. M. D’Auria, S. G. Starrfield, W. J. Thompson, and M. C. Wiescher. Proton-induced Thermonuclear Reaction Rates for $A = 20\text{--}40$ Nuclei. *The Astrophysical Journal Supplement Series*, 134(1):151, 2001.
- C. Iliadis, L. N. Downen, J. José, L. Nittler, and S. G. Starrfield. On Presolar Stardust Grains from CO Classical Novae. *The Astrophysical Journal*, 855(2):76, 2018.
- C. Iliadis, R. Longland, A. E. Champagne, and A. Coc. Charged-particle thermonuclear reaction rates: III. Nuclear physics input. *Nuclear Physics A*, 841(1):251, 2010a.
- C. Iliadis, R. Longland, A. E. Champagne, and A. Coc. Charged-particle thermonuclear reaction rates: IV. Comparison to previous work. *Nuclear Physics A*, 841(1-4):323, 2010b.
- C. Iliadis, R. Longland, A. E. Champagne, A. Coc, and R. Fitzgerald. Charged-particle thermonuclear reaction rates: II. Tables and graphs of reaction rates and probability density functions. *Nuclear Physics A*, 841(1-4):31, 2010c.
- C. Iliadis and M. C. Wiescher. Spectroscopic factors from direct proton capture. *Physical Review C*, 69(6):23, 2004.

- F. James. *Statistical Methods in Experimental Physics*. World Scientific Publishing Company, 2nd edition, 2006.
- H. Jeffreys. An Invariant Form for the Prior Probability in Estimation Problems. *Proceedings of the Royal Society of London A*, 186:453, 1946.
- J. José. *Stellar Explosions*. CRC Press, Boca Raton, FL, 2015.
- J. José, A. Coc, and M. Hernanz. Nuclear Uncertainties in the NeNa-MgAl Cycles and Production of ^{22}Na and ^{26}Al During Nova Outbursts. *The Astrophysical Journal*, 520:347, 1999.
- J. José, A. Coc, and M. Hernanz. Synthesis of intermediate-mass elements in classical novae: from Si to Ca. *The Astrophysical Journal*, 560(2):897, 2001.
- J. José and M. Hernanz. Nucleosynthesis in classical novae: CO versus ONe white dwarfs. *The Astrophysical Journal*, 494(2):680, 1998.
- J. José and M. Hernanz. The origin of presolar nova grains. *Meteoritics & Planetary Science*, 42(7-8):1135, 2007.
- J. José, M. Hernanz, S. I. Amari, K. Lodders, and E. Zinner. The imprint of nova nucleosynthesis in presolar grains. *The Astrophysical Journal*, 612(1):414, 2004.
- J. José and S. N. Shore. Observational mysteries and theoretical challenges for abundance studies. In *Classical Novae*, pages 121–140. Cambridge University Press, 2008.
- M. Kawaguti and S. Tanaka. DAWN for GEANT4 visualization. In *9th International Conference on Computing in High-Energy Physics*. Berlin, Germany, 1997.
- J. Keinonen and A. Anttila. Standard Resonance Strength in $^{27}\text{Al}(p,\gamma)^{28}\text{Si}$ Reaction. *Commentationes Physico-Mathematicae*, 46:61, 1976.
- K. J. Kelly. *Nuclear Reaction Rate Uncertainties and the $^{22}\text{Ne}(p,\gamma)^{23}\text{Na}$ Reaction: Classical Novae and Globular Clusters*. Ph.D. thesis, The University of North Carolina at Chapel Hill, 2016.
- K. J. Kelly, A. E. Champagne, L. N. Downen, J. R. Dermigny, S. Hunt, C. Iliadis, and A. L. Cooper. New measurements of low-energy resonances in the $^{22}\text{Ne}(p,\gamma)^{23}\text{Na}$ reaction. *Physical Review C*, 95(1):17, 2017.
- K. J. Kelly, C. Iliadis, L. N. Downen, and J. José. Nuclear mixing meters for classical novae. *The Astrophysical Journal*, 777:130, 2013.

- E. F. Kennedy, D. H. Youngblood, and A. E. Blaugrund. Lifetimes of the First Two Levels in ^{30}P . *Physical Review*, 158(4):897, 1967.
- G. F. Knoll. *Radiation Detection and Measurement*. John Wiley & Sons, New York, NY, 4th edition edition, 2010.
- J. Leitner, J. Kodolányi, P. Hoppe, and C. Floss. Laboratory Analysis of Presolar Silicate Stardust from a Nova. *The Astrophysical Journal Letters*, 754(2):41, 2012.
- N. Liu, L. Nittler, C. M. O. Alexander, J. Wang, M. Pignatari, J. José, and A. N. Nguyen. Stellar Origins of Extremely ^{13}C - and ^{15}N -enriched Presolar SiC Grains: Novae or Supernovae? *The Astrophysical Journal*, 820(2):1, 2016.
- N. Liu, L. Nittler, M. Pignatari, C. M. O. Alexander, and J. Wang. Stellar Origin of ^{15}N -rich Presolar SiC Grains of Type AB: Supernovae with Explosive Hydrogen Burning . *The Astrophysical Journal*, 842(1):L1, 2017.
- K. Lodders, H. Palme, and H. P. Gail. Abundances of the elements in the solar system. *Landolt Börnstein, New Series VI/4B*:560, 2009.
- R. Longland, S. Daigle, J. M. Cesaratto, C. Iliadis, and J. R. Newton. Target Backing Contamination Reduction. *TUNL Progress Report*, XLVIII:177, 2009.
- R. Longland, C. Iliadis, J. M. Cesaratto, A. E. Champagne, S. Daigle, J. R. Newton, and R. Fitzgerald. Resonance strength in $^{22}\text{Ne}(p,\gamma)^{23}\text{Na}$ from depth profiling in aluminum. *Physical Review C*, 81(5):055804, 2010a.
- R. Longland, C. Iliadis, A. E. Champagne, and C. Fox. Nuclear astrophysics studies at the LENA facility: The γ -ray detection system. *Nuclear Instruments & Methods in Physics Research A*, 566:452, 2006.
- R. Longland, C. Iliadis, A. E. Champagne, J. R. Newton, C. Ugalde, A. Coc, and R. Fitzgerald. Charged-particle thermonuclear reaction rates: I. Monte Carlo method and statistical distributions. *Nuclear Physics A*, 841(1-4):1, 2010b.
- P. B. Lyons, J. W. Toevs, and D. G. Sargood. Total Yield Measurements in $^{27}\text{Al}(p,\gamma)^{28}\text{Si}$. *Nuclear Physics A*, 130:1, 1969.
- J. MacMullin. *Validation of the Background Model for the MAJORANA DEMONSTRATOR*. Ph.D. thesis, The University of North Carolina at Chapel Hill, 2015.
- E. Mason. U Scorpii 2010 outburst: observational evidence of an underlying ONeMg white dwarf. *Astronomy & Astrophysics*, 532:L11, 2011.

- R. Middleton. A versatile high intensity negative ion source. *Nuclear Instruments & Methods in Physics Research*, 214:139, 1983.
- A. N. Nguyen and S. Messenger. Resolving the Stellar Sources of Isotopically Rare Presolar Silicate Grains Through Mg and Fe Isotopic Analyses. *The Astrophysical Journal*, 784(2):149, 2014.
- A. N. Nguyen, L. Nittler, F. J. Stadermann, R. M. Stroud, and C. M. O. Alexander. Coordinated Analyses of Presolar Grains in the Allan Hills 77307 and Queen Elizabeth Range 99177 Meteorites. *The Astrophysical Journal*, 719(1):166, 2010.
- A. N. Nguyen, F. J. Stadermann, E. Zinner, R. M. Stroud, C. M. O. Alexander, and L. Nittler. Characterization of Presolar Silicate and Oxide Grains in Primitive Carbonaceous Chondrites. *The Astrophysical Journal*, 656(2):1223, 2007.
- L. Nittler and C. M. O. Alexander. Automated isotopic measurements of micron-sized dust: application to meteoritic presolar silicon carbide. *Geochimica et Cosmochimica Acta*, 67:4961, 2003.
- L. Nittler, C. M. O. Alexander, R. Gallino, P. Hoppe, A. N. Nguyen, F. J. Stadermann, and E. K. Zinner. Aluminum-, Calcium- and Titanium-rich Oxide Stardust in Ordinary Chondrite Meteorites. *The Astrophysical Journal*, 682(2):1450, 2008.
- L. Nittler, C. M. O. Alexander, X. Gao, R. M. Walker, and E. Zinner. Stellar Sapphires: The Properties and Origins of Presolar Al_2O_3 in Meteorites. *The Astrophysical Journal*, 483(1):475, 1997.
- L. Nittler and F. Ciesla. Astrophysics with Extraterrestrial Materials. *Annual Review of Astronomy and Astrophysics*, 54(1):53, 2016.
- L. Nittler and P. Hoppe. Are presolar silicon carbide grains from novae actually from supernovae? *The Astrophysical Journal Letters*, 631:L89, 2005.
- K. Nomoto. Evolution of 8–10 M_\odot Stars Toward Electron Capture Supernovae. I. Formation of Electron-degenerate O + Ne + Mg Cores. *The Astrophysical Journal*, 277:791, 1984.
- B. M. Paine, S. R. Kennett, and D. G. Sargood. (p, γ) resonance strengths in the $s - d$ shell. *Physical Review C*, 17(5):1550, 1978.
- B. M. Paine and D. G. Sargood. (p, γ) Resonance Strengths in the $s - d$ Shell. *Nuclear Physics A*, 331:389, 1979.

- A. Parikh, J. José, F. Moreno, and C. Iliadis. The Effects of Variations in Nuclear Processes on Type I X-ray Burst Nucleosynthesis. *The Astrophysical Journal Supplement Series*, 178(1):110, 2008.
- A. Parikh, K. Wimmer, T. Faestermann, R. Hertenberg, J. José, R. Longland, H. F. Wirth, V. Bildstein, S. Bishop, A. A. Chen, *et al.* Improving the $^{30}\text{P}(p,\gamma)^{31}\text{S}$ Rate in Oxygen-neon Novae: Constraints on J^π Values for Proton-threshold States in ^{31}S . *Physical Review C*, 83(4):045806, 2011.
- A. Patil, D. Huard, and C. J. Fonnesbeck. PyMC: Bayesian Stochastic Modelling in Python. *Journal of Statistical Software*, 35(4):1, 2010.
- I. Pogrebnyak, C. Howard, C. Iliadis, R. Longland, and G. E. Mitchell. Mean proton and α -particle reduced widths of the Porter-Thomas distribution and astrophysical applications. *Physical Review C*, 88(1):015808, 2013.
- C. P. Poirier, J. Walinga, J. C. Manthuruthil, and G. I. Harris. Elastic and Inelastic Proton Scattering on Si^{29} . *Physical Review C*, 1(6):1982, 1970.
- M. Politano, S. G. Starrfield, J. W. Truran, A. Weiss, and W. M. Sparks. Hydrodynamic studies of accretion onto massive white dwarfs: ONeMg-enriched nova outbursts. I. Dependence on white dwarf mass. *The Astrophysical Journal*, 448:807, 1995.
- D. Prialnik. The evolution of a classical nova model through a complete cycle. *The Astrophysical Journal*, 310:222, 1986.
- B. Ramstein, L. H. Rosier, and R. J. de Meijer. Investigation of States in ^{30}P via the $^{30}\text{Si}(^3\text{He},t)^{30}\text{P}$ Reaction at 30 MeV. *Nuclear Physics A*, 363(0375-9474):110, 1981.
- T. Rauscher and F. K. Thielemann. Astrophysical reaction rates from statistical model calculations. *Atomic Data and Nuclear Data Tables*, 2000.
- J. P. L. Reinecke, F. B. Waanders, and P. Oberholzer. The Energy Levels of ^{30}P . *Nuclear Physics A*, 435:333, 1985.
- M. Riihonen, J. Keinonen, and A. Anttila. Hydrogen Burning of $^{29,30}\text{Si}$ in Explosive Carbon Burning. *Nuclear Physics A*, 313(1):251, 1979.
- C. Ritossa, E. García-Berro, and I. Iben, Jr. On the Evolution of Stars That Form Electron-degenerate Cores Processed by Carbon Burning. II. Isotope Abundances and Thermal Pulses in a $10 M_\odot$ Model with an ONe Core and Applications to Long-Period Variables, Classical Novae, and Accretion-induced Collapse. *The Astrophysical Journal*, 460:489, 1996.

- C. Rolfs and W. S. Rodney. *Cauldrons in the Cosmos: Nuclear Astrophysics*. The University of Chicago Press, Chicago, IL, 1988.
- G. Ryding, T. Smick, B. Park, J. Gillespie, P. Eide, T. Sakase, K. Ota, R. Horner, and D. Arnold. A 1.2 MeV, 100 mA Proton Implanter. 2012.
- A. L. Sallaska, C. Iliadis, A. E. Champagne, S. Goriely, S. G. Starrfield, and F. X. Timmes. STARLIB: A Next-Generation Reaction-Rate Library for Nuclear Astrophysics. *The Astrophysical Journal Supplement Series*, 207(1):1, 2013.
- D. G. Sargood. Charged particle reaction cross sections and nucleosynthesis. *Physics Reports*, 93(2):61, 1982.
- G. J. Schwarz. A New Abundance Analysis of the ONeMg Nova QU Vulpeculae. *The Astrophysical Journal*, 577:940, 2002.
- G. J. Schwarz, J.-U. Ness, J. P. Osborne, K. L. Page, P. A. Evans, A. P. Beardmore, F. M. Walter, L. A. Helton, C. E. Woodward, M. F. Bode, *et al.* *SWIFT* X-ray Observations of Classical Novae. II. The Super Soft Source Sample. *The Astrophysical Journal Supplement Series*, 197(2):31, 2011.
- G. J. Schwarz, S. N. Shore, S. G. Starrfield, and K. M. Vanlandingham. Abundance Analysis of the Extremely Fast ONeMg Novae V838 Herculis and V4160 Sagittarii. *The Astrophysical Journal*, 657(1):453, 2007.
- T. M. Semkow, G. Mehmood, and P. P. Parekh. Coincidence summing in gamma-ray spectroscopy. *Nuclear Instruments & Methods in Physics Research A*, 290:437, 1990.
- S. N. Shore, G. J. Schwarz, H. E. Bond, R. A. Downes, S. G. Starrfield, A. Evans, R. D. Gehrz, P. H. Hauschildt, J. Krautter, and C. E. Woodward. The Early Ultraviolet Evolution of the ONeMg Nova V382 Velorum 1999. *The Astronomical Journal*, 125:1507, 2003.
- M. S. Smith, W. R. Hix, S. Parete-Koon, L. Dessieux, M. W. Guidry, D. W. Bardayan, S. G. Starrfield, D. L. Smith, and A. Mezzacappa. Nova Nucleosynthesis Calculations: Robust Uncertainties, Sensitivities, and Radioactive Ion Beam Measurements. *AIP Conference Proceedings*, 637:161, 2002.
- P. B. Smith and P. M. Endt. Resonant Absorption of Gamma Radiation from the $\text{Si}^{30}(\text{p},\gamma)\text{P}^{31}$ Reaction. *Physical Review*, 110:1442, 1958.
- M. A. J. Snijders, T. J. Batt, P. F. Roche, M. J. Seaton, D. C. Morton, T. A. T. Spoelstra, and J. C. Blades. Nova Aquilae 1982. *Monthly Notices of the Royal Astronomical Society*, 228:329, 1987.

- S. G. Starrfield, C. Iliadis, and W. R. Hix. Thermonuclear processes. In *Classical Novae*, pages 77–101. Cambridge University Press, 2008.
- S. G. Starrfield, C. Iliadis, W. R. Hix, F. X. Timmes, and W. M. Sparks. The effects of the *pep* nuclear reaction and other improvements in the nuclear reaction rate library on simulations of the classical nova outburst. *The Astrophysical Journal*, 692(2):1532, 2009.
- S. G. Starrfield, W. M. Sparks, and J. W. Truran. Hydrodynamic models for novae with ejecta rich in oxygen, neon, and magnesium. *The Astrophysical Journal Letters*, 303:5, 1986.
- S. G. Starrfield, J. W. Truran, M. C. Wiescher, and W. M. Sparks. Evolutionary sequences for Nova V1974 Cygni using new nuclear reaction rates and opacities. *Monthly Notices of the Royal Astronomical Society*, 296(3):502, 1998.
- K. B. Swartz, D. W. Visser, and J. M. Baris. A Java-based data acquisition system for nuclear physics. *Nuclear Instruments & Methods in Physics Research A*, 463:354, 2001.
- Z. E. Switkowski, R. O’Brien, and A. K. Smith. Total Yield Measurements in $^{23}\text{Na}(p,\gamma)^{24}\text{Mg}$. *Australian Journal of Physics*, 1975.
- M. Tanabashi, K. Hagiwara, K. Hikasa, K. Nakamura, Y. Sumino, F. Takahashi, J. Tanaka, K. Agashe, G. Aielli, C. Amsler, *et al.* Review of Particle Physics. *Physical Review D*, 98(3):030001. 1898 p, 2018.
- D. R. Tilley, C. M. Cheves, J. H. Kelley, S. Raman, and H. R. Weller. Energy levels of light nuclei, $A = 20$. *Nuclear Physics A*, 636(3):249, 1998.
- J. W. Truran. Classical novae: the thermonuclear runaway model. *Progress in Particle and Nuclear Physics*, 6:177, 1981.
- C. van der Leun and P. M. Endt. Investigation of Four Resonances in the Reaction $\text{Si}^{29}(p,\gamma)\text{P}^{30}$. *Physical Review*, 110(1):96, 1958.
- J. J. M. Van Gasteren, A. J. L. Verhage, and A. Van Der Steld. Investigation of the $^{31}\text{P}(\tau,\alpha)^{30}\text{P}$ reaction at $E_\tau = 15$ MeV. *Nuclear Physics A*, 231:425, 1974.
- K. M. Vanlandingham. Private communication. 2012.
- K. M. Vanlandingham, G. J. Schwarz, S. N. Shore, S. G. Starrfield, and R. M. Wagner. New Elemental Abundances for V1974 Cygni. *The Astrophysical Journal*, 624(astroph/0501648):914, 2005.

- K. M. Vanlandingham, S. G. Starrfield, and S. N. Shore. Elemental abundances for Nova V693 Coronae Austrinae 1981. *Monthly Notices of the Royal Astronomical Society*, 290:87, 1997.
- K. M. Vanlandingham, S. G. Starrfield, S. N. Shore, and G. Sonneborn. Elemental abundances for Nova LMC 1990#1. *Monthly Notices of the Royal Astronomical Society*, 308(2):577, 1999.
- C. W. Vermette, W. C. Olsen, D. A. Hutcheon, and D. H. Sykes. A study of ^{30}P levels below 5 MeV. *Nuclear Physics A*, 111(1):39, 1968.
- D. A. Vermilyea. The Kinetics of Formation and Structure of Anodic Oxide Films on Tantalum. *Acta Metallurgica*, 1(3):282, 1953.
- C. Vollmer, P. Hoppe, F. E. Brenker, and C. Holzappel. Stellar MgSiO_3 Perovskite: A Shock-transformed Stardust Silicate Found in a Meteorite. *The Astrophysical Journal*, 666(1):L49, 2007.
- S. Wanajo, M. Hashimoto, and K. Nomoto. Nucleosynthesis in ONeMg novae: models versus observations to constrain the masses of ONeMg white dwarfs and their envelopes. *The Astrophysical Journal*, 523(1):409, 1999.
- M. Wang, G. Audi, F. G. Kondev, W. J. Huang, S. Naimi, and X. Xu. The AME2016 atomic mass evaluation (II). Tables, graphs and references. *Chinese Physics C*, 41(3):030003, 2017.
- B. Warner. Properties of novae: an overview. In *Classical Novae*, pages 16–33. Cambridge University Press, 2008.
- C. R. Westerfeldt. Charging Systems. In *Electrostatic Accelerators*, pages 89–100. Springer, Berlin Heidelberg, 2005.
- L. S. Wielunski, G. D. Paterson, J. M. Bell, and R. E. Clegg. Production of Si^+ and Cl^+ ion beams from a Freeman type ion source using low toxicity and non-corrosive vapours as source gas. *Nuclear Instruments & Methods in Physics Research B*, 215(1-2):262, 2004.
- J. S. C. Wills, J. Diserenes, R. A. Lewis, H. Schmeing, and T. Taylor. A compact high-current microwave-driven ion source. Technical report, Chalk River, Ontario, 1998.
- R. A. Wolf. Rates of Nuclear Reactions in Solid-Like Stars. *Physical Review*, 137(6B):B1634, 1965.
- C. Wrede. The $^{30}\text{P}(\text{p},\gamma)^{31}\text{S}$ reaction in classical novae: progress and prospects. AIP

Advances, 4(4):041004, 2014.

C. Wrede, J. A. Caggiano, J. A. Clark, C. M. Deibel, A. Parikh, and P. D. Parker. Thermonuclear $^{30}\text{S}(p,\gamma)^{31}\text{Cl}$ reaction in type I x-ray bursts. *Physical Review C*, 79:045808, 2009.

J. F. Ziegler, J. P. Biersack, and M. D. Ziegler. *SRIM, the Stopping and Range of Ions in Matter*. SRIM Company, 2015.